Multiplexed High-Precision Radial Velocities: Searching for Hot Jupiters in Southern Open Star Clusters

by

John Ira Bailey, III

A dissertation submitted in partial fulfillment
of the requirements for the degree of
Doctor of Philosophy
(Astronomy and Astrophysics)
in The University of Michigan
2016

Doctoral Committee:

Professor Mario L. Mateo, Chair
Professor Fred C. Adams
Professor Lee W. Hartmann
Professor John D. Monnier
Professor Russel J. White, Georgia State University

© John Ira Bailey, III 2016
All Rights Reserved

ACKNOWLEDGMENTS

I am incredibly grateful to the many people who have provided me with support, guidance, and friendship over the many years of my education. First and foremost, I would like to thank Mario Mateo, who has been a valued mentor. Mario's guidance has been instrumental in shaping my evolution from fresh faced graduate student into an Astronomer. The trust and confidence he placed in my abilities as a young graduate student to design and develop major portions of M2FS gave me an opportunity to develop skills that would otherwise have taken many more years and many different projects. Mario, you truly have been an academic father through thick and thin: whether it was debating a research direction or pushing me to bike 500 miles and up 30,000 feet of mountain in a week you have shaped me academically and made me into a better person.

My dissertation committee members, Russel White, Lee Hartmann, John Monnier, and Fred Adams have been instrumental in shaping my research and I thank them for their advice, encouragement, and insight. I am particularly grateful to Russel for his continued guidance and for first exposing me to Astronomy: I have little idea where I would be today if you had not hired me as an undergraduate so many years ago. I look forward to many more years of collaboration.

I appreciate the work of the department's administrative staff, especially Brian Cox and Jan Malaikal (and Ann, Sarah, and Li, you are not forgotten!), who ensured that my years at Michigan went smoothly. You always greeted me with a smile, were quick to respond to any question, and helped resolve the occasional logistical hurdle.

Roy and Mark your assistance and advice on computer issues has ensured things just worked and I thank you for always seeing we got the tools we needed for M2FS.

To all of my friends in Ann Arbor, thank you for making the past six years so enjoyable. Whether it was canoeing, cycling, socializing over drinks and board games, or our annual potluck your camaraderie ensured life was never dull and friends abundant. To everyone at Carnegie Observatories and especially Charlie, Vince, Jerson, Robert, Greg, Steve, Jeff, George and Eric thank you for making it a home and family. Charlie, M2FS and I both owe you a great deal for opening your home to me and providing a place to live during the oh-so-many trips to Santa Barbara Street.

Prior to graduate school, many teachers and researchers inspired me. Foy Hannum and Tim Burgess your talents have undoubtedly touched far more lives than mine alone: Know that I am forever grateful for your instruction and guidance. Foy, that you have grown from a teacher into a friend as I have grown from a high-school student into an adult means so very, very much. Drs. Rochowiak, Dimmock, Weisskopf, and Strong your guidance, kindness, wisdom, and patience has had a lasting impact. It truly is remarkable how large of an impact even a single semester can have on one's life.

To my wife, Brittany, we did it! Up and down, left and right, together and apart (sometimes for weeks at a go) we managed two degrees, our first house, a move to Belgium, and even a vacation or two. More than six years of mutual hard work means we shall henceforth be known as Drs. Bailey.

Last, but most certainly not least, I thank my family, parents Jan and John, brother Jim, and Granna. Mom, Dad without your faith and belief in me there is no doubt I would have achieved far less. Through all the years, all the schools, and all the ups and downs of life the one constant has been that at the end of the day you are there for me. Jim I look forward to when it is your turn, though degree or no I'm

proud to have you as my brother. Dearest Granna, you have, without a doubt, had such an amazing and enormous impact on me. From infancy you have been there for me and I will treasure our memories of Christmases, Thanksgivings, reunions, and most of all treasure your words of wisdom. With every passing year you have taught me something new and I treasure each and every moment we have together.

Chapters II and III of this thesis are based on work published in *SPIE Proceedings* and supported by NFS/MRI development grant 0923160. Chapter IV has been submitted for publication in *The Astronomical Journal*, and is reproduced here with permission and minor modifications. Chapters V and VI are based on work to appear in *The Astrophysical Journal*. All three were supported by NSF AAG grant 1312997 and portions by NSF AAG grant 1009634 and NASA Origins of Solar Systems grant NNX11AC32G. This research has made use of the Exoplanet Orbit Database and the Exoplanet Data Explorer at exoplanets.org. I acknowledge travel and research grants from the University of Michigan Rackham Graduate School, which enabled me to present portions of this work at various conferences and funded the filters used in my survey. Finally I acknowledge funding support from The College of Liberal Arts and Sciences at the University of Michigan.

TABLE OF CONTENTS

LIST OF FIGURES

Figure

LIST OF TABLES

Table

LIST OF APPENDICES

Appendix

ABSTRACT

The Michigan/Magellan Fiber System enables a multiplexed, precision radial velocity (pRV) survey of open star clusters for warm- and hot-Jupiter exoplanetary companions while simultaneously allowing detailed study of stellar properties. To accomplish this, I created an automated control system that enables users to rapidly reconfigure M2FS for different scientific programs and developed a novel mechanism to improve its maximum resolving power from ∼20,000 to ∼60,000. I report the results of a survey of 126 photometric members of the young (141 Myr), nearby (346 pc) open star cluster NGC 2516 and 100 photometric members plus 25 candidate members of the young (72 Myr), nearby (491 pc) open cluster NGC 2422 (M 47). I developed a prescription to spectroscopically measure T_{eff} (±30 K), [Fe/H] and [α/Fe] (±0.02 dex), and $v_r \sin(i)$ (±0.3 km/s). Observations of a reference star show my approach with M2FS can achieve RV precisions of 20–60 m/s for up to 128 stars simultaneously. RV measurements enabled memberships lists to be confirmed; 41 claimed members were rejected in NGC 2516 and 52 in NGC 2422. Twelve new members of NGC 2422 are identified, as is a separate RV clustering of 11 giant-like stars in the field of NGC 2422. I propose these giant-like stars are members of a background Milky Way halo stream. I report the discovery of 8 double-lined spectroscopic binaries (SBs) and used pRV measurements spanning 386 days to identify 54 single-lined SBs, 44 of which are new discoveries (16 and 9 as members in NGC 2516 or NGC 2422). I also identify 53 stars which exhibit significant low-amplitude variability after accounting for average levels of stellar jitter. Finally, I identify 8 low-amplitude RV variable stars as candidate hot-Jupiter hosts worth follow-up investigation.

CHAPTER I

Introduction

1.1 Exoplanets in Open Clusters

The 1600+ exoplanets discovered over the past 20 years have fundamentally altered how we see our place in the universe and are the product of enormously intensive efforts to search for and characterize these distant worlds. The select few known in open star clusters (8, presently) provide precious insight into processes governing their formation and evolution as they exist in environments (i.e. star clusters) that have well understood ages, chemical abundances, and dynamical states relative to stars in the field.

The discovery that planetary systems exhibit "hot Jupiters" (HJs; exoplanets with masses $\gtrsim 0.5$ M_{Jup} and periods typically < 10 days), as well as many closely-packed systems with substantial numbers of close "Neptunes" and "super-earths" led to drastic revisions to both theories of planet formation and dynamical evolution. Contemporary formation models for gas- and ice-giant planets typically fall into the broad categories of core accretion (Mizuno et al., 1980) or disk gravitational instability models (Boss, 1997), with current ideas favoring the core accretion model for most systems, consistent with the increase in frequency of massive exoplanets with increased stellar metallicity (e.g. Wang & Fischer, 2015), although some distant massive companions ("super-Jupiters") may be formed by gravitational fragmentation

(see discussion in Chabrier et al., 2014). It remains unclear if the orbits of hot-Jupiters evolve inward through coupling to a gaseous disk (Goldreich & Tremaine, 1980; Lin et al., 1996), via dynamical scattering off clumps and other bodies (e.g., Rasio & Ford, 1996; Jurić & Tremaine, 2008), or even secular interactions with a distant stellar companion (Kozai cycles; e.g., Fabrycky & Tremaine, 2007). Kley & Nelson (2012) and Baruteau et al. (2014) provide recent discussions. Though much effort has been spent testing these theories they all remain viable, at least for some systems (see review by Helled et al., 2014). The core reason is that diagnostics (e.g. the period-eccentricity distribution) are muddled by the wide and often unknown ages of host stars in field star exoplanetary systems. A direct solution would be to find young exoplanets with ages $\sim$1 Myr, however the extreme activity of host stars at T Tauri ages has thus far inhibited detecting planets (e.g. Huerta et al., 2008; Huélamo et al., 2008; Prato et al., 2008; Crockett et al., 2012; Bailey et al., 2012); some very young candidates nevertheless remain (e.g. Ciardi et al., 2015).

These theories do make various distinct predictions regarding the properties of hot gas giants and their orbits for the first $\sim$1 Gyr, suggesting planets found in open clusters $\lesssim$ 1 Gyr would provide valuable insight. The slower formation of gas giants via core accretion allows for the dissipation of energy and entropy, and is predicted to yield planets that are significantly cooler, smaller, and denser than those formed via disk instabilities, with the differences predicted to persist up to 1 Gyr (c.f. Marley et al., 2007; Fortney & Nettelmann, 2010; Fortney et al., 2008 vs. Galvagni et al., 2012; but see also Mordasini et al., 2012). Though this requires a relatively rare transit to measure the radius, transits are relatively more likely for hot gas giants ($\sim$ 5%; Charbonneau et al., 2007). The relative timescales of disk coupling ($\sim$10 Myr) versus dynamical scattering at ($\sim$100s Myr) could allow direct tests from the occurrence rates of HJs in younger clusters (e.g. Quinn et al., 2014). Additionally, dynamical scattering is expected to yield mostly eccentric orbits at birth, in contrast to the

circular orbits produced by disk interactions. Before tidal circularization fully erases this tracer by ∼1.6 Gyr (following Adams & Laughlin, 2006) the period-eccentricity distribution of young hot gas giants can provide a dynamical tracer of their migration history.

Indeed, considerable effort has been expended searching for such systems with known ages (e.g., Paulson et al., 2004; Bailey et al., 2012; Meibom et al., 2013; Quinn et al., 2012, 2014). The first exoplanets orbiting solar-like stars in a cluster (F, G, or K and on the main sequence) were announced by Quinn et al. (2012). To date, gas giant exoplanets orbiting main sequence (MS) stars have been discovered via transits (NGC 6811 Meibom et al., 2013) and radial velocity (RV) techniques (M 67; Brucalassi et al., 2014; Praesepe, Quinn et al., 2012; Hyades, Quinn et al., 2014), though none of the latter are also transiting systems. One system discovered in the Hyades is noteworthy for its distinctly non-zero eccentricity ($e = 0.08 \pm 0.02$) and dynamically young age, implying some form of multi-body process may have played a role in its evolution (Quinn et al., 2014). This is a clear example of how even a single hot gas giant in an open cluster has the potential to strongly inform planet-migration theories. Any such systems that also happen to be transiting will produce even more powerful constraints on gas giant formation models by revealing precise information on the sizes, densities and compositions of exoplanets with well-determined ages. Indeed, identifying transiting planets in open clusters is a key science goal of NASA's K2 mission (Howell et al., 2014) and their efforts have already identified a Neptune-sized planet in the Hyades (Mann et al., 2015).

The practical problem of finding cluster exoplanets is one of efficiency. Over two decades of exoplanetary searches RV semi-amplitudes have been measured for more than 600 systems (Han et al., 2014). In contrast, the total number of known exoplanets orbiting MS stars in open clusters remains in the mid-single digits (eight stars in as of this writing). The deficiency of known hot Jupiters in clusters is not a

consequence of higher stellar RV jitter. Measured values of this in open clusters are $\sim$15 m/s at $\sim$400 Myr (Paulson et al., 2004; Quinn et al., 2012), which is roughly an order of magnitude less than the amplitude induced by a typical hot gas giant. For example, Figure 1.1 shows the distribution of exoplanet mass versus orbital period; HJs have RV amplitudes that rage from $\sim$30 m/s to $>$ 500 m/s (more generally, the RV signal of a planet of mass M orbiting a star of mass $M_\star$ with a period P, inclination i, and eccentricity e is given by Equation 1.1). Rather, clusters tend to be considerably more distant than the closest individual field stars and are hence fainter and consequently harder to monitor. Moreover the same technique used for field stars – individual spectra, one star at a time – is typical of cluster RV surveys. Lengthy campaigns involving thousands of visits are needed to find the comparatively rare cases with detectable velocity amplitudes. RV surveys indicate only $1.2 \pm 0.4\%$ of all FGK stars in the solar neighborhood harbor HJs (Wright et al., 2012) and cluster occurrence rates appear similar (Quinn et al., 2014; Meibom et al., 2013) so hundreds of targets must be monitored.

$$K \approx 141 \text{ m/s} \left(\frac{P}{3 \text{ days}}\right)^{-1/3} \left(\frac{M}{\text{M}_{\text{Jup}}}\right) \left(\frac{M_\star}{\text{M}_\odot}\right)^{-2/3} \left(1 - e^2\right)^{1/2} \sin i \qquad (1.1)$$

In addition to the open cluster searches previously mentioned there has been a significant effort to address the efficiency issue in the past five years with the SDSS-III MARVELS project. This project surveyed $\sim$5500 Sun-like stars brighter than V = 12 at velocity precisions of $\lesssim$ 30 m/s (Paegert et al., 2015) and has recently begun producing its first results (e.g. Ge et al., 2015; Wright et al., 2013) after some initial issues with sample contamination. MARVELS is not designed to target open clusters: it is optimized for brighter field targets and enhanced sky coverage (56 targets over a seven square degree field) and thus addresses a somewhat different portion of parameter space. M2FS's multi-object capabilities are well suited to obtain highly-multiplexed RVs of stars in open clusters and should be capable of efficiently

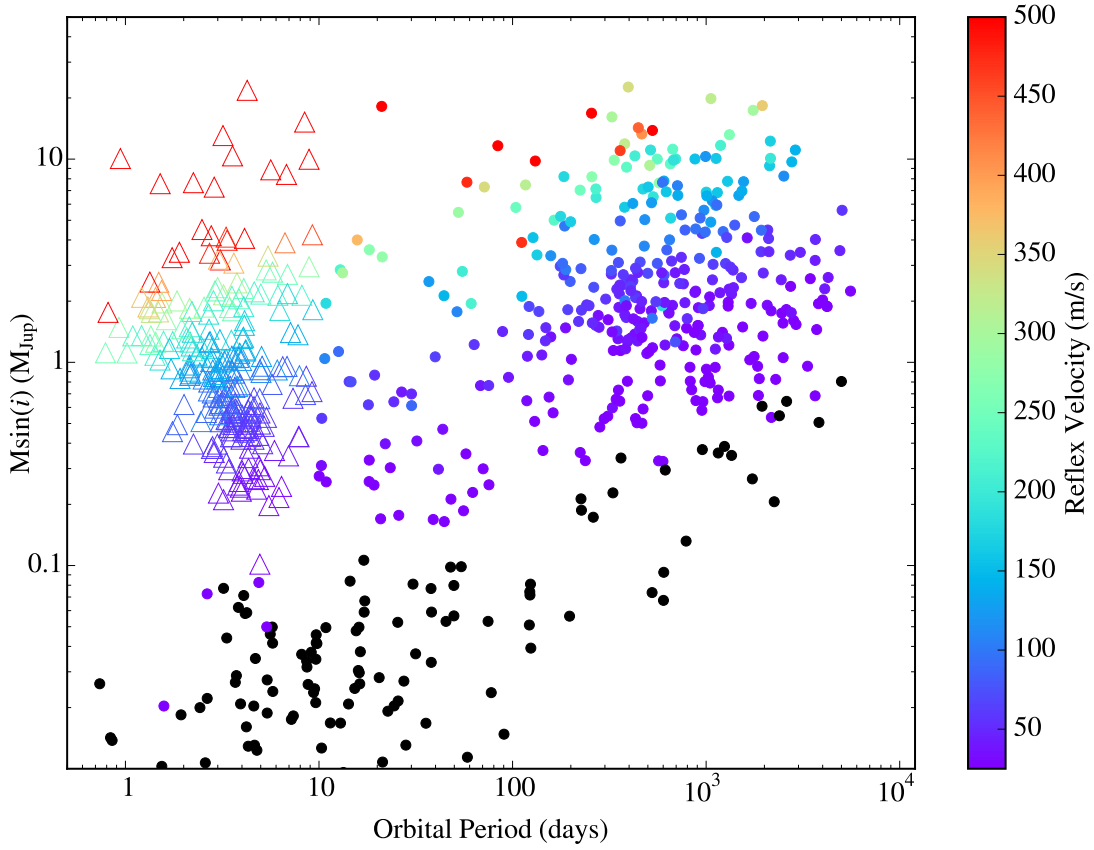

Figure 1.1: A plot of extrasolar planet masses (actually, $m \sin(i)$) vs. orbital period. Colors denote the reflex velocity induced in the host star. Black circles are cases where the induced velocity is below 25 m/s. Open triangles indicate the classic hot Jupiters ($>$ 0.1 M_{Jup} and P $<$ 10 day). Is is apparent that the vast majority of HJs induce reflex motions exceeding 50 m/s. Data is from exoplanets.org (Han et al., 2014).

surveying Sun-like (e.g. F5-K5) stars in open clusters within ∼1 kpc for HJs with the enhancements I have made as part of this thesis. Such a distance limit would enable the survey of stars in clusters that range in age from about 100 Myr to nearly 1 Gyr, well posed to address the previously mentioned issues. The next section (§1.2) of this introduction describes just such an instrument I have helped design and construct as part of this thesis. Then, as described at the end of this introduction, the second portion of this thesis describes the results from my survey of stars in stars in two open clusters designed to address these questions.

High dispersion spectroscopy of stars in open clusters has the added benefit of producing exquisite kinematics and stellar properties for the members and candidate members surveyed. The frequency and distribution of binaries can provide clues to the original configurations of clusters (e.g. how much they have expanded upon gas removal; Parker et al., 2009), with implications for understanding star formation by illustrating differences between binary properties in clusters vs. dispersed regions (Kroupa & Petr-Gotzens, 2011). The high-resolution, high S/N spectra needed for precise RVs can also provide insight into the metal abundances of cluster stars, providing a simultaneous characterization of the natal environment of any exoplanets within and also informing studies of the broader chemical structure of the Milky Way. Such is the value of this alone the BOCEE project has undertaken the task of characterizing the chemistry of a number of open clusters (Bragaglia & Tosi, 2006). The kinematic precision necessary to find even the most massive of hot Jupiters can be expected to produce target RV precisions at the 10–25 m/s level . With an anticipated precision of better than 10 μas/yr (∼20 m/s at 500 pc, Lindegren, 2010; Lindegren et al., 2012), GAIA data will offer comparable tangential velocities for stars targeted in such clusters and thereby offer an unprecedented 3D kinematic picture of stars within open clusters.

1.2 The Michigan/Magellan Fiber System

1.2.1 A Brief History Multi-Object Spectroscopy

The history of multi-object spectroscopy (MOS) dates all the way back to the close of the 19$^{\rm th}$ century when Edward Pickering used an objective prism (Pickering, 1890) to compile the Henry Draper catalogue – the first ever full-sky spectroscopic catalog. In the late 1970's, with the invention of fiber optics just a decade earlier, Hill et al. (1980) created the first fiber-fed MOS and ushered in an era where MOS are a valuable capability at many astronomical facilities around the globe. When deployed on a large, wide-field telescope, highly multiplexed MOSs – both fiber-fed and multi-slit – provide powerful capabilities and efficiencies that are impossible to match with conventional single-slit instruments. With the advent of large-scale photometric surveys – starting with SDSS and continuing into the foreseeable future with projects such as PanSTARRS, SkyMapper, DES, GAIA and LSST – the demand for powerful complementary MOS capabilities continues to grow just to keep up with the vast numbers of targets needing spectroscopic followup.

Multi-object spectrographs are now common at modern observatories, underscoring the power of the approach. Deimos (Keck Observatory), GMOS (Gemini), FORS (Very Large Telescope, VLT), Hectospec (Multiple Mirror Telescope, MMT), IMACS (Magellan), and FMOS (Subaru) are examples of workhorse instruments that support moderate- to wide-field multi-object spectroscopic capabilities on 6.5 m to 10 m class telescopes, at relatively low resolution (R$\lesssim$3000), and with multiplexing factors ranging from tens to thousands. There are now also a number of moderate- to high-resolution (R$\gtrsim$10,000) MOS. FLAMES (VLT), Hectochelle (MMT), and MMFS (Magellan, formerly) are examples that use fiber optics to pack hundreds of spectra onto large-format CCD detectors. Gemini and Subaru are planning ambitious wide-field MOS (WFMOS and PFS) to achieve multiplexing factors of a few thousand at

high spectral resolution for Northern targets, though likely not for at least a few more years. These instruments address a vast range of astronomical problems, including studies of dark matter, dark energy, quasar absorption line systems, Galactic structure, and chemical evolution to name a few. They also do so with great efficiency: For example, the first three-hour science exposure with MMFS in 2003 equaled the science output of two weeks of single-object spectroscopy on the same telescope.

As productive as MMFS was, it had a number of significant, and sometimes frustrating, shortcomings that limited its scientific reach and complicated its operation. Virtually all of these stemmed from its use of the Magellan Inamori Kyocera Echelle (MIKE) spectrograph as a back-end, which was not optimized for fibers. For example, since the MIKE CCDs have a 2:1 aspect ratio, about 40% of a typical echelle order was lost. The effective spectral resolution of MMFS ($R \sim$13,500) was notably lower than competing fiber systems (FLAMES, Hectochelle), limiting its utility for a number of projects, particularly chemical-abundance studies. MIKE also exhibits a complicated family of internal reflections that proved problematic for multi-object observations. Also, MIKE, designed with separate red- and blue-optimized cameras, uses a dichroic for full spectral coverage of single targets and, though the dichroic is removed for MMFS, there is only a limited wavelength range (480–530 nm) where all of MMFS's fibers could be used simultaneously. Finally, MIKEs cross-dispersion prism was designed to separate echelle orders from a 5 arcsecond slit, over four times more than required for fiber observations. Finally, a major operational problem with MMFS was that the MIKE injection optics had to be removed from both cameras to allow the fibers access to spectrograph focal planes and the MIKE CCDs needed to be rotated by 90 degrees to image all the fibers. Although MIKE was designed to support MMFS, the process certainly caused long-term wear and increased the risk of catastrophic damage to the injection optics and CCDs.

1.2.2 Scientific Motivation for an Upgraded System

The Michigan/Magellan Fiber System (M2FS), the successor to MMFS, was conceived of as a complete fiber-fed MOS system with its own, purpose-built spectrograph. This design allowed M2FS to both overcome MMFS's shortcomings and integrate new MOS capabilities to match or exceed the performance of many of the other MOS systems now available at other major observatories. MMFS set a very high bar for M2FS. Designed to study the internal kinematics of dwarf spheroidal galaxies (dSph), which gained importance with the discovery of internal kinematics that suggested they are dominated by dark matter (Aaronson, 1983), MMFS proved exceptionally useful for Drs. Mario Mateo and Matthew Walker to develop samples of more than 7000 stars in dSph systems, an order of magnitude better than the few hundred stars previously surveyed (c.f. Walker et al., 2007; Mateo et al., 2008; Walker et al., 2009). Though also somewhat capable of investigations focusing on kinematic and metallicity surveys of star-forming regions, kinematic studies of extragalactic globular clusters, and spectroscopy of stars in intermediate-age Magellanic Cloud star clusters MMFS's limitations severely limited its utility in these areas.

M2FS was designed to preserve the capabilities of MMFS and gain new abilities to address projects ranging from newly discovered Milky Way faint and 'ultrafaint' satellites to outflows from Young Stellar Associations. Key among these projects was the anticipated need for followup to the SkyMapper and Dark Energy Survey's (DES) searches for the so-called Milky Way 'missing satellites'. Over the past decade, mining of SDSS has produced more than a dozen new dwarf-galactic satellites (e.g. Willman et al., 2005; Zucker et al., 2006; Belokurov et al., 2007) and the population of the Local Group has nearly tripled (McConnachie, 2012). Recently nine new satellites in southern hemisphere have been discovered (Koposov et al., 2015; Bechtol et al., 2015), all needing followup spectroscopy for confirmation and the study of their kinematics and chemistry. One of the chief advantages of M2FS here is its fiber packing density:

at nearly three times that of comparable instruments and 15% better than MMFS it is capable of much more efficiently targeting these densely clustered objects. Indeed M2FS has already resulted in more than three publications focusing on the followup of these dwarfs alone (e.g. Walker et al., 2015a; Bonnivard et al., 2015; Walker et al., 2015c).

Surveys of globular clusters (GCs, both intra- and extra-Galactic) were also a key motivator. In addition to the ability to measure the kinematics and chemical abundances of extra-Galactic cluster populations (a task vital to weighing distant massive galaxies and studying their formation histories), M2FS was designed to efficiently develop complete and precise internal kinematics for Milky Way GCs allowing for a full Jeans solution and comparison with modern N-body simulations. In addition to these topics, M2FS is very capable of programs involving Halo Streams, internal kinematics and abundances of stellar open clusters and young associations (to determine initial conditions, track evolution, and calibrate stellar ages.

Finally, during the design of M2FS, I played a key role in significantly increasing its available resovling power (from R$\sim$20,000 to $\sim$55,000). This design change (described in detail in §2.3) was motivated by my desire to make M2FS capable of the cluster exoplanet science which I outlined in the preceding section and the investigation of which composes the second half of this thesis. In addition it has ushered in additional capabilities for detailed chemical abundance studies of stars in Galactic globular clusters (e.g. Roederer et al., 2015; Johnson et al., 2015a) and investigations of disk accretion variability around low-mass young stars (Briceño et al., 2016).

1.2.3 M2FS

The Michigan/Magellan Fiber System (M2FS) is a new fiber-fed, multi-object optical spectroscopic system (MOS) designed for the Magellan/Clay 6.5 m telescope at Las Campanas Observatory in Chile. Table 1.1 summarizes the basic characteristics

of M2FS and compares these to its predecessor (MMFS, see Walker et al., 2007 for a broad summary of that system) and other MOSs currently in use on comparably large telescopes (FLAMES on the VLT, Pasquini et al., 2002; HectoSpec/HectoChelle on the MMT, Fabricant et al., 2005).

M2FS is capable of taking simultaneous spectra over the 370–950 nm range for up to 256 targets over a half-degree field-of-view at a wide variety of resolutions (R$\sim$500–55,000). Fibers accept light from the sky at the f/11 Nasmyth E focal surface of the Magellan/Clay 6.5 m telescope. Each fiber samples the sky through a 1.2" aperture; can be packed to within 13" of one another with no restrictions within the M2FS field of view; and are held in place by plug plates drilled in advance of an observing run using astrometry for the desired targets. Additional details of M2FS's capabilities are provided in Table 1.2 and in Mateo et al. (2012).

M2FS consists of four basic structures (Figure 1.2):

- The M2FS Spectrograph (MSpec), which consists of twin spectrographs, each of which can be fed by up to 128 fibers to produce spectra for a variety of supported modes with available spectral resolutions ranging from under 500 to over 55,000;

- The M2FS Fiber Mount (MFib), which attaches to the rotator disk of the telescope and which holds the 256 M2FS science fibers, guider fibers and guider cameras, the Shack-Hartmann periscope to enable continuous active optics control, the fiber plug plates which hold the fibers in position during observations, and the field telecentrator which serves to define the focal surface for the fibers and make the chief rays for all field positions parallel to the telescope optical axis;

- A Wide-Field Corrector (WFC), which is mounted onto the elevation disk of the telescope at its Nasmyth-East focus and which is designed to provide excellent

Table 1.1: Basic characteristics of M2FS and other fiber MOS

Property	M2FS		MMFS		FLAMES (VLT)		Hecto (MMT)	
	HiRes	Lo/Med	Blue	Red	UVES	GIRAFFE	Spec	Chelle
Channels	2	2	2		1	1	1	1
# of Fibers	256	256	256		8	132	300	240
λ Range (nm)	370–950		360–520	500–900	480–900	370–950	370–920	
Resolution	18–55k	0.2–14k	18k	15k	46k	7–24k	1.5-3k	32k
X-Dispersed	Yes	No	Yes		Yes	No	No	No
Fiber Diam.	1.2”		1.4”		1.0”	1.2”	1.5”	
Min. Fiber Sep.	12”		14”		>30” (variable)		>30” (variable)	
Field Diam.	30’		20’		25’		60’	
V_{limit}: S/N=5, 2 hrs, 500 nm, med. seeing	21.5 R∼20k	24.0 R∼2k	20.7	20.5	21.0	22.5 R∼7k	23.5 R∼1.5k	2.05

image quality relative to the M2FS fiber apertures over a 30 arcminute diameter field of view; and

- The M2FS Calibration Unit (MCal), which is mounted in the secondary cage of the Magellan/Clay telescope to deploy a suite of spectral calibration lamps and support the M2FS Fiber Locator System (FLS).

To use M2FS, fibers are manually inserted into holes drilled in plug plates mounted at the telescope focal surface (Figure 1.3). These fibers, ∼3 m in length, then terminate at the focal surface of the collimator/cameras belonging to a pair of identical quasi-Littrow spectrographs. For historical reasons, these are identified as the ‘red’ and ‘blue’ M2FS arms, each fed by 128 fibers. The spectrographs are equipped with traditional and R0.7 echellette gratings for low and medium resolution work as well as an R2.0 echelle grating with a prism cross-disperser for high-resolution use. Filters located just below the fiber termination surface isolate specific orders, necessary for use in echelle and echellette modes. Each arm uses an E2V 4k x 4k anti-fringing CCD with 15 μm pixels. Additional details can be found in Mateo et al. (2012).

Most interaction with M2FS is via an instrument GUI running on the observers workstation, though observers also interact with MFib when it is time to manually reconfigure the fibers (see below). Grating angles, focus, slits, filter selection, grating

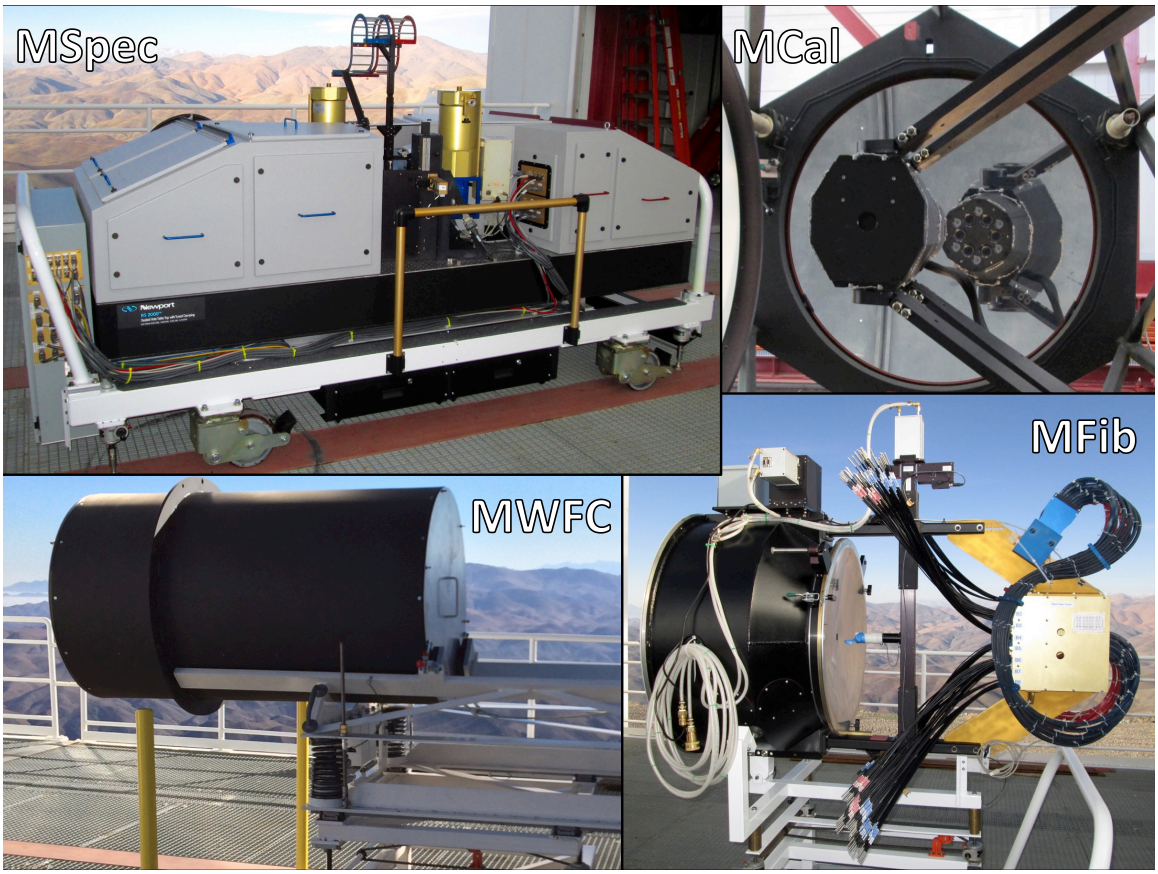

Figure 1.2: The four components of M2FS. MSpec is the heart of M2FS, housing both spectrographs and the primary electronics enclosure. MCal, the M2FS calibration unit, is permanently mounted at the Magellan/Clay prime focus where it can be deployed into the telescope optical path to provide a suite of calibration lamps. MWFS, the M2FS wide field corrector, is installed into the Nasmyth-East port of the telescope for M2FS and provides a corrected half-degree field-of-view. Finally, the M2FS Fiber mount, MFib, holds the science fibers and the guideing and Shack-Hartman systems: when installed it is bolted to the telescope rotator just after MWFC.

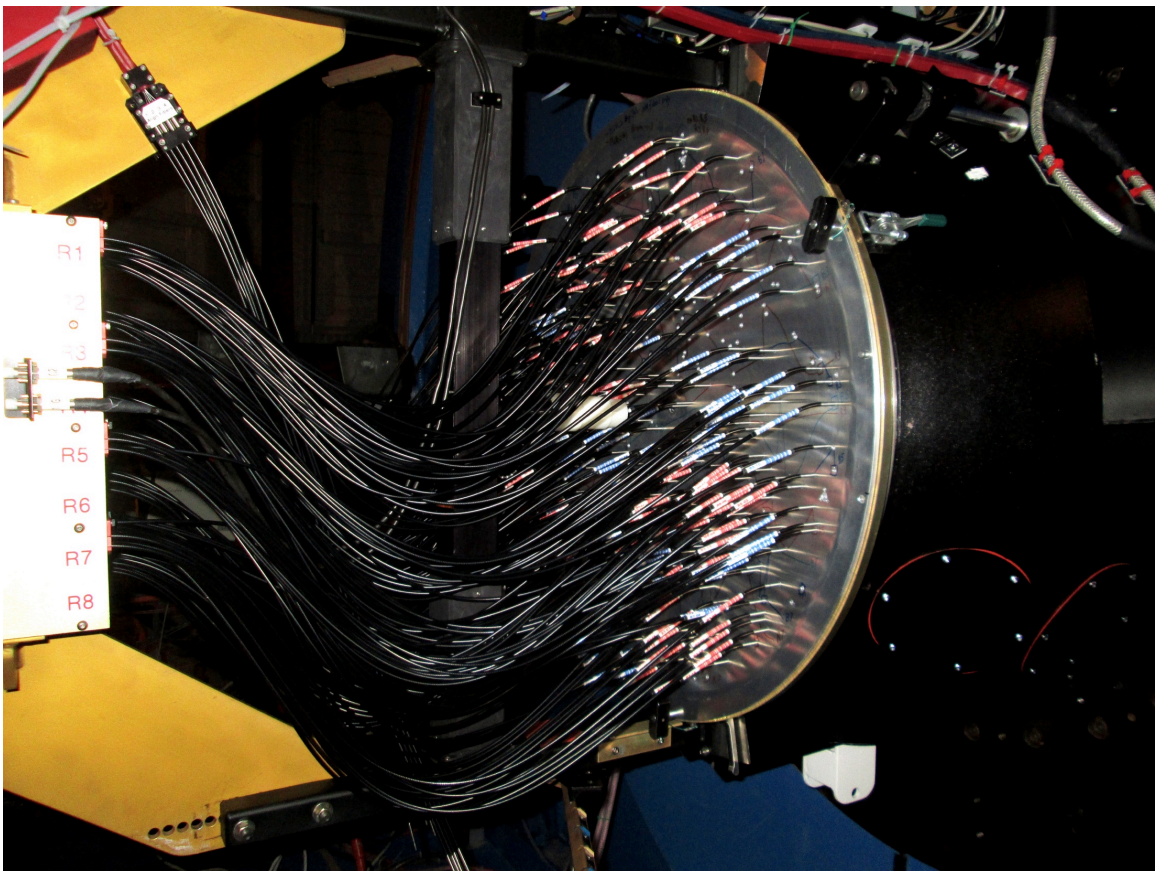

Figure 1.3: An image of MFib with fibers plugged for observing. The M2FS fibers have been inserted into holes on a plug plate following a pattern drawn on the surface with a marker (some lines are just barely visible in the sparser regions of the plate). Just behind the plate rests the M2FS telecentrator lens, forming the telescope focal surface.

selection, and CCD binning for both spectrographs are all set from the GUI, with each set of settings constituting a configuration. This makes the process of changing operating modes from one exposure to the next simple and offers the flexibility to observe with each spectrograph in a different configuration if desired.

The low-resolution grating may be manually swapped for other gratings during the day. M2FS is presently equipped with a either a 600 l/mm blue blazed grating, a 600 l/mm red blazed grating, or an echellette (R0.7, MedRes) grating on the LoRes/MedRes arm. The two LoRes and MedRes gratings are manually interchangeable with the echellette requiring a single-order filter due to the lack of a cross-disperser in the LoRes/MedRes optical train. An echelle grating (HiRes; 52.7 l/mm) plus cross disperser is always available to be selected by the user. New filters can be obtained with about two months lead time at a cost of approximately 4000 USD for a set of three. Plate configuration is done manually, with two users unplugging fibers, swapping plug plates, and re-plugging following a pattern (see §3.3.2.2). This process typically takes a half hour or less and is carried out at the Magellan/Clay Nasmyth platform. The particular fibers used for a given field depend on the order blocking filter desired. For example, a single order filter allows all 256 fibers to be used, while a filter that passes four orders might permit the use of only 80 fibers.

1.2.4 My Role

Originally proposed as a largely manual instrument, M2FS was intended to utilize vernier controls to select the dispersive element and filter and to adjust grating angles. Though this approach offered a low cost, simple, and robust solution compared to a fully automated instrument it was not particularly flexible. Within the original scope of M2FS's science justification this would not present any issue, yet early in the design phase my interest in using M2FS for an exoplanet survey coupled with various inquiries from other researchers interested in using M2FS for still other projects led

Table 1.2: Basic M2FS design and performance specifications.

Grating	HiRes (Echelle)	MedRes (Echellette)	LoRes (Standard)
Channels	2 independent; 500 mm focal length f/3.4 camera/collimators w/ 150 mm beam; SITe 4112x4096 CCD, 4 amps, broad AR coatings, anti-fringing		
# of Fibers	256 deployed + 60 spare		
Full λ range	370 – 950 nm		
Fiber Diameter	1.2 arcsec		
Min. Fiber Sep.	13 arcsec		
Field Diameter	30 arcmin		
Resolving Power	18k – 55k	8k – 15k	0.2k – 3.5k
Grating Ruling (1/mm)	52.7	115	50 – 1200 (600 available)
Grating Blaze	69° (R2.6)	35° (R0.7)	Supports 0° – 50° (8.6° & 14.5° available)
Cross-dispersed	Yes	No	No
Available Filters λ range (nm) (# of targets)	11 filters supporting 10–256 targets in 25+ M2FS orders	505-530 (256) 827-899 (256)	∼200 nm coverage, variable with grating tilt (256)
V_{lim} @ S/N =5, 2 hr, 500 nm, med. seeing, 180 μm slit	21.6	22.5	24.1

us to switch to an automated system.

While developing a robotic fiber polisher to prepare the fibers for M2FS (described in §2.2), I began working on both an initial concept to automate M2FS and ways of implementing an adjustable injection aperture to enable the higher resolutions demanded by precision RV work. These efforts culminated in my design of the fiber slit mechanism (§2.3) and responsibility for the design, development, and construction of all the systems and software necessary to automate M2FS, the fruits of which are described in Chapter III.

1.3 This Work

This work covers the two distinct phases of my efforts in pursuit of this thesis. The first phase, covered in Chapters II and III, details my participation in the design and construction of M2FS. Chapter II covers the two major hardware systems – a robotic fiber polisher and the M2FS Fiber Slit Mechanism – I developed for the instrument. Chapter III then details the automation of M2FS, covering aspects from the hardware used to the control architecture and the software developed to run the instrument and prepare plug plates. The remainder of this document then shifts to my survey of the open star clusters NGC 2516 and NGC 2422. In Chapter IV I introduce the survey sample and describe the analysis approach I have developed to simultaneously measure precise stellar parameters and line-of-sight doppler velocities for up to 128 Sun-like stars. Chapter V then reports spectroscopic results of our survey of NGC 2516 and NGC 2422. I then consider the RV variability of stars in our sample in Chapter VI, reporting both our study of stellar jitter in both clusters and what stars we identify as statistically significant RV variables and exoplanet host candidates. I conclude in Chapter VII with a brief review of M2FS's performance to date, a review of the implications of our results in NGC 2516 and NGC 2422, and describe our future plans for both M2FS and our exoplanet survey.

CHAPTER II

M2FS Hardware Systems

2.1 Introduction

This chapter presents the two key mechanical systems I designed and developed for M2FS. The first, a robotic fiber polisher, was developed to polish the fibers used in constructing M2FS. The second, the M2FS Fiber Slit Mechanism is a key component of M2FS I created to enhance the achievable resolution from R$\sim$20,000 to $\sim$55,000.

As a fiber-fed multi-object instrument, M2FS required a large number of fibers be prepared as part of the construction process. With an operational complement of 256 science fibers and 8 field acquisition fibers it was decided to prepare $\sim$ 450 fibers to allow for both manufacturing losses and a sufficient number of spares. Each end of each fiber required polishing with four successive grits (5, 2, 1, and 0.05 μm) of polishing paper. Instead of performing this task entirely by hand (as done for M2FS's predecessor) or purchasing a polisher for tens of thousands of dollars we elected to develop our own, which I describe in the first portion of this chapter (§2.2).

The remainder of this chapter is then devoted to the M2FS fiber slit mechanism (FSM or "tetris") and the fiber "shoe" assembly in which they are integrated. The development of the FSM was motivated largely by my desire to use M2FS to survey nearby open clusters for short-period, massive exoplanets – the so-called 'hot Jupiters', as sufficient RV precision would not be attainable with the original design

resolution of ∼20,000. Higher resolving powers also enabled additional science for other M2FS users: for example precision abundance studies of globular clusters (e.g. Johnson et al., 2015a) or the study of variable disk accretion around young low-mass stars (Briceño et al., 2016).

2.2 M2FS Fiber Polisher

Optical fibers are typically polished by hand for small scale jobs or by a fiber polishing machine for large batches or other situations requiring a high level of uniformity. Though there are numerous commercial fiber polishers readily capable of polishing large batches of fibers to a high degree of precision these machines typically run is excess of $10,000. While hand polishing is also capable of achieving a quality end with good technique and patience, it is done by mounting a single fiber in a small polishing puck and maneuvering it by hand in a figure eight over successively finer grits of polishing paper placed on an optically flat glass platen. Though very low cost, this process would take a significant amount of time to polish the ∼900 fiber ends required for M2FS. In lieu of either of these approaches I created a low-cost (<$1,000) fiber polisher that emulates and multiplexes the manual process.

2.2.1 Mechanical Description

The polisher, shown in Figure 2.1, is a robotic XY stage designed to move the polishing platen and paper in a lemniscate beneath a mount holding a polishing puck loaded with multiple fiber ends. The mechanism is dominated by a pair of linear slides (1), one mounted orthogonally upon the carriage of the other. Brushed, encoded DC gearmotors (2) are mounted at one end of each slide and connected to the underside of each carriage via a timing belt that then loops around a pulley mounted at the opposite end. An aluminum tray (3) with clamps at each corner is mounted upon the upper slide's carriage to hold the polishing platen and paper (4). This assembly

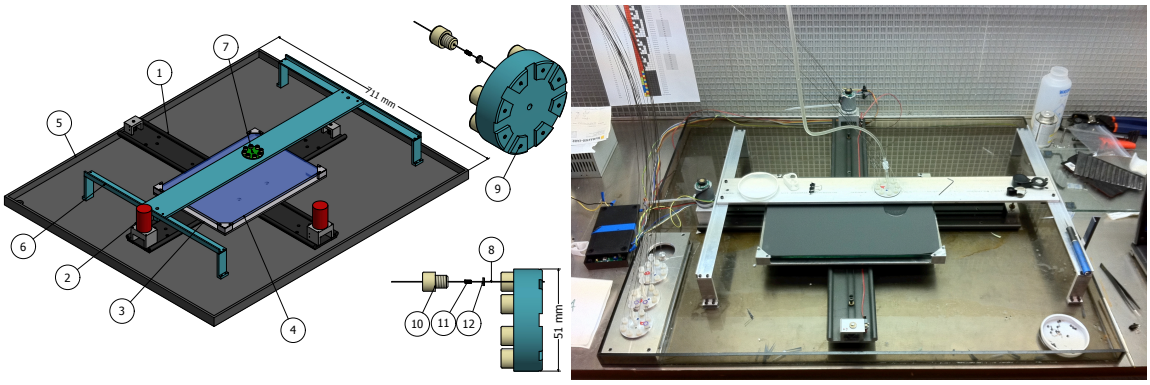

Figure 2.1: A photograph and CAD rendering of the M2FS Fiber Polisher. The left panel shows a 3D rendering of the M2FS fiber polisher with key components numbered corresponding to their descriptions in the text. An enlarged polishing puck is also shown to the right of the polisher with a fiber and associated hardware in an expanded view. The right panel shows the completed polisher (prior to the addition of a second puck position) as it starts a polishing run in the fiber lab at the University of Michigan. The photo also shows the computer power supply and electronics enclosure for the system to the left edge. Three additional fiber pucks can be seen loaded and ready for polishing to the front (lower) left.

is mounted in the center of a large plexiglass tray (5) with a gantry structure (6) mounted around it to hold the polishing pucks (7) in position.

The polishing pucks are designed to hold eight fiber ends (8) perpendicularly to the polishing surface while applying a slight, steady compressive force onto the polishing paper. Each puck consists of an aluminum disk with eight small legs, each with a stainless steel ferrule (9) press-fit into a central hole from below. A tapped hole resides above each leg allowing access to the ferrule from above. One additional hole tapped in the center of the puck connects to a distilled water source that supplies a slow drip to remove grit, glass, and metal during polishing.

Fibers are polished after having been epoxied into their hypodermic sheathing. The cladded fiber is passed through a nylon vent screw (10), a small spring (11), and forced through a thin disc of rubber (12). The fiber end is then threaded through the ferrule in a leg from above and the nut tightened into position, ensuring a degree of compliant protrusion from each fiber at the bottom of the puck. Polishing is then carried out by placing the loaded puck in position on the gantry, starting water flow,

and running the polisher with each successive grit for about 10 minutes. Additional details regarding the M2FS fibers and their preparation is given in Mateo et al. (2012).

2.2.2 Electronics

The fiber polisher is controlled by a custom circuit composed of an Atmel ATMEGA 328P microcontroller chip, a Pololu Qik 2s12v10 Serial Motor Controller, and three small buttons. The Qik controller is a low-cost 10 A brushed DC motor controller that accepts simple serial commands to perform PWM speed control of two motors independently and is used to drive the two polisher motors. The ATMEGA chip executes a custom C program that monitors the state of the polisher, commands the motor controller, accepts input from the user, and sends serial messages out over USB regarding the current state of the polishing process.

At power on the polisher first calibrates itself by driving the Y axis (perpendicular to the gantry crossmember) into the limit in reverse, zeroing, and then driving forward into limit. It then repeats the process in the X direction, moves to the starting position, and waits for user input. The start/pause button begins, resumes, or pauses polishing if provided the stage is in the starting position or polishing is presently in progress. Should the polisher be in an alternate state (e.g. in position to swap the polishing paper) It moves the stage to the start position. Pressing the preset button cycles the polisher between the starting position and the polishing paper loading position. Pressing both the preset and start button together resets the polishing path to the beginning. The reset button resets the entire polisher. The controller is implemented as a state machine with a number of interrupt handlers to monitor the quadrature encoders on each motor and service serial communication with both the motor controller and the host computer (if connected). The polishing path consists of a constant speed lemniscate with a small DC component directed to move the lemniscate down the length of the polishing surface, across, and back along the other

side.

2.2.3 Performance

We found the polisher to be an effective method of polishing the ∼900 fiber ends prepared for M2FS. Polished fiber ends were generally flat to a peak-valley of 400 nm, with a standard deviation of about 150 nm or $1/6^{\text{th}}$ of a wave as measured using a Promet FiBO fiber interferometer. By comparison, cleaving generates p-v in the 30–40 nm range. Focal ratio degradation was from 3.8 to 3.5–3.6 over the 3 m fiber length, better than required for M2FS.

Two design choices intended to save cost proved significant limitations to the durability of the polisher. First the gear motors used lack bearings on their output shafts and were coupled directly to the tensioned drive belt. This resulted in significant additional internal wear on the gearbox and would have resulted in the need for a new set of motors had the number of fiber ends been much larger. Secondly, directionless limit switches were used to reduce the number of microcontroller I/O pins, the intention being to keep track of direction information in software and act accordingly. In practice this resulted in a number of broken timing belts during testing and unnecessarily finicky operational procedures.

2.3 M2FS Slit Mechanism

The slit mechanisms make it possible for M2FS to achieve its diverse range of resolutions. These mechanisms position one of six slits over the fiber ends within the spectrograph, stopping down the 150 μm fiber core and trading throughput for higher resolving power. M2FS uses sixteen of these assemblies, called tetrises for their resemblance to a piece in the classic game. One is used for every sixteen fibers (eight per fiber "shoe"), each one individually controllable. The observer is thus able to select one of six slits for each set of sixteen fibers. The slit sizes, resulting resolutions,

Table 2.1. M2FS Fiber Slit Resolving Power

Slit Size (μm)	(pixel)	HiRes	MedRes	LoRes (600 l/mm)	Relative Throughput
180	12	18k	7.2k	1.8k	100 (100)
125	8.3	20k (27k)	8.0k	2.0k	92 (88)
96	6.3	25k (35k)	10.4k	2.6k	75 (72)
75	5.0	29k (45k)	12.1k	3.0k	61 (57)
58	3.9	32k	13.4k	3.3k	48 (45)
45	3.0	34k (55k)	14.2k	3.6k	38 (34)

Note. — Each M2FS fiber accepts light from a 1.2 arcsecond aperture into the 150 μm core. The mechanism positions a slit directly over the bare fiber at the spectrograph's injection focal surface, trading photons for resolving power without incurring any additional seeing loss. Resolutions are based on the optical design of M2FS while values given in parentheses are those measured from the the FWHM of Gaussian fits to calibration spectra in observing modes for which engineering data is available. Similarly, throughput values are computed from the geometry of the fiber/slit interface while values in parentheses have been measured using engineering data.

and light losses are given in Table 2.1. In total each mechanism is composed of twelve parts, exclusive of the fibers and fasteners (see Figure 2.2).

2.3.1 Mechanical Description

The individual components of the mechanism are described in this section with numbers in parentheses denoting the corresponding part number in Figure 2.2. The parts are fabricated out of aluminum, except for the cam (7) and driveshaft (5) which are stainless steel, the slit foil (8) which is molybdenum, and the coupler (4) which is brass. Machining was done by Optics Technology Incorporated and the slits were cut and glued to their carrier (9) by Lenox Laser.

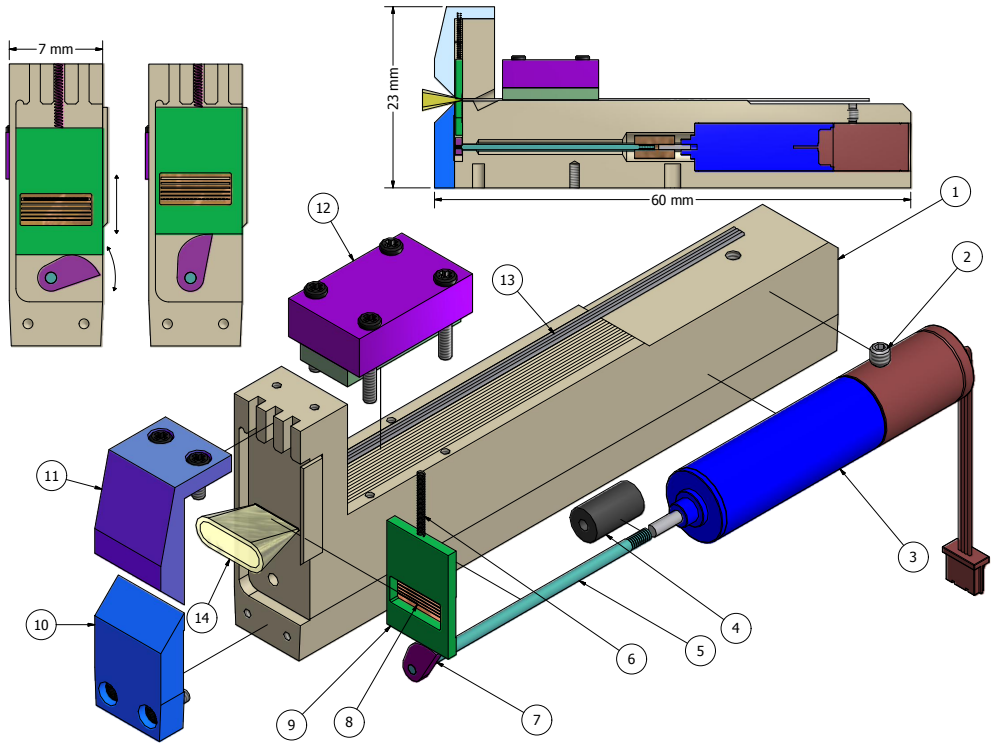

Figure 2.2: A CAD rendering of the M2FS fiber slit mechanism. The components are as follows and are described in §2.3.1: 1) The base; 2) motor set-screw; 3) step motor and integrated gear head; 4) brass shaft coupling; 5) 1 mm driveshaft; 6) preload spring; 7) constant-displacement cam; 8) slit foil; 9) slit carriage; 10) lower clamp; 11) upper clamp; 12) fiber clamp with foam bottom; 13) three of the sixteen sheathed fibers. Finally (14) is an example of a composite f/2 and f/3.2 beam from the 16 fibers. Screws are self-evident.

The tetris base (1) is the core of the entire assembly: It must precisely locate the fibers at their injection points, house the drive-train, and provide bearing surfaces for the slit mechanism, all while ensuring relative ease of assembly and serviceability. The left and right sides of the base and lower front clamp are chamfered to allow all eight assemblies to be mounted closely enough together to follow the compound curve of the injection surface. A critical feature in the tetris base is the front fiber slot – this slot is hidden in Figure 2.2 but is located at the base of the exiting beam. This aperture is 4800 x 300 μm and serves to ensure that each set of 16 fiber ends is colinear to ± 5 μm and that they all terminate on a common plane to ± 5 μm. Combined with the faceted mount (see Figure 2.3), the slots ensure that the fiber ends closely conform to the desired curved path on the spherical focal surface of the spectrograph collimator. The top V-grooves help guide fibers during installation and the angled cavity (visible in the upper image) is precisely angled to ensure a gradual transition into the front slot, thus protecting the fiber ends from damage during installation. The tetris assembly length was chosen to allow easy finger access to the fibers while they are in their respective grooves as the fiber clamp (12) is installed (locking the fibers in position) and the fiber ends are made flush to the front of the tetris base. The upper (11) and lower (10) front clamps retain the slit carriage (9) and offer the mechanism some degree of protection. The clamp chamfers ensure the beam is not vignetted.

The slit assembly consists of a carrier (9) with a central opening to which a 15 μm thick piece of Molybdenum foil (8) is glued. The six slits are laser-cut into this foil after bonding – both operations are performed by Lenox Laser. Finally, a 0.6 mm diameter precision spring (6) is glued to the top of the assembly to provide a system preload. Testing determined that 3M's CA9 cyanoacrylate performs exceptionally well in this regard. The spring is unable to buckle due to the combination of glue below and the channels (on the upper front face of the base) above. The three

Figure 2.3: The partially assembled M2FS blue side fiber shoe. Two tetrises have been installed on the faceted mount at the fore of the photo. Pairs of locating pins show the positions for the remaining six mechanisms. Two bundles of sixteen fibers can be seen entering from the rear of the shoe to their termination in their respective tetris. The eight axis motor controller is partially visible beneath the fibers.

channels allow flexibility to use one, two, or three springs to provide preload, though in practice one spring has proven sufficient.

Positioning of the slit assembly is achieved by a constant-displacement cam (7), which is snap-fitted and glued to the driveshaft (5). The driveshaft is, in turn, attached to the motor (3) via a miniature brass coupling (4). The motor is purchased as a unit from Faulhaber and consists of a 256:1 planetary gearhead mated to a 18° (20 steps/revolution) stepper motor. The system is kept under preload at all time by the aforementioned spring. The entire drive-chain has a step resolution of about 0.1 μm, twenty-five times finer than the ± 2.5 μm accuracy with which the slits must be centered on the fibers.

Assembly of the mechanism begins by affixing the driveshafts to the individual motors using a jig designed to ensure precise spacing between the motor front and the cam. Next, the slit assembly and preload spring are placed between the guides on the front face of the tetris base and glued together. Once the glue has dried, the carriage/spring assembly is removed. The motor/driveshaft assembly is inserted into the base from the rear and locked into place with the setscrew (2). The fibers are then fitted into each tetris and clamped into place, with care taken to ensure the fiber ends are recessed from the tetris front face by approximately 10 μm. The purpose of this gap, which is ensured by a combination of tooling jig and microscopic inspection, is to protect the fiber ends from abrasion by the slit foil or any dust grains that migrate between the foil and the front face of the base. The cam is press-fit and glued onto the end of the driveshaft. Finally, the carriage is replaced and the front two clamps are screwed into place.

Once the assemblies are complete they are mounted onto the faceted base (see Figure 2.3), which orients the tetrises appropriately, and the entire assembly is mounted within the fiber shoe. The motors are then connected to the control electronics via an access hatch on the underside of the shoe and the remainder of the shoe is assembled.

2.3.2 Electronics

The individual tetrises are driven by a custom eight axis stepper controller. This controller consists of a purpose-built PCB and an Arduino Mega 2560. The Arduino Mega is and Atmel ATMEGA2560 based variant of the Arduino project's[1] open-source, open-hardware electronics development platform. The custom PCB was designed as an Arduino Mega "shield" - a stackable add-on PCB used to extend the Arduino's capabilities - the board consists primarily of eight Toshiba TB6608FNG driver chips, a power chip, and a digital temperature sensor. This design allowed us to use a number of well-developed, open-source, C++ libraries for low level control, significantly simplified device code development, and saved significant cost over, for-instance, a traditional programable logic controller.

Power and communication is via USB. The shoe is designed such that a one-piece board-to-board connector makes electrical contact automatically on shoe insertion. Similarly, a switch hidden in one of the screws used to lock the shoe into place ensures that the shoe knows when it is about to be removed and it is therefore able to power down, saving its state prior to removal. The entire shoe assembly is thus hot-swappable.

2.3.3 Performance

The mechanisms have proven reliable after initial commissioning issues with fiber slippage and a few motor failures. During commissioning tests a few fibers were found to have slipped slightly forward or backward due to forces along the steel fiber conduit length. On one occasion, forward slippage proved particularly catastrophic for the slit assembly when a fiber ferrule caught on the slit array but did not give any obvious visual indication in an exposure. The ferrule then proceeded to tear the slit array when a change was attempted, only then providing a indication of the

[1] arduino.cc

failure in subsequent exposures. After this issue was discovered, we re-fashioned the silicon fiber clamping pads (see Figure 2.2) and systematically tightened the fiber clamps uniformly using a gauge pin to insure even clamp pressure. We have seen no further forward fiber slippage since this change and by ensuring there is little tension in the fiber tubing, backward slippage is also now rare. While the drive system has performed well, the motors exhibited a fairly high initial attrition rate: of the twenty-two units purchased, four failed during assembly tests. The only motor to demonstrate intermittent operation after initial commissioning tests was suspected to have been damaged during installation and this motor has since been swapped with a spare.

Slit positioning is carried out open loop so there is the possibility that the commanded slit is not well centered on the fiber end. This risk is minimized by first driving to a hard-stop and then moving to the selected slit for every move to account for backlash. Visual inspection under a microscope indicates positioning repeatability in this manner is roughly 7.5 μm, which is at the level of precision with which the slit center positions are characterized. Despite this, we see tetris-to-tetris resolution variability at the 20% level in data for both the 95 and 45 μm slits in early engineering tests. This appears to be related to carriage stiction caused by shifting of shims and dust infiltration. These effects impact slit throughput at the few tens-of-percent level based on geometric covering variability of the slit at the fiber end. Unfortunately these variations are of similar magnitude to those caused by target-fiber mis-alignment, seeing, and fiber throughput and are hence difficult to isolate.

For all but the 180 μm and 58 μm slits (slits for which engineering data has not been obtained), we have measured resolutions using the FWHM of Gaussian fits to calibration lamp profiles. These fits indicate typical resolving powers significantly higher than those quoted in and estimated from M2FSs optical design. Fortunately, the relevant quantity for an observer is the measured line width and hence for obser-

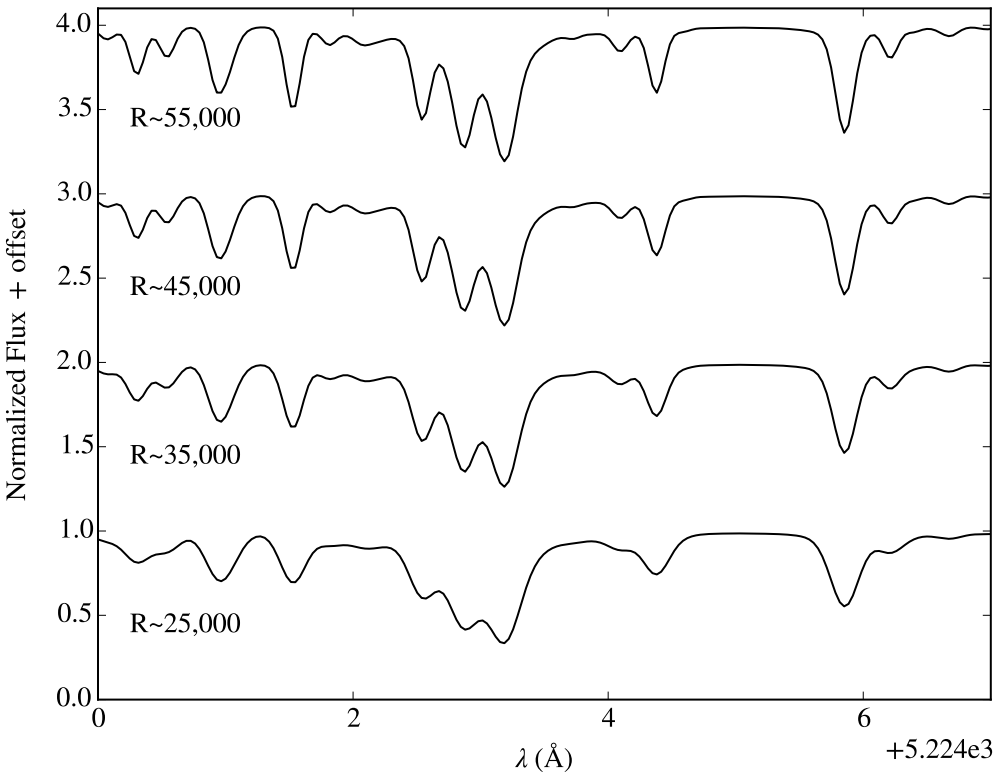

Figure 2.4: A subset of the solar spectrum (Kurucz, 2005) artificially broadened to resolving powers attainable with a selection of the M2FS slits when observing in echelle mode. This segment shows lines of Fe, Co, Cr, and Ti.

vational purposes the design resolution is very conservative. Figure 2.4 shows a small section of the Solar spectrum broadened to simulate resolving powers attainable by M2FS when using different slits in echelle mode.

CHAPTER III

M2FS Automation & Software

3.1 Introduction

A high and somewhat unanticipated level of interest in using M2FS coupled with the increased scientific versatility offered by the fiber slit mechanism made it very clear the scientific community would benefit from the increased flexibility afforded by automating M2FS. In the original concept M2FS would have required electronics for the CCDs, their shutters, the camera focus on MSpec, the Shack-Harman pickoff mirror and LED on MFib, and the calibration lamps in MCal (Figure 1.2 shows the M2FS components). The remaining optical configuration (e.g. echelle grating azimuth and elevation, LoRes/MedRes grating elevation, grating selection, and filter selection on MSpec along with the guider focus and filter selection on MFib) was to be done manually via vernier control and push/pull rods. This system, essentially that of M2FS's predecessor MMFS, was simple and robust at the expense of considerable flexibility: reconfiguring the instrument in between exposures would cost valuable time and require a sleep deprived observer to make careful adjustments. Because of this M2FS would have been largely limited to one configuration per night.

This chapter describes the systems and software I created to remove these limitations on M2FS's scientific flexibility and ease the operational burden on users. In automating M2FS I have attempted to follow these principles: 1) Use standardized

communications and interfaces whenever practical (e.g. USB TTY) ; 2) Prefer premade cables to custom wiring (e.g. DB15 cables vs. mil-spec assemblies); 3) Use open-source and hobbyist electronics solutions whenever suitable. In essence this translates to: "Try not to reinvent the wheel but if you do make it general. Use concepts widely and keep systems cheap and easily replaceable." The resulting system, save MCal which is available for use by other instruments, presents a unified, intelligent interface to the observatory network. The observer controls M2FS via a native OS X Cocoa application (developed by C. Birk of Carnegie Observatories) on the Magellan Clay observer's workstation. This front-end application presents a GUI interface to the individual text commands accepted by M2FS, interfaces with the Magellan CCD servers used by the M2FS CCDs, and offers the ability to quickly save and restore any particular instrument configuration. Actual configuration changes typically take under two minutes and have made rapid switches between different projects during observing runs simple and commonplace.

M2FS subsystems (i.e. the electronic and electromechanical components needed to automate M2FS) are described in §3.2, grouped by the M2FS component on which they reside. The controlling software is generally left for §3.3.1, save a few isolated microcontrollers for which their embedded software is locally isolated. In addition to the M2FS control software, the M2FS plugplate preparation software is a critical part of observing with M2FS. This software package, described in §3.3.2, is used to design plugplates from the input target catalogs of M2FS users and, later, determine the specific target-to-fiber assignments needed to appropriately plug the fibers.

3.2 Automation

This section describes the hardware systems involved in automating MFib, MCal, and MSpec. MWFC, though designed to allow addition of an atmospheric dispersion corrector if funded, does not yet have any moving or electronic components and is

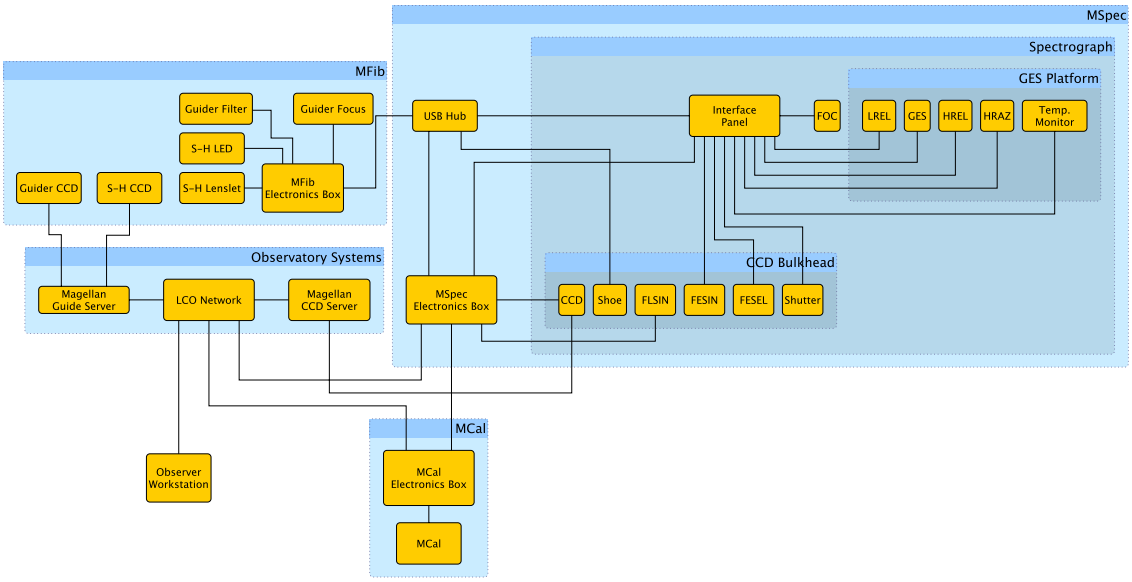

Figure 3.1: A block diagram of M2FS systems grouped by physical location.

not discussed in this section. Figure 3.1 provides a schematic overview of M2FS and its various systems.

3.2.1 MSpec

3.2.1.1 Spectrograph Systems

The M2FS spectrographs, which reside on MSpec and are both identical, can be thought of by following the path light takes through the system. Light enters the spectrograph at the fiber shoe, passing through the fiber slit apertures located in the tetris mechanisms. The photons then pass through a transmission filter, bounce off a fold mirror, continue through the camera/collimator, reflect off either the high resolution echelle grating or one of the available standard or echellette gratings, finally passing back through the camera on their way to the shutter and the CCD behind. At each step in this chain there are one or more motions which required a solution. The systems along this path are called out in Figure 3.2. We do not revisit the slits mechanism here as it was discussed at length in §2.3.

The filter exchange system (FES) consists of a filter "elevator" (FESEL) – an eight

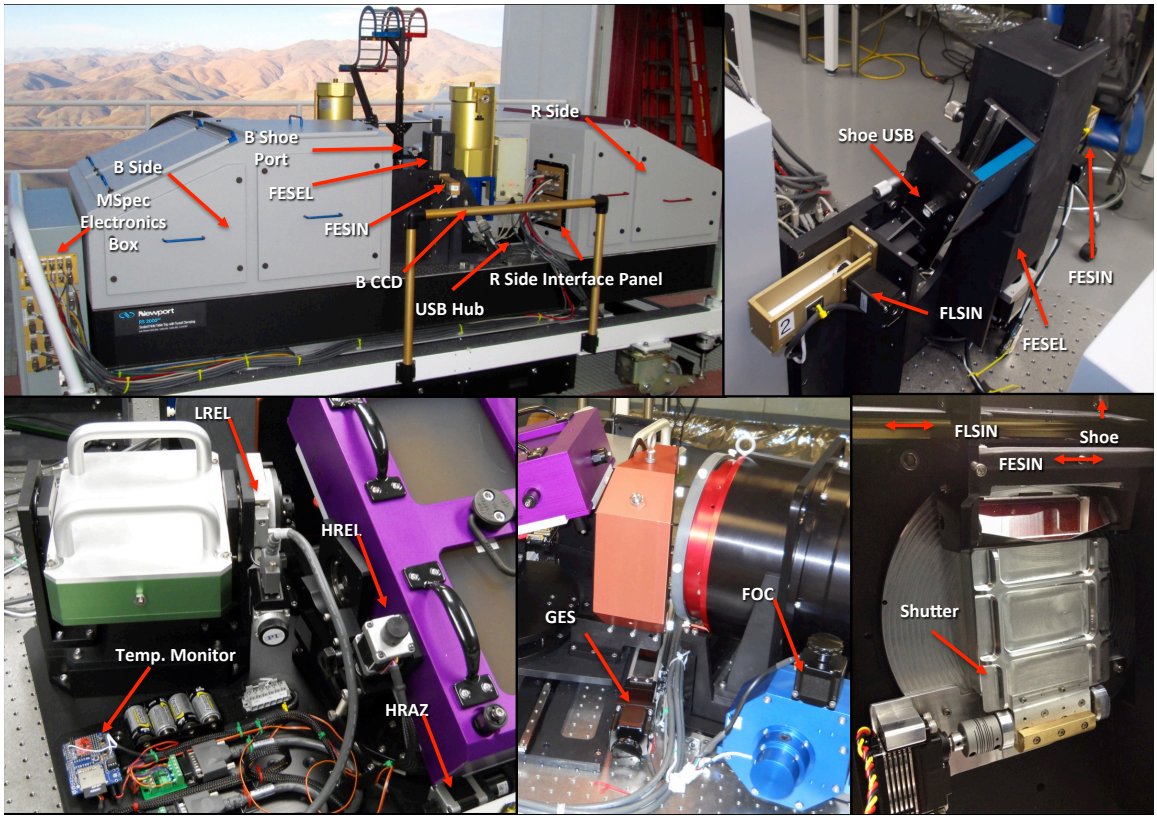

Figure 3.2: An annotated image showing the systems on MSpec.

filter carriage mounted to a vertical screw driven linear stage – and a rack-and-pinion inserter (FESIN) that pushes or pulls individual filters from the carriage into or out of the optical path. The elevator is driven by a Parker Automation LV232-01 1.8° stepper motor while the inserter is driven by a NEMA 113 1.8°(11HS20-0674S) stepper motor. As this mechanism is the only one in M2FS that presents the potential for a damage producing collision, we mitigate the risk by using a Celesco linear potentiometer as an absolute encoder on the elevator axis, using software checks to disable inserter motions when the elevator is not in a safe position. We use Melexis US1881 Hall effect sensors on the inserter to provide positive confirmation of full insertion or retraction. When not fully retracted, all motion of the elevator is inhibited in software. Unfortunately these sensors power on in a tripped state if no magnetic field is present, creating a system fault: e.g. at the start of an observing run if a filter was left inserted at the end of a previous run.

Immediately following the FES is the fiber locator system inserter (FLSIN). This mechanism is identical to the filter inserter (save a slightly shorter travel) and was added to move a pickoff mirror into the optical path for use in the fiber locator system (FLS; §3.2.4).

The next system in the optical path is the focus drive (FOC). The camera is mounted on a set of flexure mounts that allow the axial motion of camera with negligible transverse motions or tilt. This mount is driven by a LV232-01 stepper geared down to drive an eccentric cam against the mount. Its position is monitored by a Maurey 143-P93-103 rotary potentiometer on the camshaft.

Selection of either the HiRes or Lo/MedRes grating is accomplished by a linear shift of the platform on which they are mounted. This grating exchange system (GES) consists of the platform mounted on a pair of THK rails and driven by a Parker Automation ER032 series linear actuator with an integrated LV232-02 series stepper and sealed reed switches for limit sensing. Though not optically critical, the absolute

position of the stage is monitored by use of a Celesco CLP-290 linear potentiometer. The HiRes mount allows adjustment of both the echelle grating azimuth (HRAX) and elevation (HREL) by way of rotary rails and bearings, respectively, with actuation accomplished by Physik Instrumente (PI) M228.11S linear actuators. These actuators are an combined stepper and lead screw unit with integrated limit switches and a central home sensor accurate to 0.5 μm. We calibrate these axes by moving to the negative limit at low speed, quickly moving until the home sensor trips, and then moving back slowly until it trips once more. In practice this procedure yields a positioning accuracy of $\lesssim 1.75$ pixels or about half of a resolution element in M2FS's highest resolution mode on the CCD when neglecting temperature variations. The Lo/MedRes grating mount requires only elevation adjustment (LREL), which is accomplished by a PI M-038 rotary stage clamped to the axis of one of the two rotary bearings used in the mount. Calibration is achieved by running the stage until the integrated home sensor toggles and then continuing at low speed until it toggles again.

The final system consists of the shutter and CCD. The original intent was to use a Uniblitz CS-90 iris shutter and multichannel controller; these units, despite their high price, proved unreliable and would dissipate significant heat immediately adjacent the CCD field window and directly below the injection optics. Instead we developed a flap shutter that uses a HiTec 7940TH hobby servo to quickly rotate the flap into and out of the optical beam. Both shutter servos are controlled by an Arduino Uno with two daughter cards residing in the primary electronics enclosure (Figure 3.3). The custom circuit boards provide a button for local override of the shutter and the 7 VDC power needed by the servo. Each shutter is controlled by a 5 V TTL level output from the CCD sidecar that is monitored by the Arduino through an optoisolator. The Arduino runs a small C program that monitors the line and generates the servo command to open of close the shutter. The CCDs use control electronics designed and built by Ian Thompson and Jorge Estrada at Carnegie Observatories following a similar pattern

used for many of the instrument detectors in use at Las Campanas. They are entirely isolated from all other M2FS systems, interfacing via fiberoptic link directly with the Magellan/Clay CCD servers.

Each spectrograph is also equipped with a custom temperature and shock monitor mounted on the GES platform. The monitor is based on an Arduino Pro Mini and is equipped with three DS18B20 digital temperature sensors mounted on the LoRes mount, the back of the HiRes grating, and on the cross-dispersing prism.

Each of the actuators is connected to the MSpec electronics box with L-Com CPMS D-sub series cables. The shutter cables from the CCD are L-Com CC174-10 RG174 coax. The temperature monitors and fiber shoes are connected to a central USB hub that is connected directly to the control computer in the electronics enclosure.

3.2.1.2 Electronics Enclosure

An annotated image of the MSpec electronics enclosure is shown in Figure 3.3. The enclosure contains all of the drive electronics for the systems on MSpec, a 100BASE-FX transceiver to MCal, the M2FS control computer, power supplies, a heat exchanger, and an internal light. The electronics for MSpec consist of the previously mentioned shutter components and a pair of Galil DMC-4183 stepper motor controllers (one per spectrograph). The Galil controllers contain the stepper motor drivers and have been programed with a number of low-level routines to manage the motion of each axis. Each controller is connected to the control computer via USB.

The instrument control computer is a Beagleboard-xM, a 1 GHz ARM 512 MB RAM single-board computer, running Angstrom Linux 3.2 from a 16 GB microSD flash hard disk. This computer runs the majority of the instrument control software. Control of spectrograph components on MSpec and MFib is accomplished via USB, while the connection to the planned FLS Imager in MCal is via a dedicated fiber

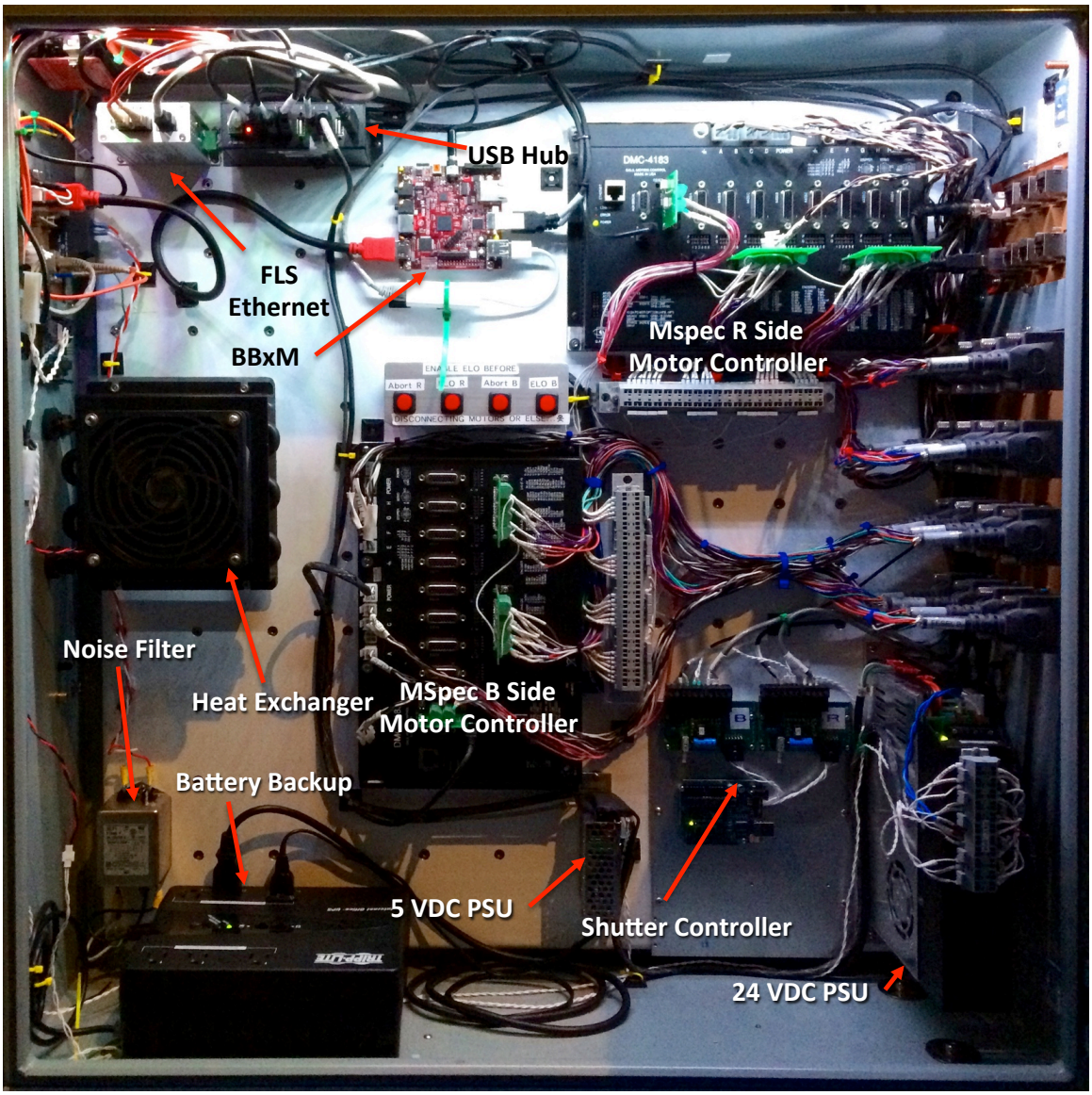

Figure 3.3: The MSpec electronics enclosure houses the M2FS control computer, the primary power supply system, shutter controller, and a pair of 8-axis motor controllers each servicing a single arm of MSpec. These systems, along with the heat exchanger and the fiber ethernet link to MCal for the as-yet unfinished FLS system, are marked above.

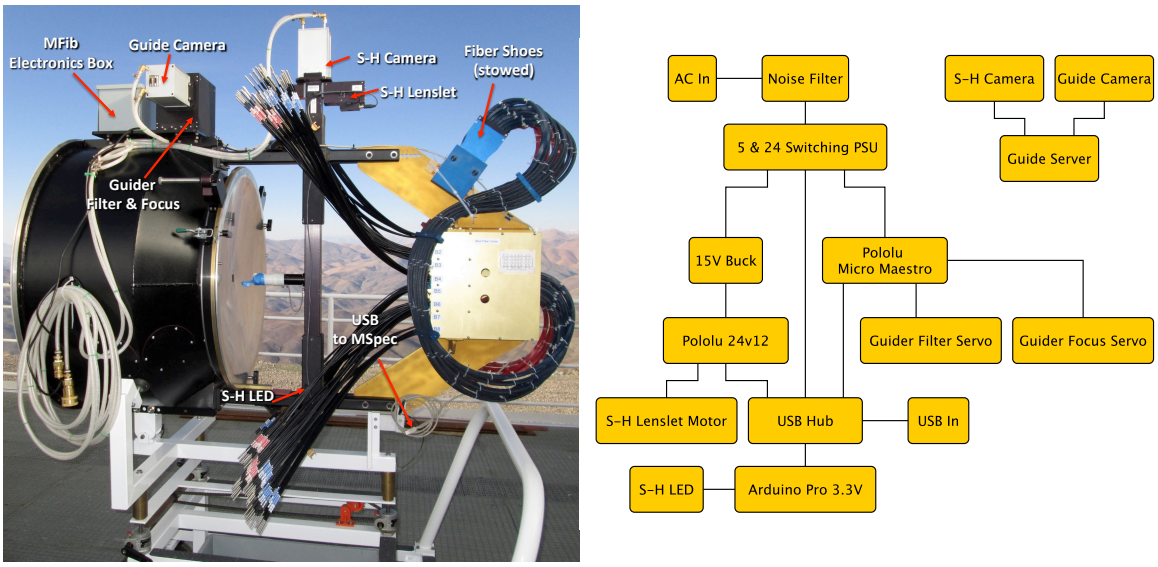

Figure 3.4: The left panel shows an annotated image of MFib with arrows pointing to key systems. The right panel shows a schematic layout of the system components on MFib. The fiber shoes, though stored on MFib, interface with MSpec when in use and are not shown on the control diagram.

ethernet link. The science cameras, guide camera, and Shack-Hartman camera are controlled by observatory computers and do not interface with the M2FS control computer. The MCal lamps are controlled independently (§3.2.3) to allow other instruments to use them when M2FS is not mounted on the telescope.

The power systems consists of a Corcom noise filter feeding a Tripplite UPS, which in turn powers a CUI 5 VDC 25 W (VGS-25-5) switching supply and a Galil PSR-12-24 24VDC 290 W power supply. The 5 V supply powers the control computer and internal box lighting and the 24 V supply powers the Galil controllers, shutter driver, both the USB hub within the enclosure and on MSpec, and the heat exchanger fan. Peak power dissipation is 95 W with a typical value of ∼50 W.

3.2.2 MFib

The M2FS Fiber Mount (MFib, see Figure 3.4) is the primary interface between the instrument and the telescope, bolting directly onto the telescope and securing both science and guide fibers in their appropriate positions in focal plane. Both

the guide camera and Shack-Hartman camera are mounted on MFib. Though the cameras are controlled by the TCS, the M2FS control system is responsible for the instrument specific components of the guide and Shack-Hartman systems. The M2FS guide system includes both a Canon camera lens and a six position filter wheel. These systems allow tweaking the guider focus and guiding at wavelengths closer to permitted by whatever filter is in use on MSpec. Both the focus and filter wheel are actuated by HiTec hobby servos driven from a Pololu Micro Maestro mounted within the guider box. The S-H system uses a brushed DC gearmotor coupled to a threaded rod to insert or remove a lenslet array from the S-H optical path. The motor is driven by a Pololu 24v12 into the forward or reverse limit as appropriate. The system also includes an Arduino used as a PWM dimmer to control the LED needed to make S-H templates at the start of each observing run.

The MFib electronics box contains a Delta noise filter, a combined CUI 5 and 24 VDC 30 W (VDG-30-D524) switching power supply, a seven port USB hub, an Arduino to control the S-H LED, and a 15 VDC buck for the S-H Lenslet drive motor. Power connections to the S-H LED, guider filter/focus box, and SH drive are all via doubled ended locking DC barrel jack cables. The S-H drive box and the guider box are connected via USB A to miniB cables. In addition there are spare USB ports to support the addition of plugging feedback displays for the the FLS system. Typical power dissipation is 5 W.

The fiber mount has five primary connections: 1) a USB link to MSpec, 2) 120 VAC to the electronics box, 3) Glycol coolant lines that feed the guide and S-H cameras in parallel, 4) power and data to the guide camera, and 5) power and data to the S-H camera. The cameras are standard LCO guide cameras which connect directly to the Magellan TCS system and operate independently of M2FS.

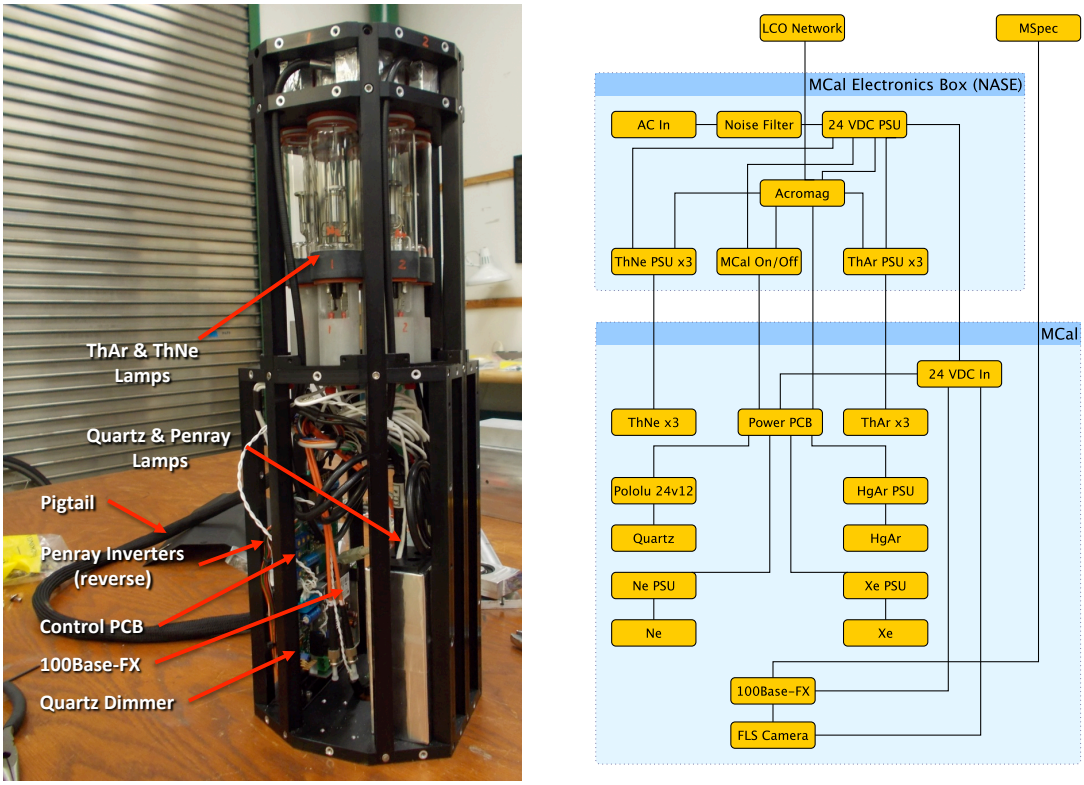

Figure 3.5: The left panel shows an annotated image of MCal. The integrating volume and light pipes for the penray and quartz lamps are not annotated but are clearly visible. The FLS Camera will be installed in the space between the circuit board on the left and the integrating volume on the right. The right panel shows a schematic layout of MCal components. The main power supply and HiRes lamp supplies are located in an electronics box on the NASE telescope platform and connected to MCal via a ∼30 m cable run through the telescope IGES chain.

3.2.3 MCal

MCal is designed to provide wavelength and continuum calibration capabilities for M2FS via a suite of hollow cathode, penray style gas discharge lamps, and a single quartz tungsten lamp. MCal is also designed to support calibration of fiber plug positions via a downward-facing network camera. MCal has onboard electronics for the quartz, penray, and FLS components; a small electronics box permanently installed on the Magellan/Clay NASE platform provides 24 VDC system power, high-voltage power, and network control. An image of the MCal internals and a schematic overview of the system are shown in Figure 3.5.

The upper half of MCal is dominated by a suite of six Thorium-Argon and Thorium-Neon hollow cathode lamps (three each). These lamps are connected via a high-voltage cable to their respective EMCO HC series ∼600 VAC power supplies in the electronics box on NASE where they are fed by a TDK 24 VDC 75 W PSU (DLP75241/E) typically running at 9.5 W and peaking at 29 W. The ThAr and ThNe lamps are each controlled as a group with illumination levels set using two of the DAC channels from an Acromag 973EN-4006 ethernet DAC. The lower half contains the Neon, Mercury-Argon, and Xenon penray lamps and the quartz lamp in an integrating volume connected to the emitting surface by fiber bundles (additional details on the design of MCal are given in Mateo et al. (2012). As each penray lamp has essentially the same drive requirements as the CCFL backlights common in older laptop computers, we were able to employ three Microsemi LXMG1614E series supplies to drive the lamps. The supplies are integrated into MCal behind the suite of circuit boards seen in the lower left of Figure 3.5 and offer extreme space and power efficiency when compared to the magnetic ballast drivers offered by the penray manufacturers. Each supply is fed by a 12 VDC line and a single Acromag channel (from the box on NASE) to set the lamp brightness. The Quartz lamp is a 6 VDC 10 W bulb which we dim using a Pololu 24v12 brushed DC motor driver configured

to accept one of the Acromag Input/Output lines as an analog speed input. The 6 and 12 VDC supplies needed by the penray and quartz lamp systems are generated locally by a number of TI PTN78060W switching regulator modules located on the power PCB. The remaining space in MCal is reserved for an Axis Communications P1357 network camera as part of the fiber locator system. This camera is fed directly off the 24 VDC input and communicates with MSpec via a 100Base-FX ethernet link.

In addition to the 24V power supply, network DAC, and high-voltage power supplies the NASE electronics box contains a Arduino equipped with a single relay used enable and disable the 24 VDC supply to MCal and prevent any heat generation when the unit is not in use. Although the Acromag controller only offers six outputs, we are able to use the control line to the ThAr lamps as a dual use line. Below 0.2 V everything is off, between 0.2–0.3 V MCal receives 24 VDC but the ThAr lamps remain off, and values between 4–5 V set the ThAr lamp intensity.

3.2.4 Fiber Locator System

The M2FS Fiber Locator System is a planned distributed subsystem designed to provide feedback on plug positions of the fibers. Although significant design and prototyping work has been done on the FLS we were unable to complete it in time for the M2FS commissioning run and development remains ongoing. The system is composed of a fiber illuminator in MSpec, a user feedback system on MFib, and an imaging camera on MCal. When in operation the illumination system will be used to successively back-illuminate the fibers during plugging while the camera located in MCal images the reverse side of the plug plate, performing spot detection and streaming the list pixel coordinated detected to the M2FS control computer. The control computer performs a geometric hashing algorithm (Lang et al., 2010) on the pixel coordinates to recover plate coordinates and searches for illumination patterns in the datastream that correspond in time to the back-illumination of individual fibers.

We have completed tests of the plate monitoring system and hashing algorithm. The fiber illumination system presently exists only as a conceptual design.

3.3 Software

This section describes the two software packages I have created for M2FS. The first package, `M2FS-Control`, consists principally of the suite of python programs written to operate M2FS but also includes a number of ancillary support programs and a significant amount of embedded control code used by a few key systems. The second software package, `hole-mapper`, consists of the python programs `plateplanner` and `platemapper`. These programs are used to generate the M2FS plug plates from the input catalogs of observers and then create the sets of fiber-target assignments, or "maps," used by the M2FS team to appropriately plug the fibers during an observing run.

3.3.1 M2FS-Control

3.3.1.1 Operating Environment and System Architecture

The M2FS control software runs on a Beagleboard-xM (BBxM), an AM37x based 1 GHz single-board computer. The BBxM is equipped with 512 MB of RAM and offers onboard USB ethernet, an HDMI interface, a 4-port USB hub, and a real-time clock (RTC). It also exposes a low-level camera bus interface which we planned to use for the initial version of the FLS system and was a principal reason for selecting the BBxM. When deploying the BBxM we discovered that the onboard ethernet chip lacks the EEPROM necessary to store a permanent MAC address and we had little success with kernel patches intended to support setting its value in software. As an alternative we use a USB-to-ethernet dongle. Similarly we were unable to successfully build the kernel such that the RTC battery charging regulator would work properly.

In practice the only ill effect is that the first few minutes of each boot's logs are timestamped with the default time of the RTC chip, once ethernet comes up the network time protocol server updates the system to the appropriate time.

The BBxM runs a custom build of Angstrom Linux 3.2 based on busybox and systemd v118 built with the BitBake toolchain on Ubuntu Linux. The software packages python, ipython, numpy, NUT and pyNUT (for monitoring the UPS), flask, and git are installed to support the instrument control software. A `udev` config file is used to create device mount points for the various M2FS hardware components, all of which are ultimately connected to the computer via USB. Though these mount points are generally based on the device serial number, the Galil controllers do not report any uniquely identifiable information and so their mounts are tied to specific USB ports on the MSpec electronics box hub. Ultimately the entire OS runs off of a 16 GB microSD flash card.

The M2FS control software is loosely based on the "director" and "agent" concept of the CFHT instrument software group (Isani, 2001). For M2FS I have created a single "Director" program that accepts textual commands over a socket connection (e.g. 'SLITS R ?') and typically passes the command on to another local agent via a local socket. The receiving agent then handles the command and interacts with the low-level hardware. Though this chain generally follows a top-down hierarchy, such a pattern is not strictly followed. Each of these programs is an implementation of a python 2.7 `Agent` class that provides common facilities for interfacing with other agents, processing commands, and general program execution. Figure 3.6 provides a graphical overview of the software system.

3.3.2 holemapper

The `holemapper` software package started as an attempt to improve the MMFS plugplate marking process. Like M2FS, MMFS used manually plugged plates to

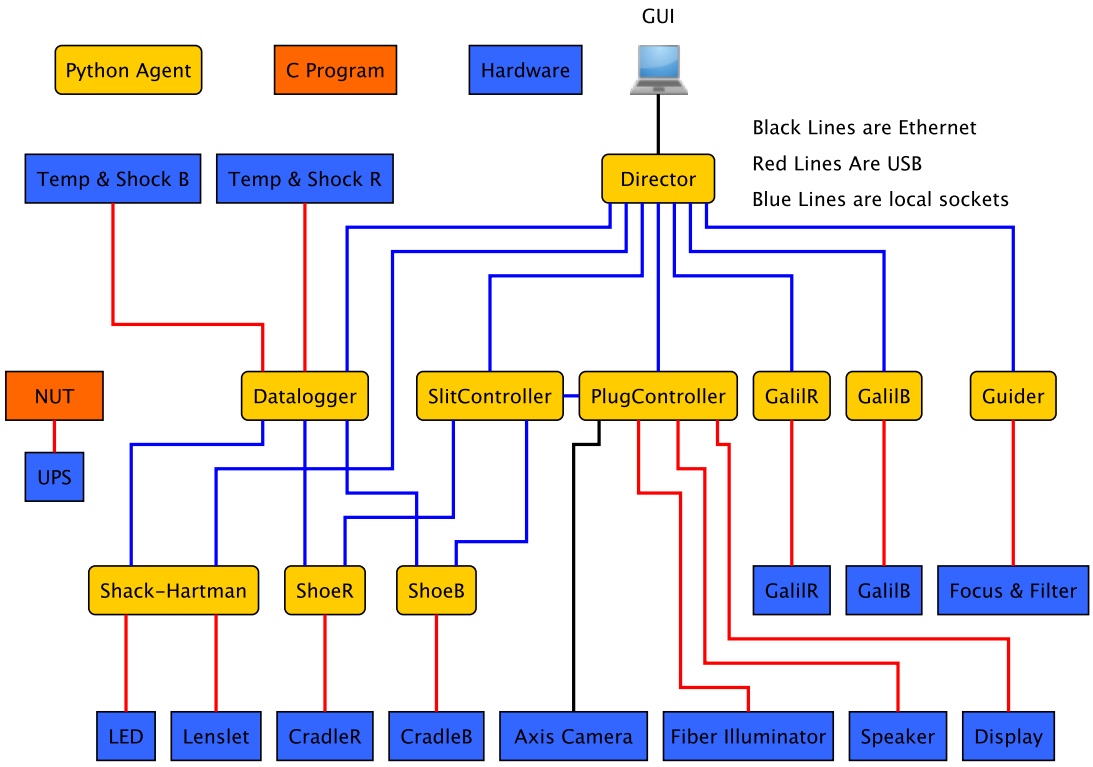

Figure 3.6: An overview of the key software components of the M2FS control system and where they fit in relation to the hardware they control. The fiber shoes and Galils also run a significant amount of onboard code.

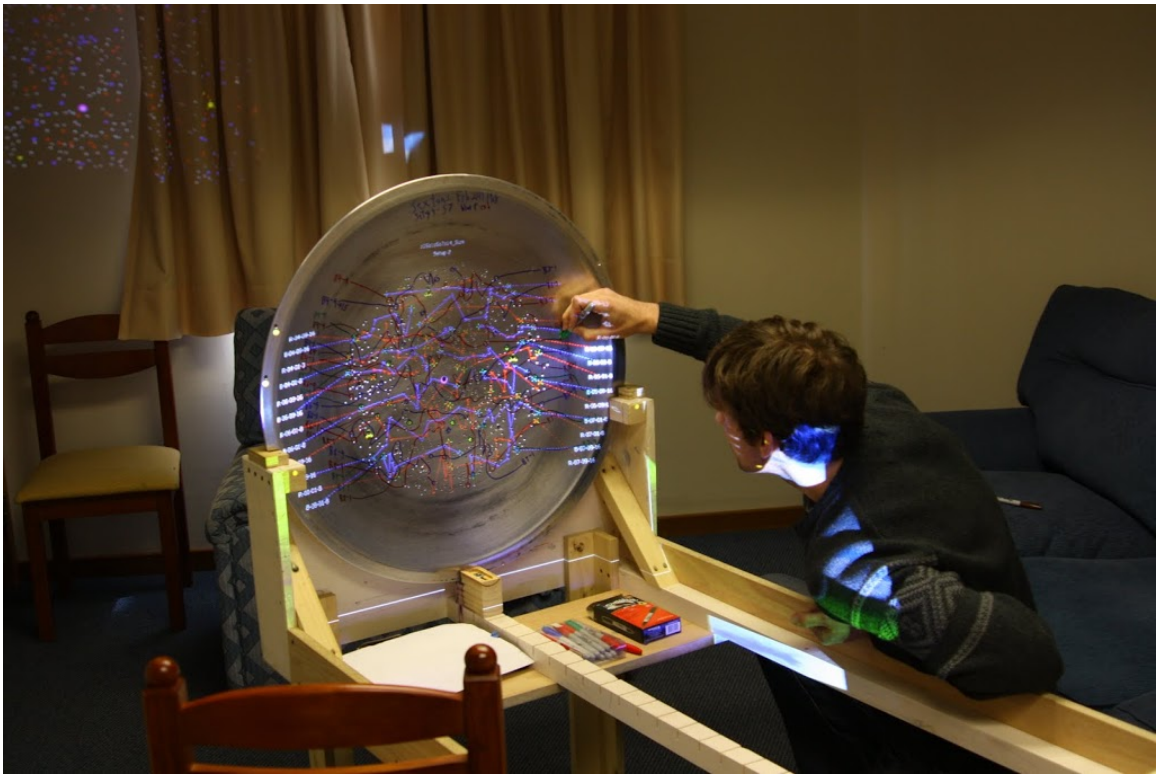

Figure 3.7: An MMFS observer preparing a plugplate. Out of the shot an LCD projector is set up to projects the required map onto the plate in a connect-the-dots fashion. Note the relatively poor ergonomics. Ultimately the ergonomics and optical aberrations of the projector near the plate edges (unusable with MMFS, but used by M2FS's wider field-of-view) led to a more simplistic approach. M2FS fiber maps are created by the `platemapper` software, printed, and marked with the diagram and plate in one's lap.

properly position fibers at the instrument focal surface (see Figure 1.3). In order to properly plug fibers into the holes drilled on each plate, observers would create a fiber-to-hole mapping using a pencil and a printout of each plate with the subset of holes needing fibers. This mapping was then drawn onto the plugplate with a marker so that while plugging the appropriate mapping was evident. I created the original `holemapper` to automate the fiber-hole mapping and then, in conjunction with a jig and projector, project an image of the map onto its plate to ease the drawing process to a simple tracing operation (see Figure 3.7). This process proved successful for MMFS and served as part of the motivation for the new `platemapper` program.

With M2FS we needed to create a new software package that handled both the

plate creation process—the task of taking target lists from users and determining where the appropriate holes should be drilled on a plate—and combine it with both the plate mapping process and the instrument control software. This new pair of programs, `plateplanner` and `platemapper`, allows additional flexibility in the plate creation process (e.g. controlling which target is lost if two targets on a plate are incompatible), helps visualize the possible field combinations, and, critically, enables M2FS FITS files to list, at least nominally, which target is in which fiber.

The `plateplanner` program, described in the next section, takes "fields" as input and generates "plates" as output. Fields, each defined in its own `.field` file, specify a list of targets, sky positions, guide stars, acquisition stars, and a single Shack-Hartman along with values for various field specific settings. Plates, each defined in its own `.plate` file, fully describe a plug plate. Each file contains all of the information in the field files used to create the plate along with the physical coordinates of the targets that were placed on the plate and a listing of the targets that were not. The plate, in conjunction with one or more "configs" (each in a `.config` file) and a "setup" (in a `.setup` file), is then used as input to the `platemapper` program to determine the fiber mapping for the plug plate. These "fiber maps" (in `.fibermap` files) are loaded onto M2FS and used by the instrument to populate the FITS file headers during observing.

3.3.2.1 plateplanner

The `plateplanner` program, shown in Figure 3.8, is used to generate both the plate file and the lists of machine coordinates used by the Carnegie Observatories machine shop to drill the holes into the physical plate. The program, which consists of ∼4000 lines of python and ∼600 lines of fortran, interfaces with heritage code that uses `SLALIB` to convert the sky coordinates into the physical positions of holes to be drilled on a plate. These positions, along with target priorities and machining

constraints, are then used to place the maximum possible number of targets on the plate.

After compiling all of the fields that need to be placed on a plate, the user runs the program, points it to the directory of field files, and then selects one or more fields to be placed on a plug plate. After translating the selected field's coordinates to machine coordinates the following algorithm is used to determine what targets make it onto the final plate:

1. For each field:
   (a) Exclude any targets outside the usable plate area.
   (b) Exclude targets that are incompatible with higher-priority targets in the same field.
   (c) Exclude sky positions ('skys') that are incompatible after satisfying the field's minimum requirement.
   (d) Keep the minimum number of guide stars required, dropping the minimal number of targets required across all fields. If an 'undroppable' target needs dropping then the fields are incompatible and may not be placed on the same plate.
   (e) Repeat the guide step for acquisition stars.
2. For each of the remaining targets and skys assign placement priorities. Undroppable target receive highest priority, opportunistic targets and droppable skys receive lowest priority.
3. Go round-robin through the fields, taking the current field's highest priority droppable target and assigning it the next highest placement priority.
4. Raise the priority of each sky by the number other skys or targets it interferes with.

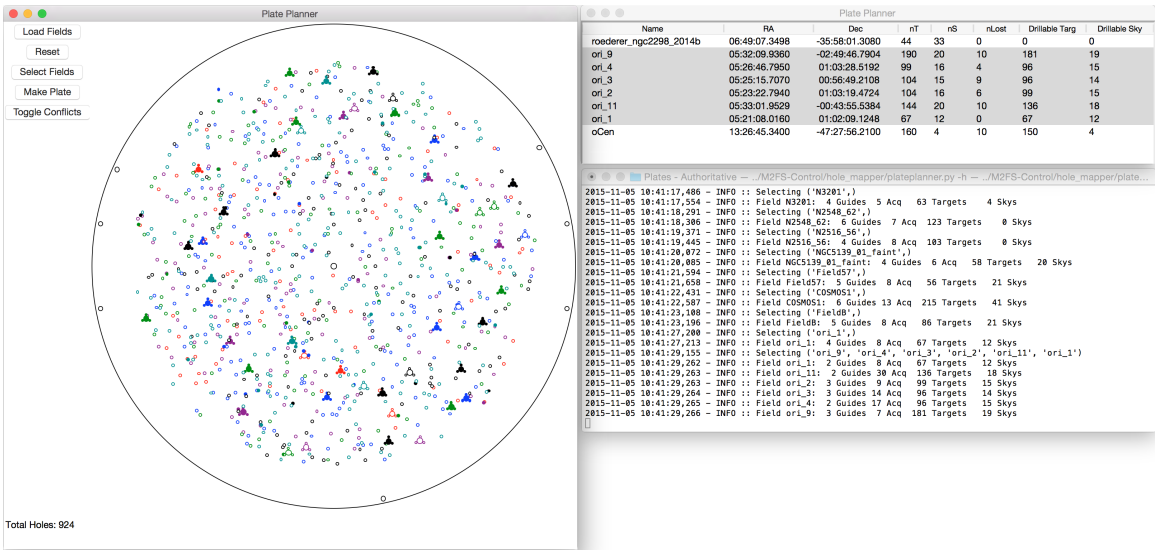

Figure 3.8: This screen capture shows the user interface of the `plateplanner` program. At left, the main window shows a graphical representation of a proposed M2FS plugplate with six different fields. Each of these fields is represented by a set of colored circles, with filled circles noting holes that can not be placed on the plate due to either conflicts with another field or operational constraints. The majority of these (the larger triangular patterns) are extra guide stars we ask users to provide to help minimize inter-field conflicts. The field selection window (upper right), displays the list of fields loaded into the program and allows the user to select one or more fields for inclusion on the plate. The console window in the lower right displays various status messages.

5. Go through the incompatible targets and skys from lowest to highest priority, eliminate the lowest, recompute the collisions, and repeat until everything is compatible. Greedily take skys (instead of eliminating) until the minimum number of skys required by each field is met.

6. Discard any excess skys

Once complete, the software creates text files with lists of the coordinates for each size hole to be drilled, a plate file for reference by the user and use by M2FS and `platemapper`, and an encapsulated postscript rendering of the plate.

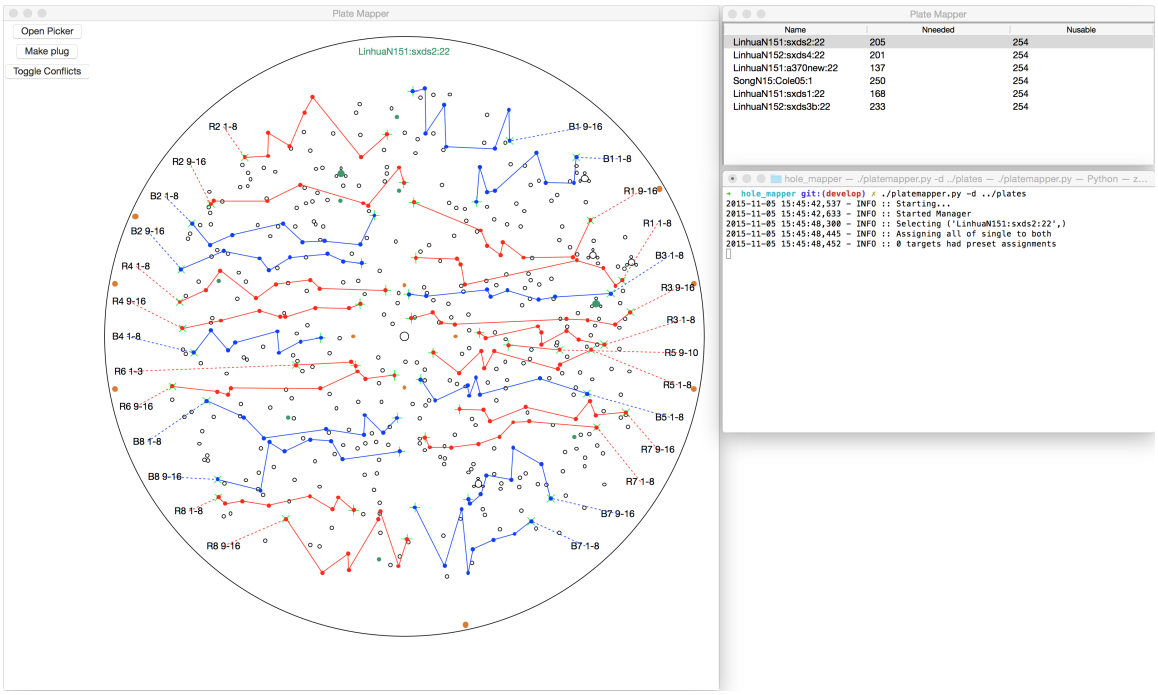

Figure 3.9: This screen capture shows the user interface of the `platemapper` program. At left, the main window shows a graphical representation of a M2FS plugplate with the assigned fiber mapping overlaid. In this instance the selected setup uses a configuration that permits observing with all 256 fibers however some remain unused as the setup only requires 205. Guide and acquisition stars used by the field are shown as filled aquamarine circles. The setup selection window (upper right), displays the list of all the setups (plate+field+config) loaded into the program and allows the user to select one or more setups to be mapped. At the time this image was made M2FS had two weak science fibers which is why the number of useable fibers is listed at 254. The console window in the lower right displays various status messages.

3.3.2.2 platemapper

The `platemapper` program, shown in Figure 3.9, is used to generate the M2FS fibermaps. The program, which consists of ∼5000 lines of python (mostly shared with `plateplanner`), uses the plate files produced by `plateplanner` and user specified setups consisting of plate+field+configuration to produce a deterministic mapping for whichever setups are selected by the user. The program creates fibermaps which are saved and uploaded to M2FS and also creates postscript files which are printed and used to transfer the fiber assignments onto each plate with a marker.

The most common scenario consists of assigning a single setup that calls for M2FS

in one order HiRes mode or in LoRes/MedRes mode with identical modes on both arms of the instrument. In this situation fiber assignment is driven exclusively by the ergonomics of the plugging process. Essentially the plate is divided into thirty-two rectangles (sixteen per side) each sized to contain eight holes. When the fibers are underutilized some regions may have no fibers and one on each side may have less than eight. Each region is assigned a group of eight fibers (e.g. R3 9–16 or B8 1–8) and the holes and fibers are paired up from left to right across the plate. In some configurations there are heavy restrictions on which fibers can be used (to prevent echelle orders from overlapping on the CCD) or more targets than available fibers. In these cases the process is essentially the same though some fibers or lower-priority targets are removed from consideration.

The program also supports much more complicated cases. The most common of these, setups that use the two M2FS spectrographs in different modes, is handled similarly to a restriction on which fibers are usable. Other cases, such as subsequent visits to a field offering more targets than usable fibers or even mixing multiple setups simultaneously, are supported and drive the vast majority of the code complexity. This latter case is sometimes used when two different projects use complementary numbers and sets of fibers: we can then assign fibers for each field at the same time and plug once, saving between 20–40 minutes of overhead. Although some internal provision has been made to allow mixed fiber slit widths within a single field, doing so reliably and in conjunction with the aforementioned complexities proves exceptionally complicated and remains untested.

CHAPTER IV

A Multiplexed Spectroscopic Survey of Two Open Clusters

4.1 Introduction

In Chapter I I described the value of exoplanets discovered in open clusters and explained how one of the core challenges to achieve this is surveying a large enough sample to develop a statistically significant sample of exoplanets within clusters at various ages. With this chapter I introduce our survey of two nearby open clusters. This survey has two primary goals: 1) to validate M2FS's ability to measure precision RVs for multiple targets simultaneously and, 2) to begin a search for exoplanetary systems of hot gas giants down to $\sim$0.1 M_{Jup} that are orbiting stars in clusters within $\sim$1 kpc.

To do this, we used M2FS to obtain multiplexed, high-resolution (R$\sim$50,000) optical spectra of solar-analogue stars (spectra types F5V to K5V) in the nearby open clusters NGC 2516 and NGC 2422. Our approach – a variant of the telluric-reference approach first proposed by Griffin & Griffin (1973) and subsequently used or studied by Cochran (1988, and references therein), Seifahrt et al. (2010), and Bailey et al. (2012) – models the observed stellar and telluric absorption features to obtain high-precision velocities and stellar parameters. We are able to measure RVs

to 25 m/s for up to 128 stars over a half-degree field-of-view simultaneously. Though motivated by a desire to identify hot gas-giant exoplanets in star clusters, these data also provide stellar parameters with high precision enabling additional investigations of cluster evolution, chemistry, and internal dynamics. This chapter describes how we selected our first open cluster targets and then used M2FS to measure precise RVs and stellar properties.

We describe our target selection and observing procedure in §4.2, followed by a descriptions of how we determined an optimal M2FS instrument configuration for this task in §4.3 and our observational dataset in §4.4. Section 4.5 describes our image reduction procedure and extraction to 1D spectra. In §4.6 we present our spectral modeling approach and describe the procedure in detail. Finally, §4.7 analyzes the quality of the measured stellar parameters and RVs.

4.2 Cluster and Spectroscopic Target Selection

To select our targets, we first created a list of potential star clusters in the Catalog of Open Cluster Data (Kharchenko et al., 2005) suitable for this project using a small number of basic selection criteria (Table 4.1) chosen to identify systems suitable for multi-object spectroscopy of solar analogs that are close enough to have members sufficiently bright to detect small-amplitude RV variability and old enough to limit stellar jitter. We imposed restrictions on cluster size (R_{cen} in Table 4.1, the core radius derived by Kharchenko et al., 2005) and richness to ensure good multiplexing efficiency, and we also placed limits on age and metallicity to exclude clusters with stars that exhibit excessive surface activity (thereby mimicking or masking the Doppler RV variations of a companion) or clusters too metal poor to efficiently form exoplanets. From the list of matching clusters, we selected NGC 2516 and NGC 2422 as our targets for this study. These ∼140 Myr and ∼75 Myr old open clusters are within 500 pc, rich in solar analogues, have angular sizes that are well-matched to the

Table 4.1. Cluster Selection Criteria

Criterion	Value	Comment
Dec (deg)	$< +10$	Visible at Magellan
DM	10.0	Bright enough for pRVs
Age (Myr)	$\gtrsim 100$	Diminished stellar activity
R_{cen} (deg)	$\lesssim 1.0$	Match to M2FS FOV
Fe/H	$\gtrsim -0.3$	Maximize HJ frequency
N_{F5-K5}	$\gtrsim 80$	Match to number of fibers

multiplexing capabilities of M2FS, and have recent photometric membership catalogs sufficiently deep for selecting solar-analog members (Jeffries et al., 2001; Prisinzano et al., 2003, hereafter J01 and P03).

Individual targets in NGC 2516 were drawn from the sample of stars studied in J01. We selected all stars they identified as photometric single (79) or photometric binary (47) members having colors and magnitudes consistent with F5V–K5V spectral types. This sample of 126 stars was then cross-matched with the UCAC4 catalog (Zacharias et al., 2013) and the UCAC4 coordinates used to prepare the plug plate. In NGC 2422 we selected all objects with colors and magnitudes consistent with F5V–K5V in the membership list P03. Due to a smaller number of known members in our field of view, we expanded our selection out in color from the MS defined by P03 members using the UCAC4 catalog until we had sufficient targets to fill the available fibers, eventually selecting an additional 25 stars in our adopted pointing in this manner. We then cross-matched the P03 targets with UCAC4 for astrometry.

The final target list was generated by selecting a central, bright star for use as a Shack-Hartman reference in each cluster that maximized the number of targets in M2FS's field of view. In NGC 2516 we intentionally mis-centered our pointing to also maximize the number of targets available for a future, additional pointing. With 128 available fibers, we are able to target every star in each half-degree field that

Table 4.2. Target Cluster and Pointing Information

Cluster	Messier	RA (2000)	Dec. (2000)	Age (Myr)	Dist. (pc)	E(B−V)	N_{ep}	N_{targ}	V	B−V
NGC 2516	...	7:58:42	−60:46:36	141	346	0.11	12	126	11.68–15.09	0.46–1.26
NGC 2422	M 47	7:36:30	−14:29:42	72	491	0.07	10	125	12.20–16.10	0.45–1.43

Note. — The coordinates listed correspond to our field centers and, although near, are not at the cluster center. Both distances and the reddening value for NGC 2422 are from Kharchenko et al. (2005). Target photometry is from J01 (NGC 2516) and P03/UCAC4 (NGC 2422). The reddening value for NGC 2516 is taken from Sung et al. (2002). The age for NGC 2516 is from Meynet et al. (1993) and for NGC 2422 from Loktin et al. (2001). We note that Kharchenko et al. (2005) gives ages of 120 Myr and 132 Myr, albeit with errors ∼70 Myr.

could plausibly be a solar-analog member. The results of this selection process are shown in Figure 4.1, which show HR diagrams and sky charts for the NGC 2516 and NGC 2422 input catalogs and targeted samples. Table 4.2 provides the coordinates, color and magnitude ranges, and number of epochs obtained for our pointings in each cluster along with cluster age, distance, and reddening. Ultimately we targeted 126 proposed photometric members in NGC 2516 and 100 proposed photometric members in NGC 2422, supplemented with 25 candidate members for a total of 125 targets in NGC 2422. We report a list of our observed targets and information on them in §4.4.

We selected an additional field in NGC 2516 with thirty-two sources with magnitudes (assuming membership) and colors consistent with B8–A4 stars (B−V= −0.1 – 0.113; $M_V = 0 - 1.7$). These stars possess essentially featureless spectra—apart from telluric features—in our wavelength range and hence can serve as useful probes to monitor the instrumental point spread function (PSF) over the full field of view of the spectrograph cameras.

Finally, we selected six stars—each in its own pointing—with similar RAs from the GAIA RVS catalog (Soubiran et al., 2013) for use as radial velocity standards. One of these, HIP 48331, was observed repeatedly and is being used as a primary reference to track our RV measurement precision over the duration of the program. Although this star hosts an exoplanetary companion, the induced RV semi-amplitude

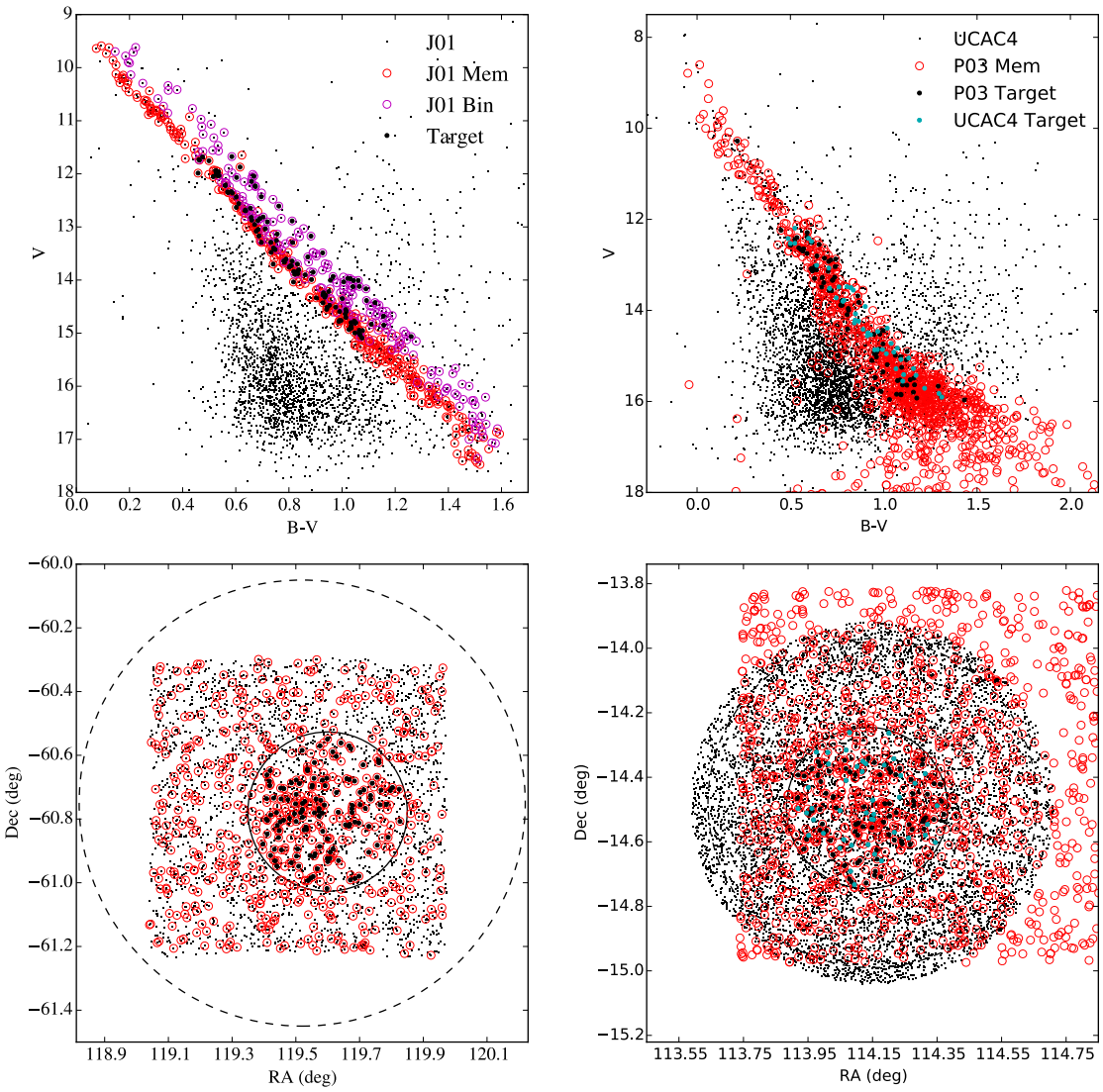

Figure 4.1: This figure shows color-magnitude diagrams and sky plots of our pointings in NGC 2516 (left) and NGC 2422 (right). The upper left panel shows stars in the J01 as minuscule black points with stars flagged as photometric single members circled in red or photometric member binaries in purple, stars we targeted are shown as large black marks. The upper right panel shows stars in the UCAC4 catalog within 1.1 cluster radii of the center of NGC 2422. Stars in the P03 catalog (which only includes photometric members) are circled in red. Our targets are shown as large black marks where from P03 and cyan marks where from UCAC4. The lower left panel again shows NGC 2516 stars, this time with all photometric members (single or binary) circled in red. The lower right panel does the same for NGC 2422. The square shapes stem from the CCD footprints used by J01 and P03. The dashed black circle represents each cluster's nominal radius as reported in Kharchenko et al. (2005) and the solid black circle the M2FS field of view around our pointing center.

Table 4.3. Standard Stars

Target	N	V_{mag}	RV (km/s)	$v \sin(i)$ (km/s)	Sp. Type	T_{eff} (K)	log(g)	[Fe/H]	[α/Fe]
HIP 48331	35	7.67	-9.510 ± 0.005	0.9	K5V	4455 ± 80	4.67	-0.18[a]	...
HIP 13388	2	8.09	65.606 ± 0.009	2.7	K1V	5095 ± 64	4.59	-0.15	0.02
HIP 10798	5	6.33	7.469 ± 0.007	2.7	G8V	5481 ± 80	4.63	-0.44	0.17
HIP 22278	3	8.52	23.456 ± 0.014	3.6	G5V	5721 ± 65	4.22	0.13	-0.01
HIP 19589	1	8.46	-5.500 ± 0.024	3.6	G0V	5825 ± 90	3.75	-0.17	0.13
HIP 31415	1	7.70	-7.479 ± 0.012	4.5	F6V	6172 ± 60	3.94	-0.31	0.12

[a] Taken from Santos et al. (2005) as Casagrande et al. (2011) flags these measurements as of poor quality, though Santos reports an error of 0.19.

Note. — This table lists the literature properties and number of epochs we obtained of the standard stars observed for this program. RVs, magnitudes, and spectral types are taken from Soubiran et al. (2013). $v_r \sin(i)$ values are from Głębocki & Gnaciński (2005). Stellar parameters are taken from Casagrande et al. (2011).

is only 0.8 m/s (Pepe et al., 2011), far below our expected measurement precision and so its variability is irrelevant for our purposes. A summary of the standard stars used for this study is presented in Table 4.3.

4.3 Instrument Configuration

For our study, we employed a two-order filter with a design passband of 7050–7370 Å (M2FS echelle orders 49 and 50). The use of a passband filter is necessary to prevent spectral orders from one fiber overlapping with those of another. This particular passband was selected after careful consideration of the optimal wavelength region to carry out telluric-reference RV measurements of solar analogue stars. We used the formalism of Butler et al. (1996) combined with synthetic spectra from the PHOENIX grid (Husser et al., 2013) to estimate the RV uncertainties for slowly-rotating, main-sequence stars with effective temperatures between 4000 and 7000 K for a range of M2FS orders redward of about 6800 Å. This uncertainty was then added in quadrature with the wavelength reference uncertainty in each order determined by applying the same formalism to the telluric absorption features present in the empirical telluric spectrum from Wallace et al. (2011). The results of this analysis

are summarized in Figure 4.2, which demonstrates how order 49, centered at 7230 Å is anticipated to exhibit the best RV precision especially at lower S/N and resolving power over the T_{eff} 4000 – 6500 K range. We selected M2FS orders 49 and 50 as we found few clusters within 1 kpc would offer more than ∼100 targets in a single M2FS field and the additional order offered the possibility of slightly better performance. The use of a two order bandpass limits us to every second M2FS fiber, thereby strictly limiting us to a multiplexing factor of 128.

In practice, the delivered filter cut off parts of both orders due to a shift in the manufactured grating blaze, rendering data from order 50 to be of little use, cutting off part of order 49, and limiting system throughput by a factor of two (Figure 4.3). Nonetheless, as we show in §4.7.2.1, this bandpass was still able to deliver excellent RV precision and reasonable S/N for stars of interest in our target clusters. A replacement filter designed for our as-manufactured grating will cover a slightly different wavelength region (7160–7360 Å), adding an additional 14 major lines while improving our throughput twofold. We anticipate this will improve our achievable velocity precision by ∼15% where we are not limited by systematics.

For the observations obtained in this study, we employed the 45 μm wide slit which projects to an average of three pixels on the detector. For this configuration we found an effective resolving power in the 40 – 60k range for most fibers (c.f Figure 4.4), with the lower end of the range driven largely by poor instrument focus in some of our images.

4.4 Observations

Since we were looking for radial velocity variations among stars in clusters that might harbor exoplanetary systems, our observing procedure involved repeat observations of our target fields (Table 4.2). To date, we have observed our pointings in NGC 2516 12 times and NGC 2422 10 times, and made 35 observations of our

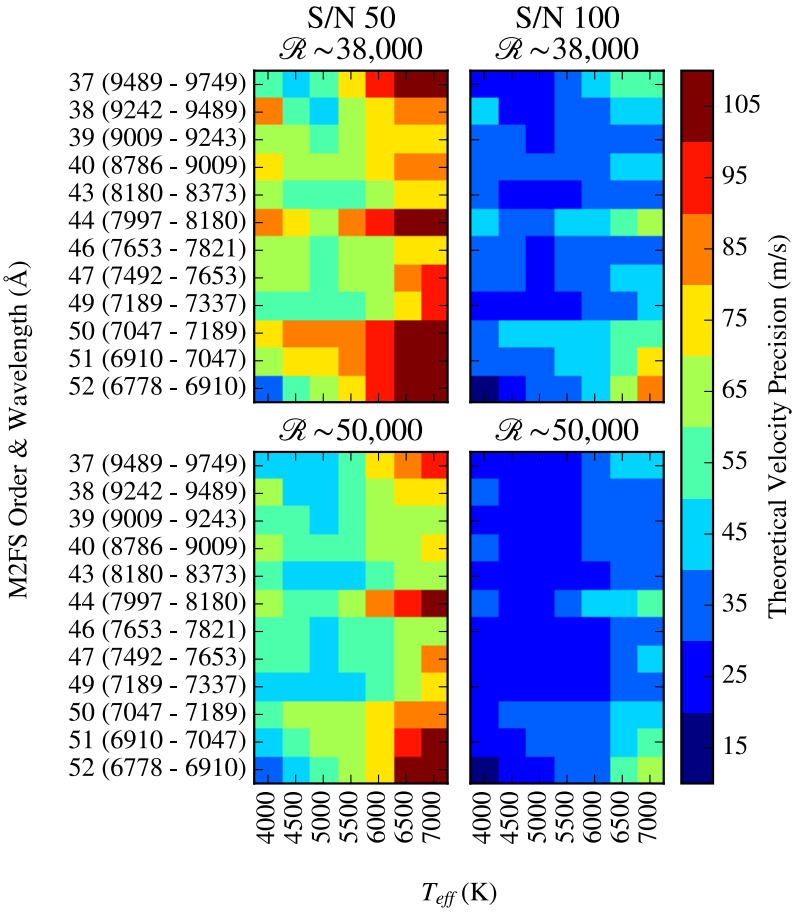

Figure 4.2: The velocity precision attainable for slowly rotating ($v_r \sin(i) = 5$ km/s), Solar abundance, dwarfs stars with T_{eff} between 4000 K and 7000 K when using telluric lines as the wavelength reference, according to the formalism of Butler et al. (1996). Each individual plot gives M2FS echelle order number and nominal wavelength range on the vertical axis and T_{eff} on the horizontal axis. In each case a log(g) of 4.5 is used, though results are not significantly affected by this choice. The two columns correspond to S/N of 50 and 100 and the rows to $\lambda/d\lambda$ of 38,000 and 50,000. Colors correspond to the attainable RV precision. It is interesting to note that this plot quantifies the assertions of Griffin & Griffin (1973) from some 43 years ago.

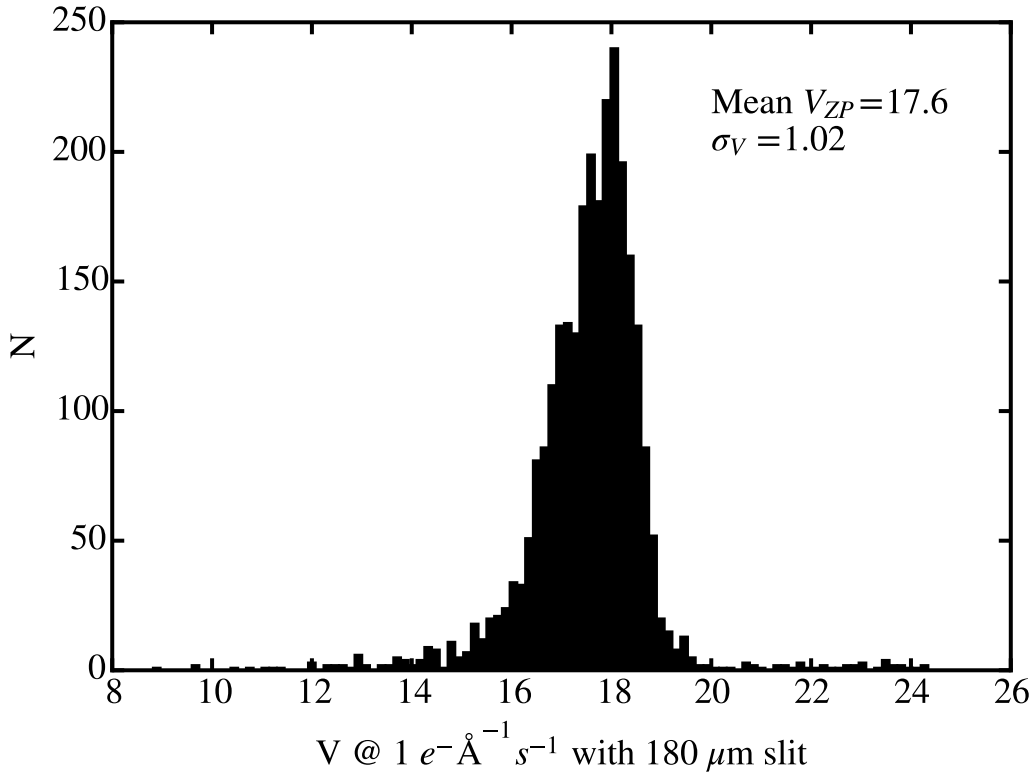

Figure 4.3: System zero point for each of our 2700 spectra corrected for variations in fiber throughput, slit losses, and to median Magellan/Clay seeing. We apply these corrections to facilitate comparing M2FS throughput between different instrument configurations. For other M2FS instrument modes we find a typical zero point of 18.3 ± 0.3 mag, significantly fainter than measured for our spectra. This loss is a direct result of our filter bandpass edge falling just prior to the blaze peak. This is corrected in the second version of our filter.

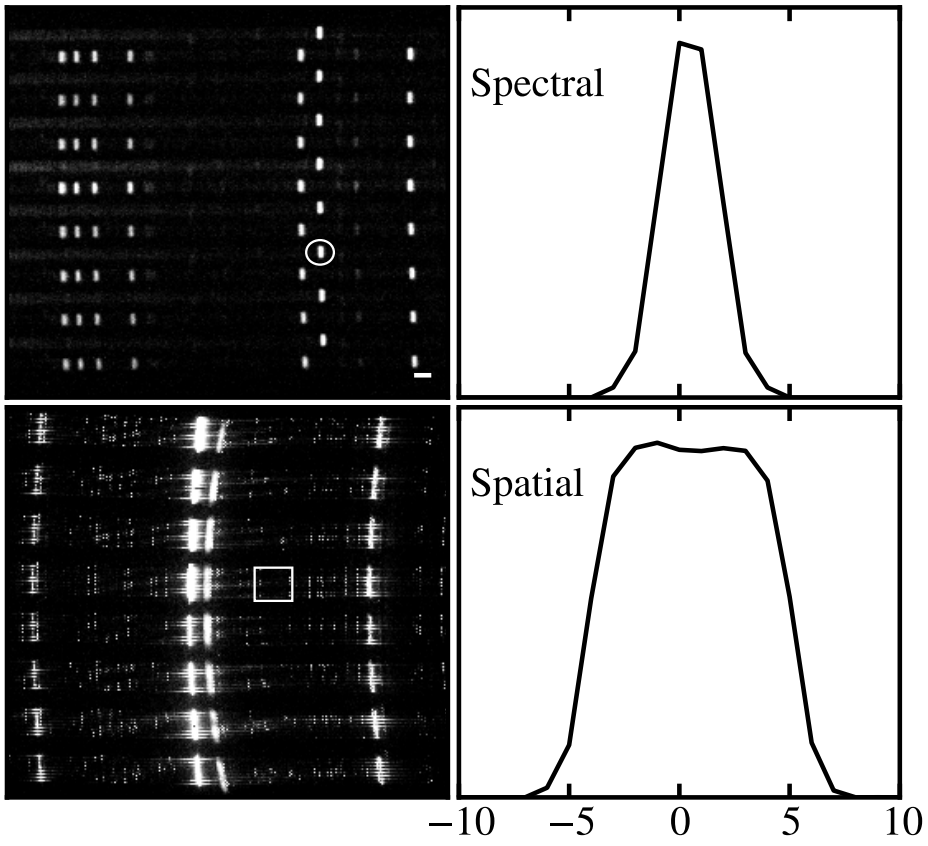

Figure 4.4: This figure shows various aspects of an M2FS ThArNe calibration image (lower-left) made in our configuration. The upper-left panel is a detailed view of the boxed region. In it the small horizontal bar to the lower-right of the image is 10 pixels long and the line profiled in the right two panels is encircled. The FWHM of the lamp lines across the image corresponds to ∼3 pixels (R∼52,000) on average.

principal RV standard HIP 48331 along with a small number of observations of the other comparison standards (Table 4.3). Observations were made in groups of 1–4 observations obtained during runs in November 2013, February 2014 and December 2014.

Fibers are positioned at the focal surface of the telescope with M2FS using aluminum plug plates that are manually installed and plugged. For a given field, each assigned fiber is positioned at a specific hole in the plate marked for that fiber. We typically deployed 128 fibers for the NGC 2516 and NGC 2422 fields, though with dead or otherwise inactive fibers excluded. Once plugged, a typical observation then consists of acquiring the field using a set of ancillary fibers and imaging optics aligned to reference stars in each field. Typical total exposure times were 2 hrs and 2.5 hrs per visit for NGC 2516 and NGC 2422, respectively. Most visits consisted of 3–5 individual exposures to aid in cosmic-ray removal and to enable measurement of the photon midpoint for barycentric correction. This yielded a median S/N of $\sim$55 ($\sim 1\sigma$ range 15 – 70) per 1D extracted pixel ($\sim$90 per resolution element). An example science frame is shown in Figure 4.5.

For each observation we obtained calibration data consisting of a Thorium-Argon-Neon lamp exposure (an example of which was shown in Figure 4.4) and a quartz lamp exposure either before or following the science frame. On some nights during which our targets were observed we also obtained either evening or morning twilight spectra.

RV standard observations were performed by placing a single fiber in a standard hole on the fiber plug plate and offsetting from the field center. Remaining fibers were left in their positions and see only sky. Typically three two minute exposures were used to obtain a spectrum of S/N$\sim$240 per extracted 1D pixel. Finally we obtained four epochs (1 or 2 per observing run) of the telluric standard calibration field in NGC 2516. These spectra have a median S/N of 160 and were obtained in 3 to 5

exposures totaling roughly one half hour.

The dates, number of stars targeted, median per-pixel S/N, and exposure times for each of our epochs is listed in Table 4.4. In two instances operational issues resulted in a small number of stars not being targeted. Over the course of our campaign an evolving set of damaged or dead fibers impacted our ability to obtain spectra of various targets. This, along with a wide magnitude range and variable seeing, resulted in a number of targets for which some (for one star all) of our spectra fell below the S/N limit (12) at which we are able to reliably run our analysis. Tables A.1 and A.2 list target IDs, literature photometry, number of usable (S/N $>$ 12) epochs, and mean per-pixel S/N for each target. They also list a number of results that are the topic of later chapters.

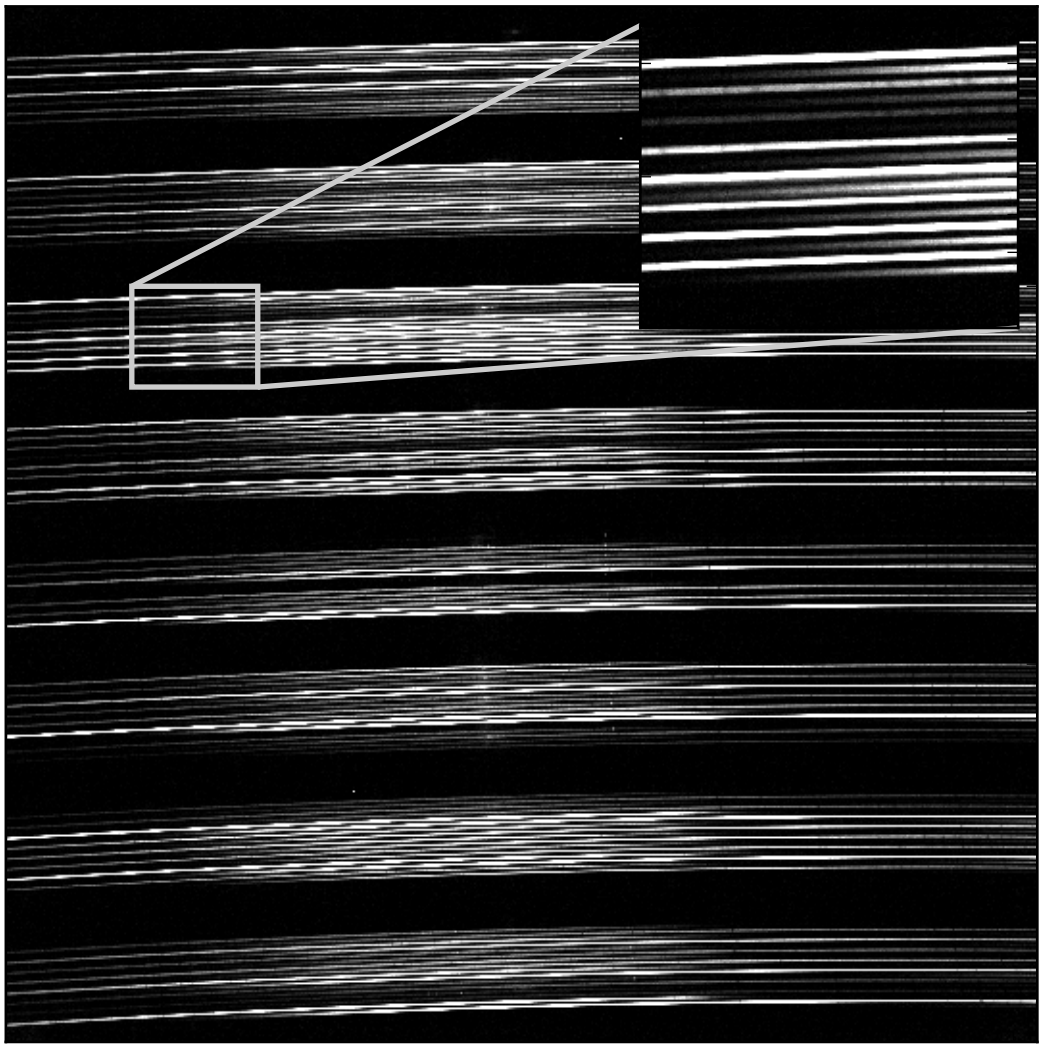

Figure 4.5: An example science frame in NGC 2516. M2FS fibers are bundled in groups of sixteen at the camera focal plane, and although we use ever other fiber we also use a two-order passband, resulting in the groups of sixteen spectra. The larger gaps in the image reflect spacing between adjacent bundles of fibers and are used to estimate the scattered light in the image. Each fiber maps to a consecutive pair of apertures (best seen in the inset): the lower is order 50 (unused) and the upper is order 49. The variability in this frame is a function of both target magnitude and fiber throughput.

Table 4.4. Cluster Observations

Date	N	Median S/N	ET (s)
NGC 2516			
2013-11-22	118	57	6600
2013-11-24	126	28	6000
2013-11-27	126	38	6300
2013-11-28	126	59	7200
2013-11-30	126	44	6800
2014-02-16	103	46	9600
2014-02-17	126	65	9000
2014-02-21	126	57	9000
2014-12-09	126	48	7200
2014-12-10	126	33	7200
2014-12-11	126	63	9000
2014-12-12	126	55	7200
NGC 2422			
2013-12-01	125	60	7200
2014-02-18	125	55	9000
2014-02-19	124	46	7200
2014-02-22	124	41	7200
2014-02-26	125	38	9000
2014-12-12	125	35	9000
2014-12-13	125	51	10150

Table 4.4 (cont'd)

Date	N	Median S/N	ET (s)
2014-12-17	125	71	9800
2014-12-20	125	57	11200
2014-12-22	125	59	10800
Telluric Standards			
2013-11-26	32	188	1800
2013-12-01	32	173	1200
2014-02-25	32	144	1800
2014-12-15	32	142	1800

4.5 Reduction

4.5.1 Image Processing

Basic data reduction follows a mostly traditional script. The four quadrant images produced by the CCD's four amplifiers were bias corrected by subtracting the median overscan column and then row. We then converted counts to electrons and used the Python implementation of the L.A. Cosmic algorithm (van Dokkum, 2001) to detect cosmic rays: this algorithm takes the Laplacian of the image and identifies cosmic rays using their steep intensity gradient. The quadrants were then packed together and stored with a variance frame consisting of electrons plus the square of each quadrant's read noise and a bad-pixel mask.

We created a cleaned, summed image by adding the electrons and variances of each pixel across a sequence of frames. Masked pixels in each component frame were repaired with their expectation value based on the other frames. A scaling value was computed for each frame to normalize throughput and exposure time variations by using the total time-normalized counts of all spectra as a proxy for throughput variability. Bad pixels in each frame were then repaired using the expectation value determined from the good pixels in other frames and the frame scaling values. The

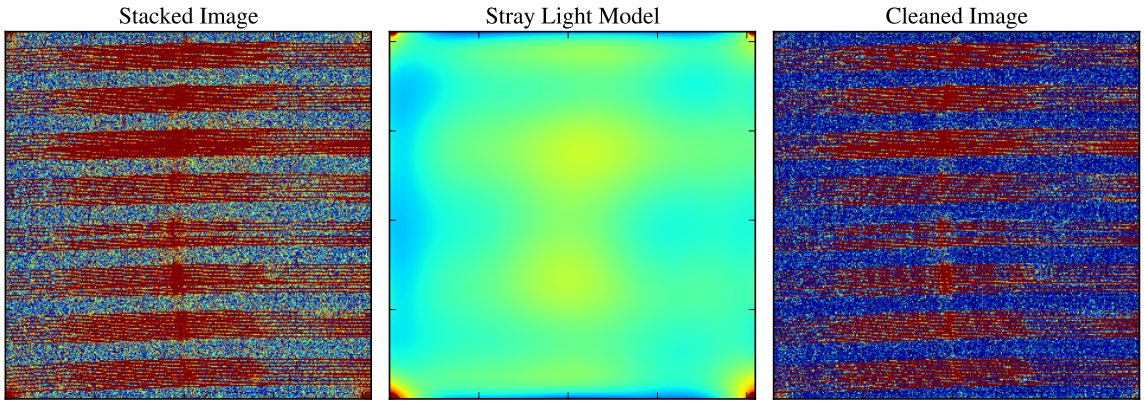

Figure 4.6: Left to right: A stacked science frame, a map of scattered light and dark current, and the cleaned frame. Amplifier glow and spectra are heavily clipped in the frames. The central, bright, vertical swath stems from Littrow ghosts. All three images share the same color scale.

variance of the final, summed pixel was inflated appropriately at every impacted pixel.

Typically one would flat-field the resulting frames, however Quartz trace flats of comparable signal-to-noise take an impractical amount of observing time and M2FS does not presently have a means of obtaining uniformly illuminated CCD frames. Engineering work shows M2FS CCDs are free from large defects and indicate pixel-to-pixel sensitivity variations of about 1.7% and only 0.25% of pixels are significantly hot or cold.

We subtracted a combined dark current and scattered light map, an example of which is shown in Figure 4.6 along with the image prior to and post subtraction. This map was computed by first modeling and removing the amplifier glow in each corner by fitting a 2D Gaussian surface. All remaining pixels within about a standard deviation of the mean light level in the dark regions between bundles of 16 fibers were then selected as "scattered light" pixels and used to fit polynomials across the image. The resulting map was Gaussian smoothed using a 32 x 64 pixel rectangle ($\sim$1.5 x 3 fiber spacings) and subtracted from the image. Without this step, these components would amount to about 150 e^- per 1D pixel in our extracted spectra, ranging from about 5% to 50% of our extracted signal for our brightest to faintest targets.

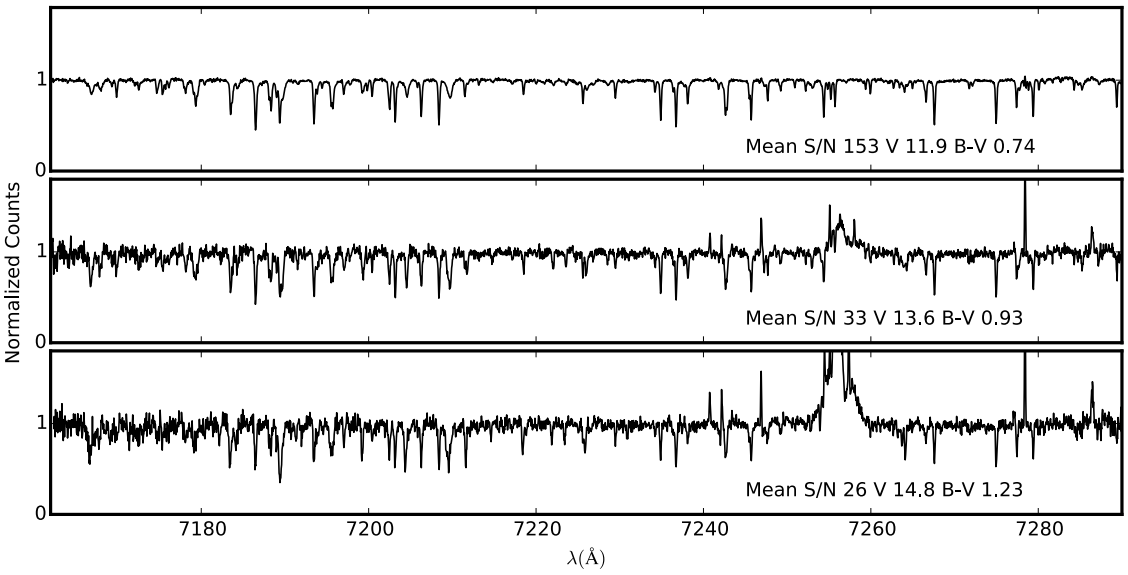

Figure 4.7: Example extracted spectra of representative F5, G5, and K5 targets. Note that sky emission lines become increasingly prominent for fainter targets. The large defect at ∼2755 Å is M2FS's Littrow ghost.

4.5.2 Extraction

Each processed frame was then extracted using the IRAF task `apall`. We first identified the approximate aperture locations and traces using dome flats taken during the day with all usable fibers plugged. The apertures were then median shifted to the locations of the quartz traces taken with each exposure to account for any temperature drift or repositioning errors in the instrument. We then extracted both the science and variance frames without variance weighting using identical apertures. Finally we continuum normalized the spectra by iteratively fitting a polynomial, each time excluding points 1 sigma below or 2 sigma above the best fit. Examples of order 49 for a ∼F5V, G5V, and K5V star in our sample are shown in Figure 4.7.

4.6 Analysis

We measured each target's stellar properties (e.g. T_{eff}, [Fe/H], [α/Fe], $v_r \sin(i)$) and line-of-sight radial velocity (RV) by fitting a model of each extracted, normalized

spectrum to the data in 1D pixel space. This approach is similar to the popular gas cell approach where molecular absorption lines from a well-calibrated gas cell (e.g. I_2, Ammonia) are used as a simultaneous probe of pixel wavelengths and the instrumental point-spread function (PSF). Here we make use of the abundant atmospheric H_2O lines in the 7230 Å region as the imprint of a giant gas "cell." This idea was originally proposed by Griffin & Griffin (1973) more than 40 years ago and has been used with success or investigated for use to measure RVs in both the optical (Cochran, 1988; Figueira et al., 2010) and the infrared (Blake et al., 2007; Prato et al., 2008; Seifahrt et al., 2010; Blake et al., 2010; Crockett et al., 2011; Bailey et al., 2012). These studies have demonstrated that telluric features are stable to 10 m/s. This should not come as a surprise as all of the water and the general bulk of our atmosphere is within the first 8 – 16 km where typical bulk motions are below 10 m/s and not along the line-of-sight. We quantify this source of uncertainty when we discuss our achieved RV precision in §4.7.2.1.

The model is constructed by combining a template of the telluric absorption spectrum, $T(\lambda)$, one or more synthetic stellar spectra, $S(\lambda; T_{eff},\ [\mathrm{Fe/H}],\ [\alpha/\mathrm{Fe}], v_r \sin(i),\ \mathrm{RV})$, a synthetic sky emission spectrum, $Sky(\lambda)$, and a Solar spectrum $Sun(\lambda; RV_\odot)$.

$$M(\lambda) = T(\lambda)^\alpha \cdot (S(\lambda; T_{eff},\ [\mathrm{Fe/H}], [\alpha/\ \mathrm{Fe}], v_r \sin(i),\ \mathrm{RV})^\beta + \gamma \cdot Sun(\lambda + s; RV_\odot)) + \eta \cdot Sky(\lambda) \quad (4.1)$$

This model is then resampled onto pixels, convolved with a model of the 1D projection of the PSF, and normalized.

$$M(pixel) = \frac{PSF(pixel; \boldsymbol{\sigma}) * M(pixel)}{N(pixel; \boldsymbol{\zeta})} \quad (4.2)$$

In the above equations the scalars $\alpha,\ \beta,\ \gamma,\ \eta,\ s$, and vectors $\boldsymbol{\sigma}$ and $\boldsymbol{\zeta}$ are model parameters which will be described in the next section and are summarized in Table 4.5.

Table 4.5. Model Parameters

Component	Symbol	N	Comment
Wavelength	$\boldsymbol{\mu}$	$\leq$8	$\lambda(pixel) = \sum_i^8 \mu_i L_i(pixel)$
PSF	$\boldsymbol{\sigma}$	1	Gaussian FWHM
		3	$FWHM(pixel) = \sum_i^2 \sigma_i L_i(pixel)$
		5	A 5^{th} order Hermite parameterization
		22	Butler et al. (1996) parameterization
Normalization	$\boldsymbol{\zeta}$	12	$norm(pixel) = \sum_i^{11} \zeta_i L_i(pixel)$
Stellar Temperature	T_{eff}	1	Snaps to 100 K grid[a]
Iron Abundance	[Fe/H]	1	Snaps to 0.1 dex grid
Alpha Abundance	[α/Fe]	1	Snaps to 0.1 dex grid
Stellar Rotation	$v_r \sin(i)$	1	
Radial Velocity	RV	1	
Airmass	α	1	Scale atmospheric transmission
Veiling	β	1	Scale stellar line depth in unison.
Solar Flux	γ	1	Fractional contribution of solar flux
Solar RV	$\text{RV}_\odot$	1	
Solar Offset	s	1	Offset between PHOENIX and Kurucz
Sky Emission	η	1	Scale SkyCalc spectrum

[a]Template spectrum with nearest value is used.

4.6.1 Model Input

4.6.1.1 Stellar Light

Our pipeline uses the PHOENIX grid as it samples a large stellar parameter space (far beyond our region of immediate interest), is the successor to the grid used in Bailey et al. (2012), and in no small part because it is the grid for which we attained the best RV precision for our RV standard. To verify this point we also checked both the Coelho (2014) grid and the AMBRE grid (de Laverny et al., 2012) and found both to result in larger RV measurement errors for our RV standard. Prior to modeling we up-sampled the PHOENIX grid (see Table 4.6) in the parameter space relevant to our target stars using linear interpolation by way of the SciPy function `map_coordinates`. Library spectra are normed by the maximum continuum value in the fitting region and linearly interpolated onto a constant $d\log(\lambda)$ grid, adopting the largest step size present in the raw spectrum, just prior to their use in the modeling pipeline.

During fitting, the surface gravity is tied to the effective temperature via Equation 4.3 which is derived from the mass-luminosity, temperature-luminosity, and mass-radius relations for lower main-sequence stars as our fits do not appear to be particularly sensitive to variations in $\log(g)$ among our main sequence targets. This weak dependence is seen in other techniques as well: Casagrande et al. (2011) reports that even variations as large as a half dex change affect T_{eff} by only a few tens of Kelvin. If left varying we found cluster members to cluster at the PHOENIX grid edge value of 6.0.

$$R \propto M^{0.9},\ L \propto M^4$$

$$L = 4\pi R^2 \sigma T_{eff}^4$$

$$g = \left(\frac{L_\odot}{4\pi\sigma}\right)^{4/11} \frac{GM_\odot}{R_\odot^{30/11} T_{eff}^{16/11}}$$

Table 4.6. Synthetic Grid Spacing

Grid	ΔT_{eff} (K)	$\Delta \log(g)$ (dex)	Δ[Fe/H] (dex)	$\Delta[\alpha/\mathrm{Fe}]$ (dex)
PHOENIX	100	0.5	0.5	0.2
Resampled PHOENIX	100	0.1	0.1	0.1

We calibrated the relation using Solar values corrected for age per the plot in Ribas (2010) ($L = 0.85$ L$_\odot$, $R = 0.925$ R$_\odot$) to obtain:

$$\log(g) = \log(\frac{9.44 \times 10^9}{T_{eff}^{16/11}}) \tag{4.3}$$

This input brings with it the astrophysical parameters T_{eff}, [Fe/H], $[\alpha/\mathrm{Fe}]$, $v_r \sin(i)$, and RV along with a feature depth parameter β which allows fudging the optical depths of all the stellar lines in unison. In the event of a spectroscopic binary we can enable multi-component modeling, using two sets of these parameters and an additional multiplicative parameter for the ratio of flux received from the two stars.

4.6.1.2 Telluric Transmission

We considered two options for the telluric transmission model: the NSO empiric transmission spectrum (Wallace et al., 2011) and the synthetic TAPAS model (Bertaux et al., 2014), nominally tailor made for the atmospheric conditions during each observation. The NSO spectrum derives from data obtained on the McMath-Pierce solar telescope using the Fourier transform spectrograph (FTS) in the late 1980s. TAPAS spectra are computed as described in Bertaux et al. (2014) for the conditions of each exposure.

When using TAPAS spectra in constructing our models for HIP 48331 we measured an RV 286 ± 8 m/s greater than when using the NSO spectrum as the template

and also observed a reduction in RV precision (c.f. §4.7.2.1). This is on the order of the uncertainty of the O_2 and H_2O line positions in the HiTran database (Rothman et al., 2009) and so is perhaps not unexpected given that it is used as the data source for TAPAS. It is interesting to note that this is also of order the shift caused by mixing the Edlén (1966) and Ciddor (1996) air/vacuum relations (e.g. converting one way with Ciddor and back with Edlén), however we are unable to ascertain a list of conversions applied between the original data and the output TAPAS spectrum and are unable to offer any firm conclusions regarding the source of the shift. We did measure better χ^2 values when using TAPAS spectra and suggest that the TAPAS pipeline models differences in atmospheric line strengths between Kitt Peak and Las Campanas well. Given the reduced RV precision we used the NSO FTS data for our analysis. This input brings with it the parameter α to logarithmically scale the absorption features as a proxy for airmass.

4.6.1.3 Sky Emission

We used the ESO SkyCalc tool (Noll et al., 2012; Jones et al., 2013) to obtain night sky emission spectra for our wavelength region. These spectra match the locations of the night sky emission lines well, though they do not always perfectly match their relative strengths. This input adds a multiplicative scaling parameter, η, to adjust the predicted count rate.

4.6.1.4 Instrumental Effects

The modeling code also includes inputs for the instrumental dispersion relation, PSF, and allows for inaccuracies in our continuum normalization. The dispersion relation is a set of Legendre polynomial coefficients ($\boldsymbol{\mu}$) which yield the wavelengths at each extracted pixel. We used a second set of Legendre polynomial coefficients ($\boldsymbol{\zeta}$) to compute a normalization polynomial that accommodates errors in continuum

normalization during extraction.

The PSF is widely understood (c.f. e.g. Butler et al., 1996; Bean et al., 2010; Bailey et al., 2012) to have a significant impact on the precision with which line centroids can be recovered and ultimately the RV precision. We investigated this effect by modeling our PSF with a Gaussian, a Gaussian with width quadratically varying along the order, the multi-Gaussian parameterization of Butler et al. (1996), and a 5th order Gauss-Hermite series (Gao priv. comm.). The results of our investigation are discussed in §4.7.2.1. We adopted the Hermite parameterization for our analysis.

4.6.2 Modeling Process

4.6.2.1 Model Construction

To compute the model described in Equations 4.1 and 4.2 the code first fetches the synthetic spectrum of nearest temperature, surface gravity, iron, and α-element abundance from our grid (recall $\log(g)$ is computed per Equation 4.3) along with the telluric absorption, Solar, and pointing dependent emission spectra. These spectra are all in excess of R$\sim$600,000.

The telluric transmission spectrum is scaled logarithmically by α and the sky emission and Solar spectra are scaled multiplicatively by η and γ, respectively. The solar spectrum is Doppler shifted by multiplying the wavelength grid by the appropriate Doppler factor.

The stellar spectrum is normalized by the maximum flux in the wavelength region to perform a simple continuum normalization while preserving the slight blackbody effect in our narrow region. In the case of a multi-star fit normalization of each spectrum is still carried out in this manner. The spectrum is scaled logarithmically by β to account for discrepancies in line depth and is then rotationally broadened via convolution with a kernel computed based on Gray (1992). We do not use the `lsf_rotate` library function of Hubeny & Lanz (2011) as it does not properly account

for the fractional contribution of samples at the kernel edge when the kernel is only a few samples wide, leading to discontinuities in χ^2 as a function of $v_r \sin(i)$: Instead we re-derive the broadening kernel using Equation 17.12 of Gray (1992) carefully accounting for grid effects. Finally the spectrum is Doppler shifted by multiplying the wavelength grid by the Doppler factor.

When modeling a double-lined spectrum this process is repeated for each star and a weighted average taken after they are placed on the sub pixel grid in the following step, with the weight a free parameter. We investigated combining the stellar components in a manner that preserves their relative flux from the synthetic library; however this often led to grossly inappropriate minima. When modeling a telluric standard spectrum the code treats the stellar component as unity.

If including scattered solar light, the solar spectrum is multiplicatively scaled by γ, s is added to the solar wavelength grid, and then the grid is multiplied by the appropriate Doppler factor.

Each of the components is linearly interpolated onto a 10^{th} pixel wavelength grid computed from the dispersion relation. We note that cubic spline interpolation significantly decreased our RV stability. These component spectra are then combined as in Equation 4.1.

This model is then convolved with the PSF kernel representing the instrument's point spread function as modified by our simplistic extraction. The kernel size was selected such that the kernel is less than 10^{-4} at the window edge and the kernel is constrained to be positive. To maintain a modicum of speed, pixel dependent convolutions are carried out via a FORTRAN subprogram. When using an asymmetric PSF we noted that the center of the enclosed power was not generally located at the central sub-pixel nor at some constant offset. We observed a shift for typical, good fits of 1.5 ± 0.86 pixels redward with the Hermite parameterization. Constraining the centroid to ± 0.05 pixels of the center confers substantial improvements to RV precision

(See §4.7.2.1). In the limit of a linear dispersion relation this effect would correspond to a simple pixel shift and would not be expected to have any impact on results, however our wavelength solutions are not linear. Our code constrains the centroid by shifting the PSF kernel and hence constrain the center of enclosed power to within ∼100 m/s of the central sub-pixel. Interpolated shifts or a PSF parameterization which constrains the enclosed power may be worth future investigation.

After convolution, the sub-pixel values are averaged to yield pixel values and the model is divided by the normalization polynomial, yielding a model spectrum.

4.6.2.2 Merit Function

We used the χ^2 statistic as a merit function to determine the optimal model. The fitter computes the weighted mean square error of our model with the normalized spectrum, masking pixels based on a wavelength mask (e.g. for sky lines, if desired), an RV dependent wavelength mask for stellar lines, and a pixel mask for detector defects and the Littrow ghosts. Wavelength masks are additive: for stability a change to the wavelength solution will not cause a pixel to unmask. The weights are computed as the ratio of the square of the continuum normalization to the variance spectrum. We noted a significant upward trend in our best-fit χ^2 with increasing signal (c.f. Figure 4.8), which we attribute to an improved ability to identify finer errors in our computed model. Visual inspection shows that PHOENIX spectra consistently mismatch stellar line depths and with increasing S/N these mismatches become more significant.

4.6.2.3 Model Fitting

Prior to fitting we visually reviewed all ∼2700 spectra and excluded spectra with average continuum S/N less than 12 per pixel, below which we are not able to obtain reliable fits. We limited all our fits to the extent of order 49 with continuum

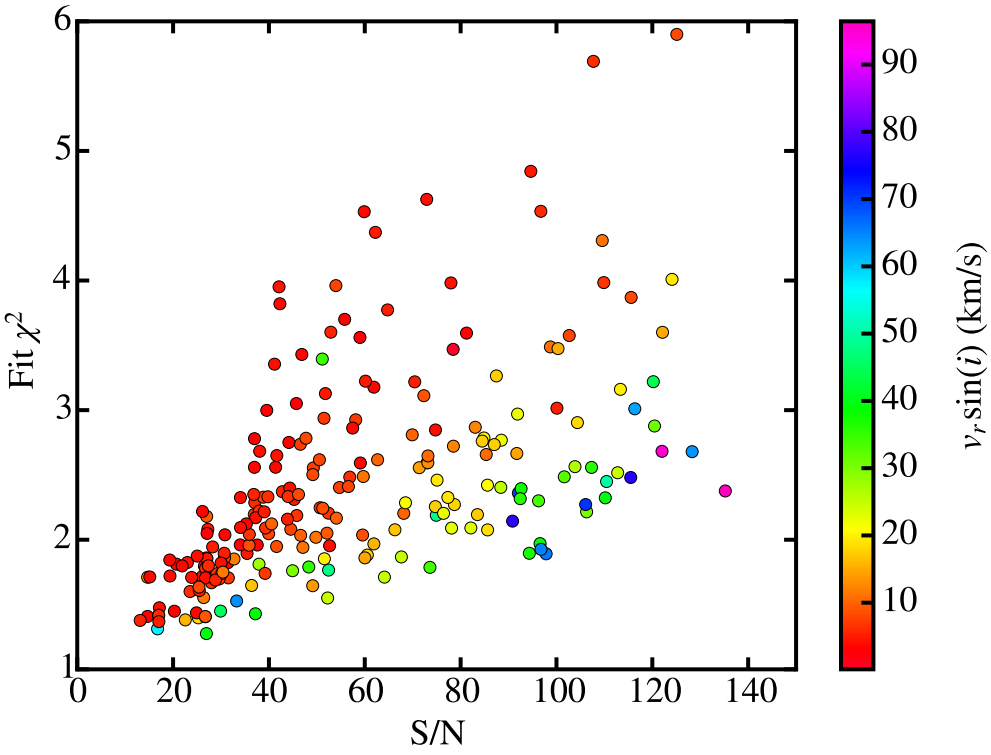

Figure 4.8: The average best-fit reduced χ^2 for each of our cluster stars plotted as a function of S/N. Colors denote the rotational velocity measured for each star. There is a distinct upward trend in χ^2 with S/N.

S/N greater than 12 or the columns between pixels 25 and 2700 (∼7160–7290 Å). These column extents were selected such that we have a slight margin at either end with which to estimate the continuum level at the order edges beyond the fitting extent. Generally fits were to all 2675 pixels in this region. We masked pixels affected by extraction artifacts, continuum normalization errors, uncorrected cosmic rays, or Littrow ghosts. After fitting we inspected the results for any failures (generally do to a poor initial RV guess) and either corrected them, flagged them to handle as exceptional cases, or excluded them from analysis.

We optimized the model in stages. 1) For a subset of spectra we first obtained an initial guess for the wavelength solution by eye. These guesses were used to bootstrap initial relations for the wavelength solution in one frame of each arm on each run. The initial PSF width was chosen such that it coincides with with M2FS's nominal resolving power in our configuration without asymmetry and an initial spectral type was chosen assuming Solar abundance and using the (B-V)-T_{eff} relation of Casagrande et al. (2010) with reddening corrected values for B-V. These parameters were then used as the initial values for a round of fits from which we constructed a predictive model of the dispersion parameters as function of M2FS arm, CCD trace position, and night. We found the $4^{th} - 7^{th}$ order wavelength parameters are neither a function of instrument temperature, (mis)focus, or run and thus adopted a simple polynomial model as a function of aperture position based on the best fit values for all ∼2600 usable spectra. We adopted the mean values as an initial guess for the $1^{st} - 3^{rd}$ order parameters and used the model to predict the wavelength zero point parameter for each exposure separately. 2) We then refit all our spectra with the initial wavelength parameters determined in phase one, holding the $4^{th} - 7^{th}$ order wavelength parameters fixed, and adopted the inverse variance weighted means of the best-fit spectral type parameters and $v_r \sin(i)$ values for each star. 3) We performed a final round of fits still holding higher order wavelength parameters fixed, now along with the spec-

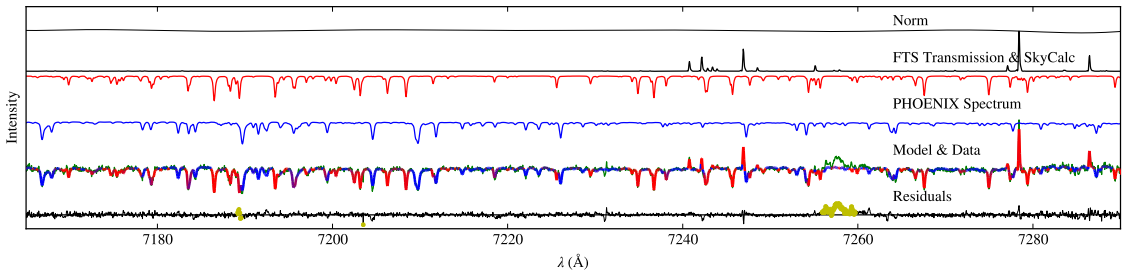

Figure 4.9: An example of a fit to a spectrum of a K1V star in NGC 2516 with a $v_r \sin(i)$ of 6 km/s. This spectrum has a mean S/N of 40. The extracted spectrum is plotted in green with the model overlaid in red, blue, and purple. Blue lines are stellar features, red telluric, and blends in purple. The yellow dots denote pixels excluded from the fitting process. Upper lines show the stellar, telluric absorption, and sky emission components of the model. The topmost line shows the normalization curve.

tral type parameters and $v_r \sin(i)$. We used the RVs from this final fit as the values we adopt for each star. Except in the case of large amplitude binaries the RV was always started from the adopted multi-epoch mean.

In §4.7 we describe the precision with which we recover these values. As our initial wavelength guesses are crude we investigated the impact priming our wavelength solution parameters with ThAr calibration fits to verify we were not introducing a fitting bias. For this test we refit all of the RV standard spectra using the IRAF identify task solutions to corresponding ThAr data for the initial wavelength solution. We found no impact. Holding the higher order wavelength parameters fixed improves RV precision by approximately ∼5 m/s at all signal-to-noise levels (c.f. §4.7.2.1). An example fit is shown in Figure 4.9.

Optimization was carried out using the `MPFIT` (Markwardt, 2009) package to minimize the weighted errors for each unmasked pixel. In previous iterations of our software we used the AMOEBA minimizer: the downhill-simplex optimizer (Nelder & Mead , 1965) appears more tolerant of poor initial guesses, but minimization takes a greater number of function evaluations, does not yield a parameter covariance matrix, and requires parameter limits be hacked on as they are not inherent to the

algorithm. We also investigated using the MCMC core of Eastman et al. (2013), and briefly explored a genetic fitter, the latter of which proved to be of similar quality but highly inefficient. We found these various methods of optimization to all be of comparable end result but with significantly prolonged computation time.

4.7 Performance

4.7.1 Stellar Properties

We estimated the statistical uncertainty of our stellar parameters from the distribution of best fit values relative to their multi-epoch means. We used the results from the second stage of our fitting pipeline (where stellar properties are allowed to vary from epoch to epoch, c.f §4.6.2.3), exclusive of spectroscopic binaries, to obtain fits to 2283 spectra of 214 targets (see Table 4.7) with which we computed the differences between the single epoch values and the adopted multi-epoch values of the stellar parameter. We then performed kernel density estimation on each parameter and computed confidence intervals. Here we present the resulting probability distribution functions (PDFs) in Figures 4.10, 4.11, 4.12, and 4.13 and the 1σ confidence intervals in Table 4.8, but defer reporting measured values until Chapter V. In addition to the overall PDFs, the plots give PDFs for subsamples grouped by spectral type and rotation rate ($v_r \sin(i) > 8$ km/s) as a test on how the broader lines impact our precision. The mean (median) $v_r \sin(i)$ of the high-rotation group is 26 (18) km/s with a standard deviation of 20 km/s and they have a mean T_{eff} of 5930 ± 700 K. Though we do not explicitly show PDFs for groupings in S/N, the PDFs for spectral type show this by proxy; later spectral types are fainter and have lower S/N spectra. We saw no evidence that the PSF form (e.g. Gaussian vs. Hermite series) affected the measured values or their uncertainties.

We estimated the accuracy of our technique for determining T_{eff}, [Fe/H], and

Table 4.7. Targets Used to Estimate Stellar Property Precision

Cluster	V	B-V	Used	Excluded
NGC 2516	11.68–15.09	0.46–1.17	108	18
NGC 2422	12.19–16.05	0.45–1.31	106	19
All	11.68–16.05	0.45–1.31	214	37

Note. — This table gives the ranges in magnitudes, colors, and number of cluster stars used to determine our statistical uncertainties in T_{eff}, [Fe/H], [α/Fe], and $v_r \sin(i)$. We excluded spectroscopic binaries from our analysis.

Table 4.8. Single Epoch Property Precision

	K5-G7		G7-G2		G1-F5		F4 and hotter	
Property	Lower	Upper	Lower	Upper	Lower	Upper	Lower	Upper
T_{eff} (K)	−44	+59	−62	+74	−95	+121	−82	+163
$[Fe/H]$ (dex)	−0.06	+0.05	−0.05	+0.06	−0.07	+0.06	−0.07	+0.05
$[\alpha/Fe]$ (dex)	−0.04	+0.04	−0.05	+0.04	−0.07	+0.04	−0.07	+0.04
$v_r \sin(i)$ (km/s)	−0.5	+0.5	−0.3	+0.4	−0.5	+0.7	−1.0	+0.9
Mean S/N	30		60		80		100	

Note. — This table gives the upper and lower limits enclosing the central 66% confidence interval for T_{eff}, [Fe/H], [α/Fe], and $v_r \sin(i)$. That is, given measurement of a single epoch, there is a 66% chance we would measure a value within the stated limits for a second epoch. Below each pair of columns we list the mean S/N of stars in each group.

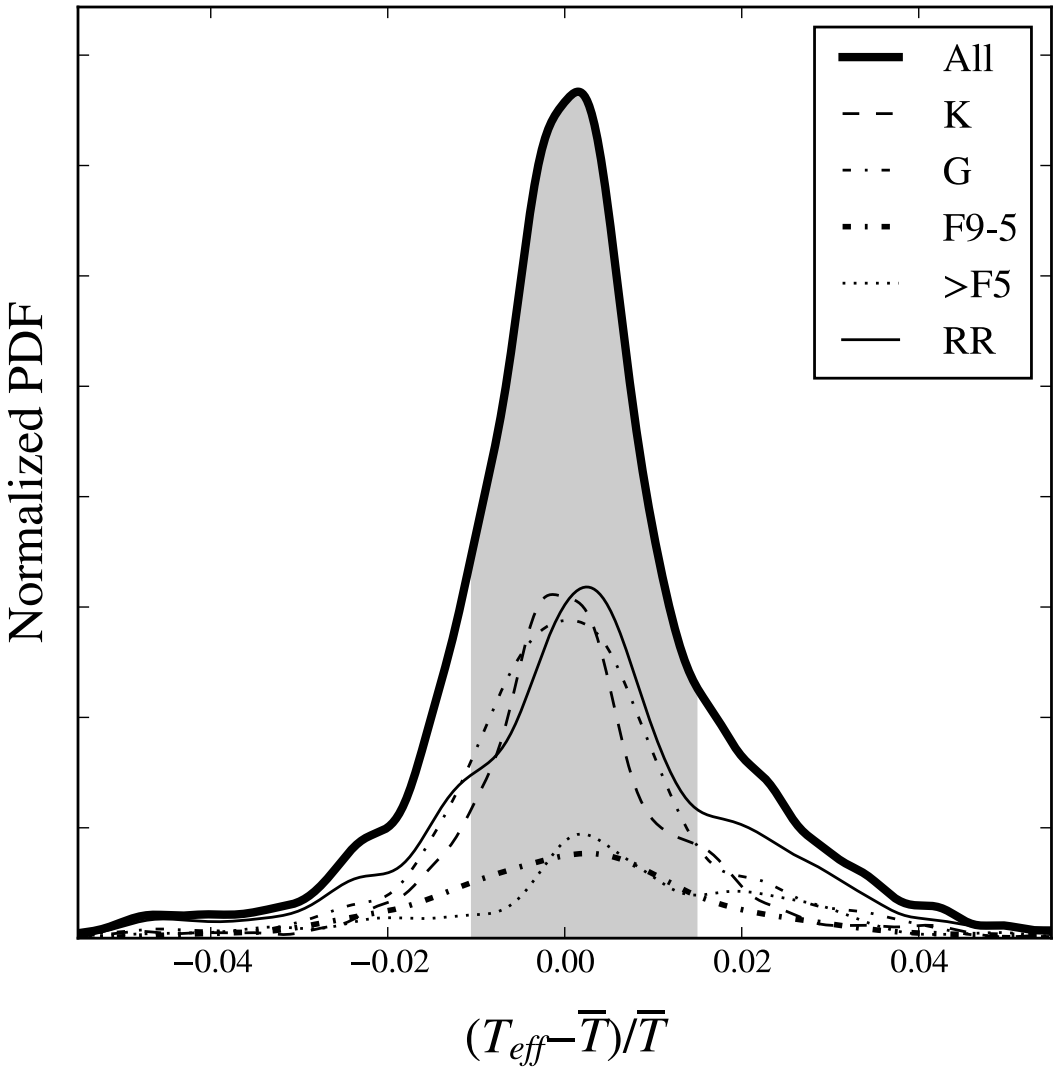

Figure 4.10: Normalized PDFs for fractional ΔT_{eff} for the entire sample and subsamples of stars as a function of spectral type and stars with $v_r \sin(i) > 8$ km/s (RR). The shaded region corresponds to 1σ for the entire sample.

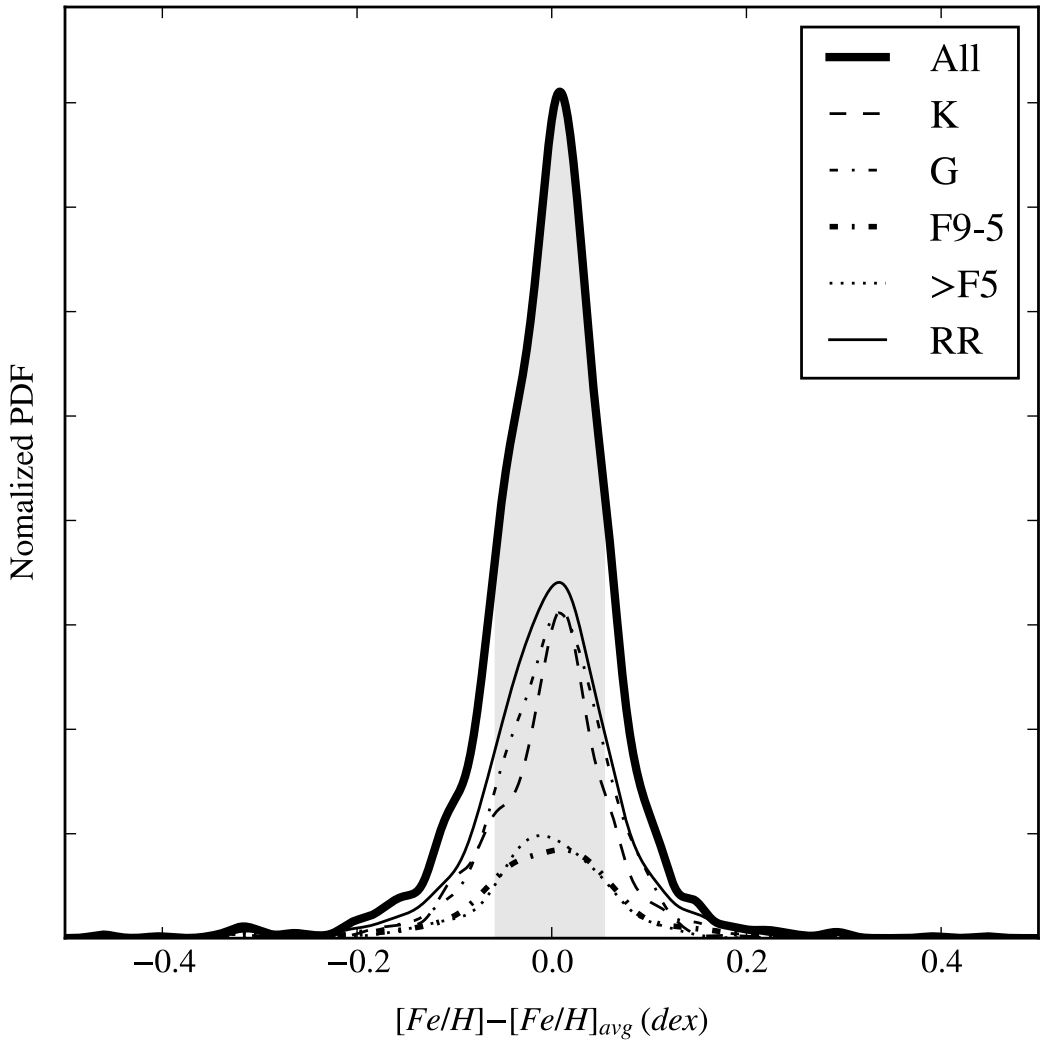

Figure 4.11: Normalized PDFs for Δ[Fe/H] for the entire sample as well as subsamples based on spectral type and stars with $v_r \sin(i) > 8$ km/s (RR). The shaded region corresponds to 1σ for the entire sample.

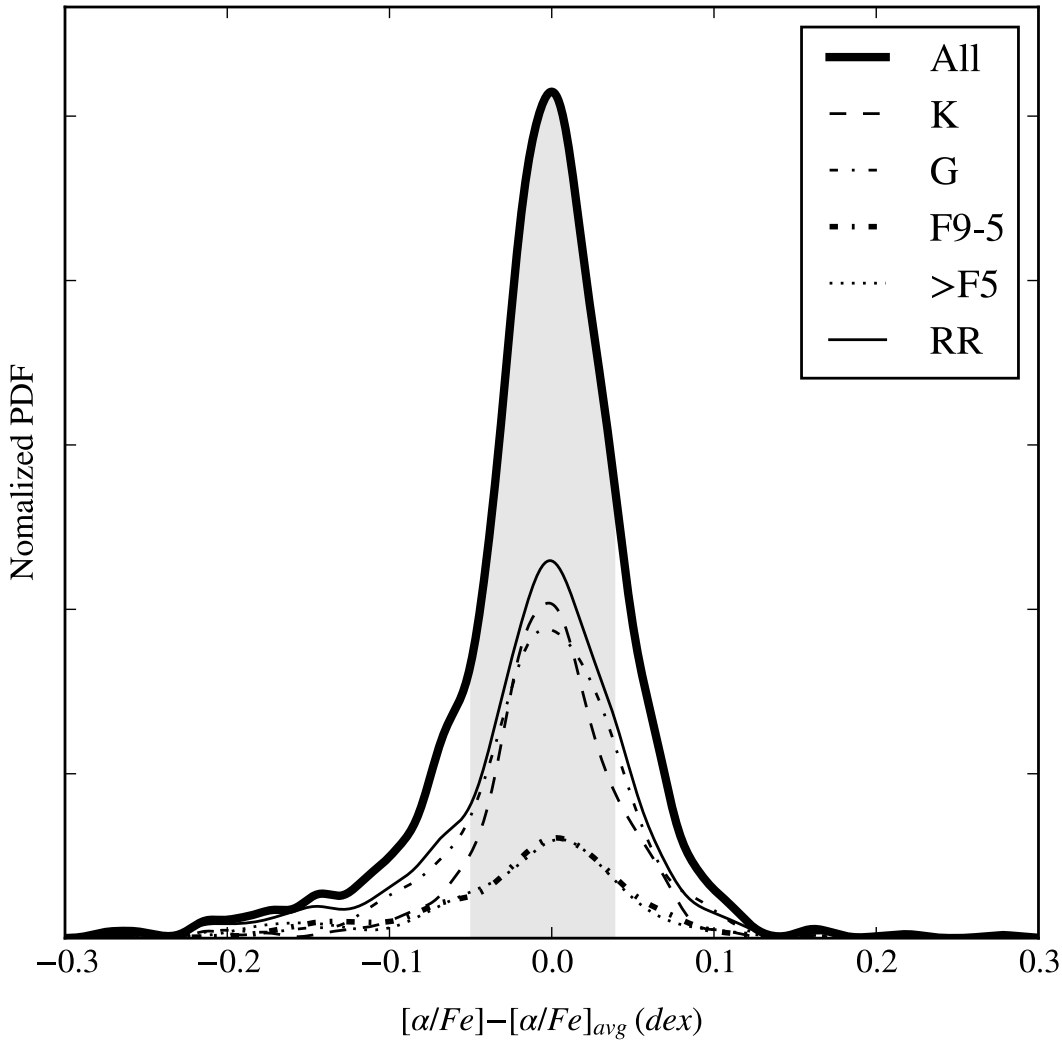

Figure 4.12: Normalized PDFs for $\Delta[\alpha/\mathrm{Fe}]$ for the entire sample as well as subsamples based on spectral type and stars with $v_r \sin(i) > 8$ km/s (RR). The shaded region corresponds to 1σ for the entire sample.

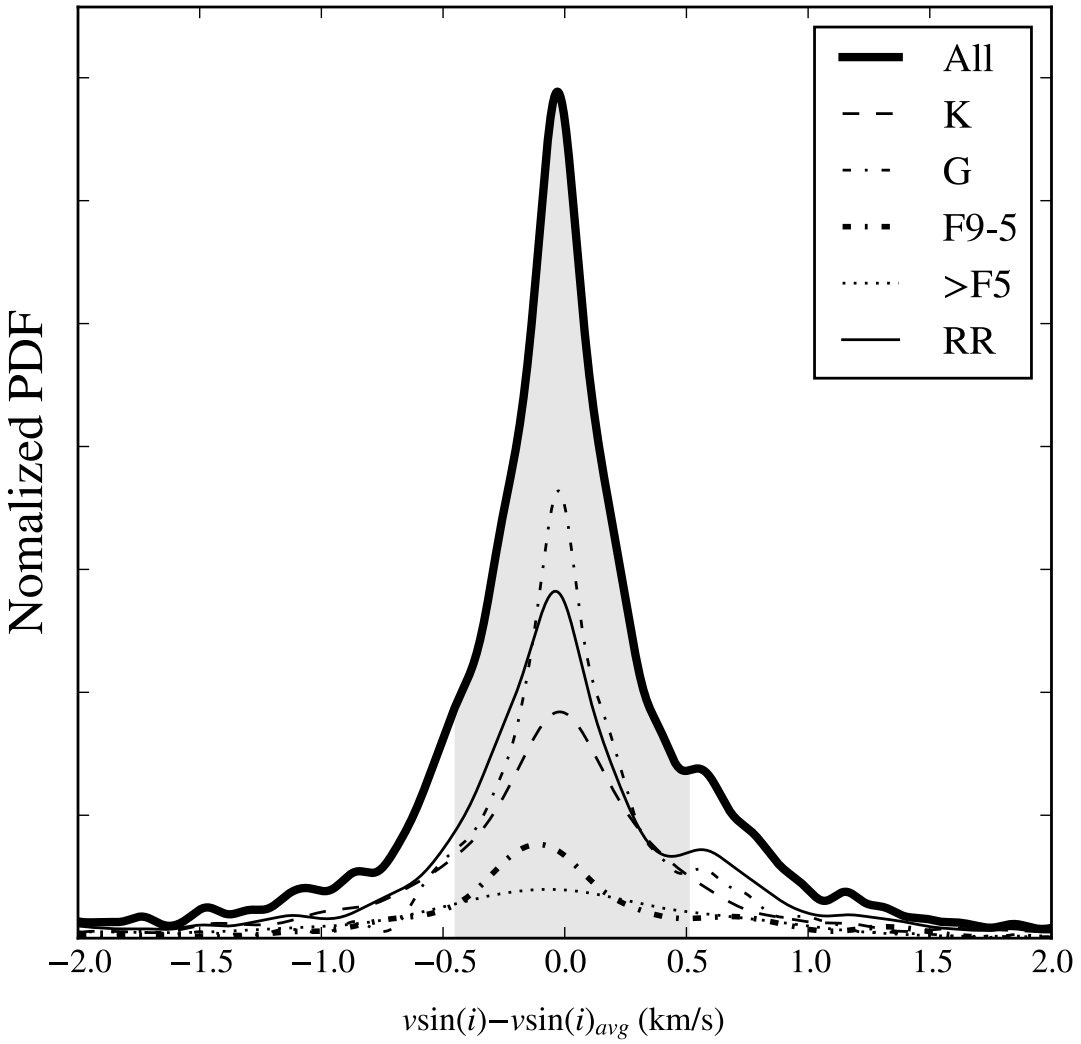

Figure 4.13: Normalized PDFs for $\Delta v_r \sin(i)$ for the entire sample as well as subsamples based on spectral type and stars with $v_r \sin(i) > 8$ km/s (RR). The shaded region corresponds to 1σ for the entire sample.

[α/Fe] by comparing the values we measured with those in the literature. Table 4.9 gives our values for the six standard stars along with those from the literature. Table 4.10 then reports the differences in these values: we adopt the averages therein as an estimate of our systematic uncertainties.

As an additional check we fit ∼900 twilight spectra and analyzed the values and differences thereby obtained. Though these values are of comparable quality, we excluded them from our average as the large number of spectra would heavily bias the results. We tested our $v_r \sin(i)$ accuracy by comparing our values with those reported in Terndrup et al. (2002), with which we have thirty-seven targets in NGC 2516 in common[2]. Our values agree to within 5 km/s for all but four stars, which are all readily identified as spectroscopic binaries. For the remaining 33 stars our adopted, multi-epoch mean values agree with a standard deviation of 2.2 km/s. We recovered the correct $v_r \sin(i)$ to better than 0.1 km/s in fits to our twilight spectra. Our code is not able to reliably measure $v_r \sin(i)$ values below ∼2 km/s (roughly one third of our velocity resolution).

[2]We did not perform this exercise on T_{eff} as their values are from colors.

Table 4.9. Measured Standard Star Properties

Ref	T_{eff} (K)	log(g)	[Fe/H] (dex)	$[\alpha/Fe]$ (dex)
HIP 48331 N=35 K5V				
This work	4463 ± 4	(4.7)	-0.05 ± 0.002	0.19 ± 0.006
S05	4505 ± 176	4.71 ± 0.96	-0.18 ± 0.19	...
S08	4715 ± 102	4.39 ± 0.28	-0.32 ± 0.03	...
N09	S08[a]	S08	S08	0.20 ± 0.18
C11	4455 ± 80	4.67	...	...
A12	S08	S08	S08	0.22 ± 0.08
T13	4400 ± 45	4.36 ± 0.1	-0.26 ± 0.14	...
HIP 13388 N=2 K1V				
This work	4991 ± 52	(4.6)	-0.38 ± 0.055	0.26 ± 0.037
C11	5095 ± 64	4.59	-0.15 ± 0.1	0.02
S08	5040 ± 48	4.39 ± 0.08	-0.45 ± 0.04	...
N09	S08	S08	S08	0.22 ± 0.1
HIP 10798 N=5 G8V				
This work	5312 ± 19	(4.6)	-0.54 ± 0.0081	0.14 ± 0.008
V05	5374 ± 44	4.69 ± 0.06	-0.47 ± 0.03	...
C11	5481 ± 80	4.63	-0.44 ± 0.1	0.17
HIP 22278 N=1 G5V				
This work	5652 ± 68	(4.5)	0.04 ± 0.056	0.08 ± 0.046
C11	5721 ± 65	4.22	0.13 ± 0.1	-0.01

Based on this analysis, we report our fits yield typical single epoch precisions of 75 K, 0.05 dex, and 0.75 km/s for T_{eff}, [Fe/H] and [α/Fe], and $v_r \sin(i)$ and mean multi-epoch precisions of 30 K, 0.02 dex, and 0.3 km/s. Our T_{eff} values are typically cooler than available literature data for our standards by $\sim$25 K and we find a similar offset when fitting twilight spectra. Iron abundance values appear elevated by a tenth dex but are driven entirely by HIP 48331: excluding HIP 48331 Δ[Fe/H] becomes -0.03 ± 0.03 dex, consistent with our twilight fits. We do not see any evidence of a systematic offset in [α/Fe] or $v_r \sin(i)$.

As an additional test on T_{eff} we compared our values with $T_{eff}(B-V)$ values computed using the relation of Casagrande et al. (2010) and reddening corrected colors. For cluster members (see §5.3.2) with $T_{eff} < 6200$ K we measured values about 100 K cooler than the reddening corrected color temperature; above 6200 K our values are about 250 K hotter. We quantified this effect for the combined set of cluster members in NGC 2516 and NGC 2422 by fitting a sigmoid to the difference in T_{eff} and T_{B-V} (Figure 4.14 and Equation 4.4). This correction has been applied to the values reported for members and probable members in Tables A.1 and A.2. We also artificially broadened the stellar lines in our spectrum of the F5 RV standard HIP 31415 from its native $\sim$4.5 km/s to values between 10–50 km/s and refit the spectrum. At higher rotation rates we see elevation in T_{eff} and [Fe/H] and a decrease in [α/Fe]. For instance, at 40 km/s we measure a increase in T_{eff} of 648 ± 163 K and [Fe/H] of 0.2 ± 0.08 dex and a decrease of [α/Fe] by 0.11 ± 0.08 dex. In general, for $v_r \sin(i) \lesssim 20$ km/s our stellar properties are largely unaffected. We may begin to see slight elevation in T_{eff} at $\sim$10 km/s, though the uncertainty is quite large (c.f. Figure 4.15). This suggests one plausible explanation for Equation 4.4 is a combination of an E(B-V) overestimate of $\sim$0.05 in both clusters and a tendency of our pipeline to overestimate T_{eff} for more rapidly rotating stars. Non-member stars show a generally linear agreement with T_{B-V} and do not follow the sigmoid.

Table 4.9 (cont'd)

Ref	T_{eff} (K)	log(g)	[Fe/H] (dex)	$[\alpha/Fe]$ (dex)
HIP 19589 N=1 G0V				
This work	5966 ± 108	(4.5)	-0.30 ± 0.067	0.15 ± 0.057
C11	5825 ± 90	3.75	-0.17 ± 0.1	0.13
K13	5705 ± 79	3.40 ± 0.15	-0.52 ± 0.1	0.28 ± 0.15
HIP 31415 N=1 F6V				
This work	6295 ± 108	(4.4)	-0.55 ± 0.067	0.21 ± 0.057
C11	6172 ± 60	3.94	-0.31 ± 0.1	0.12
Sol N=909 G2V				
This work	5726 ± 2	(4.5)	-0.03 ± 0.00	0.01 ± 0.00

[a]Value reported is from S08

References. — (K13 Kordopatis et al., 2013; C11 Casagrande et al., 2011; N09 Neves et al., 2009; S08 Sousa et al., 2008; S05 Santos et al., 2005; V05 Valenti & Fischer, 2005; T13 Tsantaki et al., 2013; A12 Adibekyan et al., 2012)

Note. — [α/Fe] values for N09 and A13 are the average of Mg, Ca, Si, and (Ti I + Ti II)/2. Note that [α/Fe] values from C11 are not direct measurements and a measured by proxy from a statistical relation reported therein. Solar values are based on fits to $\sim$900 twilight spectra. Errors quoted for our stars are based on Table 4.8. Our log(g) values are those used during fitting and should not be interpreted as a measurement. The values reported in this table do not include any adjustments for possible systematic errors.

Table 4.10. Parameter Differences

Target	Type	ΔT_{eff} (K)	Δ[Fe/H] (dex)	$\Delta[\alpha/\mathrm{Fe}]$ (dex)
HIP 48331	K5V	9 ± 37	$+0.26 \pm 0.03$	-0.03 ± 0.07
HIP 13388	K1V	-69 ± 53	$+0.03 \pm 0.05$	$+0.08 \pm 0.09$
HIP 10798	G8V	-87 ± 49	-0.07 ± 0.04	$+0.03 \pm 0.2$
HIP 22278	G5V	-69 ± 94	$+0.17 \pm 0.11$	$+0.09 \pm 0.20$
HIP 19589	G0V	209 ± 124	$+0.05 \pm 0.10$	-0.08 ± 0.13
HIP 31415	F6V	123 ± 124	-0.24 ± 0.12	$+0.09 \pm 0.21$
Average		-23 ± 24	$+0.10 \pm 0.02$	$+0.01 \pm 0.05$
Twilights	G2V	-51 ± 2	-0.03 ± 0.002	$+0.01 \pm 0.002$

Note. — Differences in our stellar parameters from the averages of the values reported in Table 4.10. Deltas are Ours – Other. Twilight values are excluded from the average as the twilight spectra suffer from significantly higher scattered light and the small uncertainties would heavily bias the average.

Fits allowing log(g) to vary show many non-member stars minimize to log(g) values 2–2.5 dex below cluster members suggesting giant or sub-giant status. Given the unknown and non-linear interplay between T_{eff} and log(g) in our spectral region it is not surprising that we see a much larger spread in between T_{eff} and T_{B-V} for non-members. Equation 4.4 can be used to correct the T_{eff} values of member stars to Casagrande's scale.

$$T_{B-V} = T_{eff} + 124 \text{ K} - \frac{415 \text{ K}}{1 + e^{-0.0054 \text{ K}^{-1}(T_{eff} - 6220 \text{ K})}} \tag{4.4}$$

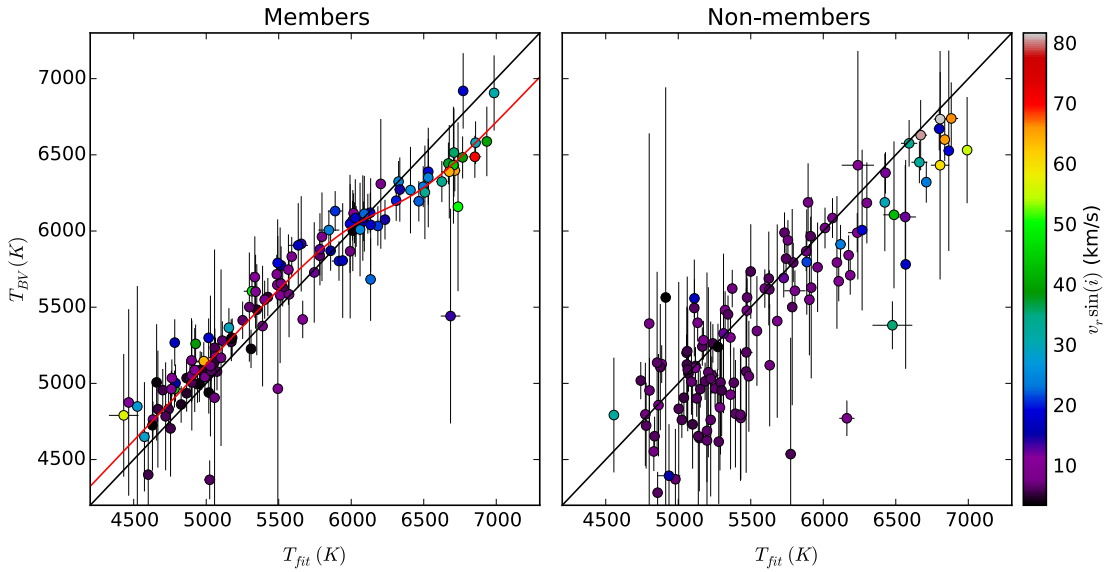

Figure 4.14: T_{eff} vs. T_{B-V} for the combined cluster sample. The left panel shows values for stars with $P_{RV} \geq 50\%$ (c.f. §5.3.2) plotted with points color showing $v_r \sin(i)$. The red line represents our correction to Casagrande's scale given in Equation 4.4. Note that Δ(B−V) of 0.05 corresponds to a ΔT∼100 K here, about the level at which many members are offset below 6200 K, and perhaps suggesting a correction to E(B−V). The left panel shows targets with $P_{RV} < 50\%$: here it seems the inapplicable reddening values for non-members enters into play. In both panels the diagonal black line shows equivalence as a guide to the eye.

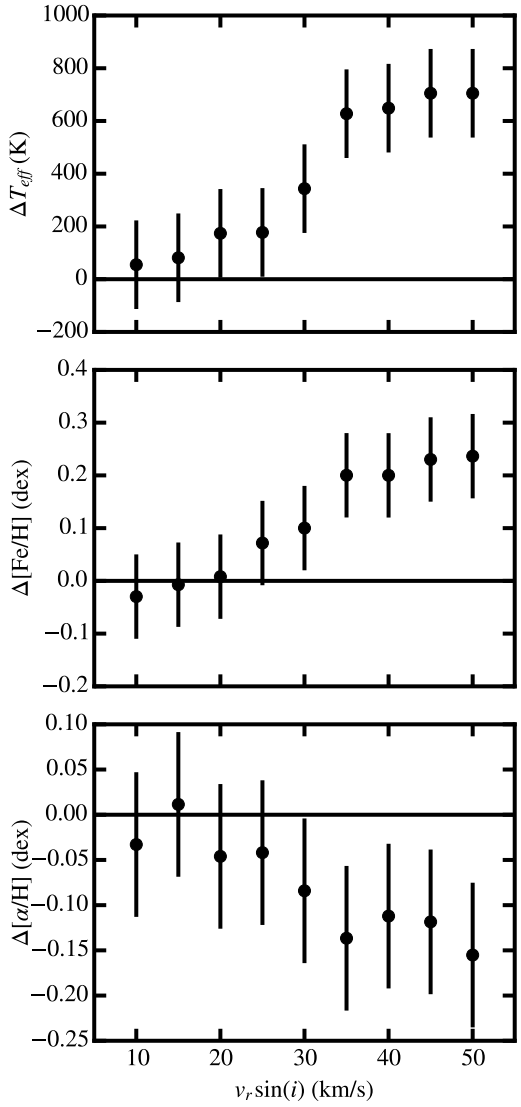

Figure 4.15: These figures show how T_{eff}, [Fe/H], and [α/Fe] measurements are affected by artificially broadening the stellar lines in the spectrum of our F5V standard HIP 31415. We stress that we do not see this behavior in cooler stars.

4.7.2 Radial Velocities

4.7.2.1 Precision

Radial velocity variations of stars without a companion stem from one of five sources: (1) an inherent photon noise error (σ_{phot}) arising from the S/N and the number and shape of the stellar and telluric lines, (2) an instrumental error (σ_{inst}) based on the characteristics of M2FS spectra, (3) an error contribution due to our analysis (σ_{anal}), (4) intrinsic stellar variability (σ_{stel}) caused by stellar activity (e.g. stellar flares or star spots), and (5) variability in the bulk atmospheric motion along the line of sight that introduces a Doppler shift on our wavelength reference (σ_{atm}). We assume that all five sources add in quadrature to produce the observed dispersion (σ_{obs}), as follows:

$$\sigma_{obs}^2 = \sigma_{phot}^2 + \sigma_{inst}^2 + \sigma_{anal}^2 + \sigma_{stel}^2 + \sigma_{atm}^2.$$

Under this assumption, the observed velocity dispersion of a star with a known σ_{stel} and observed under conditions with a known σ_{atm} can be used to estimate the quadrature sum of the first three error terms, which we refer to as an effective measurement error, σ_{meas},

$$\sigma_{meas}^2 = \sigma_{phot}^2 + \sigma_{inst}^2 + \sigma_{anal}^2.$$

Here we focus on estimating σ_{meas} as a function of S/N, based on observations of the standard star HIP 48331.

We observed HIP 48331 35 times on 19 different nights; 9 nights have more than 1 epoch. Of these we use the 31 spectra with S/N above 200 and R $> 38,000$. Eighteen spectra were obtained using the red M2FS arm and 13 using the blue arm. The S/N of these spectra span between 200 and 300, with a median of 240. Likewise, the resolving power of these spectra range from 40,000 to 64,000, with a median of 55,000. The RV measurements of HIP 48331 are illustrated in Figure 4.16; these values have a standard deviation (σ_{obs}) of 23 m/s.

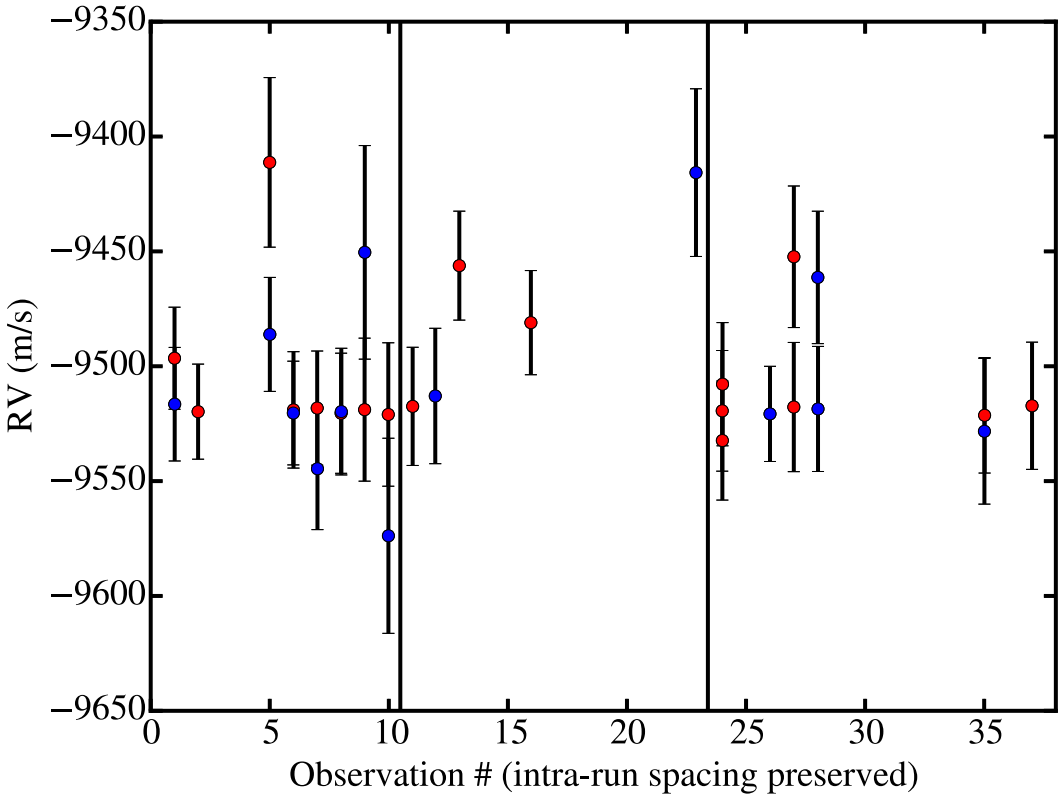

Figure 4.16: Our measurements of HIP 48331. Points are colored by the arm used for the observation, in this regard these observations represent a more stringent test of M2FS's stability than program stars which typically always use the same fiber and spectrographic channel.

To simulate lower S/N spectra that are more representative of the open cluster stars surveyed here, we generated lower S/N versions of these 31 spectra and recomputed the best fit models and RVs from which new σ_{obs} were calculated. We generated the the lower S/N spectra by sampling a Poisson process at each pixel with expectation value of the measured electrons multiplied by the desired fractional reduction in mean S/N: e. g.

$$x_i' = \text{Poission}(sn' x_i / sn)$$

where x_i is the number of electrons measured at the i^{th} pixel and prime denotes the new values. We also ensured that the simulated variance spectra included in an appropriate amount of Gaussian noise to include the effects of detector read noise. The resulting spectra had S/N levels of ∼150, 100, 80, 60, 50, 40, and 15. The spectra were then fit as described in §4.6, treating each S/N level independently. This resulted in eight RV time-series (one for each S/N level) with each standard deviation yielding a measurement of σ_{obs} at that S/N level. We also computed σ_{phot} for each of the 248 spectra by applying the algorithm described in Butler et al. (1996) to the telluric and stellar components of each best-fit model, adding the results in quadrature.

To obtain σ_{meas} from the eight σ_{obs} values calculated above, we subtracted in quadrature a stellar variability of $\sigma_{stel} = 5.0$ m/s (Soubiran et al., 2013) and an atmospheric variability of $\sigma_{atm} = 2.5$ m/s (determined as shown later in this section, see also Figure 4.21). These values can be compared directly to the the mean σ_{phot} values for each of the eight S/N bins. Oddly, we found the quadrature to be in excess of the observed variance below a S/N of ∼60. In Figure 4.17 we plot both σ_{meas} and σ_{phot}, which shows that we measure our RVs with greater precision that anticipated at low S/N. We also show the ratio of σ_{meas} to the mean of σ_{phot} at each S/N bin. As an additional reference we also plot the ratio of each bin σ_{meas} to each of the σ_{phot} in that bin. This suggests an approximately linear relation between our measurement error and the σ_{phot} value we computed for each spectrum. We adopted

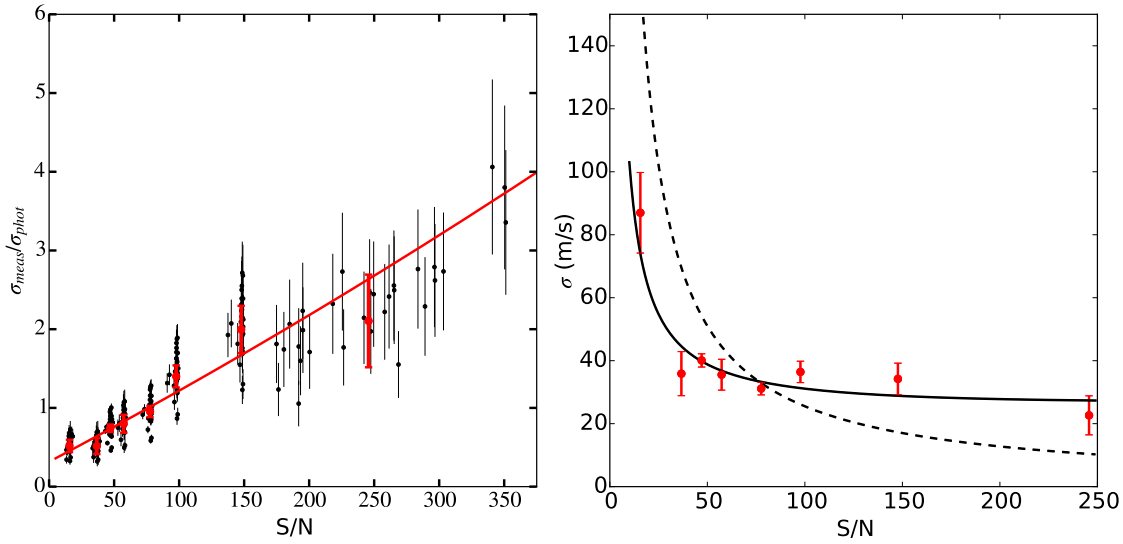

Figure 4.17: The left panel shows the ratio of σ_{meas}, computed from measurements of the RV standard at each resampled S/N step, to σ_{phot}, which is computed from the model of each spectrum. The individual points are each of the RV standard spectra and are provided for visual reference. We fit to the means at each S/N bin. Errors are as described in the text. The right, most dispersed group of points reflects the native S/N of observations of HIP 48331. The right panel shows σ_{meas} for each S/N bin along with an interpolated function generated using the fit in the left panel and the dashed curve. The dashed curve shows the mean of the σ_{phot} values computed using the models from fits to the high-S/N RV standard spectra with the calculation fed various S/N levels. This shows a clear indication that the algorithm overestimates uncertainty at low S/N. The plot also shows we are subject to a systematic floor of about 25 m/s.

errors for the ratio from two sources: (1) the standard deviation of σ_{phot} in each S/N bin contributes directly and (2) an estimate of the error in σ_{obs} that was obtained by computing our best-fit models with a small number of slightly perturbed initial RVs for each spectrum in each bin, adopting the standard deviations of the resulting σ_{obs} values as an uncertainty on σ_{meas} in each S/N bin.

We fit the ratio of σ_{meas} to the mean of the σ_{phot} for each S/N bin and used the result as a scaling relation to convert σ_{phot} to σ_{meas} provided a S/N. This technique allows us to account for some, if not all, of the increased uncertainty in spectra that are at a lower resolution (e.g. due to mis-focus) than the typical RV standard observation, are of more rapidly rotating stars, or otherwise possess a different number or strength

of stellar lines. The errors in Figure 4.16 have been scaled in this manner.

From this analysis we found M2FS to have a limiting RV precision of about 25 m/s, though the σ_{phot} values we computed at high S/N suggest an additional 10 m/s precision gain may be possible at higher S/N ratios. A potential culprit in our modeling process is as yet unclear. We used the same process to investigate the impact various modifications to our analysis have on achievable precision, some of which are discussed in further detail in the following paragraphs and illustrated in Figures 4.18 and 4.19. Finally, Figure 4.20 shows an updated version of Figure 4.2 with the corrections discussed above.

Atmospheric Variability We estimated the impact bulk atmospheric motions have on our wavelength reference by integrating the water vapor weighted wind speed along the line of sight using data from the NOAA GFS forecast models (NCEP, 2003). Using the GFS model closest in time to our data the forecast is within 3 hours of the model's initial conditions. These models have an RMSE wind vector error of about 3 m/s three days (!) in the future. Perturbing the integrals by this error has a maximum impact of about 1 m/s, with typical values less than a tenth of that. The resulting contributions for our data on HIP 48331, NGC 2516, and NGC 2422 are shown in Figure 4.21. While pointing directly into or along the jet-stream would exhibit a clear signature at the ± 5 m/s level, typical values are not particularly significant to our efforts. We adopt $\sigma_{atm} = 2.5$ m/s.

Sky Emission Ideally the spectra we obtained of our RV standard would be completely representative of our program stars. Our cluster targets are, however, significantly fainter than our RV standard and so many of them exhibit a number of strong sky emission lines (c.f. Figures 4.7 and 4.9). To better assess their impact on our RV precision we took a subset of 60 spectra and extracted and fit the spectra from images prior to stacking. This gave us a sample of 4 or 5 RVs from spectra

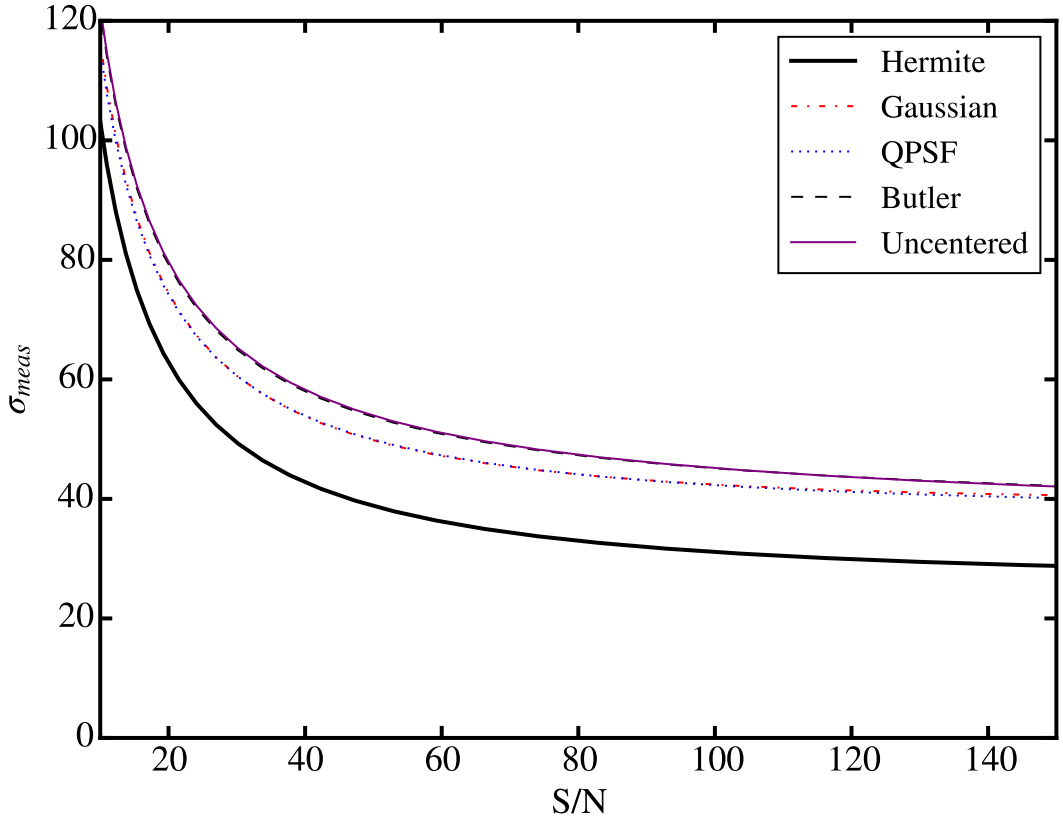

Figure 4.18: This plot shows the impact various PSF modeling choices have on σ_{meas}. The solid black line denotes σ_{meas} for our adopted analysis technique (c.f. Figure 4.17). The red dash-dotted line corresponds to our analysis but using a simple, fixed Gaussian PSF. The blue dotted line—essentially on top of the red line—is for fits done using a Gaussian PSF with a FWHM as described by a quadratic. The thin, dashed black line and the thin purple line—also nearly superimposed—correspond to fits done with the PSF prescription of Butler et al. (1996) and our adopted, Hermite prescription but without the enclosed power constrained to the central pixel.

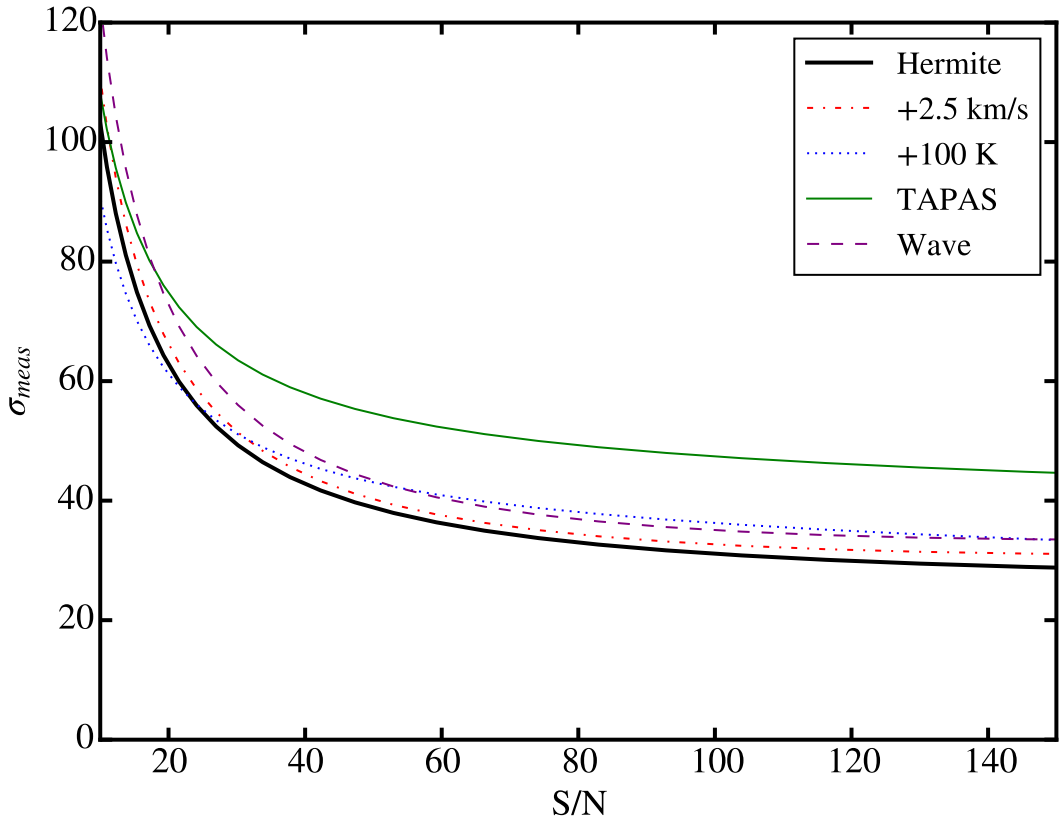

Figure 4.19: This plot shows the impact various factors have our attained RV measurement precision. The solid black line denotes σ_{meas} for our adopted analysis technique (c.f Figure 4.17). The red dash-dotted line corresponds to a fits done with a $v_r \sin(i)$ 2.5 km/s larger than the optimal value. The blue dotted line corresponds to fits done with T_{eff} forced 100 K above our adopted value. The purple dashed line is for fits done without holding the 4^{th} and higher order wavelength parameters fixed as described in §4.6.2.3. Finally, the solid green line represents our results when we use the TAPAS synthetic telluric spectra as our wavelength reference instead of the NSO empiric spectrum.

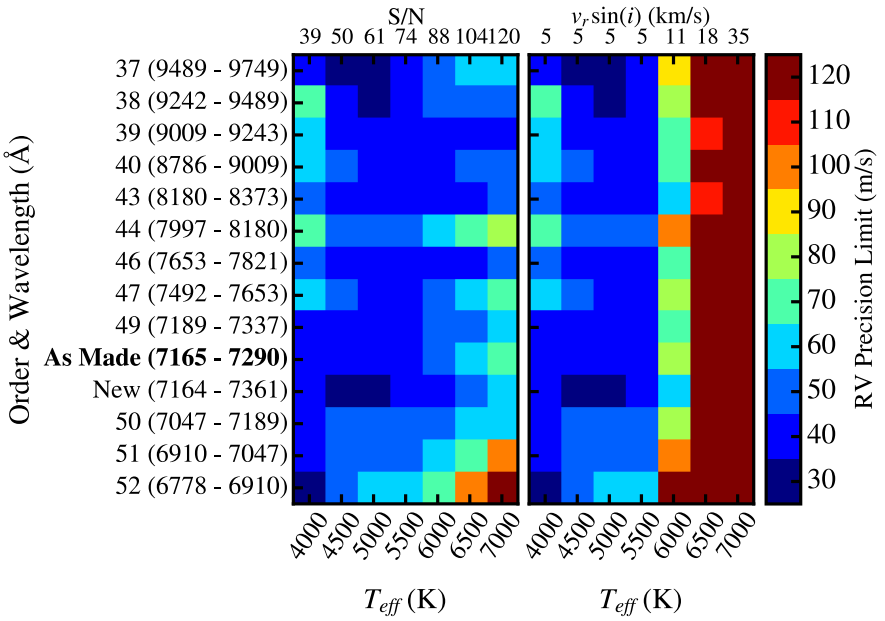

Figure 4.20: This is an updated version of Figure 4.2 where the algorithmic uncertainties have been corrected as described in §4.7.2.1. Both plots are at our median observed resolving power of 50,000. The S/N of each spectrum is determined by assuming equidistant MS dwarfs where a S/N of 50 is attained for a K5 dwarf. The resulting scale is marked at the top of the left plot, which assumes all stars have a $v_r \sin(i)$ of 5 km/s. The right plot uses the same S/N scale combined with the median $v_r \sin(i)$ values we measure for stars with the stated T_{eff} in NGC 2516 and NGC 2422. The right panel thus presents a worst case scenario for our technique as these clusters are some of the youngest suitable for precision RV work. In addition to standard M2FS orders we note the truncated order 49 used in this paper as "As Made" and our expectations for the new filter described in §4.3 as "New."

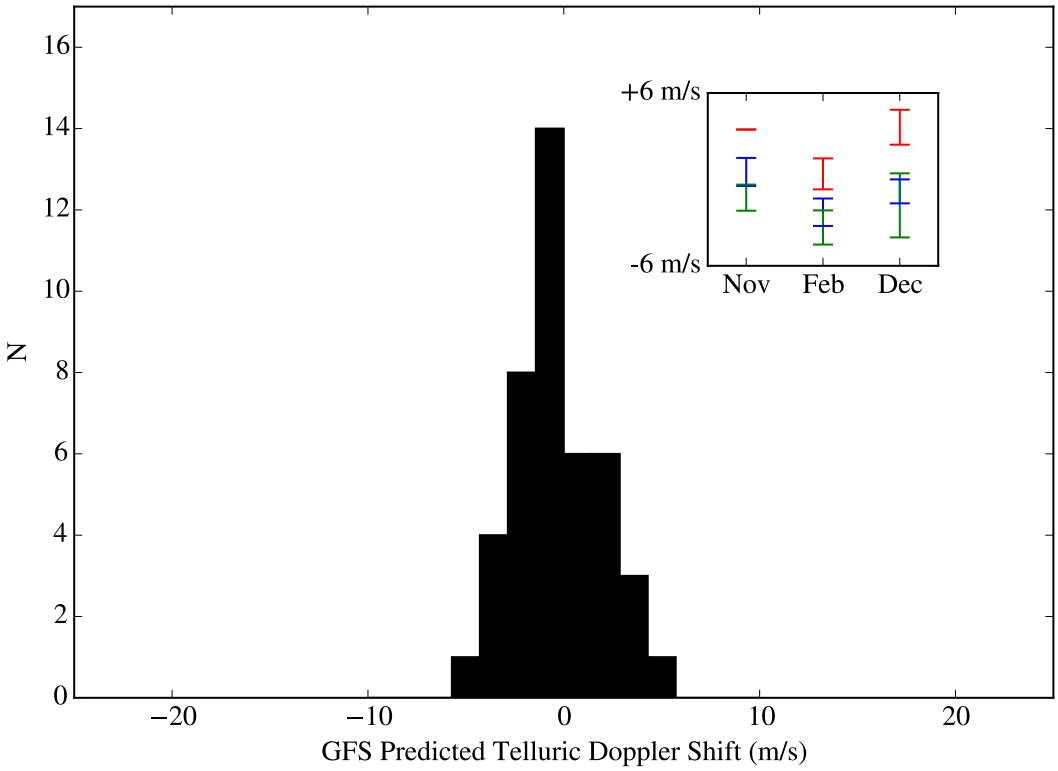

Figure 4.21: A histogram of the telluric atmosphere imposed RV shifts to observations of HIP 48331, NGC 2516, and NGC 2422. The standard deviation about zero is 2.3 m/s. The inset shows the means and standard deviations from our November 2013, February 2014, and December 2014 observing runs for the three sets of targets separately in green, blue, and red respectively.

obtained consecutively. These spectra spanned a S/N of about 15 – 45 for targets of spectral type ∼K3–F5. The σ_{obs} for these RVs was in agreement with that expected based on our σ_{meas} relation. We see some evidence that our better-than-anticipated RV precision stems from our use of the mean RV as a prior. If fit with an initial RV far from the multi-epoch mean we observe an increased σ_{obs} at low S/N, though still somewhat below that predicted by Butler et al. (1996, c.f. Figure 4.17).

PFS effects We found very little difference in the results of the multi-Gaussian parameterization of Butler et al. (1996) and a Gauss-Hermite kernel when the center of its enclosed power is not constrained to the central pixel undergoing convolution. The latter is faster with many fewer parameters and once the enclosed power is constrained we find it exhibits enhanced stability (c.f. Figure 4.18). Both yielded slightly worse performance than a simple Gaussian nor did the variable Gaussian PSF improve our RV precision. It may be worth investigating a hybrid approach where the components of the Hermite parametrization are allowed to vary with pixel.

Model Spectra As an additional test on RV precision and the impact our use of the PHOENIX grid has we also modeled twilight spectra with the empiric Solar spectrum of Kurucz (2005) as the template. We selected the ∼600 twilight spectra in images with mean S/N above 100 (100 – 650, mean of 320). For these spectra we measured a 1σ RV scatter within each twilight image of 23 ± 1.4 m/s when fitting with the PHOENIX models and 28 ± 2.3 m/s using Kurucz's empiric Solar spectra. This suggests that the PHOENIX templates are not limiting our RV precision. We saw evidence of a slight quadratic dependence of the measured RV on the spectrum's CCD position. This suggests that the RV zero point and wavelength zero points may be slightly affecting our dispersion, though we note that program stars are typically observed in the same fiber. Fitting and removing this effect reduced the scatter to 18 ± 1.2 m/s and 23 ± 2.3 m/s, respectively.

Stellar Rotation We saw some evidence that our fitting approach is biased to the initial RV for stars with $v_r \sin(i) \gtrsim 30$ km/s. We caution the reader that our errors may be underestimated by a factor of 2 – 4 in these cases and that quantities derived in later chapters (e.g. membership probabilities) should be considered of poor quality. While cross-correlating to obtain an initial RV estimate often alleviated the false minima sometimes found by the fitter for these rapid rotators, initial tests with a Bayesian analysis of our model show the NLLS fitter is underreporting the errors. Due to the long MCMC run times we have not yet performed a thorough analysis of this issue.

4.7.2.2 Accuracy

We estimated the accuracy of our RVs by looking at the differences between our values and those in the literature for each of our six standard stars. We report these differences in Table 4.11 and find an offset of about 75 m/s from the scale of Soubiran et al. (2013), albeit with significant scatter. We also saw a slight indication that RVs measured in our lowest S/N bin are slightly shifted relative to the higher S/N bins by 27 ± 17 m/s.

Table 4.11. Standard RV Differences

Target	Type	N	ΔRV (m/s)
HIP 48331	K5V	30	2 ± 7
HIP 13388	K1V	2	41 ± 40
HIP 10798	G8V	5	139 ± 7
HIP 22278	G5V	3	173 ± 17
HIP 19589	G0V	1	-77 ± 94
HIP 31415	F6V	1	173 ± 78
Average			74 ± 72

Note. — Differences in our RVs compared to the values reported in Table 4.3. Differences are Ours − Soubiran et al. (2013).

CHAPTER V

Spectroscopy of Stars in NGC 2516 and NGC 2422

5.1 Introduction

In the preceding chapter I introduced our survey of Sun-like stars in the open clusters NGC 2516 and NGC 2422 and presented our analysis technique and its performance. In this chapter I present the results of our spectroscopic analysis, highlight a number of notable stars in our sample, and report velocity based cluster membership probabilities for targets in both clusters. In §5.2 we present stellar properties for our targets and describe a small number of notable stars. Section 5.3 explains the Monte Carlo simulations we carried out to investigate a number of questions related to binarity in our sample and which we will use again in Chapter VI to investigate our tests for determining stellar jitter. We then present our membership determinations, report our measurements of cluster properties, and describe an additional grouping of stars seen in the field of NGC 2422.

5.2 Spectroscopically Measured Stellar Properties

5.2.1 Spectroscopic Results

We report T_{eff}, [Fe/H], [α/Fe], $v_r \sin(i)$, RV, σ_{RV}, membership probability (P_{RV}, see §5.3.2), and the likelihood each star is an RV variable (P_v, see Chapter VI) for our

targets in Tables A.1 and A.2. Errors reported on T_{eff}, [Fe/H], [α/Fe], and $v_r \sin(i)$ are the greater of the values reported in §4.7.1 or the target's standard error.

5.2.2 Continuum Stars, Background Giants and Spectroscopic Binaries

Five stars with colors corresponding to mid-F or late-G/early-K spectral types have exceptionally weak to no discernible evidence of any lines aside from a diffuse interstellar band (DIB) at 7224 Å (c.f. Figure 5.1; Herbig & Soderblom, 1982). Visual comparison with the most rapid rotators we are able to fit (∼90 km/s) suggests two of these (147-012316 and 147-012471 in the NGC 2516 field) are likely rapid rotators with a $v_r \sin(i)$ ∼120 km/s; the remaining four show no evidence of any features even when compared to templates with $v_r \sin(i)$ ∼200 km/s. Tables A.1 and A.2 report parameters for these stars as missing data with note 'C' for continuum as we are not able to fit their spectra, which are shown in Figure 5.1.

In addition to these five featureless spectra, a number of other stars exhibit the diffuse interstellar band at 7224 Å. None of these pass our RV membership test (§5.3.2), suggesting that there is an insufficient column depth of interstellar material within a few hundred parsecs to produce a notable feature. The diffuse band does not pose any difficulty to our fits, nor does it perturb our results as verified by masking out the region. We do find that stars with the diffuse band generally yield lower log(g) values relative to cluster members, suggesting they may be distant giants contaminating our sample.

146-012353 is listed by J01 as photometric single member 6337 in NGC 2516. It has $T_{B-V} = 6900$ K. It is 0.08 arcseconds from a source given in Damiani et al. (2003, D03) as having $\log(L_{\rm X}) < 29.75$ erg/s based on Chandra observations. Visual inspection suggests a $v_r \sin(i)$ in excess of 200 km/s. The presence of the DIB at 7224 Å suggests it is a non-member.

147-012316 is listed by J01 as photometric single member 8920 in NGC 2516. It

has $T_{B-V} = 6840$ K. D03 reports it has a flux of 1.36 ± 0.48 10^{-6} ct s^{-1} cm^{-2} and a $\log(L_{\rm X})$ of 28.85 erg/s. Visual inspection suggests a $v_r \sin(i)$ between 120–150 km/s. The presence of a DIB at 7224 Å suggests it is a non-member.

147-012471 is listed by J01 as photometric single member 12302 in NGC 2516. It has $T_{B-V} = 6625$ K. It is 0.134 arcseconds from a source in D03 with $\log(L_{\rm X}) <$ 29.96 erg/s and 0.282 arcseconds from Pillitteri et al. (2006) source 272 reported to have a MOS1 equivalent count rate of 2.18 ± 0.23 ct/s with the XMM-Newton EPIC camera. Visual inspection suggests a $v_r \sin(i)$ of $\sim$120 km/s. The presence of a DIB at 7224 Å suggests it is a non-member.

378-036424 is listed a member 956 in by P03 in NGC 2422 and has $T_{B-V} =$ 5650 K. Visual inspection suggests a $v_r \sin(i)$ in excess of 200 km/s. The presence of a DIB at 7224 Å suggests it is a non-member.

379-036213 is not listed as a member by P03 and is one of our 25 UCAC4 targets. It has $T_{B-V} = 5330$ K. Visual inspection suggests a $v_r \sin(i)$ in excess of 200 km/s. The presence of a DIB at 7224 Å suggests it is a non-member.

Eight stars are clear double lined spectroscopic binaries and noted with 'SB2' in Tables A.1 and A.2. The parameters we report here are for the stronger of the pair, but errors on these stars should be treated with a degree of caution.

We also note one high-velocity non-member in the NGC 2516 field. **146-012596** has a RV of 335.901 ± 0.048 km/s and does not show any sign of RV variability. We find a rotation rate of 3.1 km/s and note that its iron abundance runs into the lower edge of our grid, suggesting the true value may be less than -1 dex. It does exhibit the DIB at 7224 Å.

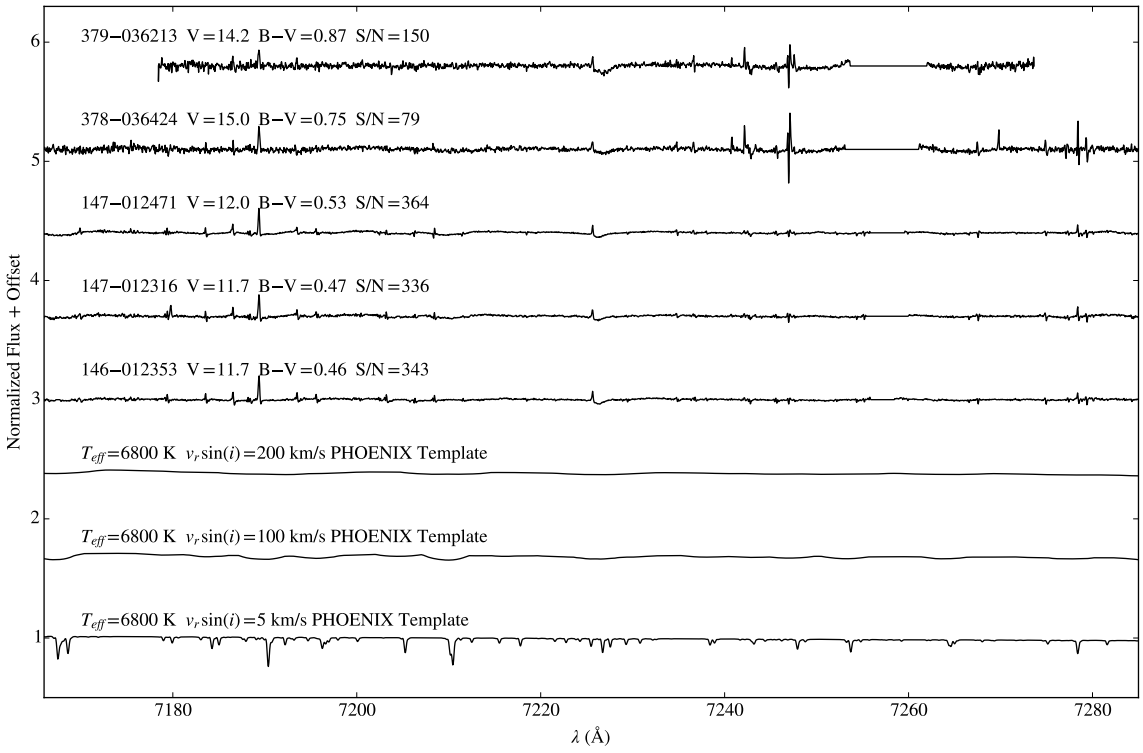

Figure 5.1: Spectra of the five near featureless objects in our sample. The individual epochs have been (mostly) cleaned of telluric absorption and emission lines and then summed to yield these high S/N spectra. Each is labeled with its UCAC4 ID, magnitude, B-V color, and summed per-pixel S/N. The bottom three spectra show a PHOENIX 6800 K dwarf at various $v_r \sin(i)$. Visually, 147-012472 and 147-012316 (4^{th} and 5^{th} down) have faint features suggesting they are rapidly rotating. The uppermost spectrum is clipped as the data at either end in some of the component epochs falls below our minimum S/N limit for fitting. A diffuse interstellar band is visible in the spectra at 7224 Å.

5.3 Cluster Properties

5.3.1 Companion Simulations

The many epochs of precise RVs we obtained allowed us to potentially identify stars orbited by stellar or substellar companions. We performed Monte Carlo simulations including both binary stars and exoplanets to investigate the level of RV variability we would expect, gauge companion detectability, and investigate how likely binaries are to pass our membership tests. Figures 5.2 and 5.3 show the input distributions for period, eccentricity, and companion mass for the binary and exoplanet populations, these are distributed according to Duchêne & Kraus (2013, DK13; for binaries) and Udry & Santos (2007, for exoplanets). We chose a total exoplanet fraction such that we would expect 1.2% of stars to have hot-Jupiter companions consistent with Wright et al. (2012) and a binary fraction of 45% consistent with DK13.

Measurement errors for each simulated RV were generated by first creating a sample of fake mean σ_{meas} values from the distribution of σ_{meas} values in our data. We then sampled a Gaussian distribution with width corresponding to the mean spread in σ_{meas} ($\sim$10 m/s) for each target to perturb the fake errors chosen for each "star". In this way we generate unique errors on each simulated RV measurement that mirror our sample (see Figure 5.4). We "observe" each simulated star at our sample cadence by sampling Gaussians located at each RV where each Gaussian is given the width of the corresponding simulated error and compute σ_{obs} and P_v (see Chapter VI) for each simulated target. We also compute random systemic velocities for each star using our measured cluster velocity dispersions to investigate how our binaries fare against our membership test.

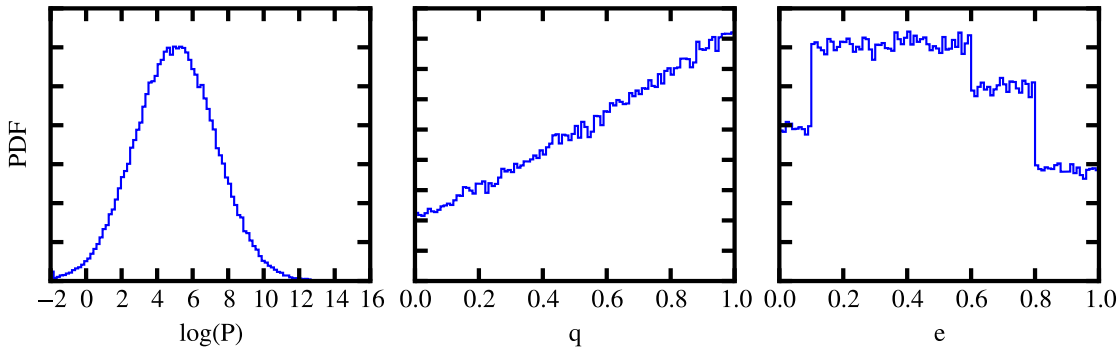

Figure 5.2: The period, mass ratio, and eccentricity distributions of stellar binaries in our companion simulations, though not evident in the plot the mass ratio and eccentricity distributions are conditioned on the period. Distributions are based on those given in Duchêne & Kraus (2013).

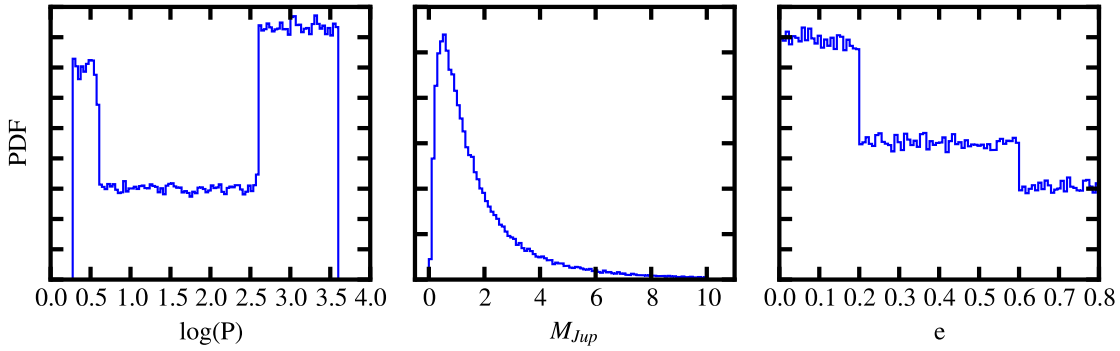

Figure 5.3: The period, mass ratio, and eccentricity distributions of exoplanetary companions in our companion simulations. Distributions are based on those given in Udry & Santos (2007).

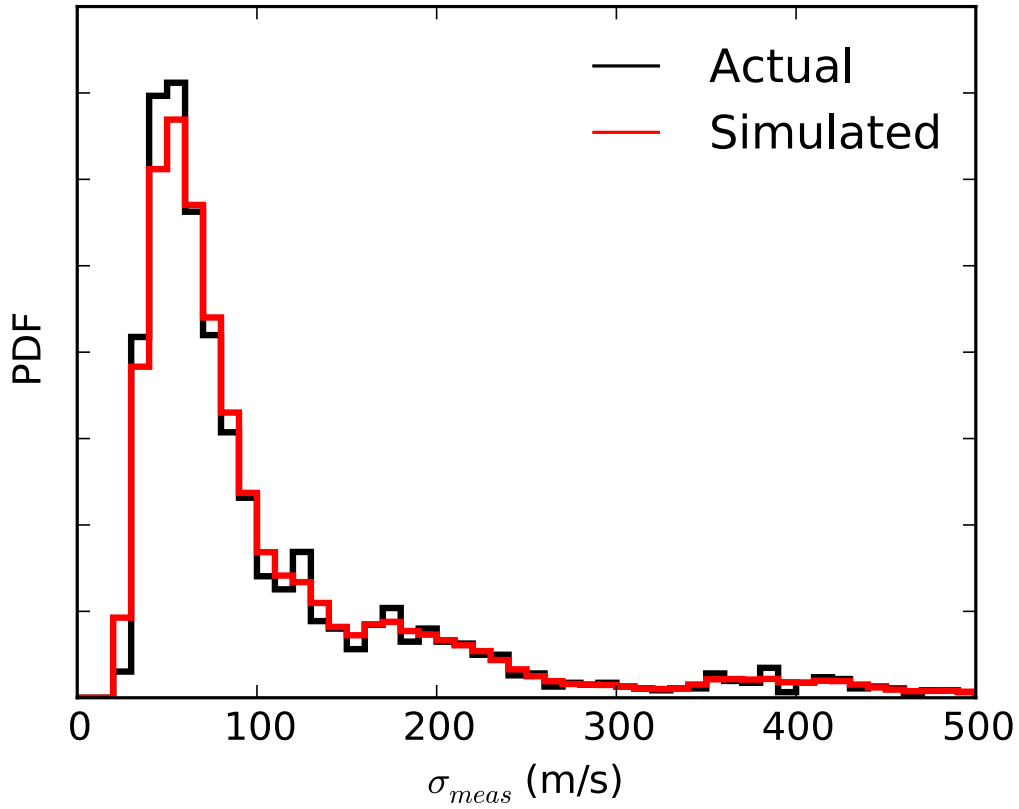

Figure 5.4: The distribution of σ_{meas} values of our spectra and the distribution of σ_{meas} values we generate for our companion simulations.

5.3.2 Membership and Binarity

To determine membership probabilities, we assumed that stars in our sample are drawn either from a Gaussian distribution centered on the cluster or from a Besançon (Robin et al., 2003) distribution of MW stars along the cluster line of sight. We computed an observed probability density function (PDF) from the normalized sum of Gaussian PDFs for each of our target stars: that is we locate a Gaussian at each measured RV with σ corresponding to the bootstrapped errors on the weighted mean. We then fit the PDF with a weighted sum of a Gaussian and the Besançon PDF and compute a membership probability for each star using Equation 5.1, where $f_{cluster}(v)$ is the fitted Gaussian PDF component and $f_{MW}(v+c)$ is the Milky Way component with a constant to allow small shifts in the center of the distribution. We adopt targets with $P_{RV} > 50\%$ as members. Integrated over each cluster we expect this to yield a false positive rate of 12% in NGC 2516 and 13% in NGC 2422. Figures 5.5 and 5.6 show histograms of our target RVs and the Besançon RVs in the left panels, our PDF and best fit model in the middle panel, and a comparison of the resulting CDFs in the right panel. In NGC 2422 we noted a second clustering of stars far removed from both the cluster and the Besançon distribution. We added a second Gaussian to account for this population (§5.3.4) and note it does not affect our membership in NGC 2422 in any way.

$$P_{RV}(v) = \frac{f_{cluster}(v)}{f_{cluster}(v) + f_{MW}(v+c)}. \tag{5.1}$$

This membership test is exceptionally harsh on binaries in the cluster. Using our companion simulations, we find that in both clusters 30% of the time we would observe a binary system to have $P_{RV} < 50\%$, our threshold for membership. Large amplitude binaries fare much worse: ∼67% of stars with a stellar variability, σ_{stel}, greater than 300 m/s will fail a 50% cut. We define the stellar variability as $\sqrt{\sigma^2_{obs} - \overline{\sigma^2_{meas}}}$. For

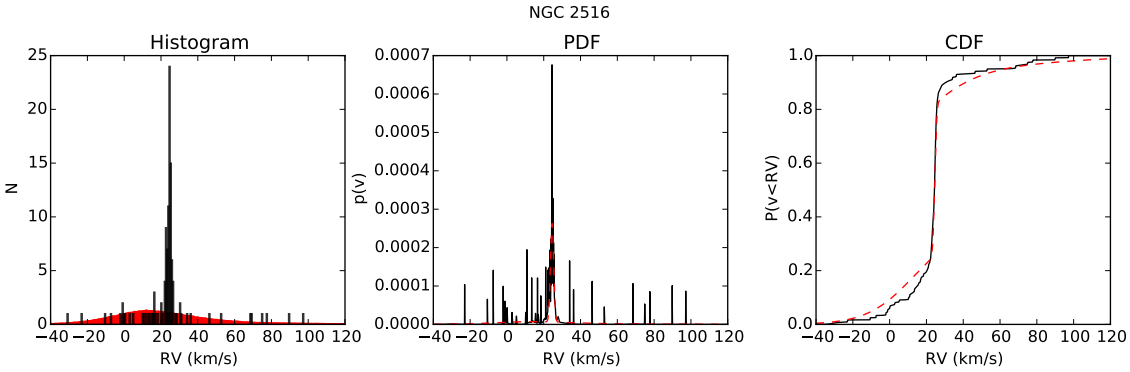

Figure 5.5: Left: A histogram of the measured RVs of our targets in NGC 2516 superimposed over a scaled histogram of stars in a Besançon model along the line of sight to NGC 2516 with matching cuts on V and B-V. Middle: A PDF constructed from our RVs and their measurement errors. Our best fit model is drawn as a dashed line. Right: The continuous distribution function for our PDF (solid) and the best-fit model (dashed).

our observations, this definition neglects a ∼2.5 m/s uncertainty caused by the bulk motions in our atmosphere on the telluric lines we use as a wavelength reference (c.f. §4.7.2.1). To adopt a more forgiving approach we consider stars with $\sigma_{stel} > 300$ m/s having a RV within $2\sigma_{\overline{RV}}$ of the $P_{RV} = 50\%$ threshold to be a probable members. This relaxed criterion reduces the exclusion of large amplitude binaries from 67% to 31%.

We adopt $\sigma_{stel} = 300$ m/s as the dividing line between what we will refer to as 'single' and 'binary' stars. This will identify 69% of all binaries as single members though the vast majority of these have periods longer than 50 yr. The cut has a 9% false-positive rate, one fifth of which are expected to be (very-massive) planetary companions flagged as binaries. We use the codes NM (non-member), PM (probable-member), and M (member) to denote the levels of membership certainty and B and SB2 to denote either RV binaries or spectroscopic binaries in Tables A.1 and A.2.

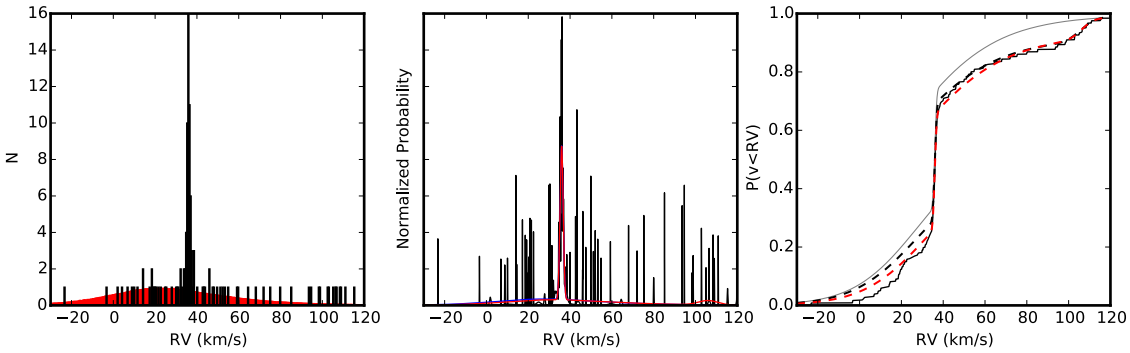

Figure 5.6: Left: A histogram of the measured RVs of our targets in NGC 2422 superimposed over a scaled histogram of the RV distribution stars in a Besançon model along our pointing's line of sight with matching cuts on V and B-V. Middle: A PDF constructed from our RVs and their measurement errors. Our adopted model is plotted as a red line. Right: The continuous distribution functions for our data (solid) and the best-fit models. The thin grey line is for a simple Besançon+Gaussian model. The dashed black line includes a second Gaussian for the overdensity of stars at ∼106 km/s and the dashed red line includes both the second Gaussian and an allowance for a mean shift (measured to be −4.9 km/s) in the Besançon RVs. The modifications alter P_{RV} by no more than 1.2% with a mean of 0.2%.

5.3.2.1 Membership and Binarity in NGC 2516

From our sample of 126 stars we identify 53 of 80 stars with $\sigma_{stel} < 300$ m/s as probable members. Our simulation predicts 11% of members will be excluded by this cut. Thirty-seven percent of these are expected to be binaries with 99% (95%) having P>8.6 (25) yr. Of these, two were labeled as photometric non-members by J01 (146-012470 and 147-012335, each failing one of J01's three tests) and twelve as photometric binaries. J01 estimated contamination fractions of 15 ± 8% for single and 30 ± 11% for binary members over the relevant color range. We find 17 of 29 photometric binaries meeting our cut to be RV non-members and 10 of 51 J01 single members to be contamination. After correcting for our sensitivity, our findings agree with their contamination estimates for single members but find they underestimate photometric binary contamination by ∼22%. For stars with $\sigma_{stel} \geq 300$ m/s, we identify 28 of 42 stars as member binaries, 8 of which were included by the relaxed

criterion. Of these, 18 are new binaries not identified by J01 while 10 were identified as photometric binaries. Six of the binary non-members were listed as J01 single members and 8 binary non-members as binary members in J01. Two of these stars (1 member, 1 non) failed our test for RV variability significance described in §6.3 and so we consider them companionless. We are unable to fully assess the membership status of the 3 featureless stars in NGC 2516. Although J01 classified them as single members, we classify them as non-members due to the presence of a diffuse interstellar band.

5.3.2.2 Membership and Binarity in NGC 2422

From our sample of 125 stars we identify 44 of 97 non-binary stars as probable, non-binary members. Our simulation predicts 14% of members will be excluded by this cut. Of these members, 37% can be expected to be binaries with 99% (95%) having P>8 (23) yr. Seven of these stars were not included in P03's membership list and are new candidate members from our UCAC4 targets. P03 does not distinguish between single and photometric binaries. For stars with $\sigma_{stel} \geq 300$ m/s, we identify 13 of 25 stars as member binaries, 5 of which were included by the relaxed criterion. Five of the 13 were not included in P03's membership list and originate from our UCAC4 targets. Three of these stars (2 members, 1 non) fail our test for RV variability significance described in §6.3 and so we consider them single members. We are unable to fully assess the membership status of the 2 featureless stars (one from P03, one from UCAC4) in NGC 2422. We classify them as non-members due to the presence of a diffuse interstellar band.

Finally we note seven stars –378-036692, 378-036906, 379-035967, 379-035982, 377-035049, 378-036136, 378-036960 – that pass our membership test in NGC 2422 but that are somewhat removed from the rest of the main sequence in the temperature-magnitude plane (c.f. Figure 5.7, 3 below, 4 above). The relative areas of the Be-

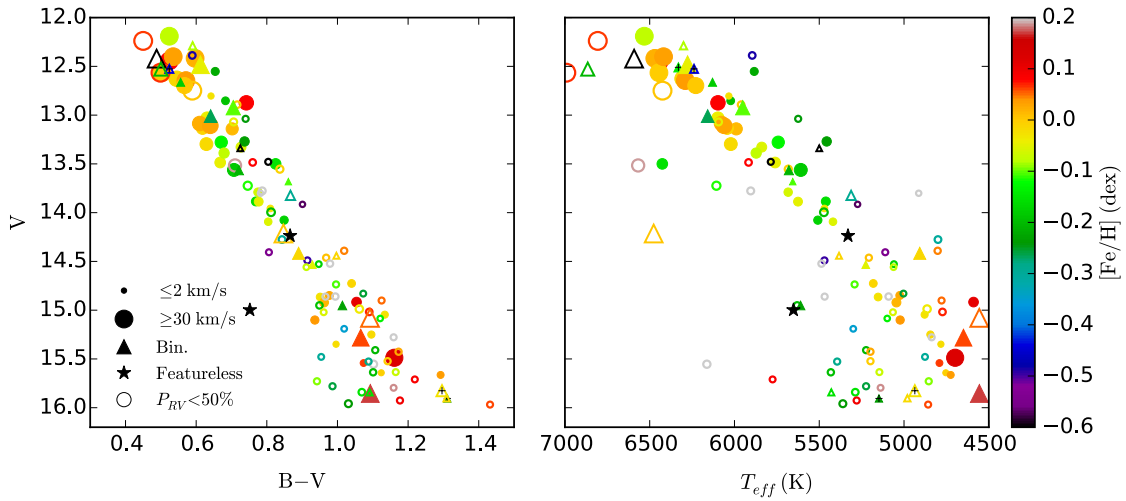

Figure 5.7: Color- (left) and temperature-magnitude (right) diagrams for targets in NGC 2422. Stars we identified as probable members (see §5.3.2) are shown as filled circles or, for binaries, triangles. Double lined binaries have a tiny black + on them. Color shows [Fe/H] and point size $v_r \sin(i)$. Hollow points show the same for targets that do not pass our membership test. The filled black stars correspond to the featureless spectra discussed in §5.2.2 and are plotted using T_{B-V}. We have corrected the T_{eff} values of members using Equation 4.4.

sançon and cluster Gaussian PDFs suggest that we could expect 7 field stars to pass as RV members. All but 378-036960 yield log(g) values consistent with MS stars and we also note it is one of only two mid-F that pass our membership test and have a $v_r \sin(i) \lesssim 25$ km/s (c.f. Figure 5.11). Two of the seven, 378-036692 and 379-035967, were flagged as members by P03, the rest were targets selected from UCAC4. Three of them, 378-036906, 378-036136, 378-036960 have errors on B–V in excess of 0.13 mag.

5.3.3 Cluster Results

We now turn our attention to the aggregate properties of our targeted clusters: systemic RV, velocity dispersion, iron and α-element abundances, and binary fractions. We determined RV and cluster velocity dispersion as part of our membership fit in the preceding section and now report those values in Table 5.1. We derived [Fe/H] and [α/Fe] values from Gaussian KDEs of the member stars (Figures 5.8 and

5.9). In both clusters we measure significantly lower iron abundances for G stars than the cluster as a whole (-0.04 dex) and also note elevated abundances in F stars, especially in NGC 2516. This latter point is expected given the higher stellar rotation and its effect on our [Fe/H] values (c.f Figure 4.15). α-element abundances present a significantly more complicated picture, suggesting our analysis would benefit from a traditional abundance analysis to test for systematics in our science targets not present in our standard stars (e.g. due to their uniformly low $v_r \sin(i)$). We also look at the distribution of stellar rotation with T_{eff}, observing uniformly elevated rotation rates in F stars and a large spread in K stars. Our distribution in both clusters appears consistent with the overall trend for the similarly aged Pleiades (c.f. e.g. Queloz et al., 1998), though we do not see elevated rotation in G stars and see significantly more rotation in our K stars. Monte Carlo simulations indicate that for our sample size we would expect to see no G stars with elevated $v_r \sin(i)$ 14% of the time in NGC 2516 and 17% of the time in NGC 2422. For K stars the Pleiades sample reported in Queloz et al. (1998) has no early to mid K stars with rotation rates above $\sim$20 km/s, at odds with our sample. Comparing our NGC 2516 and and NGC 2422 samples we find they are in agreement except for early K stars, where we see many higher rotation stars in the NGC 2516, despite its older age. A Monte Carlo simulation suggests only a 9% chance their early K distributions are similar. Figures 5.10 and 5.11 show the distribution of our $v_r \sin(i)$ values and Table 5.2 reports mean and standard deviation values for $v_r \sin(i)$.

We combine our data for $v_r \sin(i)$, [Fe/H], membership, and binarity in Figures 5.7 and 5.12 to show color- and temperature-magnitude diagrams for our clusters. As previously mentioned, the enhanced metallicity among members hotter than $\sim$6000 K is likely an artifact of the star's higher stellar rotation and our fitting approach. The disagreement between G and K stars does not follow from this as our K star spectra do appear to not suffer from the same fitter issue.

5.3.3.1 NGC 2516

Abundance Our iron abundance of -0.08 ± 0.01 dex is only slightly inconsistent the with value of $+0.01\pm0.07$ dex reported by Terndrup et al. (2002) using spectroscopy of two stars, neither of which is in our sample. We measure an α-element enhancement of 0.03 ± 0.01 dex, though we suspect this value is driven down by our fitter's interaction with high rotation rates in hotter stars (c.f. Figure 4.15).

Binarity We identified 27 of 81 members as probable binaries for an measured binary fraction of $33 \pm 5\%$. With a false positive rate of 9% on binarity, a false negative rate of 31% on membership, and a false positive rate on membership of $\sim$12% this suggests that 4 of the non-member binaries are members, 2 of the 27 are not binaries, and 3 of the 27 are not members. With these corrections we would predict 25 $(0.91 \cdot (27 + 0.31 \cdot 13 - 0.12 \cdot 27))$ binaries with $\sigma_{stel} > 300$ m/s in a sample of 78 $(81 - 0.12 \cdot 81 + 0.31 \cdot 13 + 0.05 \cdot 28)$ members for an observed binary fraction of 32%. Our simulation predicts only 15% of stars should have $\sigma_{stel} > 300$ m/s at a binary fraction of 45%, 27% at 85% (the total fraction suggested in J01), and 31% at 100%. We find a binary fraction of 100^{+0}_{-15}%. For comparison, in J01 47 of our 126 targets (37%) were flagged as photometric binaries, though recall we do not flag 12 of their photometric binaries as binaries with our test. We further investigate the composition of these binaries in §6.3.

5.3.3.2 NGC 2422

Abundance Our iron abundance of -0.05 ± 0.02 dex is moderately inconsistent the $+0.11 \pm 0.1$ dex value reported by Nissen (1988) using Strömgren photometry of 11 stars. We measure an α-element enhancement of 0.02 ± 0.01 dex, again we suspect this is driven down by our fitter's handling of high rotation in cluster F stars (c.f. Figure 4.15).

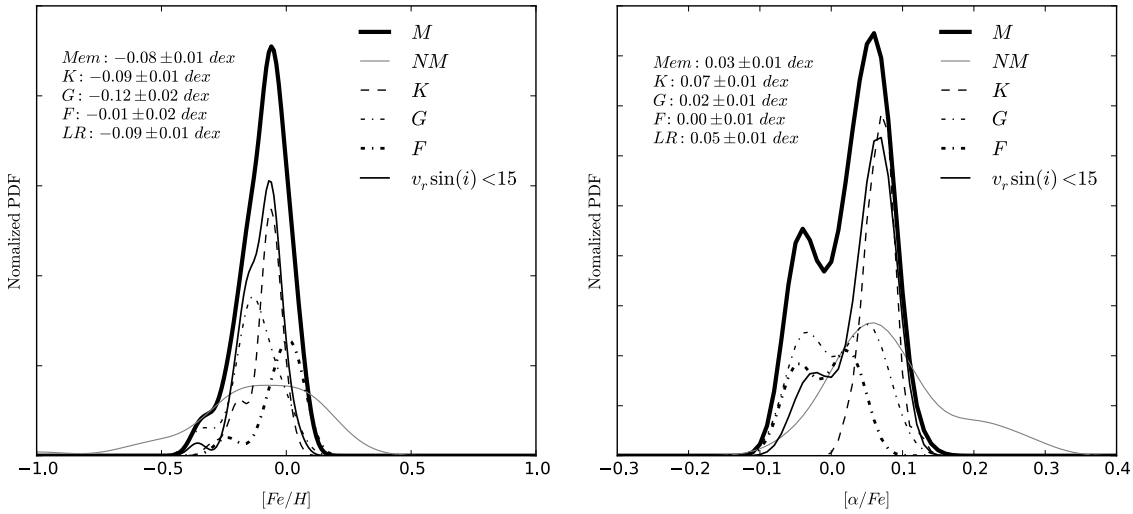

Figure 5.8: Gaussian kernel density estimates of [Fe/H] (left) and [α/Fe] (right) in NGC 2516. The thin black line shows the full member population and the the thin grey line the non-member sample. The other lines show the distributions for various subsets of our sample.

Binarity We have identified 11 of 57 members as probable binaries for a measured binary fraction of $19 \pm 5.2\%$. With a false positive rate of 9% on binarity, a false negative rate of 31% on membership, and a false positive rate on membership of 13%. This suggests that 3 of the 11 non-member binaries are true binary members, 1 of the 11 members are not binaries, and 1 of the 11 members are not members. With these corrections we would predict 12 binaries with $\sigma_{stel} > 300$ m/s in a sample of 59 members for an observed binary fraction of 20%. Our simulation predicts a total binary fraction of $62 \pm 16\%$ would produce our observed binary fraction. We further investigate the composition of these binaries in §6.3.

5.3.4 A distant association

In NGC 2422 we noted an overdensity of ∼11 stars at ∼106 km/s, well removed from the cluster and the Besançon model distribution. We introduced an additional Gaussian component to our membership model that accounted for this grouping and substantially improved our continuous distribution function (c.f. Figure 5.6). These

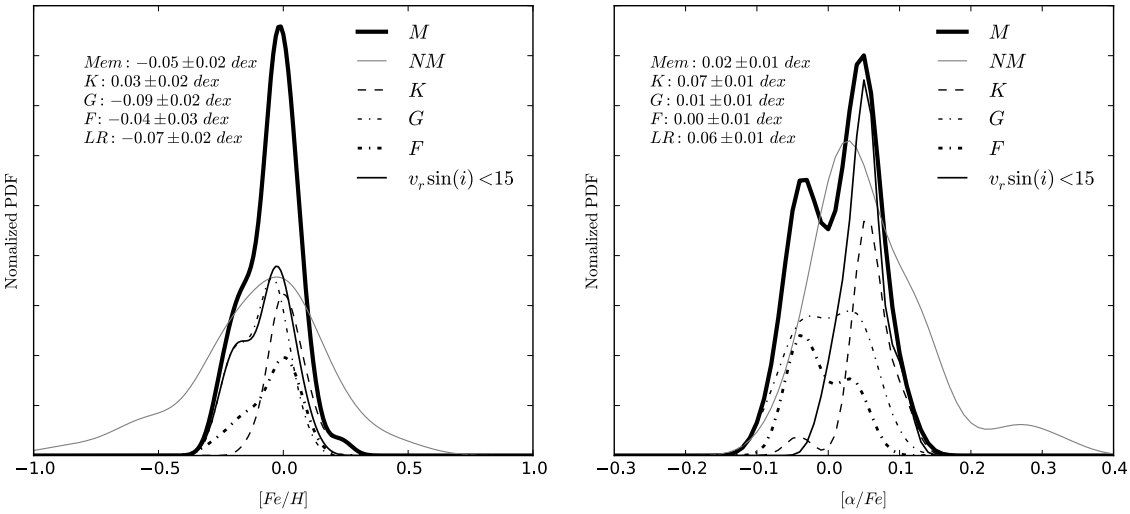

Figure 5.9: Gaussian kernel density estimates of [Fe/H] (left) and [α/Fe] (right) in NGC 2422. The thin black line shows the full member population and the the thin grey line the non-member sample. The other lines show the distributions for various subsets of our sample.

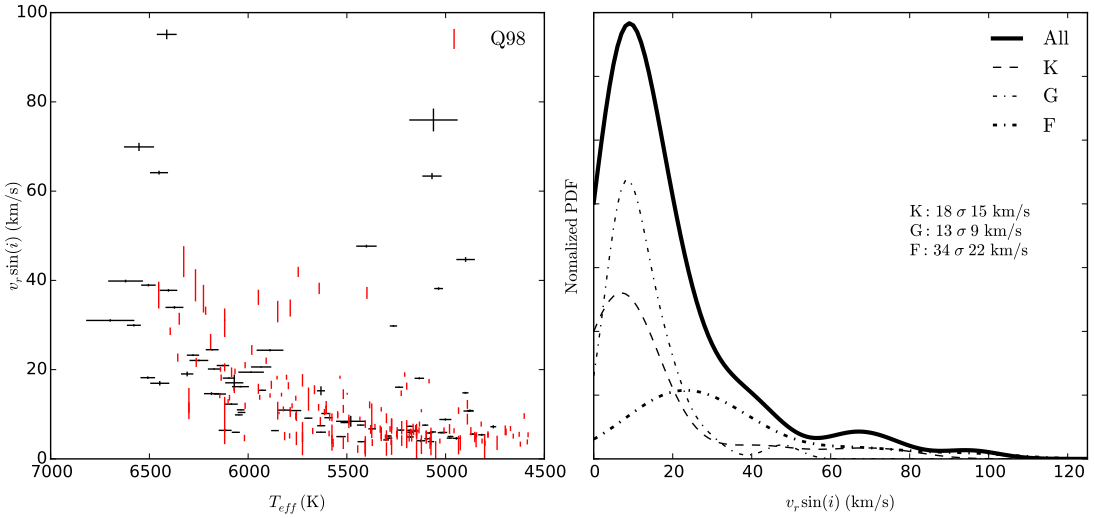

Figure 5.10: The left panel shows the $v_r \sin(i)$ values we measure for members in NGC 2516 as a function of corrected T_{eff} along with values for stars in the Pleiades taken from Tables 3 and 4 of Queloz et al. (1998) in red. We have used Casagrande et al. (2010) with [Fe/H]=+0.02 and E(B–V)=0.04 to convert colors to temperatures. The left panel shows Gaussian KDEs for the members grouped by spectral type.

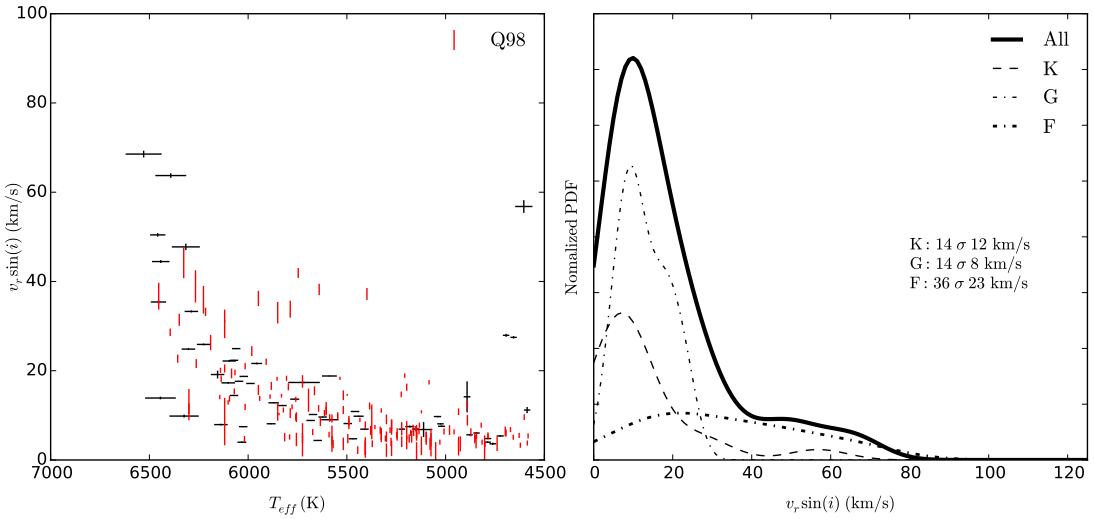

Figure 5.11: The left panel shows the $v_r \sin(i)$ values we measure for members in NGC 2422 as a function of corrected T_{eff} along with values for stars in the Pleiades taken from Tables 3 and 4 of Queloz et al. (1998) in red. We have used Casagrande et al. (2010) with [Fe/H]=+0.02 and E(B–V)=0.04 to convert colors to temperatures. The left panel shows Gaussian KDEs for the members grouped by spectral type.

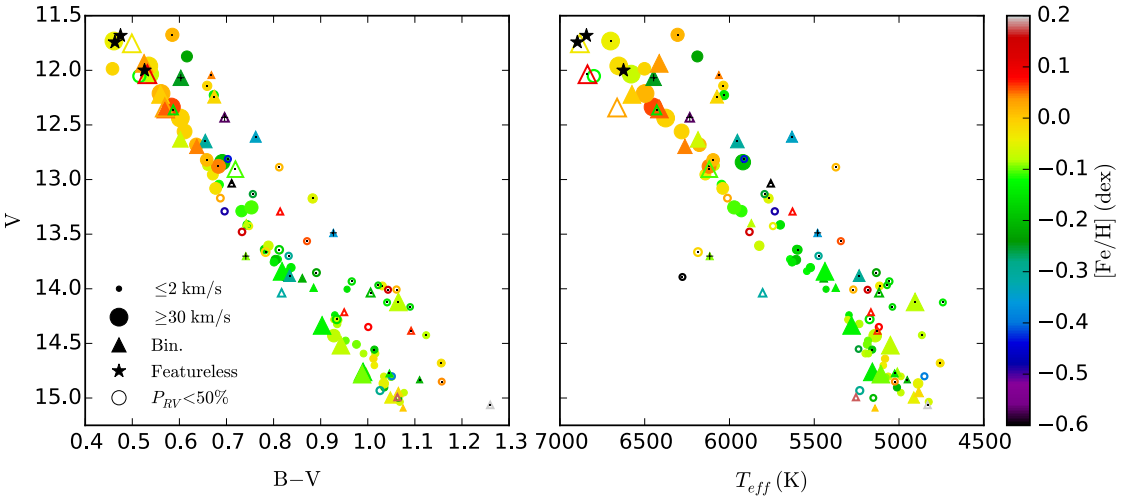

Figure 5.12: Color- (left) and temperature-magnitude (right) diagrams for targets in NGC 2516. Stars we identified as probable members (see §5.3.2) are shown as filled circles or, for binaries, triangles. Double lined binaries have a tiny black + on them and targets J01 identifies as photometric binaries a tiny black dot. Color shows [Fe/H] and point size $v_r \sin(i)$. Hollow points show the same for targets that do not pass our membership test. The filled black stars correspond to the featureless spectra discussed in §5.2.2 and are plotted using T_{B-V}. We have corrected the T_{eff} values of members using Equation 4.4.

Table 5.1. Cluster Properties

Cluster	N	RV (km/s)	σ_{RV} (km/s)	[Fe/H] (dex)	[α/Fe] (dex)	Bin. Frac.
NGC 2516	81	24.61 ± 0.002	0.723 ± 0.002	-0.08 ± 0.01	0.03 ± 0.01	$100^{+0}_{-15}\%$
NGC 2422	57	35.96 ± 0.020	0.750 ± 0.020	-0.05 ± 0.02	0.02 ± 0.01	$62 \pm 16\%$

Note. — This table reports the number of members in NGC 2516 and NGC 2422 and their aggregate properties. We report the the mean RV and width from the Gaussian fit and the mean values for [Fe/H] and [α/Fe] of RV members. We also give our estimates for the total binary fraction.

Table 5.2. Aggregate $v_r \sin(i)$ Values

Cluster	$T_{eff} \geq 6100$ K (km/s)	5250 K $\leq T_{eff} <$ 6100 K (km/s)	$T_{eff} <$5250 K (km/s)
NGC 2516	33 ± 20.9 (N=20)	13 ± 9.0 (N=24)	14 ± 18.0 (N=33)
NGC 2422	31 ± 16.2 (N=11)	13 ± 5.6 (N=24)	13 ± 12.8 (N=18)
Non-Members	31 ± 26.1 (N=25)	5 ± 1.3 (N=44)	5 ± 5.4 (N=44)

Note. — This table reports mean and standard deviation values for $v_r \sin(i)$ measurements of targets with $P_{RV} > 50\%$ in each of our targeted clusters as well as an aggregate value for all stars that to not pass our membership cut, grouped by T_{eff}.

stars cluster at 106.8 ± 1.3 km/s with a σ_{RV} of 3.76 km/s. They have a mean $v_r \sin(i)$ of 3.9 ± 0.7 km/s and all exhibit a diffuse interstellar band located 7224.2 Å. When we fit them allowing log(g) to vary they yield values ∼2.25 dex lower than cluster members in NGC 2422. As a secondary test we fit them using the pipeline of Walker et al. (2015b) which indicates log(g) of 0.5–1.5. These tests strongly suggest these stars are giants or supergiants, though there is no star formation at the distance required by a supergiant. Assuming 1.22 magnitudes of extinction and 0.39 magnitudes of reddening per Schlafly & Finkbeiner (2011); an average V magnitude of 15.5; and a de-reddened color temperature of ∼5500 K we would suggest these stars are either G2 supergiants at 150 kpc or G5 giants at ∼13 kpc. NGC 2422 is located at $l = 231, b = +3$ along a line of sight to the Monoceros stream, suggesting that these stars may be part of that stream.

CHAPTER VI

RV Variability in NGC 2516 and NGC 2422

6.1 Introduction

In this chapter I now turn to focus on the time variability of the radial velocities we have measured for stars, both member and non-member, binary and single within our NGC 2516 and NGC 2422 samples. Prior to determining which stars are statistically significant RV variables and may host stellar, sub-stellar, or exoplanetary companions, I first describe our approach to assessing the level of stellar activity induced RV variability (which we refer to as stellar "jitter") in §6.2. The level of activity in each cluster is of critical importance as it effectively lowers our sensitivity to less massive companions and, if left unaccounted for, could cause stars without companions to appear as false detections. We investigate the level of jitter in three slowly rotating ($v_r \sin(i) < 15$ km/s) sub-populations in our sample: members in NGC 2516, members in NGC 2422, and the combined set of non-members. With an estimate of the typical stellar activity induced RV variability in each sample, we then turn to assessing which stars in our sample exhibit statistically significant variability in §6.3. Therein we define a probability of statistically significant variability both with and without stellar jitter and use the companion simulation described in §5.3.1 to estimate our sensitivity to stellar, brown dwarf, and exoplanetary companions. Finally, we report the number of candidate companion host stars that we would suggest merit followup.

6.2 Stellar Jitter

Young stars are well known to exhibit stellar activity (e.g. evolving surface spots, flaring) which can induce measurable shifts in line profiles thereby shifting recovered RVs from their true values (for a review see Lagrange et al., 2013). Younger stars – such as those in the ∼140 Myr and ∼75 Myr old clusters we have targeted – are often avoided in exoplanet searches for fear of stellar jitter hindering detection of low-amplitude RV variability. Levels in excess of 300 m/s are seen at ages of a few Myr (c.f. Figure 3, Lagrange et al., 2013) while others have reported values of ∼100 or 60 m/s at 15 Myr and ∼200 Myr (Bailey et al., 2012; Paulson & Yelda , 2006, though the former is the IR where jitter is reduced by about a factor of 2 due to decreased star-spot contrast). Stars older than ∼500 Myr show significantly reduced activity with levels below 20 m/s in the optical (Paulson et al., 2004; Quinn et al., 2012). To date, there is no generally accepted level of jitter as a function of age at intermediate ages, though this may be because there is not one: The large spread in stellar rotation and activity exhibited by coeval stars with ∼50–300 Myr ages may well mean a one-size-fits-all approach is not applicable (Lagrange et al., 2013). In this section we investigate the level of stellar jitter, σ_{jitter}, seen in stars in both of our clusters.

In §5.3.2 we introduced σ_{stel} to quantify the level of stellar velocity variability we see beyond that explained by our measurement errors alone. There we tacitly assumed that any variability seen above a 300 m/s threshold was induced purely by the presence of a stellar companion, neglecting any variations caused by stellar activity. As levels at these ages are likely $\lesssim$ 150 m/s (c.f. Lagrange et al., 2013) that choice did not appreciably affect our binary determinations and allowed us to defer the detailed issued until now. As a reminder we defined σ_{stel} as $\sqrt{\sigma^2_{obs} - \overline{\sigma^2_{meas}}}$ where σ^2_{obs} is the measurement weighted variance in our RV measurements and $\overline{\sigma^2_{meas}}$ is the mean measurement variance. Here we acknowledge the contribution of jitter

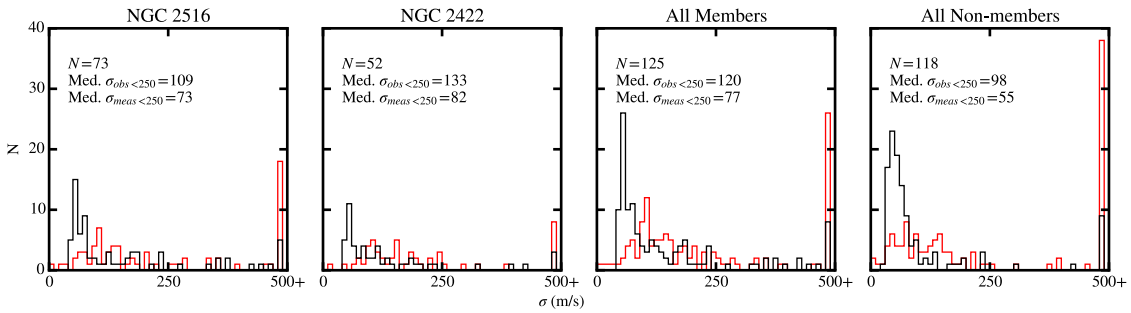

Figure 6.1: These plots show the distributions of σ_{meas} and σ_{obs} for groups of stars in our sample. From left to right: NGC 2516 members, NGC 2422 members, all members, and all non-members. The solid line shows the distribution of median σ_{meas} and red line the distribution of σ_{obs}. Distributions are clipped at 500 m/s. The number of targets, in each distribution as well as the median values for targets below 250 m/s are shown in each figure.

explicitly with the approximation that $\sigma^2_{stel} = \sigma^2_{companion} + \sigma^2_{jitter}$ and point out that in the absence of a companion σ_{stel} serves as a measure of σ_{jitter}. Figure 6.1 shows the distributions of σ_{meas} and σ_{obs} for members in each of our clusters, the combined sample (as the clusters are of similar age), and of non-members. These distributions show clear indication that most stars in our sample exhibit greater variability than one would expect from measurement errors alone. The non-member distributions exhibit increased overlap at low amplitude, as might be expected in a population composed of older field dwarfs and giants and hence subject to less stellar activity (e.g. Johnson et al., 2010).

We employ two different approaches to estimate a typical value for σ_{jitter} in each cluster. Method 1 is to ask what the mean level of stellar variability is in our sample, i.e. What is $\sqrt{\overline{\sigma^2_{stel}}}$? The second, more involved method is to assume that our RVs are drawn from Gaussians at each star's RV with width $\sigma^2 = \sigma^2_{meas} + \sigma^2_{stel}$, write down the likelihood function for σ_{stel} given our data, and find its maximum. In both cases we must consider the contribution of genuine companions (recall from §5.3.2 we expect at least 37% of stars with $\sigma_{stel} < 300$ m/s to be long period binaries). We do so in two ways: First we compute the mean or expectation value iteratively, excluding any

stars with a $\geq 99\%$ chance of being a variable ($P_v \geq 0.99$, see §6.3) in the presence of the jitter inferred from the previous iteration. Second we perform both tests with our simulated population (§5.3.1) in the presence of added Gaussian jitter. These simulations show that both methods yield answers that agree at the m/s level and recover a jitter estimate ∼10 m/s under the input value.

We use the 30 and 20 non-binary members ($\sigma_{stel} < 300$ m/s) with a corrected $T_{eff} < 5800$ K and $v_r \sin(i) < 15$ km/s (c.f. Figure 6.2) in NGC 2516 and NGC 2422 to estimate the level of stellar activity in our targets. In practice the temperature and rotation cuts are equivalent to a measurement error cut of $\sigma_{meas} < 100$ m/s, which we use when testing our approach with the simulation. The two tests we perform are described in the following paragraphs and results listed in Table 6.1. Figure 6.3 shows the starting and final samples for method two, though the set of used targets is similar for first method. We do observe significant variability in our non-member sample however we would argue that the poorer accuracy of our stellar templates used for these fits (i.e. very inaccurate log(g) values and hence poorly optimized T_{eff} and [Fe/H]) may mean we underestimated our measurement errors.

Method 1 We compute $\overline{\sigma^2_{stel}}$. This yields a value of 122 ± 58 m/s using 30 stars in NGC 2516 which converges to 38 ± 29 m/s (N=18) after iteratively excluding probable variables. In NGC 2422 we measure a value of 130 ± 50 m/s using 20 stars which converges to 121 ± 44 m/s (N=18) after iteratively excluding stars with $P_v \geq 0.99$. Our simulation suggests that these values systematically underestimate the true variability by 10 m/s. Table 6.1 also reports values for the non-member population.

Method 2 We assume that our RVs (x_{ij}) are drawn from a set of Gaussian's each located a star's relative motion along the line of sight (μ_i) and a standard deviation

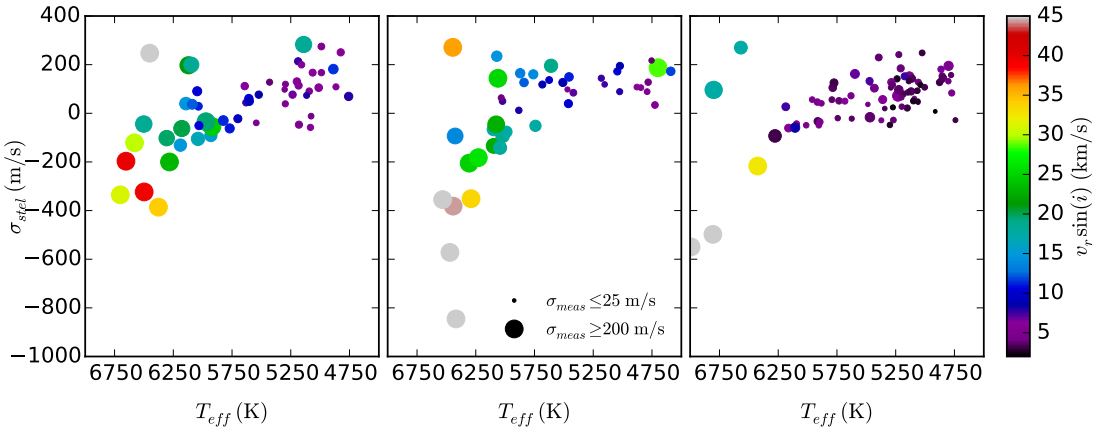

Figure 6.2: These plots show σ_{stel} as a function of T_{eff} for non-binaries in NGC 2516 (left), NGC 2422 (middle), and the combined sample of non-members (right). Point sizes are scaled by the mean measurement error for each target and point color is used to show $v_r \sin(i)$. We plot negative values for σ_{stel} by computing the root of the absolute value of the variance and preserving the sign. The large number of rapidly rotating stars with negative σ_{stel} is a result of our fitter exhibiting a strong preference for the initial RV in spectra with broad features. Based on this figure we adopt the $T_{eff} < 5800$ K and $v_r \sin(i) < 15$ km/s sample to study stellar activity in our sample.

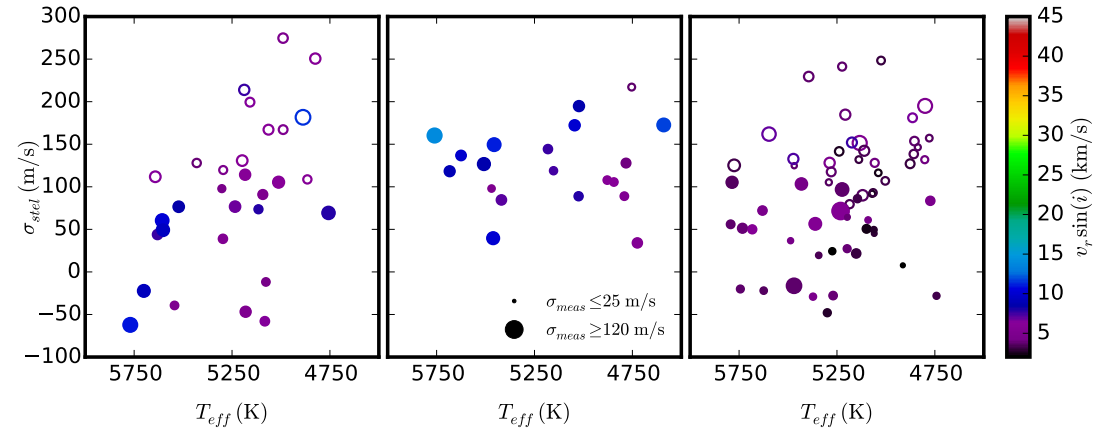

Figure 6.3: These plots show starting and ending samples of σ_{stel} used to estimate stellar activity levels in NGC 2516 (left), NGC 2422 (middle), and the combined sample of non-members (right) with method two (method one is similar). Point sizes are scaled by the mean measurement error for each target and point color is used to show $v_r \sin(i)$. Open circles denote targets that were excluded by the $P_v \geq 0.99$ cut when iterating. Negative values for σ_{stel} are the root of the absolute value of the variance with the sign preserved.

corresponding to quadrature sum of $\sigma_{meas,i}$ and σ_{stel}:

$$(x_{11}, x_{ij}, ..., x_{NM_i}) \sim N(\mu_i, \sqrt{\sigma^2_{meas,i} + \sigma^2_{stel}}).$$

The likelihood function for which is

$$f_{\sigma_{stel},\mu_1,...,\mu_N}(\mathbf{X_1}, ..., \mathbf{X_N}) = \prod_{i=1}^{\mathrm{N}} \prod_{j=1}^{\mathrm{M_i}} \frac{1}{\sqrt{2\pi(\sigma^2_{meas,i} + \sigma^2_{stel})}} e^{-\frac{x_{ij}-\mu_i}{2(\sigma^2_{meas,i}+\sigma^2_{stel})}}$$

where N is the number of stars and $\mathrm{M_i}$ is the number of observations of star i. Noting that

$$\frac{1}{M_i} \sum_{j=1}^{M_i} (x_{ij} - \overline{x_i})^2 \approx \sigma^2_{obs,i}$$

and assuming $\mu_i \approx \overline{x_i}$ we can take the log and write the log-likelihood as

$$l(\sigma_{stel}) = -\frac{1}{2} \sum_{i=1}^{N} \mathrm{M_i} \left(\frac{\sigma^2_{obs,i}}{\sigma^2_{meas,i} + \sigma^2_{stel}} + \log(2\pi \ (\sigma^2_{meas,i} + \sigma^2_{stel})) \right)$$

Here N is the number of stars under consideration and M_i the number of observations of star i. The peak of this function then provides an estimate of typical σ_{stel} for the sample of stars, which after iterating should be predominately driven by companion-free (or effectively so) stars. We find $\sigma_{stel} = 130 \pm 10$ m/s using 30 stars in NGC 2516 which converges to 67±10 m/s (N=18) after iteratively excluding stars with $P_v > 0.99$. In NGC 2422 we measure a value of 135 ± 10 m/s using 20 stars which converges to 128 ± 10 m/s (N=19). Our simulation suggests that these values systematically underestimate the true variability by 10 m/s. Table 6.1 also reports values for the combined sample and the non-member population.

In Figure 6.4 I show the levels of jitter we measure in NGC 2516 and NGC 2422 alongside measurements of stellar jitter in single stars from Lagrange et al. (2013, measured using HARPS at ∼530 nm) and the average values determined for a number

Table 6.1. Stellar Jitter

Method	σ_{jitter} (m/s) NGC 2516	NGC 2422	Non-members
$\sqrt{\overline{\sigma^2_{stel}}}$	48 ± 29 (14)	131 ± 44 (18)	90 ± 31 (45)
MLE	77 ± 10 (8)	138 ± 10 (19)	56 ± 7 (30)
Average	74 ± 9	138 ± 2	58 ± 7

Note. — This table reports our estimates of σ_{jitter} obtained via the two methods described in the text. Numbers in parentheses give the sample size. An additional 10 m/s has been added to the reported values based on the result of our simulations.

of open clusters and associations also in the optical. Our results in both clusters appear generally consistent with existing results. Our elevated jitter in NGC 2422 could be seen as a confirmation of the age reported by (Loktin et al., 2001). We note that our observed rotation rates in NGC 2422 (c.f. Table 5.2) are consistent with those in NGC 2516 and the binary fraction in NGC 2516 is far higher, suggesting that neither stellar rotation nor binarity are to blame for NGC 2422's higher activity. In both of our clusters, and NGC 2516 especially, we measured a wide range of σ_{stel} in our non-variable population, suggesting there is indeed a large spread in activity induced RV variability among the stars in our clusters as is exemplified by the spread in single stars at $\sim$75 Myr.

6.3 Stellar Variability

We now turn our attention to identifying which stars in our sample exhibit statistically significant RV variability. Our goal here is to provide a refined pool of targets that merit followup with some combination of single-object RV spectroscopy

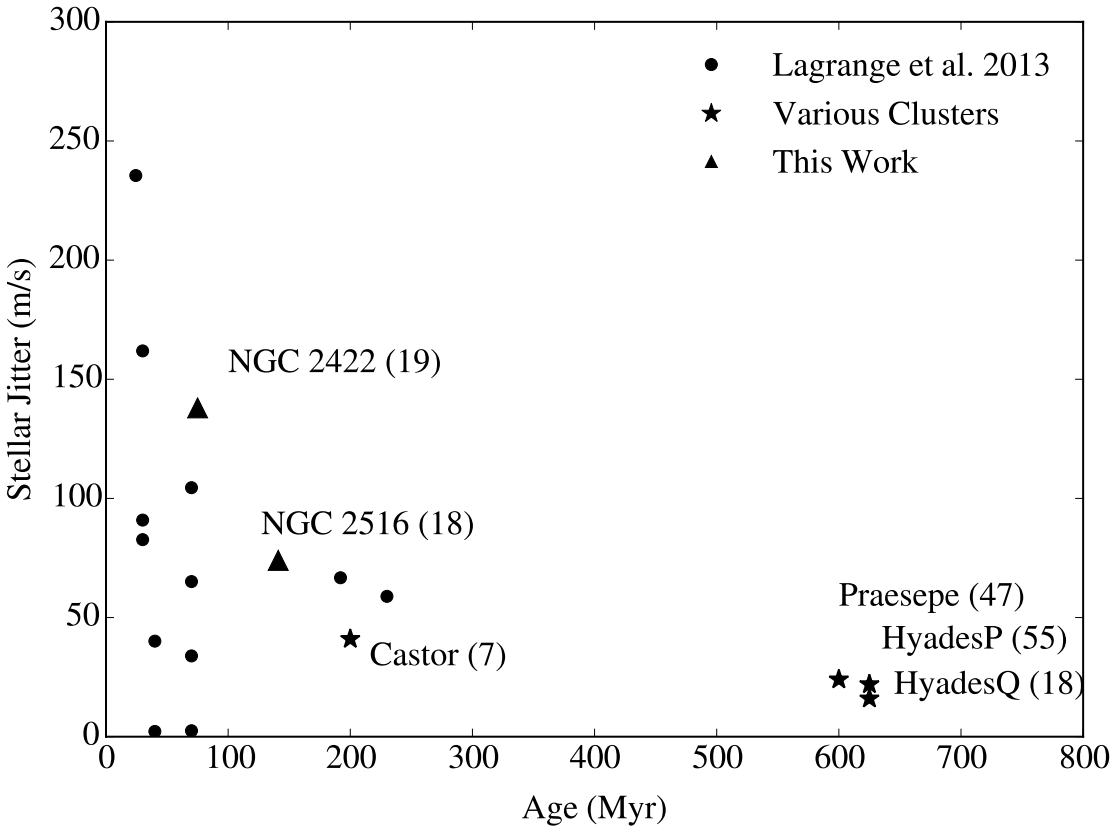

Figure 6.4: Determinations of stellar jitter for a number of single stars (circles) from Lagrange et al. (2013), averages from stars in open clusters and young associations Paulson & Yelda (2006); Paulson et al. (2004); Quinn et al. (2012, 2014) (stars), and our results in NGC 2516 and NGC 2422 (triangles). For clusters and associations we note the name and number of stars used in the average.

and multi-band photometric monitoring to assess wether stellar surface activity is responsible for the variability we see. We compute the raw probability that each star is an RV variable and the probability each star is an RV variable in the presence of the appropriate σ_{jitter} from Table 6.1. This probability, $\mathrm{P_v} = \mathrm{P}(\mathrm{X} < \chi^2)$, is computed using the RVs and σ_{meas} values of each star, in the latter case incorporating σ_{jitter} by adding in quadrature with σ_{meas}. In both cases we exclude RV outliers $> 3\sigma_{obs}$ from the mean RV: this excludes a single epoch for 42 stars and 2 epochs in another two stars for a total of 44 RVs across our sample of ∼2500 observations. The former raw P_v then is an estimate of the likelihood each star exhibits any sort of velocity variability while the latter estimates the probability variations are induced by a companion. These probabilities are reported in Tables A.1 and A.2.

We performed the same analysis on our simulated RVs to estimate the false-positive and negative rates for stellar and exoplanetary companions as a function of P_v cut and gauge our companion sensitivity. Figures 6.5 and 6.6 show our false positive and negative rates as a function of P_v along with the number of exoplanets, binaries, and false variables we would expect in a population of 100 stars for each of our clusters. This indicates that for a P_v cut of 0.96 we can expect a roughly equivalent number of exoplanet candidates as false positives while being sensitive to 92% of binaries with $P \lesssim 50$ years and ∼40% of simulated exoplanets with $P < 50$ days. In detail, assuming NGC 2516 has a binary fraction of 85%, consistent with J01, our simulations predict the binary variables ($\sigma_{stel} > 300$ m/s) to be composed of 99% stellar multiples with 0.85% exoplanets, and 0.15% false positives, assuming a jitter of 75 m/s. Low amplitude variables should be composed of 84% stellar, 12% exoplanets, and 4% false positives. In NGC 2422 we adopt a binary fraction of 62% and predict binaries to be composed of 97.6% stellar, 1.4% exoplanets, and 1% false positives. Our 'single' sample should consist of 67% binaries, 12% exoplanets, and 21% false positives.

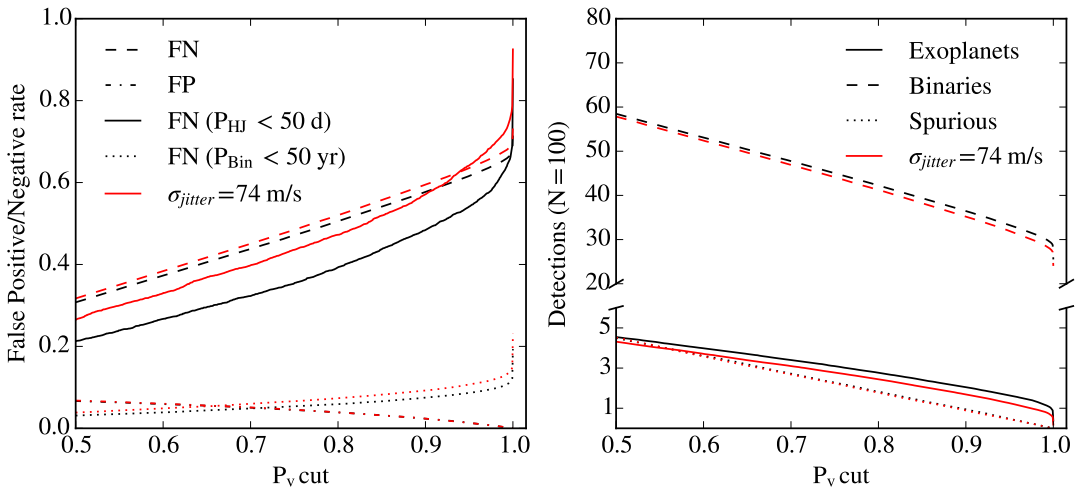

Figure 6.5: The left panel shows the false positive a negative rates of our variability test for binaries and exoplanets in our companion simulation both with and without additional stellar variability. The right panel shows the number of true binaries (not merely binaries with $\sigma_{stel} > 300$ m/s), exoplanet-hosting, and spuriously variable stars we would expect to flag in a sample of 100 stars. Though not shown, we note a binary fraction of 100% would increase the expected number of binary detections by $\sim$7 roughly independent of P_v cut. This simulation was run assuming a binary fraction of 85% consistent with J01 and assuming the cadence of our 12 observations in NGC 2516.

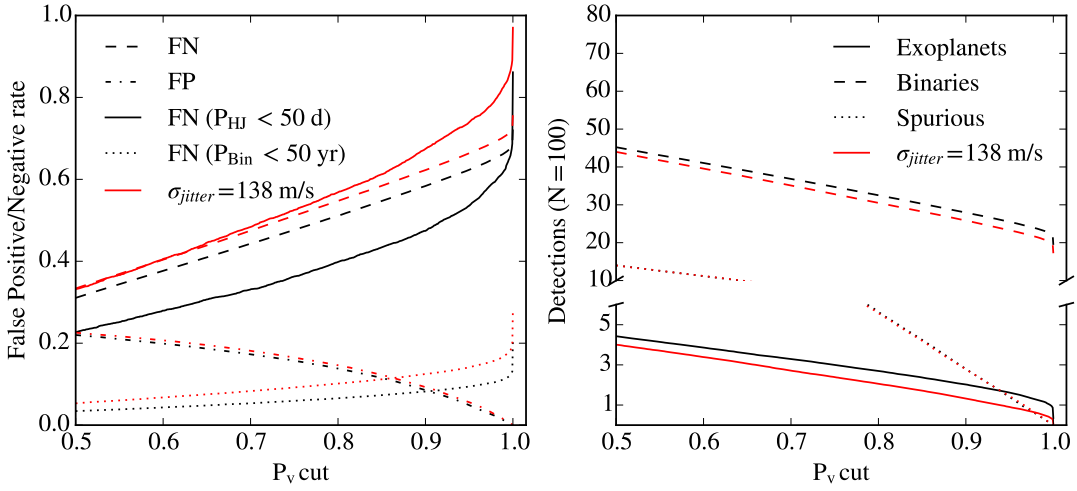

Figure 6.6: The left panel shows the false positive a negative rates of our variability test for binaries and exoplanets in our companion simulation both with and without additional stellar variability. The right panel shows the number of true binaries (not merely binaries with $\sigma_{stel} > 300$ m/s), exoplanet-hosting, and spuriously variable stars we would expect to flag in a sample of 100 stars. This simulation was run assuming a binary fraction of 62% and assuming the cadence of our 10 observations in NGC 2422.

6.4 RV Variables

Adopting a P_v threshold of 0.96, we report the number of significant binary and single variables we see in Table 6.2 both with and without the appropriate average σ_{jitter} from Table 6.1. Of the 67 stars with $\sigma_{stel} > 300$ m/s, 5 failed our P_v cut and were counted as single, non-variable members: these stars all have $\sigma_{obs} \lesssim 1500$ m/s and $v_r \sin(i) \gtrsim 40$ km/s and have large measurement errors. Fifty-three of our "single" stars exhibit significant variability after accounting for stellar jitter.

Using a binary fraction of 100% in NGC 2516, a $\sigma_{jitter} = 74$ m/s, our observation spacing, and our adopted threshold of $P_v = 0.96$ we would expect 39% of members to exhibit significant variability and 30% of members to both exhibit significant variability and have $\sigma_{stel} > 300$ m/s. As mentioned in §5.3.3 we found a slightly elevated 33% of members for the latter. We find a total variability rate of 53%, significantly higher that the 39% value we expect. Our simulation shows we would expect about 50% for the total variability rate if the true value for σ_{jitter} were in agreement with NGC 2422. As we only used stars with $T_{eff} < 5800$ K and $v_r \sin(i) < 15$ km/s when computing σ_{jitter} one possibility is that hotter or more rapidly rotating stars make up the majority of these variables: that is not the case. Only three of the sixteen low amplitude variables are hot enough or fast enough rotators to be affected by this cut: excluding them lowers our total variability to 49%. We would suggest that additional data (e.g. activity indicators) or targeted monitoring is needed to address the source of this disagreement.

In NGC 2422, with a binary fraction of 62% and $\sigma_{jitter} = 138$ m/s we would expect 25% of members to exhibit significant variability and 20% of members to both exhibit variability and pass our binary test. Previously we found 19% for the latter and here we find a total variability rate of 25% ($(11+3)/57$), both in good agreement with our expectations.

We used the `gatspy` package to compute Lomb-Scargle periodograms and estimate

significance via a bootstrap simulation for all of our RV variable stars. Of the 62 binaries, 38 exhibit periodogram peaks with $> 95\%$ significance and have periods ranging from just over a day (our data suffers from a strong alias below $\sim$1.1 days) to $\sim$3.5 years. Nine non-binary stars also exhibited significant peaks with seven between 1.5–5.8 days, one at 21 days, and one at 27 days. Appendix B gives plots of the RV time series and periodograms for all of our RV variables robust to the average jitter. Points shown as a red x were excluded for being a $> 3\sigma$ outlier. RVs for stars with significant periodogram peaks are also plotted phased to the most significant peak with 95% and 99% significance contours shown. In some cases the plotted points do not sufficiently sample the period space to show that the peak crosses the 95% threshold. NGC 2516 has undergon extensive X-Ray study and we use the captions of the individual plots to mention any known X-Ray variability from Damiani et al. (2003, D03), Wolk et al. (2004, W04), or Pillitteri et al. (2006, P06) for X-ray data in NGC 2516. Tables 6.3 and 6.4 provide details on the variables in NGC 2516 and NGC 2422, with each specifying the appropriate figure in Appendix B.

Table 6.2. Stellar Variability in NGC 2516 and NGC 2422

	NGC 2516		NGC 2422	
Group	M	NM	M	NM
Usable Targets	81	41	57	65
RV Variables	52	26	35	47
RV Variables incl. σ_{jitter}	43	23	14	35
SB2	2/3 (2)	1/1 (1)	2/2	1/2
$\sigma_{stel} \geq 300$ m/s	16/27 (10)	8/13 (7)	7/11	7/11
$\sigma_{stel} < 300$ m/s	2/16 (4)	1/10 (8)	0/3	6/24

Note. — A breakdown of RV variability in our sample. The number of usable targets excludes the 5 featureless spectra described in §5.2.2, the one star in NGC 2516 for which no usable data was obtained, and the one mistakenly targeted early-type star in NGC 2422. The first of each pair of numbers is the number of RV variables with at least a 95% significant periodogram peak (c.f. §6.4) this number is followed by the total number of statistically significant ($P_v > 0.96$) RV variables. In all cases I adopted a jitter level of 74 m/s in NGC 2516, 138 m/s in NGC 2422, and 58 m/s in the field. The numbers reported in parentheses for NGC 2516 are the number of stars in the category reported as photometric binaries by J01. Sections 5.3.2 and 6.3 describe the expected makeup of these groups in terms of multiples, long-period multiples, exoplanets, and false positives. Tables 6.3 and 6.4 provide details on the variables in NGC 2516 and NGC 2422.

Table 6.3. Variables in NGC 2516

UCAC4	Flags	N	$\overline{\text{S/N}}$	T_{eff} (K)	$v_r \sin(i)$ (km/s)	RV (m/s)	σ_{obs} (m/s)	σ_{meas} (m/s)	σ_{stel} (m/s)	P_v	Period (days)	Figure
147-012265	PMSB2	11	115	6447 ± 50	16.9 ± 0.5	37677 ± 11052	35789	196	35789	1.00	...	B.1
147-012424	PMSB2	12	54	6116^{+35}_{-33}	6.4 ± 0.2	15450 ± 6734	23160	75	23160	1.00	30.0	B.2
146-012601	PMB	10	36	5239 ± 19	16.1 ± 0.2	31158 ± 6325	19304	159	19303	1.00	1.9	B.3
147-012249	MB	12	51	5372^{+17}_{-13}	6.7 ± 0.1	25997 ± 4535	16386	62	16386	1.00	23.2	B.4
147-012499	PMSB2	12	51	5480 ± 79	8.4 ± 1.3	18343 ± 4125	14814	87	14814	1.00	78.7	B.5
146-012500	PMB	11	27	5001 ± 30	8.8 ± 0.2	16724 ± 4637	12569	267	12567	1.00	3.7	B.6
146-012622	NMSB2	11	59	6234 ± 207	9.2 ± 0.3	-1954 ± 4049	11821	176	11819	1.00	16.2	B.7
146-012455	PMB	12	45	5430^{+21}_{-18}	7.6 ± 0.1	28014 ± 3450	11231	74	11231	1.00	113.5	B.8
147-012487	NMB	12	85	6408^{+35}_{-28}	$10.4^{+0.2}_{-0.1}$	15591 ± 2803	9182	105	9181	1.00	16.3	B.9
148-012940	PMB	11	108	6063^{+22}_{-19}	6.0 ± 0.1	30821 ± 2475	8563	47	8562	1.00	10.8	B.10
146-012358	NMB	11	27	4833 ± 18	4.5 ± 0.2	69487 ± 3072	8545	60	8545	1.00	14.1	B.11
146-012557	NMB	12	74	5731 ± 34	4.9 ± 0.2	-30760 ± 2369	8502	68	8502	1.00	1283.6	B.12
147-012308	MB	11	93	6403^{+49}_{-45}	37.8 ± 0.3	25169 ± 2493	8136	399	8126	1.00	...	B.13
147-012432	MB	11	39	5022 ± 19	5.9 ± 0.2	26179 ± 2333	7340	60	7340	1.00	559.5	B.14
147-012270	NMB	7	46	5117 ± 60	7.5 ± 0.6	16154 ± 2929	7084	80	7084	1.00	34.3	B.15
147-012164	MB	12	97	6070 ± 46	17.0 ± 1.9	23279 ± 1930	6851	163	6849	1.00	6.0	B.16
147-012262	MB	11	25	4945 ± 19	4.6 ± 0.3	23031 ± 2187	6679	84	6678	1.00	27.6	B.17
148-012906	MB	11	100	5631^{+22}_{-19}	15.3 ± 1.0	26429 ± 1406	4613	115	4611	1.00	497.4	B.18
147-012376	MB	5	17	5042 ± 116	76.7 ± 2.5	25225 ± 2351	4591	1322	4397	1.00	...	B.19
147-012474	NMB	12	37	5111 ± 20	3.7 ± 0.1	-500 ± 975	3353	43	3353	1.00	545.3	B.20
147-012175	MB	12	26	4877^{+17}_{-13}	10.8 ± 0.2	23748 ± 981	3231	108	3229	1.00	445.5	B.21
148-012943	PMB	12	122	6412 ± 48	95.1 ± 1.1	22513 ± 1032	3135	1326	2841	1.00	...	B.22
147-012290	NMB	11	47	5160^{+18}_{-13}	3.4 ± 0.2	12026 ± 942	3126	42	3125	1.00	987.3	B.23
147-012280	MB	11	106	6553 ± 79	69.9 ± 0.9	25578 ± 978	3111	1052	2928	1.00	...	B.24
146-012365	MB	12	52	5864^{+21}_{-18}	6.3 ± 0.1	22849 ± 882	2896	78	2895	1.00	492.3	B.25
147-012220	NMB	12	91	6887 ± 80	76.5 ± 1.1	20925 ± 807	2488	1306	2118	1.00	...	B.26
147-012205	NMB	12	73	5631^{+21}_{-18}	4.0 ± 0.1	14106 ± 625	1985	41	1984	1.00	52.0	B.27
147-012406	NMB	11	92	6645 ± 67	36.2 ± 0.7	21242 ± 414	1351	448	1275	1.00	...	B.28
146-012483	MB	12	30	4899 ± 48	44.7 ± 0.5	22790 ± 367	1191	498	1082	1.00	2.7	B.29
147-012433	MB	11	25	5126 ± 23	4.1 ± 0.3	25744 ± 321	999	64	997	1.00	82.0	B.30
146-012424	MB	12	86	5934 ± 50	20.6 ± 0.1	25703 ± 302	926	185	907	1.00	...	B.31
147-012306	MB	11	37	5035 ± 23	38.2 ± 0.3	26249 ± 264	793	382	694	1.00	...	B.32
146-012520	MB	12	52	5401 ± 50	47.7 ± 0.3	24940 ± 229	648	460	455	0.99	...	B.33

Table 6.3 (cont'd)

UCAC4	Flags	N	$\overline{\text{S/N}}$	T_{eff} (K)	$v_r \sin(i)$ (km/s)	RV (m/s)	σ_{obs} (m/s)	σ_{meas} (m/s)	σ_{stel} (m/s)	P_v	Period (days)	Figure
147-012251	MB	11	69	6182^{+36}_{-29}	24.5 ± 0.2	24331 ± 195	519	326	404	1.00	...	B.34
147-012272	MB	11	76	6249 ± 47	22.1 ± 0.2	24747 ± 152	454	230	392	1.00	...	B.35
147-012231	NMB	8	19	5250^{+26}_{-22}	4.5 ± 0.4	15581 ± 149	435	59	431	1.00	...	B.36
146-012416	NMB	11	68	6118 ± 44	25.0 ± 0.2	27520 ± 127	398	251	309	1.00	...	B.37
146-012534	MB	12	45	5264 ± 19	29.8 ± 0.2	24480 ± 132	396	249	308	1.00	...	B.38
146-012369	NMB	11	32	5791 ± 64	7.2 ± 0.8	5191 ± 130	379	138	352	1.00	...	B.39
146-012602	MB	11	23	4900^{+18}_{-15}	14.8 ± 0.2	23787 ± 115	358	147	327	1.00	95.0	B.40
146-012421	M	11	25	5133 ± 25	18.0 ± 0.2	26057 ± 112	336	181	283	1.00	...	B.41
146-012444	M	11	27	4974^{+18}_{-13}	5.0 ± 0.2	25696 ± 95	282	65	275	1.00	...	B.42
147-012463	M	12	68	6127^{+35}_{-30}	$20.9^{+0.2}_{-0.1}$	24565 ± 98	276	192	197	0.98	...	B.43
147-012166	M	12	27	4817 ± 18	5.4 ± 0.2	24584 ± 72	260	70	251	1.00	...	B.44
147-012503	M	12	61	6097^{+35}_{-27}	18.1 ± 0.2	24371 ± 91	260	166	200	0.99	...	B.45
147-012380	NM	11	27	5030^{+18}_{-14}	3.2 ± 0.2	2714 ± 78	254	53	248	1.00	...	B.46
147-012407	M	11	39	5181^{+18}_{-13}	7.3 ± 0.2	22685 ± 69	225	70	214	1.00	...	B.47
147-012446	M	11	44	5154^{+18}_{-16}	6.3 ± 0.2	23504 ± 68	208	61	199	1.00	...	B.48
147-012375	M	12	30	4883 ± 25	10.7 ± 0.2	25355 ± 61	207	99	182	1.00	...	B.49
146-012368	NM	12	39	5609 ± 25	6.5 ± 0.2	22379 ± 56	186	91	162	1.00	...	B.50
147-012307	M	11	30	5064^{+18}_{-14}	6.0 ± 0.2	24607 ± 60	180	67	167	1.00	...	B.51
146-012532	M	11	28	4979^{+18}_{-14}	4.7 ± 0.2	24935 ± 57	178	60	167	1.00	2.2	B.52
147-012156	NM	6	13	5125^{+24}_{-19}	4.9 ± 0.5	17041 ± 80	170	95	141	0.99	...	B.53
147-012460	NM	12	40	5163^{+17}_{-15}	7.3 ± 0.1	22417 ± 54	166	68	152	1.00	...	B.54
147-012428	NM	12	34	5240 ± 18	2.9 ± 0.2	74928 ± 49	153	58	142	1.00	...	B.55
146-012330	M	9	24	5182^{+20}_{-15}	6.4 ± 0.2	24284 ± 51	145	72	125	1.00	5.8	B.56
146-012470	M	11	37	5429^{+22}_{-19}	3.9 ± 0.1	23245 ± 47	140	57	128	1.00	...	B.57
146-012487	NM	10	34	5058^{+19}_{-14}	3.7 ± 0.3	-1191 ± 44	136	55	124	1.00	...	B.58
146-012374	M	12	46	5631 ± 25	6.0 ± 0.1	23340 ± 40	133	72	112	0.99	...	B.59
147-012349	M	11	39	5285^{+18}_{-13}	4.6 ± 0.2	25375 ± 39	132	55	120	1.00	...	B.60
146-012681	M	10	36	5005 ± 20	5.9 ± 0.2	24628 ± 43	126	75	101	0.97	...	B.61
147-012400	NM	12	46	5040^{+17}_{-13}	2.7 ± 0.1	97180 ± 36	125	45	116	1.00	...	B.62
146-012635	M	11	37	4862^{+18}_{-13}	5.6 ± 0.2	22942 ± 37	122	56	109	1.00	...	B.63
146-012496	NM	5	19	5111 ± 33	2.9 ± 0.6	20 ± 50	108	71	81	1.00	...	B.64
147-012199	NM	12	59	5067^{+17}_{-13}	2.7 ± 0.1	89852 ± 30	101	42	92	1.00	1.6	B.65
146-012372	NM	11	37	5194^{+18}_{-16}	3.3 ± 0.2	77675 ± 34	97	56	80	0.98	...	B.66

Table 6.3 (cont'd)

UCAC4	Flags	N	$\overline{S/N}$	T_{eff} (K)	$v_r \sin(i)$ (km/s)	RV (m/s)	σ_{obs} (m/s)	σ_{meas} (m/s)	σ_{stel} (m/s)	Period P_v	Period (days)	Figure

Note. — RV Variables in the NGC 2516 field. The period is given for stars having a more than six epochs and a peak (aside from the alias seen at ∼1 day) exceeding 95% significance. Derived values used our mean jitter level of 138 m/s for members and 58 m/s for non-members.

Table 6.4. Variables in NGC 2422

UCAC4	Flags	N	$\overline{S/N}$	T_{eff} (K)	$v_r \sin(i)$ (km/s)	RV (m/s)	σ_{obs} (m/s)	σ_{meas} (m/s)	σ_{stel} (m/s)	P_v	Period (days)	Figure
378-036252	PMSB2	10	156	6324 ± 73	9.8 ± 0.3	47929 ± 12207	38107	95	38107	1.00	7.3	B.67
377-035049	MSB2	10	24	5112 ± 47	6.8 ± 1.7	37337 ± 7180	19124	117	19124	1.00	10.1	B.68
378-036176	NMSB2	10	122	6102 ± 148	9.1 ± 1.2	4337 ± 4762	14124	110	14123	1.00	1.3	B.69
379-035886	NMSB2	7	15	4999 ± 44	9.2 ± 4.4	26035 ± 3938	11504	190	11502	1.00	...	B.70
379-035649	PMB	10	60	5648^{+23}_{-21}	4.4 ± 0.1	38661 ± 2646	8366	41	8366	1.00	15.4	B.71
379-036197	NMB	10	110	6299^{+38}_{-30}	6.6 ± 0.2	11379 ± 2426	7216	59	7215	1.00	160.8	B.72
379-035982	MB	8	42	4890^{+21}_{-16}	14.1 ± 3.5	36530 ± 2159	5799	120	5798	1.00	2.0	B.73
378-036328	MB	10	116	6138^{+38}_{-30}	7.9 ± 0.2	36928 ± 1520	5051	69	5050	1.00	27.7	B.74
379-035884	NMB	10	124	6846^{+52}_{-40}	19.0 ± 0.3	59672 ± 1476	4667	235	4661	1.00	559.4	B.75
378-036136	MB	10	27	5586 ± 41	9.0 ± 0.2	35631 ± 1181	3506	108	3505	1.00	543.7	B.76
377-034854	NMB	10	94	6543 ± 105	38.3 ± 1.0	24943 ± 932	2713	1020	2514	1.00	55.2	B.77
379-036066	PMB	8	88	5957 ± 28	21.6 ± 0.2	38029 ± 778	2125	198	2116	1.00	...	B.78
378-036422	NMB	10	67	5310 ± 23	10.9 ± 0.2	43789 ± 633	1821	82	1819	1.00	59.8	B.79
379-036005	PMB	10	86	6155^{+38}_{-30}	19.1 ± 0.8	38391 ± 426	1386	207	1371	1.00	...	B.80
379-036194	NMB	9	28	5425 ± 29	4.1 ± 0.2	106551 ± 465	1314	66	1312	1.00	...	B.81
378-036137	NMB	10	81	5503 ± 24	3.0 ± 0.2	119993 ± 361	1123	49	1122	1.00	230.3	B.82
378-036814	MB	10	49	5221^{+19}_{-15}	6.9 ± 0.2	36322 ± 335	1023	68	1021	1.00	67.9	B.83
377-035019	NMB	10	48	4555^{+19}_{-14}	35.2 ± 0.6	32857 ± 261	805	238	769	1.00	...	B.84
378-036277	NMB	10	61	5382^{+23}_{-20}	3.4 ± 0.1	27815 ± 229	721	38	720	1.00	1286.7	B.85
378-036531	MB	10	73	5672^{+23}_{-20}	10.2 ± 0.1	37361 ± 199	635	78	630	1.00	...	B.86
379-035545	NMB	10	23	4980^{+19}_{-14}	4.3 ± 0.2	115336 ± 141	389	64	384	1.00	...	B.87
379-035711	MB	10	38	4656^{+19}_{-14}	27.5 ± 0.3	35190 ± 131	378	184	330	1.00	...	B.88
377-034937	NM	10	75	6563^{+38}_{-30}	17.0 ± 0.2	18602 ± 103	296	139	261	1.00	...	B.89
377-035026	M	10	92	6072^{+23}_{-20}	14.5 ± 0.1	36139 ± 82	252	110	227	0.99	...	B.90
377-034926	NM	10	34	5214 ± 24	4.1 ± 0.2	98342 ± 77	241	55	234	1.00	...	B.91
378-036663	NM	9	30	5397 ± 27	3.9 ± 0.3	79984 ± 86	231	65	222	1.00	...	B.92
378-036905	M	9	31	4761^{+20}_{-15}	3.6 ± 0.3	35560 ± 75	215	47	210	0.99	...	B.93
378-036547	NM	9	17	4800 ± 21	5.1 ± 0.6	19528 ± 75	210	94	188	1.00	...	B.94
378-036894	M	10	36	5026^{+19}_{-17}	8.1 ± 0.2	36279 ± 66	201	69	189	0.98	...	B.95
377-034990	NM	10	25	5230 ± 40	4.2 ± 0.2	105039 ± 58	192	69	179	1.00	...	B.96
378-036447	NM	10	36	4864^{+19}_{-14}	6.4 ± 0.2	38416 ± 66	186	60	176	1.00	...	B.97
378-036274	NM	10	21	4852^{+19}_{-17}	3.5 ± 0.3	14484 ± 58	160	59	149	1.00	...	B.98
377-034927	NM	10	37	4773^{+19}_{-14}	3.3 ± 0.2	6905 ± 52	159	46	153	1.00	...	B.99

Table 6.4 (cont'd)

UCAC4	Flags	N	$\overline{S/N}$	T_{eff} (K)	$v_r \sin(i)$ (km/s)	RV (m/s)	σ_{obs} (m/s)	σ_{meas} (m/s)	σ_{stel} (m/s)	P_v	Period (days)	Figure
377-035048	NM	6	27	5125^{+24}_{-21}	3.2 ± 0.4	45989 ± 65	150	68	134	1.00	...	B.100
379-035798	NM	10	38	4839^{+19}_{-14}	3.9 ± 0.2	102809 ± 44	148	42	142	1.00	2.9	B.101
378-036680	NM	10	51	5472^{+23}_{-20}	7.1 ± 0.1	10075 ± 53	145	69	128	1.00	...	B.102
378-036662	NM	9	21	4857^{+20}_{-15}	3.4 ± 0.2	119830 ± 52	145	57	133	1.00	...	B.103
379-036032	NM	7	15	5776 ± 54	3.1 ± 0.5	8763 ± 64	142	79	118	0.98	4.1	B.104
378-036665	NM	10	28	5303 ± 29	4.8 ± 0.2	109015 ± 47	142	70	124	1.00	...	B.105
378-036349	NM	10	38	4806^{+19}_{-14}	3.9 ± 0.2	-3348 ± 51	137	48	128	1.00	...	B.106
377-034915	NM	9	27	4880^{+20}_{-17}	2.7 ± 0.3	18566 ± 51	136	60	122	1.00	...	B.107
378-036777	NM	9	26	5143^{+20}_{-15}	3.4 ± 0.2	72053 ± 44	135	46	127	1.00	4.5	B.108
378-037002	NM	9	22	5288^{+25}_{-22}	3.7 ± 0.3	106495 ± 45	128	60	113	1.00	...	B.109
378-036376	NM	10	42	5468^{+23}_{-20}	3.7 ± 0.2	51164 ± 43	126	37	121	1.00	20.5	B.110
378-036080	NM	10	59	5784 ± 28	3.3 ± 0.2	20198 ± 48	126	76	101	0.96	27.5	B.111
378-036806	NM	9	27	5420 ± 27	4.2 ± 0.4	102882 ± 47	125	77	98	0.96	...	B.112
378-036256	NM	10	31	5002^{+19}_{-17}	3.4 ± 0.3	31331 ± 41	116	52	103	1.00	1.4	B.113
378-036312	NM	10	41	5289^{+23}_{-20}	3.5 ± 0.2	53252 ± 37	110	42	102	1.00	...	B.114
379-035569	NM	10	35	5064^{+19}_{-14}	3.0 ± 0.4	-23236 ± 36	103	50	90	0.98	...	B.115

Note. — RV Variables in the NGC 2422 field. The period is given for stars having a more than six epochs and a peak (aside from the alias seen at ∼1 day) exceeding 95% significance. Derived values used our mean jitter level of 138 m/s for members and 58 m/s for non-members.

CHAPTER VII

Conclusion

7.1 Introduction

In the preceding chapters I presented my role in the design and construction of the Michigan/Magellan Fiber System and described the search for hot Jupiters in open clusters I have begun using its unique capabilities. Chapter II both presented the M2FS Fiber Polisher—a robotic tool I created to prepare the ends of the M2FS fiber-optic cables—and described the hardware, electronics, and performance of the M2FS Fiber Slit Mechanism, a key component of M2FS that nearly triples the achievable resolving power and enables new science programs with the instrument. In Chapter III I explained the control architecture and software I created to convert M2FS from a manually configured, relatively fixed purpose instrument to one capable of executing a wide range of concurrent and intermingled projects.

The remaining chapters then switched focus and described the development of and first results from a multiplexed spectroscopic survey of Sun-like stars the the open clusters NGC 2516 and NGC 2422. Chapter IV described in detail the cluster and stellar target selection, observational dataset, and analysis methodology, showing that M2FS can measure RVs for up to 128 Sun-like simultaneously with a precision of 25–60 m/s and stellar parameters precise at the 30 K, 0.02 dex, and 0.3 km/s level in T_{eff}, [Fe/H] and [α/Fe], and $v_r \sin(i)$. Chapters V and VI then reported

the first results of this project, covering spectroscopic properties, aggregate cluster parameters, and membership results in Chapter V followed by consideration of stellar jitter and RV variability in Chapter VI.

I reported new determinations of RVs, [Fe/H] and [α/Fe], and $v_r \sin(i)$ for the 126 and 125 F5–K5 stars surveyed in the core 0.5° fields of NGC 2516 and NGC 2422 along with estimates for total cluster binary fractions of 100^{+0}_{-15}% and 62 ± 16%. Of the surveyed stars, 81 and 57 proved to be RV members with 12 of our candidate members passing our RV membership test in NGC 2422. I reported identification of 52 large-amplitude ($\sigma_{stel} \geq 300$ m/s, c.f. §5.3.2) binaries, including the discovery of 45 new binaries (17 NGC 2516, 11 NGC 2422, 17 non-member) and 8 newly discovered SB2s. The sample of which is 99% complete within our fields for P $\lesssim$ 8 yr. Our dataset was sufficient to identify candidate periods for 38 of these binaries, values for which are given in Tables 6.3 and Table 6.4. After determining and accounting for an average stellar jitter of 74 m/s in NGC 2516 and 138 m/s in NGC 2422, I reported the identification of 53 statistically significant low-amplitude RV variables, two of which were members in NGC 2516. Nine of these low-amplitude RV variables exhibited at least 95% significant Lomb-Scargle periodogram peaks and 8 of which had periods and RV amplitudes consistent with a possible planetary companion and merit prompt follow-up observations. I now close with a review of M2FS' status and early science results and then turn to consider future prospects for the exoplanet search capabilities we have demonstrated.

7.2 M2FS: Present and Future

7.2.1 M2FS Today

The enhancements I described in Chapters II and III have proven broadly valuable to the astronomical community. In the first year alone, M2FS was used for studies

ranging from the far extra-galactic (searches for young galaxies at Z of 3–4, Blanc et al., 2016), in through the Galactic neighborhood (dwarf galaxy chemodynamics, Walker et al., 2015a,c), to the nearby (kinematics of young stars, Kounkel et al., 2016; stellar accretion disks, Briceño et al., 2016; and exoplanet searches, this work) Since commissioning in August 2013, M2FS has obtained data that has led to eight submitted or published papers, with at least another five in preparation and seen ∼90 nights of allocated time with an open shutter fraction of ∼75% (excluding weather). The following paragraphs describe two such projects that have especially benefited from M2FS's unique capabilities.

The first of these, published in Johnson et al. (2015a,b) focused on the accurate measurement of chemical abundances of stars in globular clusters. Their work in particular has benefitted from the slit flexibility by enabling them to, in a single night and with minimal down time for instrument reconfiguration, observe both bright targets at high resolving power (narrow slit) and faint targets at lower resolving power (wide slit). A similar project not using M2FS would have required time with one or more telescope/instrument combinations. Additionally, the M2FS fiber packing density allowed the authors to probe much closer and with higher efficiency to the dense cores of of their target globular clusters than is possible with any other multi-object spectrograph.

Another example is the work published in Roederer et al. (2015). Here the authors used M2FS to study the abundance patterns of heavy elements in globular clusters. Their feedback has indicated they find M2FS ideal for such studies because of (1) the large multiplexing capability of M2FS, which enables the study of many stars per cluster (∼50/setup); (2) the flexibility of the order-selecting filters, which enables optimizing the wavelength range for the absorption under study, and (3) the fiber slit mechanism, which allow them to optimize the HiRes echelle resolution for the targets of interest. As they aim to detect and measure dozens of absorption lines

associated with neutral or ionized species of elements heavier than the iron-group (atomic number > 30) they require the ability to resolve lines that are often weak and blended at resolving powers below R$\sim$35,000. These capabilities are opening new windows to study the (in)homogeneity of heavy elements in globular clusters, which gives new insights into the formation and evolution of these systems.

7.2.2 Future Plans

Near Term We have started tests for an improved M2FS flat field system and to finish the incomplete Fiber Locator System (FLS). M2FS presently uses the 10 W quartz-halogen bulb in MCal to produce trace-flats for calibration. This system works well for LoRes/MedRes trace flats and reasonably well for HiRes observations at redder wavelengths and lower S/N and resolving power. Projects requiring high S/N, high-resolution spectra such as the work described in this thesis require exceptionally long quartz exposures: a 10 minute exposure yields flats with per-pixel S/N$\sim$100. We are presently investigating two prototypes to alleviate this issue. The first consists of an acrylic diffuser added to the top of MCal and illuminated by a range of LEDs covering the 370–950 nm range. Initial tests show this system would enable 1–10 s trace flats in any M2FS configuration, but would require careful attention to relative LED illumination levels as the system is quite capable of saturating the CCDs. LoRes flats would require fitting with a rather high ($\gtrsim 10^{\text{th}}$) order polynomial to account for the broad Gaussian emission of the LEDs and regardless of observing mode these flats would not be suitable to estimate the instrument blaze function or any low-order inhomogeneities across the CCD chips. We are also considering the introduction of a small number of electroluminescent sheets within the MSpec optical train each equipped with a filter. These sheets would very nearly uniformly illuminate the M2FS CCDs and offer the ability to take true CCD flats, however they would not illuminate the pixels with identical wavelengths seen in observations (as a trace flat does); their

introduction also presents a number of mechanical challenges for integration into the MSpec optical train.

The M2FS Fiber Locator System (FLS) is designed to identify which fibers have been inserted into which holes on the plug plate, allowing confirmation that each fiber is in the correct hole and eliminating (or at least identifying) our ∼1 in 500 fiber positioning error rate. Our initial design for the FLS, intended to be a part of M2FS at first light, proved too complicated and was deferred for time. We have begun work on a simpler system that works by back-illuminating the fibers from MSpec and imaging the inner surface of the plug plate from a camera located in MCal.

Long Term We have carried out preliminary design work for the addition of a suite of M2FS integral field units (IFUs). These IFUs would offer pitches of ∼0.6, 1.25, and 2.5 arcseconds employing between ∼250–600 fibers with fields of 15–40 arcseconds and would, for instance, enable full spectroscopic investigation of lensed galaxies or comprehensive investigation of the chemodynamics of stars and gas in dwarf irregular galaxies. Aside from the construction of the IFUs themselves, this system would add two new electro-mechaincal systems. The would be a controller for the trombone-style atmospheric dispersion corrector that would be added to MWFC to support the IFUs to zenith angles of 50–60°. The second would consist of a selector system integrated into the IFU fiber shoes allowing M2FS to switch between each of the units on the fly.

7.3 An Expanded Survey

In Chapter IV I presented our program to use the Michigan/Magellan Fiber System to obtain multiplexed spectroscopy of solar analog stars in nearby (< 1 kpc) open clusters with the intent of identifying exoplanet host stars for subsequent followup. Our technique uses telluric lines in the 7230 Å region as a wavelength reference and

is presently capable of measuring RVs with a precision of 30–60 m/s, depending on S/N. We also obtain precise and accurate measurements of T_{eff}, [Fe/H], [α/Fe], and $v_r \sin(i)$ for all of our target stars, thereby enabling detailed characterization of the cluster environment. Chapters V and VI then presented the first findings (e.g. stellar properties, cluster binarity, stellar jitter) from our program for targets in NGC 2516 and NGC 2422 and identified a number of candidate exoplanet hosts.

Given M2FS's unique ability to efficiently determine stellar properties and precision RVs, here I briefly summarize the broader scientific impact this instrument could have for both finding exoplanets in open clusters and improving our understanding of the stars in these clusters.

7.3.1 M2FS as a Tool for Finding Planets in Open Clusters

Though once unexpected, it is now clear that a great many hot-gas giants exist. Assuming 1.2% of F5–K5 stars in open clusters harbor hot gas planets (P $<$ 10 days, $M \sin(i) > 0.1$ M_{Jup}, Wright et al., 2012; Meibom et al., 2013) and given our achieved precision we can predict the limits of our technique. For example, we expect M2FS will be capable of attaining a S/N 25 spectrum of a K5V star at a DM of 9.5 in 4 hours (effectively 2 minutes per star). This would be sufficient for an RV precision of $\sim$55 m/s, with brighter members increasingly limited by the systematics in our analysis. In this hypothetical cluster we would then be sensitive to $\sim$75% of known hot gas giants. Figure 7.1 shows our anticipated RV measurement precision as a function of distance modulus using the new filter. This implies we could reasonably expect one Hot-Jupiter per M2FS pointing, provided targets are available for the majority of fibers.

Table 7.1 lists the eight nearby open clusters which matched the cluster selection criteria given in §4.2. From these clusters we can obtain $\sim$15 M2FS pointings and would expect about as many exoplanet candidates. We highlight that these clusters

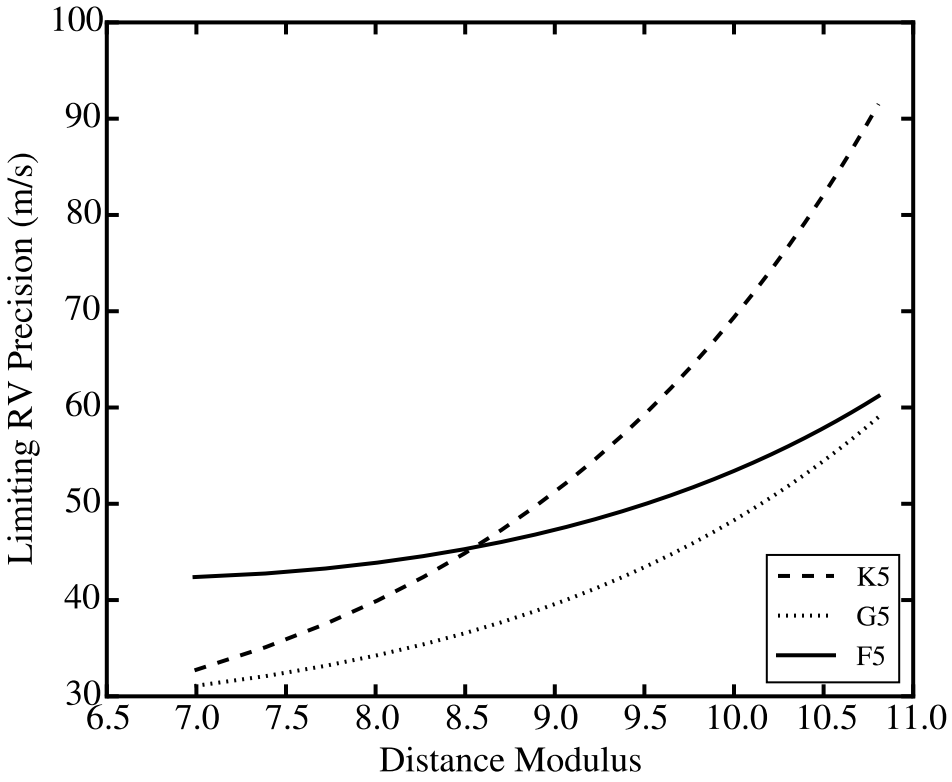

Figure 7.1: Our anticipated RV precision for quiescent, slowly-rotating (< 10 km/s) K5, G5, and F5 stars as a function of distance modulus after 2.5 hours observing in one arc second seeing with M2FS.

span range of ages and are thus well suited to help build a sample of exoplanets that addresses the formation and migration issues presented in Chapter I.

This program would also well characterize stellar jitter as a function of age. This issue is not yet well constrained (c.f. Mahmud et al., 2011; Lagrange et al., 2013, and §6.2): the present state of our knowledge was largely summarized in Figure 6.4, which showed the stellar jitter as a function of age for a number of younger stars, clusters, and associations. The clusters in Table 7.1 will further probe the younger ages ($<$ 200 Myr) where present data does not offer a clear picture, help fill in the gap between 200–600 Myr, and extend the range to just shy of 1 Gyr. Extant data is also far from homogenous: It is a mix of both optical and infrared spectroscopy for single stars, associations, and clusters. By surveying a large number of stars in clusters over a range of ages we can well constrain the evolution of stellar jitter with age and would, in conjunction with e.g. the chromospheric activity-jitter relation of Hillenbrand et al. (2015), allow for a definitive analysis of jitter, age, and activity indices.

We note that M2FS's strength is in identification: though the ability to survey large numbers of stars at this precision is unmatched, we suggest that followup of promising candidates is better suited to traditional monitoring programs.

7.3.2 M2FS as a Tool for Studying Open Cluster Stellar Populations

The success of any large scale RV survey of open clusters for planets depends critically on having a carefully vetted sample to survey. M2FS is poised to do this. First, precision RVs will help confirm membership, especially when combined with GAIA proper motions. Second, precision RVs can identify SBs, that are typically poor targets for exoplanet searches. Finally, the high dispersion spectra allow measures of $v_r \sin(i)$, T_{eff}, and metallicity, with the latter two yielding stellar masses from evolutionary models. When coupled with photometric periods determined with LSST,

Table 7.1. Current and Future Target Clusters

Cluster	Messier	Age (Myr)	Distance (pc)	R_{cen} (deg)	[Fe/H] (dex)	N	$N_{Targeted}$
NGC 2516	...	141	346	0.4	−0.18	330	126 (12); 128 (1)
NGC 2422	M 47	72	491	0.3	+0.02	160	125 (10)
NGC 2548	...	520	790	1.1	+0.08	125	128 (2)
IC 4725	M 25	93	560	0.5	−0.30	100	...
NGC 2546	...	140	930	0.8	+0.12	200	...
NGC 6475	M 7	180	300	0.8	+0.14	150	...
NGC 6494	...	330	650	0.5	+0.09	200	...
NGC 5822	...	900	800	0.5	−0.02	500	...

Note. — Here we list the eight clusters suitable for survey with M2FS. R_{cen} refers to the approximate half-light radius of the cluster, while N is the approximate number of members available near the cluster center. $N_{Targeted}$ reports how many stars have already been observed with the number of epochs obtained in parentheses. We have already begun expanding our sample to NGC 2548 and a second pointing in NGC 2516.

we could even determine stellar inclinations and identify edge-on systems. The flexible nature of M2FS also means that we could also obtain spectra of the Ca II H and K region for all of our targets with relatively a modest overhead ($\sim$20 min total for targets in NGC 2516 and NGC 2422), further helping calibrate stellar ages.

A number of recent papers have also highlighted the importance both stellar multiplicity and metallicity play in star formation and have drawn attention to various gaps in current simulations of cluster evolution (Paunzen et al., 2010; Geller et al., 2010; Duchêne et al., 2007). Our stellar properties directly address such gaps by characterizing the cluster chemical environment while our RVs allow robust identification of binaries and brown dwarfs (constrained by our time baseline), characterizing the kinematic environment. Such a dataset can contribute to the initial conditions used in dynamical simulations of cluster formation.

We also note there is an absence of precision internal kinematics for open clusters. This dataset is useful to study the internal dynamics of open clusters at the 10 m/s level. With an anticipated precision of better than 10 μas/yr ($\sim$ 20 m/s at 500 pc) (Lindegren, 2010; Lindegren et al., 2012), once GAIA data is available for our targets the combined dataset will offer an unprecedented 3D kinematic picture of the Sun-like stars within open clusters, providing a useful tool to study internal kinematics.

APPENDICES

APPENDIX A

Properties of Targets in NGC 2516 and NGC 2422

Table A.1. Properties of Targets in NGC 2516

UCAC4	J01	RA	Dec.	V	B−V	N	$\overline{S/N}$	T_{eff} (K)	log(g) (dex)	[Fe/H] (dex)	[α/Fe] (dex)	$v_r \sin(i)$ (km/s)	$\overline{RV}$ (m/s)	σ_{obs} (m/s)	σ_{meas} (m/s)	P_{mem}	P_v	$P_{v,jitter}$	Note
147-012265	7864	7:58:02.39	-60:46:47.30	12.1	0.60	11	115	6447 ± 50	4.4	-0.25 ± 0.04	$+0.04^{+0.01}_{-0.02}$	16.9 ± 0.5	$+37677 \pm 11052$	35789	196	0	100	100	PMSB2V
147-012424	11307	7:59:34.11	-60:42:58.33	13.7	0.74	12	54	6116^{+35}_{-33}	4.5	-0.09 ± 0.02	$+0.03^{+0.01}_{-0.02}$	6.4 ± 0.2	$+15450 \pm 6734$	23160	75	0	100	100	PMSB2V
146-012601	11233	7:59:32.10	-60:48:45.05	13.9	0.83	10	39	5239 ± 19	4.6	-0.29 ± 0.02	$+0.12 \pm 0.01$	16.1 ± 0.2	$+31158 \pm 6325$	19304	159	0	100	100	PMBV
147-012249	7590	7:57:55.49	-60:43:20.76	14.0	0.88	12	51	5372^{+17}_{-13}	4.6	-0.14 ± 0.01	$+0.06 \pm 0.01$	6.7 ± 0.1	$+25997 \pm 4535$	16386	62	86	100	100	MBV
147-012499	12874	8:00:20.60	-60:42:37.53	13.5	0.93	12	51	5480 ± 79	4.5	-0.36 ± 0.10	$+0.06 \pm 0.01$	8.4 ± 1.3	$+18343 \pm 4125$	14814	87	0	100	100	PMSB2V
146-012500	8967	7:58:31.51	-60:53:10.22	14.8	1.00	11	27	5001 ± 30	4.6	-0.08 ± 0.02	$+0.08 \pm 0.03$	8.8 ± 0.2	$+16724 \pm 4637$	12569	267	0	100	100	PMBV
146-012622	11713	7:59:47.44	-60:49:22.95	12.4	0.70	11	59	6234 ± 207	4.5	-0.57 ± 0.11	$+0.10 \pm 0.04$	9.2 ± 0.3	-1954 ± 4049	11821	176	0	100	100	NMSB2V
146-012455	8192	7:58:11.24	-60:49:59.89	13.9	0.86	12	45	5430^{+21}_{-18}	4.6	-0.23 ± 0.01	$+0.05 \pm 0.01$	7.6 ± 0.1	$+28014 \pm 3450$	11231	74	0	100	100	PMBV
147-012487	12649	8:00:14.51	-60:45:15.40	12.4	0.59	12	85	6408^{+35}_{-28}	4.4	$-0.16^{+0.01}_{-0.02}$	$+0.02^{+0.01}_{-0.02}$	$10.4^{+0.2}_{-0.1}$	$+15591 \pm 2803$	9182	105	0	100	100	NMBV
148-012940	10736	7:59:17.05	-60:34:13.33	12.0	0.67	11	108	6063^{+22}_{-19}	4.5	$+0.05^{+0.01}_{-0.02}$	$+0.03^{+0.01}_{-0.02}$	6.0 ± 0.1	$+30821 \pm 2475$	8563	47	0	100	100	PMBV
146-012358	6465	7:57:25.59	-60:56:51.02	15.1	1.26	11	29	4833 ± 18	4.6	$+0.22 \pm 0.03$	$+0.10 \pm 0.02$	4.5 ± 0.2	$+69487 \pm 3072$	8545	60	0	100	100	NMBV
146-012557	10152	7:59:00.75	-60:55:48.91	13.0	0.71	12	74	5731 ± 34	4.5	-0.59 ± 0.05	$+0.19 \pm 0.02$	4.9 ± 0.2	-30760 ± 2369	8502	68	0	100	100	NMBV
147-012308	8660	7:58:23.62	-60:37:22.02	12.4	0.57	11	93	6403^{+49}_{-45}	4.4	$+0.06 \pm 0.02$	-0.01 ± 0.02	37.8 ± 0.3	$+25169 \pm 2493$	8136	399	96	100	100	MBV
147-012432	11485	7:59:40.00	-60:42:31.21	14.8	1.05	11	39	5022 ± 19	4.6	-0.15 ± 0.01	$+0.09 \pm 0.02$	5.9 ± 0.2	$+26179 \pm 2333$	7340	60	78	100	100	MBV
147-012270	7959	7:58:05.14	-60:46:11.90	14.0	1.01	7	46	5117 ± 60	4.6	-0.20 ± 0.03	$+0.06 \pm 0.02$	7.5 ± 0.6	$+16154 \pm 2929$	7084	80	0	100	100	NMBV
147-012164	6029	7:57:14.19	-60:40:52.50	12.2	0.67	12	97	6070 ± 46	4.5	-0.01 ± 0.02	-0.04 ± 0.01	17.0 ± 1.9	$+23279 \pm 1930$	6851	163	87	100	100	MBV
147-012262	7788	7:58:00.45	-60:41:19.67	14.8	1.11	11	25	4945 ± 19	4.6	-0.21 ± 0.02	$+0.05 \pm 0.01$	4.6 ± 0.3	$+23031 \pm 2187$	6679	84	76	100	100	MBV
148-012906	9486	7:58:43.75	-60:32:56.75	12.6	0.76	11	100	5631^{+22}_{-19}	4.5	$-0.35^{+0.01}_{-0.02}$	$+0.04^{+0.01}_{-0.02}$	15.3 ± 1.0	$+26429 \pm 1406$	4613	115	61	100	100	MBV
147-012376	10046	7:58:57.55	-60:43:00.96	14.8	0.99	5	25	5042 ± 116	4.6	-0.21 ± 0.05	$+0.04 \pm 0.07$	76.7 ± 2.5	$+25225 \pm 2351$	4591	1322	96	100	100	MBV
147-012474	12362	8:00:06.35	-60:42:33.32	14.4	1.09	12	37	5111 ± 20	4.6	$+0.06 \pm 0.01$	$+0.04 \pm 0.02$	3.7 ± 0.1	-500 ± 975	3353	43	0	100	100	NMBV

Table A.1 (cont'd)

UCAC4	J01	RA	Dec.	V	B−V	N	$\overline{\mathrm{S/N}}$	T_{eff} (K)	log(g) (dex)	[Fe/H] (dex)	[α/Fe] (dex)	$v_r \sin(i)$ (km/s)	$\overline{RV}$ (m/s)	σ_{obs} (m/s)	σ_{meas} (m/s)	P_{mem}	P_v	$P_{v,jitter}$	Note
147-012175	6268	7:57:20.82	-60:44:03.48	14.9	1.07	12	26	4877^{+17}_{-13}	4.6	-0.02 ± 0.02	$+0.08 \pm 0.02$	10.8 ± 0.2	$+23748 \pm 981$	3231	108	95	100	100	MBV
148-012943	10817	7:59:19.74	-60:34:43.67	11.9	0.53	12	122	6412 ± 48	4.4	$+0.04^{+0.01}_{-0.02}$	$+0.01 \pm 0.04$	95.1 ± 1.1	$+22513 \pm 1032$	3135	1326	34	100	100	PMBV
147-012290	8262	7:58:12.89	-60:38:52.80	14.2	0.95	11	47	5160^{+18}_{-13}	4.6	$+0.07 \pm 0.01$	$+0.08 \pm 0.02$	3.4 ± 0.2	$+12026 \pm 942$	3126	42	0	100	100	NMBV
147-012280	8099	7:58:08.85	-60:44:40.22	12.2	0.56	11	106	6553 ± 79	4.4	-0.00 ± 0.02	$+0.00 \pm 0.02$	69.9 ± 0.9	$+25578 \pm 978$	3111	1052	94	100	100	MBV
146-012365	6570	7:57:28.43	-60:51:29.42	13.4	0.74	12	52	5864^{+21}_{-18}	4.5	-0.08 ± 0.02	-0.03 ± 0.01	6.3 ± 0.1	$+22849 \pm 882$	2896	78	64	100	100	MBV
147-012220	7189	7:57:45.10	-60:47:53.02	11.8	0.50	12	91	6887 ± 80	4.4	-0.02 ± 0.02	$+0.05 \pm 0.02$	76.5 ± 1.1	$+20925 \pm 807$	2488	1306	0	100	100	NMBV
147-012205	6880	7:57:36.64	-60:42:16.76	13.3	0.81	12	73	5631^{+21}_{-18}	4.5	$+0.08 \pm 0.01$	$+0.05 \pm 0.01$	4.0 ± 0.1	$+14106 \pm 625$	1985	41	0	100	100	NMBV
147-012406	10863	7:59:21.34	-60:46:02.82	12.3	0.57	11	92	6645 ± 67	4.4	$+0.10 \pm 0.07$	$-0.05^{+0.01}_{-0.02}$	36.2 ± 0.7	$+21242 \pm 414$	1351	448	0	100	100	NMBV
146-012454	8172	7:58:10.72	-60:49:32.39	12.0	0.53	11	120	6834 ± 51	4.4	$+0.11 \pm 0.02$	$+0.05 \pm 0.03$	76.0 ± 0.8	$+20324 \pm 457$	1236	961	0	95	95	NV
146-012483	8645	7:58:23.39	-60:54:56.84	14.1	1.06	12	30	4899 ± 48	4.6	-0.09 ± 0.03	$+0.05 \pm 0.02$	44.7 ± 0.5	$+22790 \pm 367$	1191	498	60	100	100	MBV
147-012433	11549	7:59:42.13	-60:46:00.00	15.1	1.08	11	25	5126 ± 23	4.6	$+0.02 \pm 0.01$	$+0.06 \pm 0.01$	4.1 ± 0.3	$+25744 \pm 321$	999	64	92	100	100	MBV
146-012424	7743	7:57:59.32	-60:56:53.47	12.6	0.65	12	86	5934 ± 50	4.5	-0.32 ± 0.04	$+0.07 \pm 0.03$	20.6 ± 0.1	$+25703 \pm 302$	926	185	92	100	100	MBV
147-012302	8529	7:58:19.86	-60:41:58.19	12.3	0.58	11	98	6451^{+49}_{-45}	4.4	$+0.07 \pm 0.03$	$-0.04^{+0.01}_{-0.02}$	64.1 ± 0.4	$+22887 \pm 350$	866	830	67	75	74	NV
148-012916	9835	7:58:51.86	-60:35:20.21	14.8	0.99	12	33	5069 ± 51	4.6	-0.09 ± 0.02	$+0.03 \pm 0.02$	63.4 ± 0.7	$+24953 \pm 326$	855	780	97	85	85	NV
147-012306	8634	7:58:22.93	-60:40:20.41	14.5	0.94	11	37	5035 ± 23	4.6	-0.07 ± 0.02	$+0.08 \pm 0.02$	38.2 ± 0.3	$+26249 \pm 264$	793	382	74	100	100	MBV
146-012520	9465	7:58:43.26	-60:55:25.75	13.8	0.82	12	52	5401 ± 50	4.6	-0.14 ± 0.02	$+0.03 \pm 0.02$	47.7 ± 0.3	$+24940 \pm 229$	648	460	97	99	99	MBV
147-012251	7595	7:57:55.62	-60:40:39.27	12.6	0.60	11	69	6182^{+36}_{-29}	4.4	-0.07 ± 0.02	$-0.05^{+0.01}_{-0.02}$	24.5 ± 0.2	$+24331 \pm 195$	519	326	97	100	100	MBV
147-012271	7962	7:58:05.25	-60:47:40.30	12.0	0.54	11	110	6621 ± 59	4.4	$-0.02^{+0.01}_{-0.02}$	$+0.02 \pm 0.02$	39.9 ± 0.3	$+24031 \pm 205$	465	505	96	51	49	NV
147-012272	7967	7:58:05.30	-60:45:03.34	12.7	0.64	11	76	6249 ± 47	4.4	$+0.04 \pm 0.02$	$-0.06^{+0.01}_{-0.02}$	22.1 ± 0.2	$+24747 \pm 152$	454	230	97	100	100	MBV
147-012231	7322	7:57:48.14	-60:41:11.98	15.0	1.06	8	25	5250^{+26}_{-22}	4.6	$+0.18 \pm 0.02$	$+0.01 \pm 0.02$	4.5 ± 0.4	$+15581 \pm 149$	435	59	0	100	100	NMBV

Table A.1 (cont'd)

UCAC4	J01	RA	Dec.	V	B−V	N	$\overline{\mathrm{S/N}}$	T_{eff} (K)	log(g) (dex)	[Fe/H] (dex)	[α/Fe] (dex)	$v_r \sin(i)$ (km/s)	$\overline{RV}$ (m/s)	σ_{obs} (m/s)	σ_{meas} (m/s)	P_{mem}	P_v	$P_{v,jitter}$	Note
146-012416	7585	7:57:55.40	-60:48:27.19	12.9	0.72	11	70	6118 ± 44	4.5	-0.14 ± 0.05	-0.05 ± 0.02	25.0 ± 0.2	$+27520 \pm 127$	398	251	0	100	100	NMBV
146-012534	9676	7:58:48.05	-60:54:14.36	14.3	0.90	12	45	5264 ± 19	4.6	-0.14 ± 0.02	$+0.06 \pm 0.01$	29.8 ± 0.2	$+24480 \pm 132$	396	249	97	100	100	MBV
146-012369	6649	7:57:30.93	-60:48:31.74	14.0	0.82	11	33	5791 ± 64	4.5	-0.30 ± 0.05	$+0.01 \pm 0.03$	7.2 ± 0.8	$+5191 \pm 130$	379	138	0	100	100	NMBV
146-012602	11240	7:59:32.32	-60:58:45.94	15.0	1.05	11	24	4900^{+18}_{-15}	4.6	-0.04 ± 0.02	$+0.08 \pm 0.01$	14.8 ± 0.2	$+23787 \pm 115$	358	147	95	100	100	MBV
147-012171	6106	7:57:16.27	-60:47:13.56	12.0	0.54	12	106	6579^{+47}_{-24}	4.4	$-0.06^{+0.01}_{-0.02}$	$+0.02^{+0.01}_{-0.02}$	29.9 ± 0.3	$+24537 \pm 149$	350	371	97	55	51	NV
146-012421	7678	7:57:57.68	-60:53:38.94	14.4	0.93	11	27	5133 ± 25	4.6	-0.06 ± 0.02	$+0.05 \pm 0.02$	18.0 ± 0.2	$+26057 \pm 112$	336	181	83	100	100	MV
147-012351	9328	7:58:40.05	-60:41:42.97	12.2	0.56	11	97	6505^{+49}_{-38}	4.4	$+0.02 \pm 0.02$	$+0.03^{+0.01}_{-0.02}$	38.9 ± 0.3	$+23070 \pm 173$	331	463	78	17	16	NV
146-012444	8055	7:58:07.68	-60:50:01.94	15.0	1.08	11	28	4974^{+18}_{-13}	4.6	-0.06 ± 0.02	$+0.06 \pm 0.01$	5.0 ± 0.2	$+25696 \pm 95$	282	65	92	100	100	MV
147-012329	9054	7:58:33.39	-60:44:27.41	12.8	0.69	11	52	5889 ± 68	4.5	-0.24 ± 0.05	$+0.03 \pm 0.02$	24.3 ± 0.2	$+25273 \pm 112$	280	286	96	83	78	NV
147-012463	12216	8:00:02.65	-60:36:55.50	12.9	0.68	12	68	6127^{+35}_{-30}	4.5	$+0.06^{+0.01}_{-0.02}$	$-0.05^{+0.01}_{-0.02}$	$20.9^{+0.2}_{-0.1}$	$+24565 \pm 98$	276	192	97	99	98	MV
147-012166	6070	7:57:15.40	-60:38:53.38	15.0	1.07	12	27	4817 ± 18	4.6	-0.06 ± 0.03	$+0.07 \pm 0.01$	5.4 ± 0.2	$+24584 \pm 72$	260	70	97	100	100	MV
147-012503	13006	8:00:24.05	-60:42:03.69	12.8	0.66	12	61	6097^{+35}_{-27}	4.5	$+0.02^{+0.01}_{-0.02}$	$-0.06^{+0.01}_{-0.02}$	18.1 ± 0.2	$+24371 \pm 91$	260	166	97	100	99	MV
147-012380	10132	7:59:00.28	-60:46:42.37	14.8	1.16	11	29	5030^{+18}_{-14}	4.6	$+0.04 \pm 0.01$	$+0.03 \pm 0.02$	3.2 ± 0.2	$+2714 \pm 78$	254	53	0	100	100	NMV
147-012407	10871	7:59:21.55	-60:46:45.37	14.5	0.98	11	39	5181^{+18}_{-13}	4.6	-0.09 ± 0.01	$+0.07 \pm 0.01$	7.3 ± 0.2	$+22685 \pm 69$	225	70	50	100	100	MV
146-012334	6096	7:57:15.95	-60:54:51.67	12.1	0.52	12	84	6772 ± 65	4.4	-0.12 ± 0.03	$+0.06^{+0.01}_{-0.02}$	17.2 ± 0.3	$+10358 \pm 84$	217	194	0	83	77	NV
147-012446	11782	7:59:50.15	-60:43:34.21	14.6	1.01	11	44	5154^{+18}_{-16}	4.6	-0.19 ± 0.03	$+0.07 \pm 0.01$	6.3 ± 0.2	$+23504 \pm 68$	208	61	92	100	100	MV
147-012375	10040	7:58:57.22	-60:36:12.69	14.9	1.03	12	30	4883 ± 25	4.6	-0.05 ± 0.01	$+0.05 \pm 0.01$	10.7 ± 0.2	$+25355 \pm 61$	207	99	96	100	100	MV
147-012335	9164	7:58:35.72	-60:46:52.50	13.3	0.75	12	52	5985 ± 66	4.5	-0.13 ± 0.05	-0.05 ± 0.02	19.4 ± 0.2	$+23333 \pm 83$	206	209	88	77	65	NV,U
146-012368	6605	7:57:29.37	-60:50:10.36	13.6	0.81	12	39	5609 ± 25	4.5	-0.17 ± 0.01	-0.01 ± 0.02	6.5 ± 0.2	$+22379 \pm 56$	186	91	23	100	100	NMV
147-012307	8654	7:58:23.50	-60:46:49.70	14.8	1.05	11	30	5064^{+18}_{-14}	4.6	-0.05 ± 0.01	$+0.08 \pm 0.01$	6.0 ± 0.2	$+24607 \pm 60$	180	67	97	100	100	MV

Table A.1 (cont'd)

UCAC4	J01	RA	Dec.	V	B−V	N	$\overline{\mathrm{S/N}}$	T_{eff} (K)	log(g) (dex)	[Fe/H] (dex)	[α/Fe] (dex)	$v_r \sin(i)$ (km/s)	$\overline{RV}$ (m/s)	σ_{obs} (m/s)	σ_{meas} (m/s)	P_{mem}	P_v	$P_{v,jitter}$	Note
147-012289	8261	7:58:12.86	-60:38:36.59	12.0	0.46	11	104	6508^{+49}_{-31}	4.4	-0.01 ± 0.02	$+0.03^{+0.01}_{-0.02}$	18.2 ± 0.3	$+24239 \pm 73$	179	184	97	62	51	NV
146-012532	9655	7:58:47.45	-60:55:24.35	14.8	1.03	11	30	4979^{+18}_{-14}	4.6	-0.06 ± 0.02	$+0.06 \pm 0.01$	4.7 ± 0.2	$+24935 \pm 57$	178	60	97	100	100	MV
147-012156	5877	7:57:10.35	-60:39:41.50	13.9	0.89	6	17	5125^{+24}_{-19}	4.6	-0.22 ± 0.03	$+0.09 \pm 0.02$	4.9 ± 0.5	$+17041 \pm 80$	170	95	0	100	99	NMV
147-012216	7104	7:57:42.71	-60:44:20.72	12.7	0.64	12	85	6173^{+35}_{-27}	4.4	$+0.02^{+0.01}_{-0.02}$	$-0.04^{+0.01}_{-0.02}$	$20.1^{+0.2}_{-0.1}$	$+25344 \pm 68$	169	180	96	56	41	NV
147-012460	12118	8:00:00.22	-60:40:08.28	14.3	0.93	12	40	5163^{+17}_{-15}	4.6	-0.15 ± 0.01	$+0.08 \pm 0.02$	7.3 ± 0.1	$+22417 \pm 54$	166	68	26	100	100	NMV
147-012428	11441	7:59:38.68	-60:37:48.42	14.6	0.94	12	34	5240 ± 18	4.6	-0.25 ± 0.02	$+0.23 \pm 0.01$	2.9 ± 0.2	$+74928 \pm 49$	153	58	0	100	100	NMV
147-012465	12235	8:00:03.04	-60:37:24.38	11.7	0.46	12	120	6698 ± 84	4.4	$-0.05^{+0.01}_{-0.02}$	$+0.04^{+0.01}_{-0.02}$	31.0 ± 0.3	$+25817 \pm 112$	146	366	90	0	0	NV
146-012330	5911	7:57:11.09	-60:48:15.55	14.6	1.02	9	28	5182^{+20}_{-15}	4.6	-0.05 ± 0.01	$+0.08 \pm 0.02$	6.4 ± 0.2	$+24284 \pm 51$	145	72	97	100	100	MV
146-012328	5901	7:57:10.83	-60:50:50.17	13.0	0.67	12	60	6143^{+35}_{-27}	4.5	$-0.03^{+0.01}_{-0.02}$	$-0.05^{+0.01}_{-0.02}$	$14.5^{+0.2}_{-0.1}$	$+24378 \pm 55$	142	136	97	76	51	NV
146-012470	8433	7:58:16.83	-60:54:52.58	14.0	0.96	11	38	5429^{+22}_{-19}	4.6	$-0.16^{+0.01}_{-0.02}$	$+0.05^{+0.01}_{-0.02}$	3.9 ± 0.1	$+23245 \pm 47$	140	57	86	100	100	MV
146-012509	9175	7:58:36.47	-60:50:18.36	11.7	0.59	11	118	6308^{+36}_{-29}	4.4	$+0.02^{+0.01}_{-0.02}$	$-0.04^{+0.01}_{-0.02}$	19.1 ± 0.5	$+25353 \pm 64$	138	172	96	29	20	NV
146-012487	8689	7:58:24.47	-60:54:34.27	13.9	0.97	10	37	5058^{+19}_{-14}	4.6	-0.16 ± 0.01	$+0.12 \pm 0.01$	3.7 ± 0.3	-1191 ± 44	136	55	0	100	100	NMV
146-012524	9513	7:58:44.17	-60:56:01.08	14.5	0.95	11	29	5179^{+18}_{-13}	4.6	-0.09 ± 0.02	$+0.09 \pm 0.02$	6.0 ± 0.2	$+24284 \pm 49$	134	70	97	100	96	NV
146-012374	6852	7:57:36.08	-60:48:12.73	13.7	0.81	12	46	5631 ± 25	4.5	-0.14 ± 0.02	$+0.02 \pm 0.01$	6.0 ± 0.1	$+23340 \pm 40$	133	72	88	100	99	MV
147-012349	9286	7:58:39.05	-60:45:21.76	14.2	0.93	11	39	5285^{+18}_{-13}	4.6	-0.14 ± 0.01	$+0.07 \pm 0.01$	4.6 ± 0.2	$+25375 \pm 39$	132	55	95	100	100	MV
147-012187	6452	7:57:25.21	-60:46:47.32	13.0	0.68	12	68	6047^{+21}_{-18}	4.5	-0.12 ± 0.02	-0.03 ± 0.01	9.9 ± 0.1	$+23917 \pm 42$	130	93	96	99	87	NV
145-012171	9459	7:58:42.99	-61:01:05.06	14.9	1.03	6	20	5245 ± 45	4.6	-0.28 ± 0.03	$+0.15 \pm 0.02$	5.5 ± 0.4	$+52825 \pm 62$	126	111	0	95	87	NV
146-012681	13349	8:00:35.53	-60:48:26.33	14.9	1.04	10	39	5005 ± 20	4.6	-0.19 ± 0.03	$+0.04 \pm 0.01$	5.9 ± 0.2	$+24628 \pm 43$	126	75	97	100	97	MV
147-012400	10735	7:59:17.02	-60:40:34.17	14.2	1.09	12	46	5040^{+17}_{-13}	4.6	-0.16 ± 0.01	$+0.22 \pm 0.01$	2.7 ± 0.1	$+97180 \pm 36$	125	45	0	100	100	NMV
146-012635	12134	8:00:00.49	-60:52:55.97	14.4	1.12	11	39	4862^{+18}_{-13}	4.6	-0.06 ± 0.01	$+0.05 \pm 0.01$	5.6 ± 0.2	$+22942 \pm 37$	122	56	72	100	100	MV

Table A.1 (cont'd)

UCAC4	J01	RA	Dec.	V	B−V	N	$\overline{\mathrm{S/N}}$	T_{eff} (K)	log(g) (dex)	[Fe/H] (dex)	[α/Fe] (dex)	$v_r \sin(i)$ (km/s)	$\overline{RV}$ (m/s)	σ_{obs} (m/s)	σ_{meas} (m/s)	P_{mem}	P_v	$P_{v,jitter}$	Note
147-012450	11867	7:59:52.62	-60:41:16.00	12.6	0.61	11	85	6281^{+36}_{-29}	4.4	$+0.00 \pm 0.02$	$-0.07^{+0.01}_{-0.02}$	23.2 ± 0.2	$+24519 \pm 76$	119	233	97	2	1	NV
147-012165	6049	7:57:14.75	-60:41:41.82	14.7	1.01	12	31	5093^{+17}_{-13}	4.6	-0.04 ± 0.01	$+0.09 \pm 0.02$	4.5 ± 0.2	$+25188 \pm 38$	110	61	96	100	86	NV
147-012423	11304	7:59:34.02	-60:45:18.42	14.3	0.93	12	42	5301^{+17}_{-13}	4.6	-0.06 ± 0.01	$+0.09 \pm 0.01$	4.3 ± 0.1	$+24029 \pm 36$	109	48	96	100	95	NV
146-012480	8584	7:58:21.62	-60:58:50.28	14.7	1.16	11	27	4759^{+18}_{-13}	4.6	-0.01 ± 0.02	$+0.05 \pm 0.01$	7.2 ± 0.3	$+24329 \pm 43$	109	84	97	99	69	NV
147-012304	8536	7:58:20.31	-60:41:39.79	12.9	0.66	11	83	6085^{+36}_{-29}	4.5	$-0.06^{+0.01}_{-0.02}$	$-0.04^{+0.01}_{-0.02}$	12.3 ± 0.2	$+25584 \pm 45$	109	102	94	79	42	NV
146-012496	8827	7:58:27.88	-60:57:22.31	14.3	1.00	5	22	5111 ± 33	4.6	$+0.08 \pm 0.02$	$+0.12 \pm 0.03$	2.9 ± 0.6	$+20 \pm 50$	108	71	0	100	100	NMV
147-012247	7553	7:57:54.50	-60:45:08.25	13.8	0.84	12	51	5513^{+21}_{-19}	4.5	-0.14 ± 0.01	$+0.05 \pm 0.02$	8.1 ± 0.1	$+24638 \pm 38$	105	72	97	100	71	NV
146-012418	7619	7:57:56.11	-60:54:59.05	14.3	0.94	12	30	5228 ± 19	4.6	-0.08 ± 0.01	$+0.08 \pm 0.01$	6.4 ± 0.1	$+24508 \pm 35$	105	71	97	100	78	NV
146-012583	10753	7:59:17.94	-60:49:00.58	13.7	0.80	10	48	5609 ± 24	4.5	-0.19 ± 0.05	-0.01 ± 0.02	10.2 ± 0.1	$+24422 \pm 40$	102	85	97	96	60	NV
147-012199	6705	7:57:32.20	-60:44:13.23	14.0	1.02	12	59	5067^{+17}_{-13}	4.6	-0.17 ± 0.01	$+0.18 \pm 0.02$	2.7 ± 0.1	$+89852 \pm 30$	101	42	0	100	100	NMV
146-012596	11031	7:59:26.15	-60:59:11.31	13.9	0.82	11	40	6277^{+36}_{-29}	4.5	-1.00 ± 0.30	$+0.28 \pm 0.02$	3.1 ± 0.3	$+335901 \pm 48$	100	137	0	29	18	NV
146-012372	6724	7:57:32.78	-60:53:49.04	14.0	1.04	11	39	5194^{+18}_{-16}	4.6	$+0.15 \pm 0.01$	$+0.03 \pm 0.01$	3.3 ± 0.2	$+77675 \pm 34$	97	56	0	100	98	NMV
148-012841	7941	7:58:04.70	-60:35:03.83	13.1	0.68	10	69	6034 ± 46	4.5	-0.02 ± 0.02	$-0.06^{+0.01}_{-0.02}$	16.2 ± 0.2	$+24565 \pm 56$	97	145	97	14	7	NV
147-012356	9446	7:58:42.56	-60:40:19.92	13.6	0.78	11	54	5594^{+22}_{-19}	4.5	$-0.16^{+0.01}_{-0.02}$	$+0.01^{+0.01}_{-0.02}$	9.2 ± 0.1	$+24866 \pm 34$	97	83	97	93	58	NV
147-012397	10605	7:59:13.40	-60:40:23.96	13.6	0.79	11	49	5722 ± 34	4.5	-0.08 ± 0.02	$-0.05^{+0.01}_{-0.02}$	10.9 ± 0.1	$+22578 \pm 43$	96	101	42	62	34	NV
147-012154	5862	7:57:09.97	-60:44:10.20	13.3	0.73	11	64	5930^{+22}_{-21}	4.5	-0.12 ± 0.02	$-0.04^{+0.01}_{-0.02}$	15.4 ± 0.1	$+25679 \pm 48$	96	133	93	18	8	NV
147-012317	8923	7:58:30.73	-60:46:01.05	14.0	1.03	11	51	5103^{+18}_{-13}	4.6	-0.04 ± 0.01	$+0.07 \pm 0.01$	7.6 ± 0.2	$+24433 \pm 34$	92	55	97	100	67	NV
146-012543	9852	7:58:52.31	-60:53:37.70	12.1	0.66	12	110	6038^{+21}_{-18}	4.5	-0.01 ± 0.01	-0.05 ± 0.01	11.0 ± 0.1	$+24501 \pm 33$	82	77	97	78	21	NV
146-012580	10723	7:59:16.66	-60:49:20.26	13.7	0.78	11	55	6189^{+36}_{-29}	4.5	-0.01 ± 0.02	-0.00 ± 0.02	7.2 ± 0.2	$+36232 \pm 33$	81	77	0	85	43	NV
146-012474	8465	7:58:18.13	-60:59:05.25	13.3	0.70	11	55	5736 ± 23	4.5	-0.48 ± 0.02	$+0.08^{+0.01}_{-0.02}$	3.9 ± 0.2	$+46326 \pm 32$	80	62	0	98	55	NV

Table A.1 (cont'd)

UCAC4	J01	RA	Dec.	V	B−V	N	$\overline{\mathrm{S/N}}$	T_{eff} (K)	log(g) (dex)	[Fe/H] (dex)	[α/Fe] (dex)	$v_r \sin(i)$ (km/s)	$\overline{RV}$ (m/s)	σ_{obs} (m/s)	σ_{meas} (m/s)	P_{mem}	P_v	$P_{v,jitter}$	Note
146-012325	5833	7:57:09.38	-60:48:02.77	12.4	0.60	11	73	6359^{+49}_{-45}	4.4	-0.01 ± 0.02	-0.01 ± 0.02	33.9 ± 0.3	$+23481 \pm 118$	79	394	90	0	0	NV
146-012624	11716	7:59:47.48	-60:54:15.26	13.8	0.80	11	57	5630^{+22}_{-19}	4.5	$-0.14^{+0.01}_{-0.02}$	-0.01 ± 0.02	7.4 ± 0.1	$+25003 \pm 31$	77	64	97	95	31	NV
147-012244	7483	7:57:52.86	-60:46:59.71	13.1	0.76	12	75	5783^{+21}_{-18}	4.5	-0.25 ± 0.01	$+0.12 \pm 0.01$	3.8 ± 0.1	$+13533 \pm 26$	77	53	0	100	73	NV
148-012888	8999	7:58:32.23	-60:34:12.93	13.4	0.74	11	52	5695^{+22}_{-19}	4.5	-0.17 ± 0.03	$+0.01^{+0.01}_{-0.02}$	9.1 ± 0.1	$+24060 \pm 36$	77	80	96	65	12	NV
146-012347	6322	7:57:21.91	-60:53:42.25	13.2	0.88	11	51	5762 ± 31	4.5	-0.06 ± 0.03	$-0.04^{+0.01}_{-0.02}$	10.8 ± 0.1	$+25070 \pm 32$	70	93	97	26	7	NV
147-012193	6676	7:57:31.53	-60:42:10.80	14.3	0.94	12	43	5288^{+17}_{-13}	4.6	-0.06 ± 0.01	$+0.07 \pm 0.01$	5.1 ± 0.1	$+25077 \pm 26$	69	57	97	96	24	NV
146-012361	6501	7:57:26.43	-60:49:13.03	12.8	0.70	12	73	5916^{+21}_{-18}	4.5	-0.43 ± 0.02	$+0.12 \pm 0.01$	3.8 ± 0.2	-23007 ± 26	67	74	0	65	25	NV
146-012585	10783	7:59:19.00	-60:59:28.27	13.5	0.73	11	55	5877^{+22}_{-19}	4.5	$+0.14^{+0.01}_{-0.02}$	$+0.05^{+0.01}_{-0.02}$	4.5 ± 0.1	$+21058 \pm 23$	64	49	0	99	42	NV
147-012514	13316	8:00:34.36	-60:42:22.55	12.2	0.67	12	99	6034^{+21}_{-20}	4.5	-0.15 ± 0.02	-0.02 ± 0.01	10.4 ± 0.1	$+24578 \pm 30$	64	81	97	25	4	NV
146-012318	5631	7:57:04.17	-60:52:43.75	15.0	1.06	9	23	5134^{+20}_{-19}	4.6	-0.21 ± 0.02	$+0.21 \pm 0.02$	3.6 ± 0.2	$+18437 \pm 26$	60	58	0	74	27	NV
146-012521	9475	7:58:43.48	-60:51:42.44	13.7	0.83	11	48	5467^{+22}_{-19}	4.5	-0.31 ± 0.02	$+0.27^{+0.01}_{-0.02}$	3.9 ± 0.1	$+68508 \pm 21$	50	54	0	70	13	NV
147-012447	11788	7:59:50.30	-60:44:14.93	14.6	0.99	8	32	5179^{+21}_{-16}	4.6	-0.07 ± 0.02	$+0.06 \pm 0.01$	4.9 ± 0.2	$+24542 \pm 29$	49	69	97	40	3	NV
147-012311	8737	7:58:26.13	-60:44:13.56	14.8	1.05	8	31	5073^{+21}_{-16}	4.6	-0.07 ± 0.02	$+0.09 \pm 0.02$	3.8 ± 0.2	$+22877 \pm 25$	49	52	65	67	11	NV
146-012464	8298	7:58:13.83	-60:59:34.82	14.0	1.06	11	38	5272^{+22}_{-19}	4.6	$+0.03^{+0.01}_{-0.02}$	$+0.03^{+0.01}_{-0.02}$	3.9 ± 0.2	-2056 ± 19	44	52	0	64	6	NV
148-012927	10281	7:59:04.49	-60:33:40.04	13.4	0.75	11	58	5743^{+22}_{-19}	4.5	$-0.05^{+0.01}_{-0.02}$	$+0.01^{+0.01}_{-0.02}$	3.6 ± 0.1	$+34078 \pm 19$	43	48	0	69	6	NV
146-012657	12754	8:00:17.27	-60:51:27.09	13.6	0.87	11	60	5343^{+22}_{-19}	4.6	$+0.06^{+0.01}_{-0.02}$	$+0.07^{+0.01}_{-0.02}$	3.1 ± 0.1	-7427 ± 16	43	38	0	91	15	NV
146-012403	7312	7:57:47.91	-60:56:13.08	13.8	0.83	11	45	5526 ± 25	4.5	-0.14 ± 0.03	$+0.05^{+0.01}_{-0.02}$	5.0 ± 0.1	$+24968 \pm 18$	34	52	97	11	0	NV
147-012320	8932	7:58:30.91	-60:47:26.08	12.9	0.81	11	65	5374 ± 23	4.5	$+0.02 \pm 0.02$	$+0.07^{+0.01}_{-0.02}$	4.2 ± 0.1	$+10837 \pm 15$	32	43	0	30	2	NV
147-012336	9146	7:58:35.87	-60:40:40.73	14.1	1.04	10	47	4740^{+19}_{-14}	4.6	-0.14 ± 0.01	$+0.07 \pm 0.01$	3.2 ± 0.2	-10667 ± 15	31	42	0	30	1	NV
147-012408	10894	7:59:22.17	-60:45:26.72	11.9	0.62	11	122	6181 ± 37	4.4	-0.23 ± 0.03	$+0.03 \pm 0.02$	14.5 ± 0.3	$+24491 \pm 39$	27	134	97	0	0	NV

Table A.1 (cont'd)

UCAC4	J01	RA	Dec.	V	B−V	N	$\overline{\mathrm{S/N}}$	T_{eff} (K)	log(g) (dex)	[Fe/H] (dex)	[α/Fe] (dex)	$v_r \sin(i)$ (km/s)	$\overline{RV}$ (m/s)	σ_{obs} (m/s)	σ_{meas} (m/s)	P_{mem}	P_v	$P_{v,jitter}$	Note
146-012574	10547	7:59:11.46	-60:49:05.66	14.6	1.01	9	41	5079^{+20}_{-15}	4.6	-0.02 ± 0.02	$+0.07 \pm 0.02$	5.8 ± 0.2	$+24541 \pm 19$	8	58	97	0	0	NV
147-012416	11014	7:59:25.49	-60:40:50.88	13.2	0.69	11	71	6013^{+22}_{-19}	4.5	$+0.03^{+0.01}_{-0.02}$	$+0.02^{+0.01}_{-0.02}$	5.0 ± 0.1	$+16646 \pm 14$	5	49	0	0	0	NV
146-012353	6377	7:57:23.29	-60:55:52.00	11.7	0.46	12	107	...	...	...	...	...	...	...	...	...	...	...	NMC
146-012595	11029	7:59:26.10	-60:48:34.01	14.8	1.05	11	8	...	...	...	...	...	...	...	...	...	...	...	X
147-012316	8920	7:58:30.58	-60:46:29.86	11.7	0.47	11	106	...	...	...	...	...	...	...	...	...	...	...	NMC
147-012471	12302	8:00:04.88	-60:45:19.47	12.0	0.53	12	116	...	...	...	...	...	...	...	...	...	...	...	NMC

Note. — Literature and measured properties of our targets in NGC 2516. Coordinates are from UCAC4 and photometry from J01, except for targets with a U which use UCAC4 photometry. We report the number of spectra obtained and the average S/N of those spectra along with our adopted T_{eff}, [Fe/H], [α/Fe], and $v_r \sin(i)$ values for each star. Errors on our stellar parameters are the larger of the standard error on the mean of the multi-epoch fits and the nominal error reported in Table 4.8 corrected by $\sqrt{\mathrm{N}}$, for additional details see §5.2. T_{eff} values for members are adjusted by Equation 4.4. Mean RVs, σ_{obs}, and σ_{meas} values are reported for each star, followed by membership probabilities (§5.3.2) and variability probabilities (both raw and accounting for stellar jitter, §6.3). Finally we report codes for each star: M=Member, NM=Nonmember, PM=Probable Member (from our relaxed criterion, §5.3.2), B=$\sigma_{stel} > 300$ m/s binary, SB2=Double lined spectroscopic binary, C=Continuum (featureless) star, U=UCAC4 photometry. One star lacking any parameters is reported with a X: We never obtained a spectrum of sufficient S/N to analyze this star.

Table A.2. Properties of Targets in NGC 2422

UCAC4	J01	RA	Dec.	V	B−V	N	$\overline{S/N}$	T_{eff} (K)	log(g) (dex)	[Fe/H] (dex)	[α/Fe] (dex)	$v_r \sin(i)$ (km/s)	$\overline{RV}$ (m/s)	σ_{obs} (m/s)	σ_{meas} (m/s)	P_{mem}	P_v	$P_{v,jitter}$	Note
378-036252	1110	7:35:57.52	-14:32:40.72	12.5	0.62	10	156	6324 ± 73	4.4	-0.14 ± 0.02	$+0.02 \pm 0.02$	9.8 ± 0.3	$+47929 \pm 12207$	38107	95	0	100	100	PMSB2V
377-035049	...	7:36:42.89	-14:39:32.72	15.9	1.31	10	24	5112 ± 47	4.6	-0.12 ± 0.12	$+0.06 \pm 0.01$	6.8 ± 1.7	$+37337 \pm 7180$	19124	117	84	100	100	MSB2V,U
378-036176	...	7:35:49.35	-14:29:46.56	12.5	0.52	10	122	6102 ± 148	4.5	-0.54 ± 0.19	$+0.05 \pm 0.05$	9.1 ± 1.2	$+4337 \pm 4762$	14124	110	0	100	100	NMSB2V,U
379-035886	...	7:36:28.65	-14:21:02.77	15.8	1.30	7	16	4999 ± 44	4.6	-0.04 ± 0.05	$+0.11 \pm 0.03$	9.2 ± 4.4	$+26035 \pm 3938$	11504	190	0	100	100	NMSB2V,U
379-035649	1113	7:35:54.38	-14:21:09.14	13.7	0.86	10	60	5648^{+23}_{-21}	4.5	-0.11 ± 0.02	$+0.03^{+0.01}_{-0.02}$	4.4 ± 0.1	$+38661 \pm 2646$	8366	41	4	100	100	PMBV
379-036197	1218	7:37:14.62	-14:20:42.23	12.3	0.59	10	110	6299^{+38}_{-30}	4.4	-0.08 ± 0.02	$+0.03^{+0.01}_{-0.02}$	6.6 ± 0.2	$+11379 \pm 2426$	7216	59	0	100	100	NMBV
379-035982	...	7:36:44.97	-14:21:44.82	14.4	0.89	8	45	4890^{+21}_{-16}	4.6	-0.01 ± 0.01	$+0.05 \pm 0.01$	14.1 ± 3.5	$+36530 \pm 2159$	5799	120	95	100	100	MBV,U
378-036328	1105	7:36:08.08	-14:29:42.08	12.7	0.56	10	116	6138^{+38}_{-30}	4.5	-0.18 ± 0.02	$+0.04^{+0.01}_{-0.02}$	7.9 ± 0.2	$+36928 \pm 1520$	5051	69	92	100	100	MBV
379-035884	...	7:36:28.13	-14:22:57.42	12.5	0.50	10	124	6846^{+52}_{-40}	4.4	-0.19 ± 0.02	$+0.02 \pm 0.02$	19.0 ± 0.3	$+59672 \pm 1476$	4667	235	0	100	100	NMBV,U
378-036136	...	7:35:45.32	-14:30:36.97	15.0	1.01	10	27	5586 ± 41	4.5	-0.25 ± 0.03	$+0.05^{+0.01}_{-0.02}$	9.0 ± 0.2	$+35631 \pm 1181$	3506	108	96	100	100	MBV,U
377-034854	...	7:36:10.72	-14:37:11.19	12.4	0.49	10	94	6543 ± 105	4.4	-0.64 ± 0.05	$+0.11 \pm 0.04$	38.3 ± 1.0	$+24943 \pm 932$	2713	1020	0	100	100	NMBV,U
379-036066	1069	7:36:57.00	-14:22:20.59	12.9	0.71	8	88	5957 ± 28	4.5	-0.11 ± 0.02	$-0.04^{+0.01}_{-0.02}$	21.6 ± 0.2	$+38029 \pm 778$	2125	198	39	100	100	PMBV
378-036422	1093	7:36:22.77	-14:34:04.96	13.8	0.87	10	67	5310 ± 23	4.6	-0.29 ± 0.02	$+0.06^{+0.01}_{-0.02}$	10.9 ± 0.2	$+43789 \pm 633$	1821	82	0	100	100	NMBV
379-036005	...	7:36:48.60	-14:15:46.79	13.0	0.64	10	86	6155^{+38}_{-30}	4.5	-0.26 ± 0.02	$-0.03^{+0.01}_{-0.02}$	19.1 ± 0.8	$+38391 \pm 426$	1386	207	13	100	100	PMBV,U
379-036194	397	7:37:14.38	-14:21:35.00	15.8	1.09	9	28	5425 ± 29	4.5	-0.16 ± 0.02	-0.01 ± 0.02	4.1 ± 0.2	$+106551 \pm 465$	1314	66	0	100	100	NMBV
378-036871	1217	7:37:14.82	-14:32:14.89	12.2	0.45	10	135	6801 ± 54	4.4	$+0.08 \pm 0.02$	$+0.00 \pm 0.02$	96.1 ± 0.8	$+32248 \pm 532$	1143	1276	0	49	49	NV
378-036137	1119	7:35:45.34	-14:35:33.32	13.3	0.72	10	81	5503 ± 24	4.5	$-0.75^{+0.01}_{-0.02}$	$+0.33 \pm 0.02$	3.0 ± 0.2	$+119993 \pm 361$	1123	49	0	100	100	NMBV
378-036541	...	7:36:36.16	-14:28:15.13	12.2	0.52	10	92	6802 ± 96	4.4	-0.06 ± 0.03	$+0.03 \pm 0.02$	68.5 ± 0.8	$+33648 \pm 473$	1076	1162	19	56	56	NV,U
378-036491	544	7:36:29.51	-14:29:29.29	15.9	1.09	6	17	4604 ± 44	4.7	$+0.23 \pm 0.05$	-0.04 ± 0.05	56.8 ± 1.4	$+36151 \pm 541$	1072	904	96	91	90	NV
378-036814	...	7:37:08.51	-14:25:07.30	14.5	0.93	10	49	5221^{+19}_{-15}	4.6	-0.06 ± 0.02	$+0.08 \pm 0.01$	6.9 ± 0.2	$+36322 \pm 335$	1023	68	96	100	100	MBV,U

Table A.2 (cont'd)

UCAC4	J01	RA	Dec.	V	B−V	N	$\overline{\mathrm{S/N}}$	T_{eff} (K)	log(g) (dex)	[Fe/H] (dex)	[α/Fe] (dex)	$v_r \sin(i)$ (km/s)	$\overline{RV}$ (m/s)	σ_{obs} (m/s)	σ_{meas} (m/s)	P_{mem}	P_v	$P_{v,jitter}$	Note
379-035908	...	7:36:30.84	-14:21:28.32	14.2	0.85	9	28	6615 ± 145	4.4	$+0.07 \pm 0.05$	-0.06 ± 0.05	37.5 ± 1.0	$+64553 \pm 391$	878	792	0	88	88	NV,U
378-036527	...	7:36:35.22	-14:31:47.79	12.5	0.61	10	75	6315 ± 65	4.4	-0.02 ± 0.04	-0.05 ± 0.02	47.7 ± 0.7	$+33617 \pm 340$	823	647	17	97	95	NV,U
377-035019	...	7:36:37.68	-14:38:18.94	15.1	1.09	10	48	4555^{+19}_{-14}	4.7	$+0.05 \pm 0.01$	$+0.04 \pm 0.01$	35.2 ± 0.6	$+32857 \pm 261$	805	238	1	100	100	NMBV,U
378-036277	652	7:36:00.57	-14:33:56.69	14.4	1.00	10	61	5382^{+23}_{-20}	4.5	$-0.01^{+0.01}_{-0.02}$	$+0.06^{+0.01}_{-0.02}$	3.4 ± 0.1	$+27815 \pm 229$	721	38	0	100	100	NMBV
378-036531	1084	7:36:35.59	-14:33:20.28	13.6	0.72	10	73	5672^{+23}_{-20}	4.5	-0.21 ± 0.02	$+0.02^{+0.01}_{-0.02}$	10.2 ± 0.1	$+37361 \pm 199$	635	78	83	100	100	MBV
378-036290	1107	7:36:03.64	-14:35:44.15	12.6	0.50	10	128	6992 ± 295	4.4	$+0.07^{+0.01}_{-0.02}$	$+0.02 \pm 0.02$	62.3 ± 0.6	$+1816 \pm 296$	540	782	0	15	15	NV
378-036882	1061	7:37:15.56	-14:31:48.76	12.6	0.50	10	107	6454^{+52}_{-34}	4.4	$+0.01 \pm 0.02$	-0.01 ± 0.02	35.4 ± 0.4	$+36004 \pm 201$	481	413	97	88	83	NV
379-035545	730	7:35:38.94	-14:23:34.83	15.9	1.31	10	23	4980^{+19}_{-14}	4.6	-0.02 ± 0.02	$+0.03 \pm 0.01$	4.3 ± 0.2	$+115336 \pm 141$	389	64	0	100	100	NMBV
379-035711	...	7:36:02.15	-14:21:32.17	15.3	1.07	10	38	4656^{+19}_{-14}	4.7	$+0.07 \pm 0.03$	$+0.05 \pm 0.02$	27.5 ± 0.3	$+35190 \pm 131$	378	184	94	100	100	MBV,U
379-036022	1221	7:36:50.06	-14:22:59.62	12.4	0.54	10	97	6392 ± 76	4.4	$+0.04^{+0.01}_{-0.02}$	-0.01 ± 0.02	63.7 ± 0.5	$+35053 \pm 293$	316	906	93	0	0	NV
377-034937	...	7:36:22.10	-14:43:57.74	13.5	0.71	10	75	6563^{+38}_{-30}	4.4	$+0.20 \pm 0.02$	-0.01 ± 0.03	17.0 ± 0.2	$+18602 \pm 103$	296	139	0	100	100	NMV,U
377-035192	926	7:37:04.92	-14:36:26.72	15.5	1.16	9	28	4694^{+20}_{-15}	4.7	$+0.12 \pm 0.02$	$+0.04 \pm 0.01$	27.9 ± 0.3	$+35208 \pm 130$	288	231	94	95	77	NV
377-035026	1081	7:36:39.13	-14:37:30.81	13.1	0.62	10	92	6072^{+23}_{-20}	4.5	$-0.05^{+0.01}_{-0.02}$	$-0.04^{+0.01}_{-0.02}$	14.5 ± 0.1	$+36139 \pm 82$	252	110	96	100	99	MV
379-035815	1096	7:36:18.60	-14:22:59.85	13.1	0.64	10	88	6060^{+23}_{-20}	4.5	$+0.04^{+0.01}_{-0.02}$	$-0.08^{+0.01}_{-0.02}$	25.0 ± 0.1	$+35807 \pm 93$	241	201	96	90	63	NV
377-034926	...	7:36:19.93	-14:36:39.08	15.4	1.11	10	34	5214 ± 24	4.6	-0.22 ± 0.02	-0.02 ± 0.01	4.1 ± 0.2	$+98342 \pm 77$	241	55	0	100	100	NMV,U
378-036554	...	7:36:37.04	-14:30:51.74	12.4	0.60	10	110	6458^{+52}_{-26}	4.4	$+0.02^{+0.01}_{-0.02}$	$+0.03^{+0.01}_{-0.02}$	50.4 ± 0.4	$+35165 \pm 209$	239	622	94	0	0	NV,U
378-036880	1062	7:37:15.40	-14:33:35.57	13.6	0.71	10	75	5588 ± 40	4.5	-0.18 ± 0.02	$+0.05 \pm 0.03$	18.8 ± 0.1	$+36300 \pm 87$	237	145	96	100	91	NV
378-036663	477	7:36:48.87	-14:28:53.91	15.5	1.09	9	32	5397 ± 27	4.5	-0.28 ± 0.02	$+0.02 \pm 0.02$	3.9 ± 0.3	$+79984 \pm 86$	231	65	0	100	100	NMV
377-035145	1220	7:36:58.85	-14:36:21.82	12.4	0.52	9	120	6443^{+54}_{-45}	4.4	$+0.08 \pm 0.02$	-0.03 ± 0.02	44.5 ± 0.3	$+35915 \pm 163$	219	444	97	3	2	NV
378-036905	384	7:37:18.16	-14:27:08.93	15.6	1.12	9	31	4761^{+20}_{-15}	4.6	-0.02 ± 0.02	$+0.05 \pm 0.01$	3.6 ± 0.3	$+35560 \pm 75$	215	47	96	100	99	MV

Table A.2 (cont'd)

UCAC4	J01	RA	Dec.	V	B−V	N	$\overline{\mathrm{S/N}}$	T_{eff} (K)	log(g) (dex)	[Fe/H] (dex)	[α/Fe] (dex)	$v_r \sin(i)$ (km/s)	$\overline{RV}$ (m/s)	σ_{obs} (m/s)	σ_{meas} (m/s)	P_{mem}	P_v	$P_{v,jitter}$	Note
377-035018	1083	7:36:37.63	-14:42:12.99	12.7	0.59	10	102	6416^{+38}_{-31}	4.4	$+0.00 \pm 0.02$	$-0.04^{+0.01}_{-0.02}$	32.1 ± 0.2	$+32023 \pm 118$	213	308	0	16	14	NV
378-036547	...	7:36:36.68	-14:31:51.06	14.3	0.84	9	17	4800 ± 21	4.6	-0.30 ± 0.03	$+0.11 \pm 0.02$	5.1 ± 0.6	$+19528 \pm 75$	210	94	0	100	100	NMV,U
378-036894	389	7:37:16.84	-14:31:29.77	15.1	0.94	10	36	5026^{+19}_{-17}	4.6	$+0.04 \pm 0.01$	$+0.11 \pm 0.02$	8.1 ± 0.2	$+36279 \pm 66$	201	69	96	100	98	MV
377-034990	...	7:36:32.55	-14:36:31.39	14.5	0.97	10	25	5230 ± 40	4.6	$+0.02 \pm 0.02$	-0.00 ± 0.02	4.2 ± 0.2	$+105039 \pm 58$	192	69	0	100	100	NMV,U
378-036906	...	7:37:18.22	-14:32:45.64	14.9	1.05	10	33	4587^{+19}_{-14}	4.7	$+0.11 \pm 0.01$	$+0.06 \pm 0.01$	11.2 ± 0.7	$+35762 \pm 62$	188	86	96	100	92	NV,U
379-035615	1116	7:35:49.28	-14:22:26.11	13.4	0.68	10	73	5871 ± 27	4.5	-0.07 ± 0.02	$-0.04^{+0.01}_{-0.02}$	12.8 ± 0.1	$+34507 \pm 68$	186	97	81	100	79	NV
378-036447	564	7:36:24.69	-14:34:46.34	15.0	1.06	10	36	4864^{+19}_{-14}	4.6	-0.04 ± 0.01	$+0.05 \pm 0.01$	6.4 ± 0.2	$+38416 \pm 66$	186	60	12	100	100	NMV
378-036721	1067	7:36:58.40	-14:35:54.39	13.5	0.67	10	71	5764^{+23}_{-22}	4.5	-0.04 ± 0.02	-0.01 ± 0.02	13.6 ± 0.1	$+35855 \pm 63$	181	95	97	100	77	NV
379-036043	462	7:36:53.88	-14:23:30.13	14.9	0.96	9	44	5041^{+20}_{-19}	4.6	$+0.02 \pm 0.01$	$+0.10 \pm 0.02$	9.7 ± 0.2	$+35178 \pm 67$	180	70	94	100	87	NV
378-036976	1055	7:37:27.91	-14:25:17.60	13.1	0.61	10	78	6072 ± 23	4.5	$+0.02^{+0.01}_{-0.02}$	$-0.05^{+0.01}_{-0.02}$	22.3 ± 0.1	$+35037 \pm 84$	177	187	93	61	28	NV
379-035967	1078	7:36:41.76	-14:23:32.31	13.3	0.74	10	60	5459^{+23}_{-20}	4.6	$-0.24^{+0.01}_{-0.02}$	$+0.06^{+0.01}_{-0.02}$	10.9 ± 0.1	$+34960 \pm 58$	168	87	92	100	76	NV
378-036274	994	7:36:00.22	-14:26:58.98	15.7	0.94	10	21	4852^{+19}_{-17}	4.6	-0.10 ± 0.02	$+0.12 \pm 0.01$	3.5 ± 0.3	$+14484 \pm 58$	160	59	0	100	100	NMV
377-034927	583	7:36:19.95	-14:43:27.77	14.9	1.12	10	37	4773^{+19}_{-14}	4.6	$+0.05 \pm 0.01$	$+0.10 \pm 0.02$	3.3 ± 0.2	$+6905 \pm 52$	159	46	0	100	100	NMV
377-035048	501	7:36:42.38	-14:42:30.87	14.4	0.81	6	33	5125^{+24}_{-21}	4.6	-0.55 ± 0.02	$+0.15 \pm 0.02$	3.2 ± 0.4	$+45989 \pm 65$	150	68	0	100	100	NMV
377-034813	1106	7:36:05.38	-14:38:22.90	13.3	0.73	10	78	5829 ± 24	4.5	$-0.05^{+0.01}_{-0.02}$	$-0.03^{+0.01}_{-0.02}$	12.2 ± 0.1	$+36913 \pm 57$	149	87	93	100	50	NV
379-035798	...	7:36:15.66	-14:18:55.64	15.3	1.16	10	38	4839^{+19}_{-14}	4.6	$+0.33 \pm 0.01$	-0.06 ± 0.01	3.9 ± 0.2	$+102809 \pm 44$	148	42	0	100	100	NMV,U
379-035796	1098	7:36:15.53	-14:22:22.55	13.9	0.78	10	70	5622^{+23}_{-20}	4.5	$-0.05^{+0.01}_{-0.02}$	$-0.01^{+0.01}_{-0.02}$	9.6 ± 0.1	$+35728 \pm 53$	148	66	96	100	52	NV
378-036454	1091	7:36:25.15	-14:32:30.22	12.7	0.57	10	104	6225^{+38}_{-35}	4.4	$+0.01 \pm 0.02$	$-0.04^{+0.01}_{-0.02}$	25.9 ± 0.2	$+37686 \pm 87$	146	237	67	8	3	NV
378-036710	...	7:36:56.63	-14:27:42.59	14.1	0.85	9	45	5496^{+25}_{-21}	4.5	$-0.17^{+0.01}_{-0.02}$	$+0.04^{+0.01}_{-0.02}$	8.2 ± 0.1	$+36684 \pm 54$	146	81	95	100	64	NV,U
378-036681	...	7:36:52.73	-14:34:13.32	14.7	1.04	5	48	5181^{+26}_{-20}	4.6	-0.01 ± 0.02	$+0.06 \pm 0.02$	7.5 ± 0.2	$+35216 \pm 71$	146	57	94	100	67	NV,U

Table A.2 (cont'd)

UCAC4	J01	RA	Dec.	V	B−V	N	$\overline{\mathrm{S/N}}$	T_{eff} (K)	log(g) (dex)	[Fe/H] (dex)	[α/Fe] (dex)	$v_r \sin(i)$ (km/s)	$\overline{RV}$ (m/s)	σ_{obs} (m/s)	σ_{meas} (m/s)	P_{mem}	P_v	$P_{v,jitter}$	Note
378-036680	1072	7:36:52.73	-14:35:40.04	14.0	0.81	10	51	5472^{+23}_{-20}	4.5	-0.21 ± 0.02	$+0.02 \pm 0.02$	7.1 ± 0.1	$+10075 \pm 53$	145	69	0	100	100	NMV
378-036662	479	7:36:48.66	-14:34:38.30	16.0	1.43	9	22	4857^{+20}_{-15}	4.6	$+0.06 \pm 0.02$	$+0.03 \pm 0.01$	3.4 ± 0.2	$+119830 \pm 52$	145	57	0	100	100	NMV
378-036960	...	7:37:25.53	-14:29:17.32	13.5	0.82	9	53	6444 ± 80	4.4	-0.14 ± 0.05	$+0.05 \pm 0.03$	13.9 ± 0.3	$+37016 \pm 79$	144	175	91	39	12	NV,U
379-036032	...	7:36:52.41	-14:20:32.94	15.7	1.22	7	16	5776 ± 54	4.5	$+0.08 \pm 0.02$	-0.02 ± 0.03	3.1 ± 0.5	$+8763 \pm 64$	142	79	0	100	98	NMV,U
378-036665	475	7:36:49.24	-14:31:12.88	15.8	1.07	10	28	5303 ± 29	4.6	-0.14 ± 0.02	$+0.05^{+0.01}_{-0.02}$	4.8 ± 0.2	$+109015 \pm 47$	142	70	0	100	100	NMV
377-034984	541	7:36:31.10	-14:43:39.53	15.3	1.00	10	27	4787^{+19}_{-15}	4.6	-0.02 ± 0.01	$+0.05 \pm 0.01$	4.0 ± 0.2	$+36058 \pm 47$	138	61	97	100	52	NV
378-036349	...	7:36:11.04	-14:30:09.93	14.4	1.02	10	38	4806^{+19}_{-14}	4.6	$+0.05 \pm 0.01$	$+0.06 \pm 0.01$	3.9 ± 0.2	-3348 ± 51	137	48	0	100	100	NMV,U
377-034915	911	7:36:18.31	-14:42:57.07	15.5	0.95	9	29	4880^{+20}_{-17}	4.6	-0.30 ± 0.02	$+0.15 \pm 0.01$	2.7 ± 0.3	$+18566 \pm 51$	136	60	0	100	100	NMV
378-036777	436	7:37:04.11	-14:32:47.27	15.8	1.16	9	28	5143^{+20}_{-15}	4.6	$+0.17 \pm 0.01$	$+0.07 \pm 0.02$	3.4 ± 0.2	$+72053 \pm 44$	135	46	0	100	100	NMV
379-035991	1075	7:36:46.43	-14:21:38.78	13.8	0.78	10	72	5684^{+23}_{-20}	4.5	-0.06 ± 0.02	$+0.00^{+0.01}_{-0.02}$	8.9 ± 0.1	$+34565 \pm 50$	133	68	83	100	37	NV
378-037002	340	7:37:30.87	-14:30:54.73	15.9	1.18	9	23	5288^{+25}_{-22}	4.6	$+0.10^{+0.01}_{-0.02}$	$+0.01^{+0.01}_{-0.02}$	3.7 ± 0.3	$+106495 \pm 45$	128	60	0	100	100	NMV
378-036376	...	7:36:15.58	-14:24:34.94	14.9	0.97	10	42	5468^{+23}_{-20}	4.5	$+0.42 \pm 0.02$	$+0.21 \pm 0.04$	3.7 ± 0.2	$+51164 \pm 43$	126	37	0	100	100	NMV,U
378-036080	...	7:35:38.75	-14:29:48.22	13.5	0.80	10	59	5784 ± 28	4.5	-0.91 ± 0.02	$+0.29 \pm 0.03$	3.3 ± 0.2	$+20198 \pm 48$	126	76	0	100	96	NMV,U
379-035707	...	7:36:01.64	-14:19:22.99	14.9	0.95	10	47	5152^{+19}_{-14}	4.6	-0.04 ± 0.03	$+0.10 \pm 0.01$	6.9 ± 0.2	$+36568 \pm 44$	125	50	95	100	37	NV,U
378-036806	427	7:37:07.50	-14:28:25.40	15.6	1.10	9	27	5420 ± 27	4.5	-0.21 ± 0.02	$+0.03 \pm 0.02$	4.2 ± 0.4	$+102882 \pm 47$	125	77	0	100	96	NMV
379-035920	1003	7:36:32.81	-14:20:33.11	15.8	0.99	8	19	5207 ± 35	4.6	-0.26 ± 0.02	$+0.06 \pm 0.01$	3.5 ± 0.4	$+54819 \pm 51$	124	85	0	99	95	NV
378-036632	1141	7:36:45.64	-14:28:55.25	13.0	0.63	10	87	6101 ± 38	4.5	-0.04 ± 0.03	$-0.04^{+0.01}_{-0.02}$	17.3 ± 0.2	$+34800 \pm 59$	123	142	89	48	8	NV
378-036772	...	7:37:03.74	-14:35:19.49	15.0	1.13	10	38	4879^{+19}_{-14}	4.6	-0.03 ± 0.01	$+0.06 \pm 0.01$	5.6 ± 0.2	$+35404 \pm 39$	116	52	95	100	34	NV,U
378-036256	...	7:35:58.23	-14:34:24.75	14.8	1.07	10	31	5002^{+19}_{-17}	4.6	-0.25 ± 0.01	$+0.12 \pm 0.01$	3.4 ± 0.3	$+31331 \pm 41$	116	52	0	100	100	NMV,U
378-036232	672	7:35:55.65	-14:29:58.95	15.2	1.10	10	40	4843^{+19}_{-14}	4.6	-0.01 ± 0.02	$+0.05 \pm 0.01$	6.0 ± 0.2	$+35835 \pm 40$	114	52	96	100	28	NV

Table A.2 (cont'd)

UCAC4	J01	RA	Dec.	V	B−V	N	$\overline{\mathrm{S/N}}$	T_{eff} (K)	log(g) (dex)	[Fe/H] (dex)	[α/Fe] (dex)	$v_r \sin(i)$ (km/s)	$\overline{RV}$ (m/s)	σ_{obs} (m/s)	σ_{meas} (m/s)	P_{mem}	P_v	$P_{v,jitter}$	Note
377-035021	1082	7:36:38.15	-14:41:29.26	13.3	0.63	10	77	6022^{+23}_{-20}	4.5	$-0.01^{+0.01}_{-0.02}$	$-0.06^{+0.01}_{-0.02}$	18.7 ± 0.1	$+36828 \pm 58$	111	147	94	25	4	NV
378-036312	634	7:36:05.81	-14:27:35.43	14.7	1.00	10	41	5289^{+23}_{-20}	4.6	-0.11 ± 0.02	$+0.07^{+0.01}_{-0.02}$	3.5 ± 0.2	$+53252 \pm 37$	110	42	0	100	100	NMV
378-036795	1065	7:37:06.35	-14:33:42.36	13.3	0.67	10	85	5717 ± 78	4.5	-0.13 ± 0.04	$+0.00 \pm 0.02$	17.4 ± 0.2	$+35929 \pm 49$	105	120	97	47	6	NV
379-035792	1099	7:36:14.64	-14:20:49.40	14.0	0.81	10	65	5469^{+23}_{-20}	4.6	$-0.03^{+0.01}_{-0.02}$	$+0.05^{+0.01}_{-0.02}$	4.8 ± 0.1	$+36246 \pm 39$	105	44	96	100	13	NV
379-036006	478	7:36:48.62	-14:22:24.97	14.1	0.80	10	58	5411^{+23}_{-20}	4.6	$-0.05^{+0.01}_{-0.02}$	$+0.05^{+0.01}_{-0.02}$	6.9 ± 0.1	$+35166 \pm 39$	103	64	94	100	17	NV
379-035569	713	7:35:43.45	-14:23:46.08	15.0	0.96	10	35	5064^{+19}_{-14}	4.6	-0.06 ± 0.01	$+0.12 \pm 0.01$	3.0 ± 0.4	-23236 ± 36	103	50	0	100	98	NMV
379-035844	572	7:36:22.71	-14:23:31.93	14.8	0.98	10	49	5021^{+19}_{-17}	4.6	$+0.03 \pm 0.01$	$+0.07 \pm 0.01$	7.6 ± 0.2	$+36468 \pm 37$	102	57	96	100	14	NV
378-036802	927	7:37:07.11	-14:27:04.14	15.5	1.07	8	38	4786^{+21}_{-16}	4.6	$+0.06 \pm 0.01$	$+0.06 \pm 0.02$	4.8 ± 0.2	$+35977 \pm 40$	100	52	97	100	21	NV
379-035948	516	7:36:37.48	-14:21:15.32	15.0	1.09	9	27	4773^{+20}_{-16}	4.6	$+0.07 \pm 0.02$	$+0.03 \pm 0.01$	4.8 ± 0.2	$+47529 \pm 40$	98	57	0	100	90	NV
378-036529	528	7:36:35.31	-14:31:14.62	15.6	1.17	10	37	5135 ± 19	4.6	-0.07 ± 0.02	$+0.04 \pm 0.01$	4.1 ± 0.3	$+110886 \pm 37$	96	49	0	100	94	NV
378-036074	733	7:35:38.31	-14:27:52.53	16.0	1.03	9	24	5326 ± 32	4.6	-0.25 ± 0.02	$+0.02 \pm 0.02$	5.6 ± 0.2	$+98905 \pm 38$	95	80	0	90	71	NV
377-034949	1092	7:36:24.35	-14:39:57.01	12.6	0.54	9	117	6301^{+40}_{-32}	4.4	-0.02 ± 0.03	$-0.04^{+0.01}_{-0.02}$	24.8 ± 0.2	$+36834 \pm 80$	93	226	94	1	0	NV
378-036161	...	7:35:46.92	-14:34:48.42	14.5	0.91	7	18	5458 ± 56	4.5	-0.54 ± 0.05	$+0.27 \pm 0.03$	3.7 ± 0.4	$+39973 \pm 48$	93	98	0	69	52	NV,U
377-034882	1147	7:36:14.37	-14:40:27.67	12.9	0.74	9	96	6094^{+40}_{-32}	4.5	$+0.08 \pm 0.02$	-0.08 ± 0.02	22.2 ± 0.2	$+35989 \pm 63$	92	164	97	6	1	NV
378-036163	1117	7:35:47.28	-14:30:41.19	13.1	0.70	10	87	5988^{+23}_{-20}	4.5	$+0.02^{+0.01}_{-0.02}$	$-0.04^{+0.01}_{-0.02}$	17.1 ± 0.1	$+36547 \pm 47$	92	122	95	25	2	NV
377-034671	711	7:35:43.53	-14:37:18.12	15.0	0.95	10	35	5626^{+23}_{-20}	4.5	-0.20 ± 0.02	$+0.04^{+0.01}_{-0.02}$	4.7 ± 0.1	$+22514 \pm 32$	90	58	0	100	88	NV
377-035031	1080	7:36:39.54	-14:39:14.27	13.9	0.77	10	63	5441 ± 26	4.6	$-0.16^{+0.01}_{-0.02}$	$+0.09 \pm 0.02$	9.8 ± 0.1	$+35610 \pm 38$	88	81	96	80	4	NV
378-036808	1064	7:37:07.79	-14:29:15.38	12.8	0.64	9	85	6032^{+25}_{-21}	4.5	-0.04 ± 0.02	$+0.01 \pm 0.02$	4.0 ± 0.2	$+36134 \pm 32$	82	56	96	100	7	NV
378-036230	1111	7:35:55.47	-14:33:50.41	12.9	0.68	10	103	6025^{+23}_{-20}	4.5	-0.19 ± 0.02	$+0.01^{+0.01}_{-0.02}$	7.5 ± 0.1	$+35808 \pm 31$	77	62	96	93	2	NV
378-036155	...	7:35:46.73	-14:25:52.77	13.5	0.76	9	49	5932^{+25}_{-21}	4.5	$+0.08 \pm 0.02$	$+0.02 \pm 0.02$	4.6 ± 0.1	$+52047 \pm 32$	74	61	0	95	53	NV,U

Table A.2 (cont'd)

UCAC4	J01	RA	Dec.	V	B−V	N	$\overline{\mathrm{S/N}}$	T_{eff} (K)	log(g) (dex)	[Fe/H] (dex)	[α/Fe] (dex)	$v_r \sin(i)$ (km/s)	$\overline{RV}$ (m/s)	σ_{obs} (m/s)	σ_{meas} (m/s)	P_{mem}	P_v	$P_{v,jitter}$	Note
379-036075	...	7:36:57.64	-14:23:41.06	13.7	0.75	10	60	6099 ± 35	4.5	-0.11 ± 0.03	$+0.01 \pm 0.02$	7.9 ± 0.1	$+19211 \pm 36$	74	96	0	38	16	NV,U
378-036626	1077	7:36:44.65	-14:32:20.42	12.9	0.72	10	95	5960^{+23}_{-20}	4.5	$+0.00 \pm 0.02$	$+0.01^{+0.01}_{-0.02}$	4.8 ± 0.1	$+17221 \pm 27$	74	51	0	99	61	NV
379-035811	...	7:36:18.37	-14:15:39.70	13.6	0.84	10	57	5678^{+23}_{-20}	4.5	-0.01 ± 0.02	$-0.02^{+0.01}_{-0.02}$	5.8 ± 0.1	$+42619 \pm 28$	73	56	0	98	57	NV,U
379-035717	646	7:36:02.67	-14:22:53.35	15.5	1.14	9	43	5200^{+20}_{-17}	4.6	$+0.00 \pm 0.02$	$+0.03 \pm 0.01$	3.9 ± 0.2	$+67963 \pm 26$	72	37	0	100	76	NV
378-036239	669	7:35:56.23	-14:24:48.04	15.1	1.12	7	30	5085 ± 25	4.6	-0.14 ± 0.02	$+0.14 \pm 0.02$	2.4 ± 0.3	$+108411 \pm 33$	71	53	0	100	62	NV
378-036945	358	7:37:23.12	-14:31:49.48	15.7	1.29	10	27	4724^{+19}_{-18}	4.6	$+0.04 \pm 0.01$	$+0.04 \pm 0.01$	5.4 ± 0.2	$+36171 \pm 29$	70	64	96	87	1	NV
377-034920	...	7:36:19.09	-14:41:29.42	14.9	0.99	10	46	5085^{+19}_{-14}	4.6	$+0.24 \pm 0.01$	-0.02 ± 0.03	4.3 ± 0.2	$+75276 \pm 26$	70	38	0	100	65	NV,U
379-035855	...	7:36:24.10	-14:22:00.36	14.6	0.91	9	41	5062^{+20}_{-15}	4.6	-0.07 ± 0.01	$+0.15 \pm 0.01$	2.9 ± 0.2	$+59268 \pm 23$	62	40	0	100	53	NV,U
378-036692	1071	7:36:54.12	-14:30:33.64	12.6	0.65	9	125	5883^{+25}_{-22}	4.5	-0.22 ± 0.02	$+0.04^{+0.01}_{-0.02}$	8.1 ± 0.1	$+36184 \pm 27$	60	61	96	68	1	NV
378-036177	696	7:35:49.66	-14:30:14.66	14.5	0.95	9	58	5057^{+20}_{-15}	4.6	-0.17 ± 0.01	$+0.12 \pm 0.01$	3.2 ± 0.2	$+46105 \pm 21$	54	33	0	100	37	NV
379-035635	...	7:35:52.90	-14:19:18.81	15.4	1.17	10	38	5195^{+19}_{-17}	4.6	$+0.03 \pm 0.01$	$+0.00 \pm 0.01$	4.0 ± 0.2	$+93612 \pm 23$	54	48	0	87	20	NV,U
379-035657	674	7:35:55.43	-14:21:52.05	14.5	0.98	10	42	5487^{+23}_{-20}	4.5	$+0.22^{+0.01}_{-0.02}$	$+0.06 \pm 0.02$	3.7 ± 0.1	$+30361 \pm 19$	50	36	0	99	20	NV
378-036365	...	7:36:13.84	-14:35:35.19	13.9	0.90	10	78	5270^{+23}_{-20}	4.6	$-0.57^{+0.01}_{-0.02}$	$+0.26^{+0.01}_{-0.02}$	$nan \pm 0.1$	$+94669 \pm 20$	48	43	0	87	15	NV,U
379-035644	1223	7:35:53.90	-14:23:41.74	12.4	0.59	9	103	5895^{+25}_{-21}	4.5	-0.48 ± 0.04	$+0.12^{+0.01}_{-0.02}$	4.7 ± 0.1	$+21489 \pm 24$	47	60	0	32	6	NV
378-036506	...	7:36:31.26	-14:30:36.59	15.6	1.10	10	28	6148 ± 53	4.5	$+0.20 \pm 0.03$	-0.00 ± 0.03	6.3 ± 0.3	$+20814 \pm 28$	45	76	0	7	1	NV,U
377-034958	1089	7:36:26.15	-14:39:29.87	12.6	0.57	9	100	6284^{+40}_{-32}	4.4	$+0.03 \pm 0.02$	$-0.05^{+0.01}_{-0.02}$	33.3 ± 0.2	$+37123 \pm 112$	42	354	92	0	0	NV
378-036485	1088	7:36:28.69	-14:33:10.23	13.0	0.74	9	66	5633^{+25}_{-22}	4.5	$-0.24^{+0.01}_{-0.02}$	$+0.05^{+0.01}_{-0.02}$	3.4 ± 0.3	$+85164 \pm 19$	38	45	0	47	6	NV
378-036892	...	7:37:16.52	-14:34:44.38	13.1	0.71	10	97	6099^{+23}_{-20}	4.5	$-0.05^{+0.01}_{-0.02}$	$+0.01 \pm 0.02$	5.6 ± 0.1	$+29863 \pm 21$	33	55	0	8	1	NV,U
378-036186	...	7:35:50.71	-14:31:54.94	13.8	0.78	10	61	4911^{+19}_{-15}	4.6	$+0.50 \pm 0.15$	-0.07 ± 0.04	$nan \pm 0.2$	$+43268 \pm 13$	28	28	0	73	1	NV,U
378-036947	1058	7:37:23.29	-14:25:11.61	13.1	0.62	9	79	6050^{+25}_{-21}	4.5	$-0.01^{+0.01}_{-0.02}$	$-0.03^{+0.01}_{-0.02}$	17.6 ± 0.1	$+36509 \pm 44$	17	143	96	0	0	NV

Table A.2 (cont'd)

UCAC4	J01	RA	Dec.	V	B−V	N	$\overline{S/N}$	T_{eff} (K)	log(g) (dex)	[Fe/H] (dex)	[α/Fe] (dex)	$v_r \sin(i)$ (km/s)	$\overline{RV}$ (m/s)	σ_{obs} (m/s)	σ_{meas} (m/s)	P_{mem}	P_v	$P_{v,jitter}$	Note
377-035323	...	7:37:24.29	-14:36:07.19	13.8	0.79	9	52	5907 ± 32	4.5	$+0.20 \pm 0.02$	$+0.11 \pm 0.03$	5.5 ± 0.1	$+14070 \pm 17$	11	51	0	0	0	NV,U
378-036984	344	7:37:29.05	-14:28:27.74	15.2	1.02	8	40	5297^{+26}_{-22}	4.6	$-0.35^{+0.01}_{-0.02}$	$+0.11^{+0.01}_{-0.02}$	3.0 ± 0.2	$+49934 \pm 16$	9	49	0	0	0	NV
378-036424	956	7:36:22.93	-14:32:45.46	15.0	0.75	10	31	...	...	...	...	...	...	...	...	...	...	...	NMC
378-036788	1166	7:37:05.66	-14:24:24.53	10.3	0.22	10	233	...	...	...	...	...	...	...	...	...	...	...	C
379-036213	...	7:37:16.41	-14:23:19.50	14.2	0.87	10	49	...	...	...	...	...	...	...	...	...	...	...	NMC,U

Note. — Literature and measured properties of our targets in NGC 2422. Coordinates are from UCAC4 and photometry from P03, except for targets not in P03 where it is taken from UCAC4. We report the number of spectra obtained and the average S/N of those spectra along with our adopted T_{eff}, [Fe/H], [α/Fe], and $v_r \sin(i)$ values for each star. Errors on our stellar parameters are the larger of the standard error on the mean of the multi-epoch fits and the nominal error reported in Table 4.8 corrected by $\sqrt{N}$, for additional details see §5.2. T_{eff} values of members are adjusted by Equation 4.4. Mean RVs, σ_{obs}, and σ_{meas} values are reported for each star, followed by membership probabilities (§5.3.2) and variability probabilities (both raw and accounting for stellar jitter, §6.3). Finally we report codes for each star: M=Member, NM=Nonmember, PM=Probable Member (from our relaxed criterion, §5.3.2), B=$\sigma_{stel} > 300$ m/s binary, SB2=Double lined spectroscopic binary, C=Continuum (featureless) star, U=UCAC4 photometry.

APPENDIX B

Plots of Radial Velocity Variables in NGC 2516 and NGC 2422

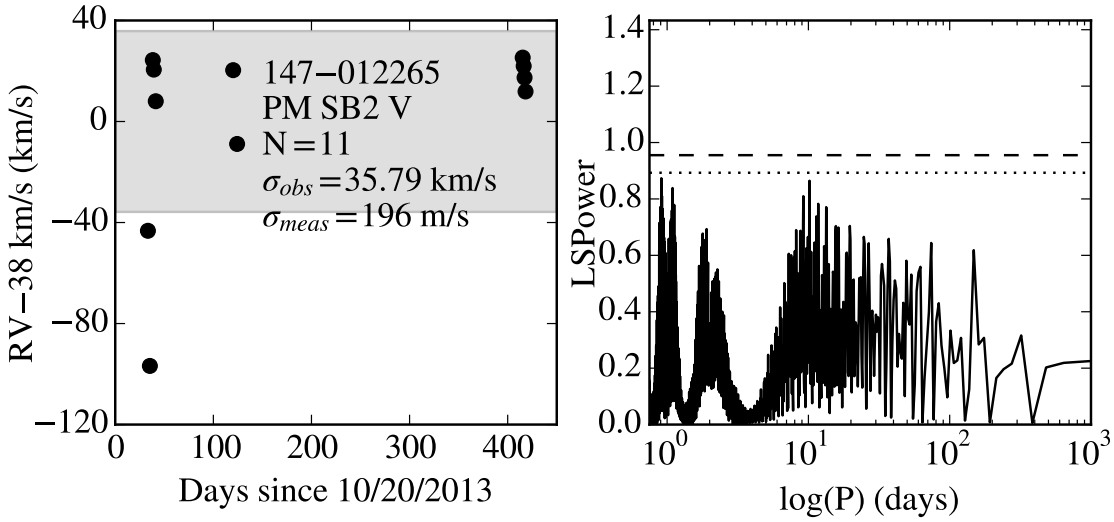

Figure B.1: 147-012265 is a double-lined binary possible member in NGC 2516 with a T_{eff} of 6710 ± 50 K and a $v_r \sin(i)$ of 16.9 ± 0.5 km/s. It has $\sigma_{obs} = 35789$ m/s and $\sigma_{meas} = 196$ m/s. D03 reports a flux of 24.74 ± 1.89 10^{-6}cts^{-1}cm^{-2}. W04 target 76 is 0.38 arcseconds away and is reported as binary. They report it is bright in ACIS exposures with stochastic variability. In HRC exposures it is bright with no variability. Errors shown include the mean σ_{jitter}.

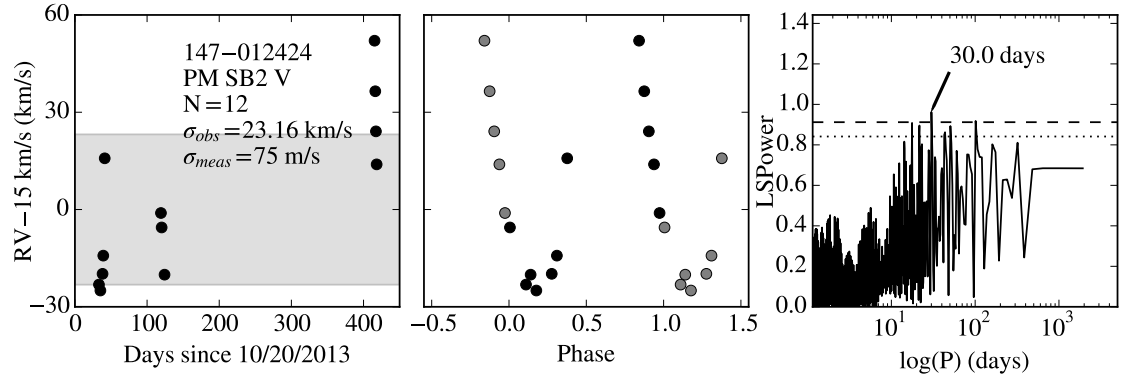

Figure B.2: 147-012424 is a double-lined binary possible member in NGC 2516 with a T_{eff} of 6175^{+35}_{-33} K and a $v_r \sin(i)$ of 6.4 ± 0.2 km/s. It has $\sigma_{obs} = 23160$ m/s and $\sigma_{meas} = 75$ m/s. D03 reports $\log(L_x) \leq 29.40$ erg/s. The most significant periodogram peak is at 30.0 days. Grey points are duplicated data to guide the eye. Errors shown include the mean σ_{jitter}.

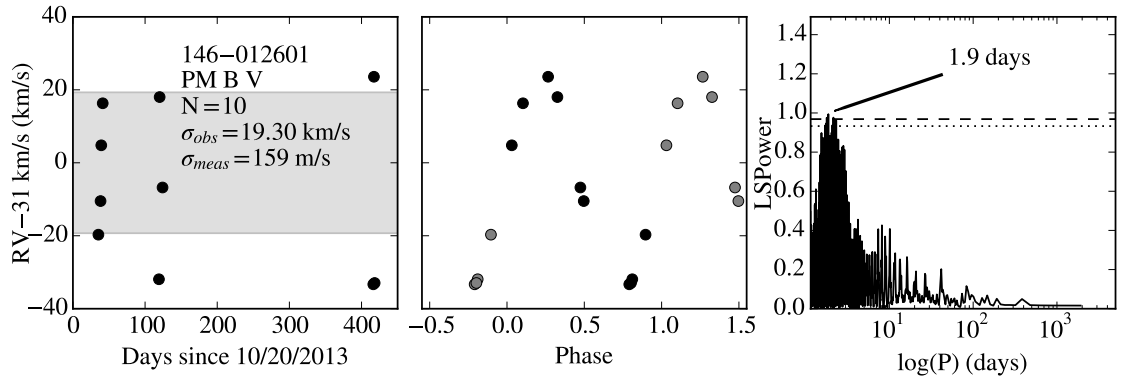

Figure B.3: 146-012601 is a binary possible member in NGC 2516 with a T_{eff} of 5116 ± 19 K and a $v_r \sin(i)$ of 16.1 ± 0.2 km/s. It has σ_{obs} = 19304 m/s and σ_{meas} = 159 m/s. D03 reports a flux of 34.62 ± 2.77 10^{-6}cts^{-1}cm^{-2}. W04 target 186 is 0.38 arcseconds away and is reported as binary. They report it is bright in ACIS exposures with stochastic variability. In HRC exposures it is bright with no variability. The most significant periodogram peak is at 1.9 days. Grey points are duplicated data to guide the eye. Errors shown include the mean σ_{jitter}.

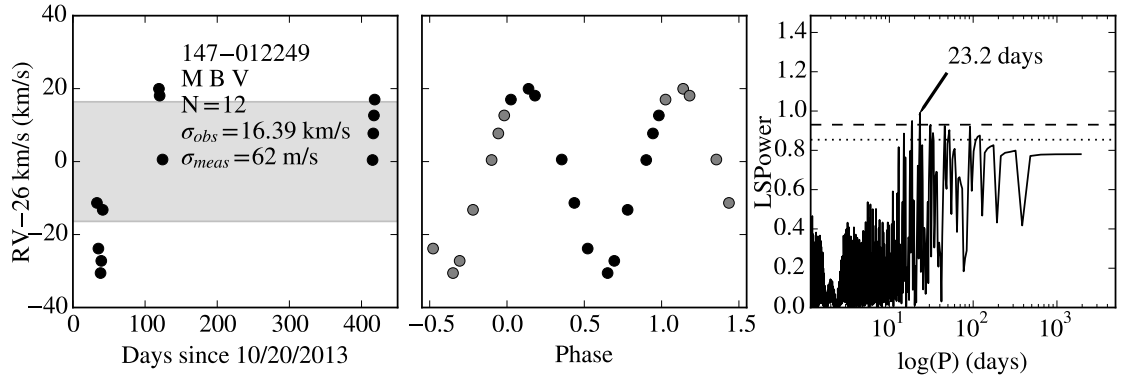

Figure B.4: 147-012249 is a binary member in NGC 2516 with a T_{eff} of 5250^{+17}_{-13} K and a $v_r \sin(i)$ of 6.7 ± 0.1 km/s. It has σ_{obs} = 16386 m/s and σ_{meas} = 62 m/s. D03 reports a flux of 2.10 ± 1.16 10^{-6}cts^{-1}cm^{-2}. The most significant periodogram peak is at 23.2 days. Grey points are duplicated data to guide the eye. Errors shown include the mean σ_{jitter}.

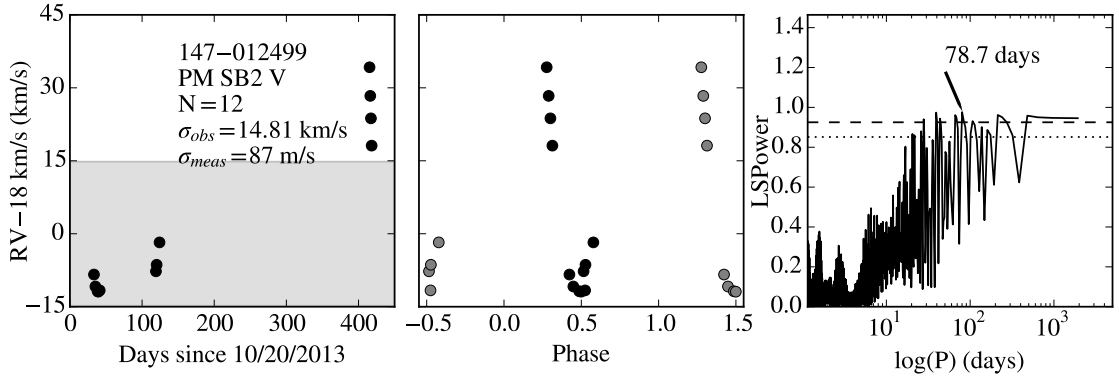

Figure B.5: 147-012499 is a double-lined binary possible member in NGC 2516 with a T_{eff} of 5360 ± 79 K and a $v_r \sin(i)$ of 8.4 ± 1.3 km/s. It has $\sigma_{obs} = 14814$ m/s and $\sigma_{meas} = 87$ m/s. D03 reports $\log(L_x) \leq 30.26$ erg/s. The most significant periodogram peak is at 78.7 days. Grey points are duplicated data to guide the eye. Errors shown include the mean σ_{jitter}.

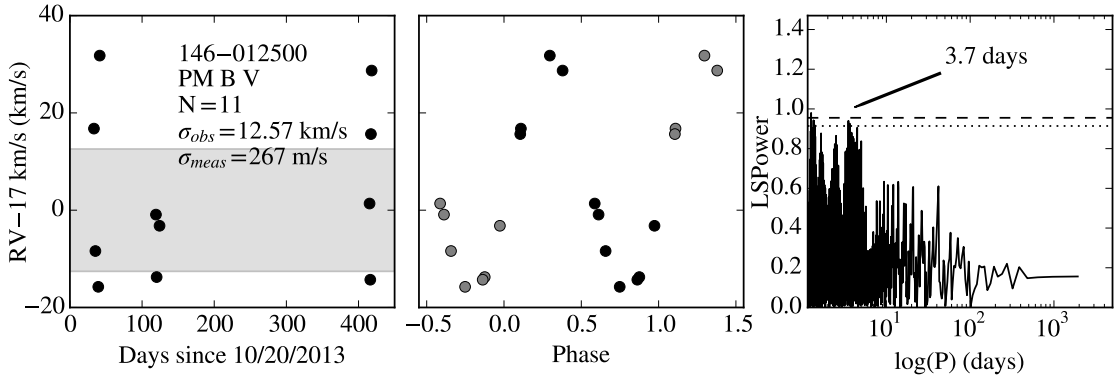

Figure B.6: 146-012500 is a binary possible member in NGC 2516 with a T_{eff} of 4877 ± 30 K and a $v_r \sin(i)$ of 8.8 ± 0.2 km/s. It has $\sigma_{obs} = 12569$ m/s and $\sigma_{meas} = 267$ m/s. D03 reports a flux of 11.33 ± 1.44 10^{-6}cts^{-1}cm^{-2}. W04 target 129 is 0.38 arcseconds away and is not reported as binary. They report it is faint in ACIS exposures. In HRC exposures it is moderate with quiescent level variability. The most significant periodogram peak is at 3.7 days. Grey points are duplicated data to guide the eye. Errors shown include the mean σ_{jitter}.

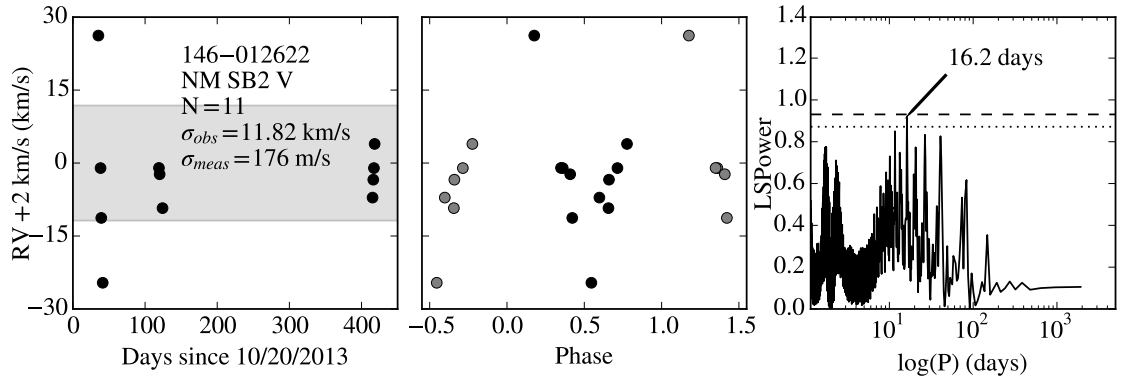

Figure B.7: 146-012622 is a double-lined binary non-member in NGC 2516 with a T_{eff} of 6234 ± 207 K and a $v_r \sin(i)$ of 9.2 ± 0.3 km/s. It has $\sigma_{obs} = 11821$ m/s and $\sigma_{meas} = 176$ m/s. D03 reports $\log(L_x) \leq 29.52$ erg/s. The most significant periodogram peak is at 16.2 days. Grey points are duplicated data to guide the eye. Errors shown include the mean σ_{jitter}.

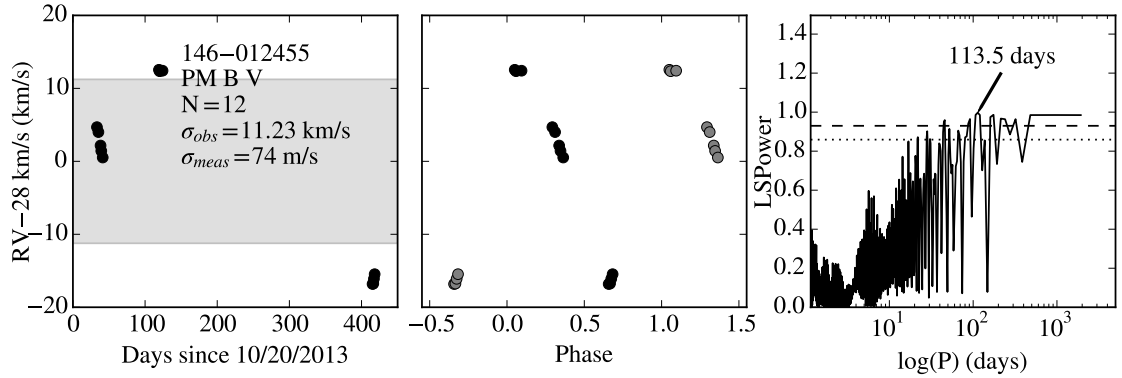

Figure B.8: 146-012455 is a binary possible member in NGC 2516 with a T_{eff} of 5308^{+21}_{-18} K and a $v_r \sin(i)$ of 7.6 ± 0.1 km/s. It has $\sigma_{obs} = 11231$ m/s and $\sigma_{meas} = 74$ m/s. D03 reports a flux of 3.67 ± 0.64 10^{-6}cts^{-1}cm^{-2}. The most significant periodogram peak is at 113.5 days. Grey points are duplicated data to guide the eye. Errors shown include the mean σ_{jitter}.

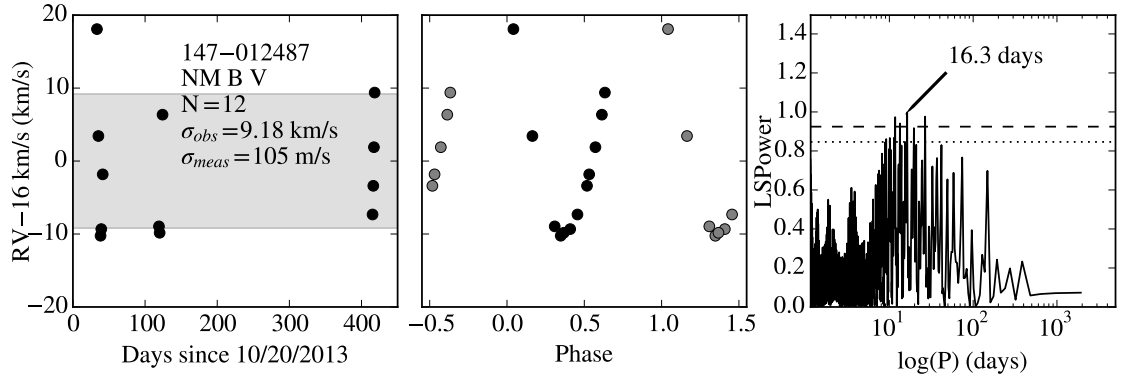

Figure B.9: 147-012487 is a binary non-member in NGC 2516 with a T_{eff} of 6408^{+35}_{-28} K and a $v_r \sin(i)$ of $10.4^{+0.2}_{-0.1}$ km/s. It has $\sigma_{obs} = 9182$ m/s and $\sigma_{meas} = 105$ m/s. D03 reports $\log(L_x) \leq 30.20$ erg/s. The most significant periodogram peak is at 16.3 days. Grey points are duplicated data to guide the eye. Errors shown include the mean σ_{jitter}.

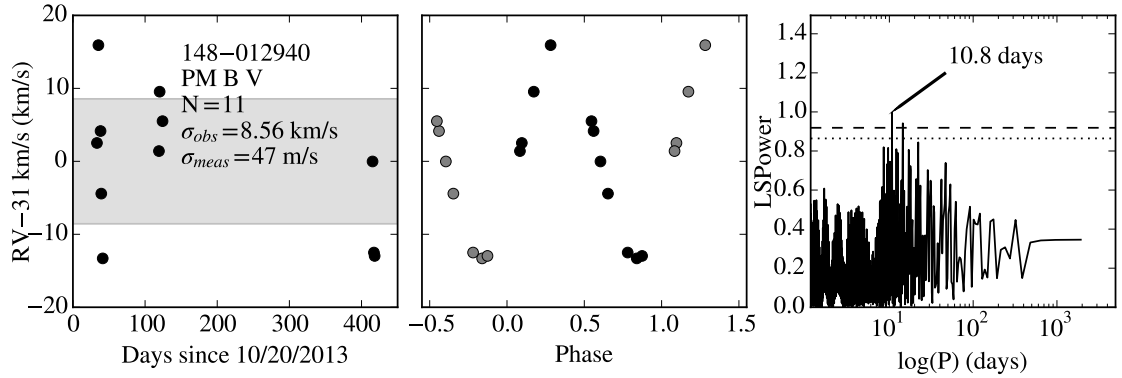

Figure B.10: 148-012940 is a binary possible member in NGC 2516 with a T_{eff} of 6064^{+22}_{-19} K and a $v_r \sin(i)$ of 6.0±0.1 km/s. It has $\sigma_{obs} = 8563$ m/s and $\sigma_{meas} = 47$ m/s. D03 reports $\log(L_x) \leq 29.92$ erg/s. The most significant periodogram peak is at 10.8 days. Grey points are duplicated data to guide the eye. Errors shown include the mean σ_{jitter}.

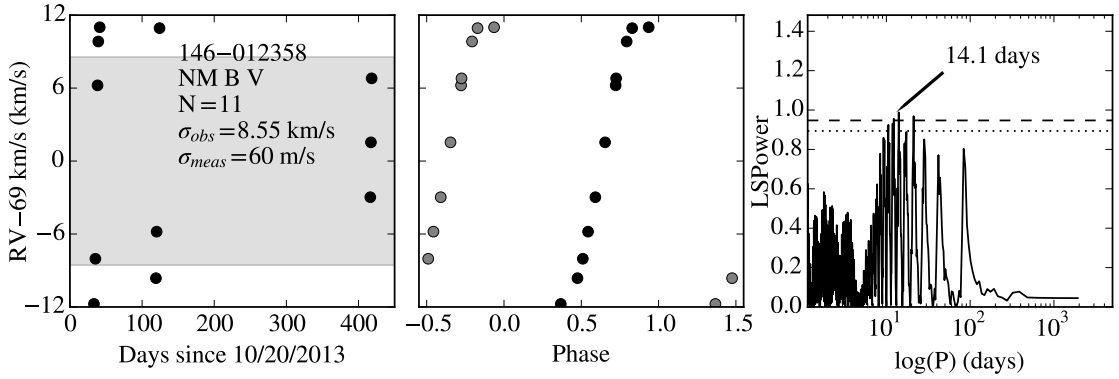

Figure B.11: 146-012358 is a binary non-member in NGC 2516 with a T_{eff} of 4833 ± 18 K and a $v_r \sin(i)$ of 4.5 ± 0.2 km/s. It has σ_{obs} = 8545 m/s and σ_{meas} = 60 m/s. D03 reports $\log(L_x) \leq 29.78$ erg/s. The most significant periodogram peak is at 14.1 days. Grey points are duplicated data to guide the eye. Errors shown include the mean σ_{jitter}.

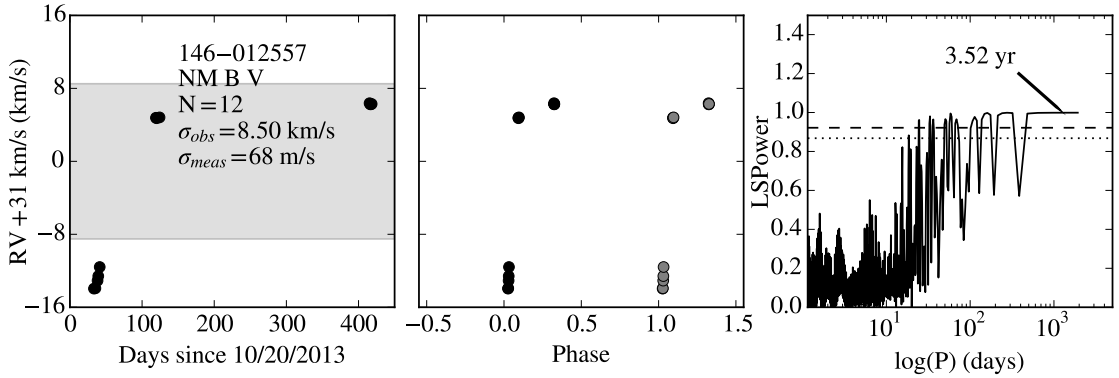

Figure B.12: 146-012557 is a binary non-member in NGC 2516 with a T_{eff} of 5731 ± 34 K and a $v_r \sin(i)$ of 4.9 ± 0.2 km/s. It has σ_{obs} = 8502 m/s and σ_{meas} = 68 m/s. D03 reports $\log(L_x) \leq 29.76$ erg/s. The most significant periodogram peak is at 3.52 years. Grey points are duplicated data to guide the eye. Errors shown include the mean σ_{jitter}.

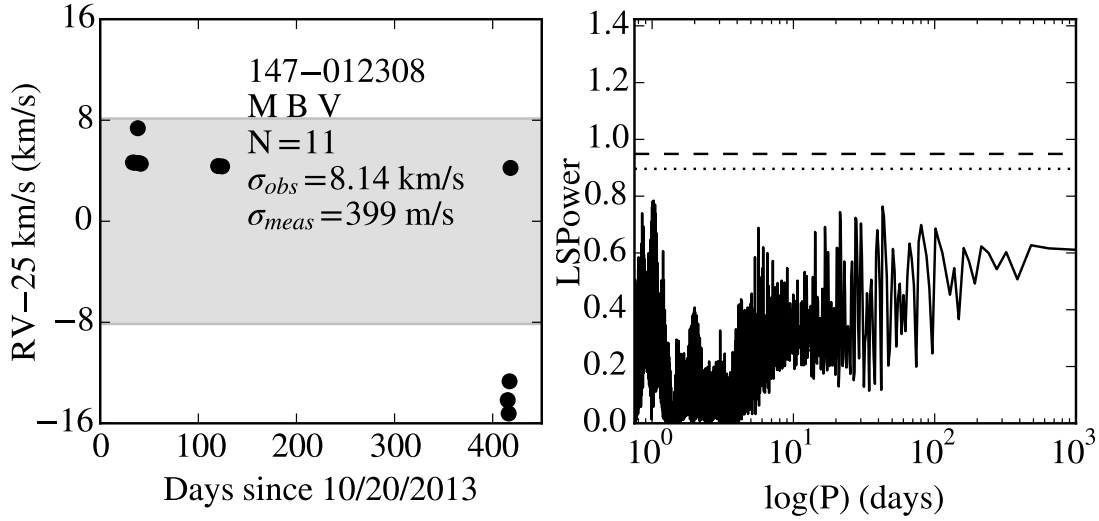

Figure B.13: 147-012308 is a binary member in NGC 2516 with a T_{eff} of 6658^{+49}_{-45} K and a $v_r \sin(i)$ of 37.8 ± 0.3 km/s. It has σ_{obs} = 8136 m/s and σ_{meas} = 399 m/s. D03 reports a flux of 17.79 ± 1.65 10^{-6}cts^{-1}cm^{-2}. W04 target 119 is 1.19 arcseconds away and is not reported as binary. They report it is bright in ACIS exposures with no variability. In HRC exposures it is moderate with no variability. Errors shown include the mean σ_{jitter}.

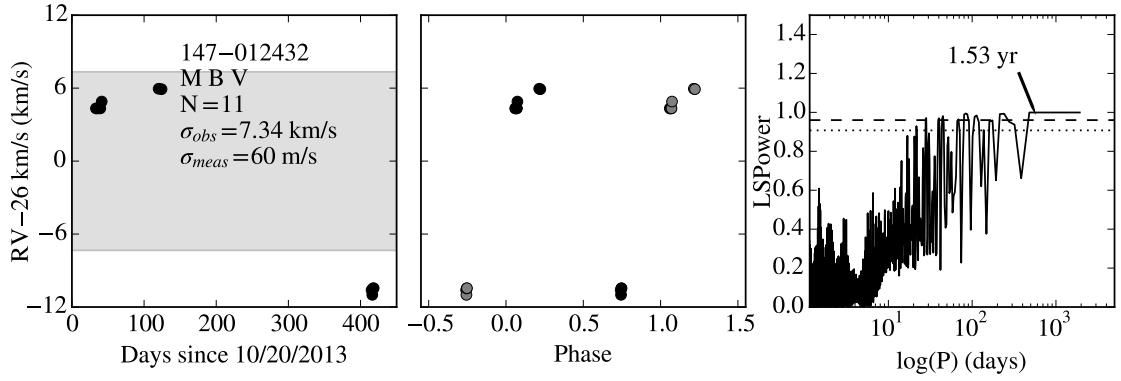

Figure B.14: 147-012432 is a binary member in NGC 2516 with a T_{eff} of 4898 ± 19 K and a $v_r \sin(i)$ of 5.9 ± 0.2 km/s. It has σ_{obs} = 7340 m/s and σ_{meas} = 60 m/s. D03 reports a flux of 5.87 ± 1.64 10^{-6}cts^{-1}cm^{-2}. W04 target 188 is 1.16 arcseconds away and is reported as binary. They report it is faint in ACIS exposures. In HRC exposures it is moderate with no variability. The most significant periodogram peak is at 1.53 years. Grey points are duplicated data to guide the eye. Errors shown include the mean σ_{jitter}.

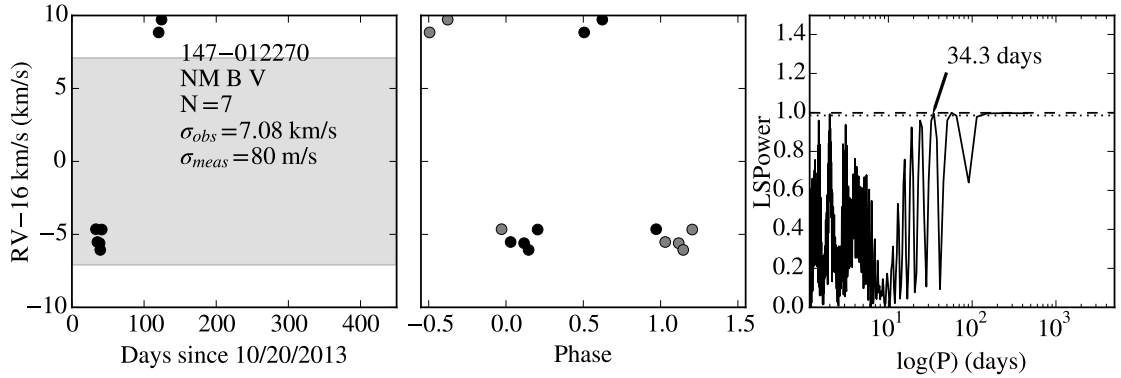

Figure B.15: 147-012270 is a binary non-member in NGC 2516 with a T_{eff} of 5117 ± 60 K and a $v_r \sin(i)$ of 7.5 ± 0.6 km/s. It has $\sigma_{obs} = 7084$ m/s and $\sigma_{meas} = 80$ m/s. D03 reports a flux of 5.57 ± 0.84 10^{-6}cts^{-1}cm^{-2}. The most significant periodogram peak is at 34.3 days. Grey points are duplicated data to guide the eye. Errors shown include the mean σ_{jitter}.

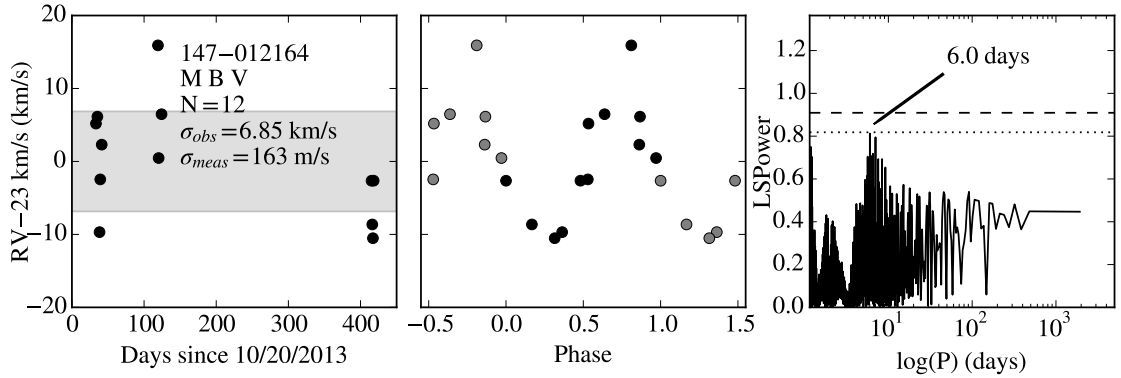

Figure B.16: 147-012164 is a binary member in NGC 2516 with a T_{eff} of 6078 ± 46 K and a $v_r \sin(i)$ of 17.0 ± 1.9 km/s. It has $\sigma_{obs} = 6851$ m/s and $\sigma_{meas} = 163$ m/s. D03 reports a flux of 15.65 ± 2.37 10^{-6}cts^{-1}cm^{-2}. W04 target 9 is 0.44 arcseconds away and is reported as binary. . In HRC exposures it is bright with no variability. The most significant periodogram peak is at 6.0 days. Grey points are duplicated data to guide the eye. Errors shown include the mean σ_{jitter}.

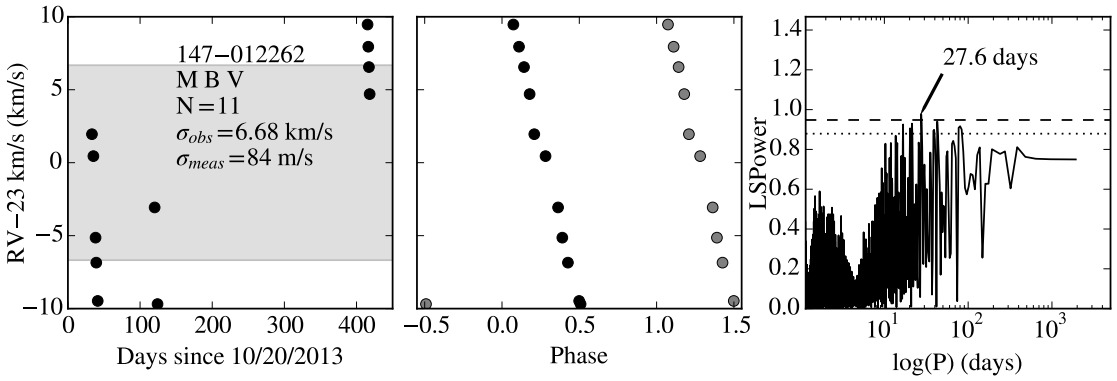

Figure B.17: 147-012262 is a binary member in NGC 2516 with a T_{eff} of 4821 ± 19 K and a $v_r \sin(i)$ of 4.6 ± 0.3 km/s. It has $\sigma_{obs} = 6679$ m/s and $\sigma_{meas} = 84$ m/s. D03 reports $\log(L_x) \leq 28.89$ erg/s. The most significant periodogram peak is at 27.6 days. Grey points are duplicated data to guide the eye. Errors shown include the mean σ_{jitter}.

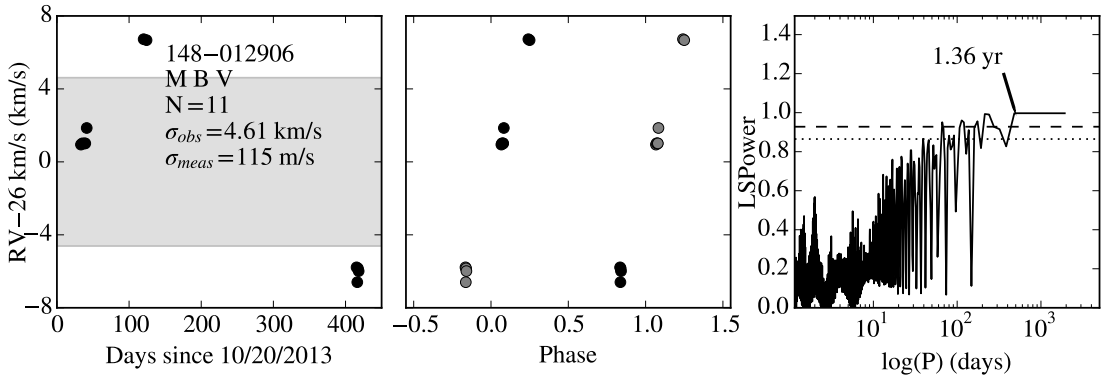

Figure B.18: 148-012906 is a binary member in NGC 2516 with a T_{eff} of 5516^{+22}_{-19} K and a $v_r \sin(i)$ of 15.3 ± 1.0 km/s. It has $\sigma_{obs} = 4613$ m/s and $\sigma_{meas} = 115$ m/s. D03 reports a flux of 21.64 ± 5.13 10^{-6}cts^{-1}cm^{-2}. W04 target 154 is 1.88 arcseconds away and is reported as binary. . In HRC exposures it is bright with stochastic variability. The most significant periodogram peak is at 1.36 years. Grey points are duplicated data to guide the eye. Errors shown include the mean σ_{jitter}.

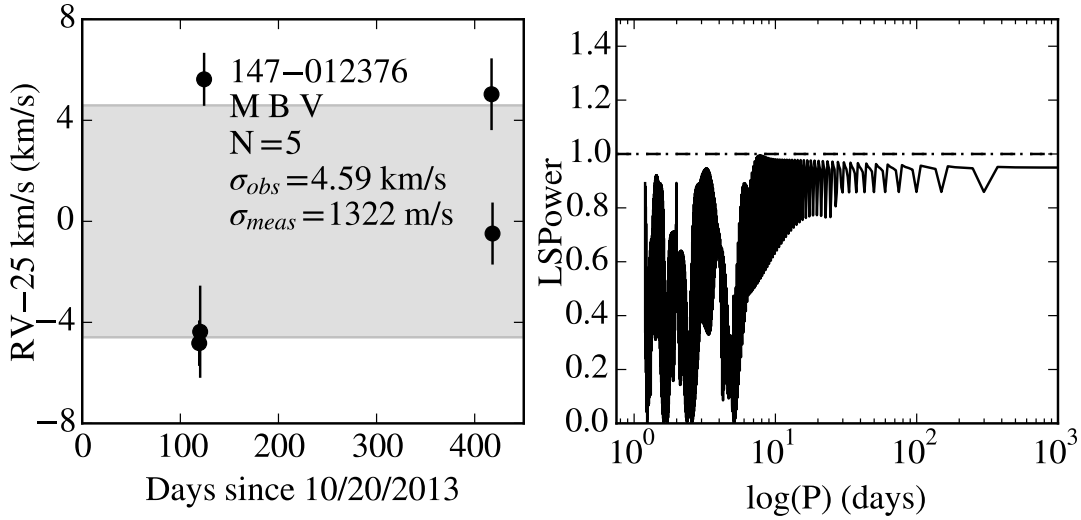

Figure B.19: 147-012376 is a binary member in NGC 2516 with a T_{eff} of 4918 ± 116 K and a $v_r \sin(i)$ of 76.7 ± 2.5 km/s. It has $\sigma_{obs} = 4591$ m/s and $\sigma_{meas} = 1322$ m/s. D03 reports a flux of 20.47 ± 1.38 10^{-6}cts^{-1}cm^{-2}. W04 target 167 is 0.07 arcseconds away and is not reported as binary. They report it is bright in ACIS exposures with no variability. In HRC exposures it is bright with no variability. Errors shown include the mean σ_{jitter}.

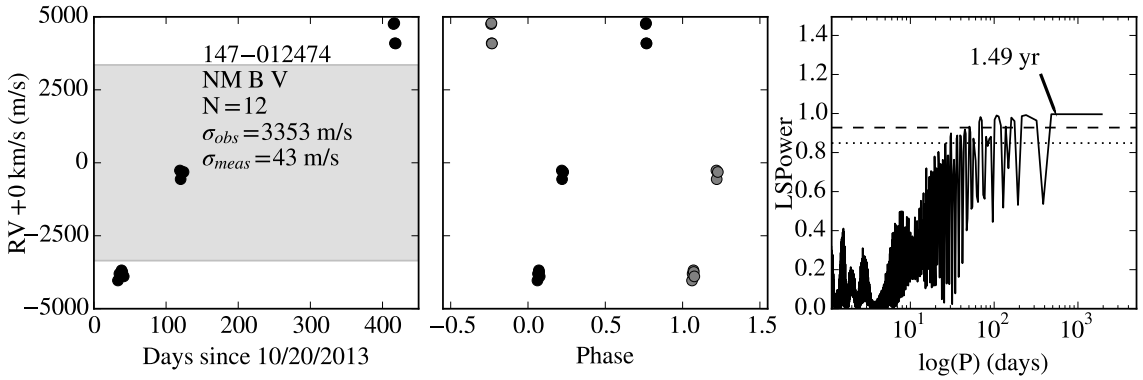

Figure B.20: 147-012474 is a binary non-member in NGC 2516 with a T_{eff} of 5111 ± 20 K and a $v_r \sin(i)$ of 3.7 ± 0.1 km/s. It has $\sigma_{obs} = 3353$ m/s and $\sigma_{meas} = 43$ m/s. D03 reports $\log(L_x) \leq 29.97$ erg/s. The most significant periodogram peak is at 1.49 years. Grey points are duplicated data to guide the eye. Errors shown include the mean σ_{jitter}.

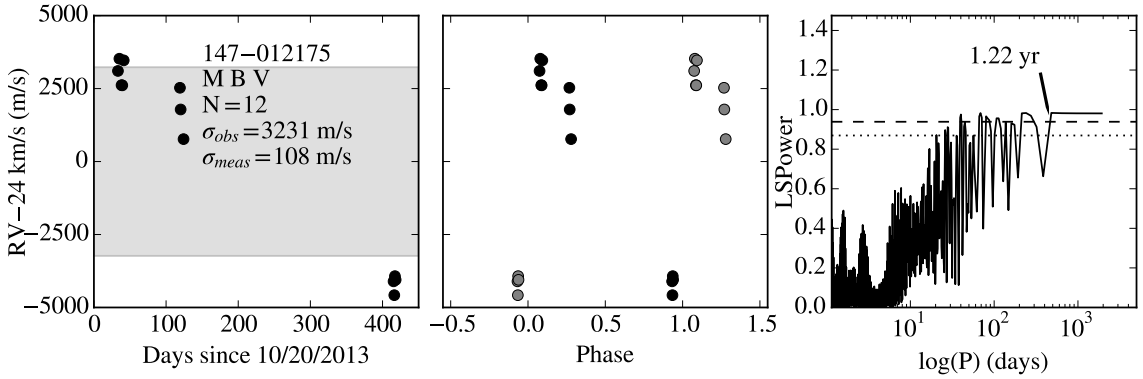

Figure B.21: 147-012175 is a binary member in NGC 2516 with a T_{eff} of 4752^{+17}_{-13} K and a $v_r \sin(i)$ of 10.8 ± 0.2 km/s. It has $\sigma_{obs} = 3231$ m/s and $\sigma_{meas} = 108$ m/s. D03 reports a flux of 4.79 ± 1.09 10^{-6}cts^{-1}cm^{-2}. W04 target 14 is 0.54 arcseconds away and is not reported as binary. They report it is faint in ACIS exposures. In HRC exposures it is moderate with no variability. The most significant periodogram peak is at 1.22 years. Grey points are duplicated data to guide the eye. Errors shown include the mean σ_{jitter}.

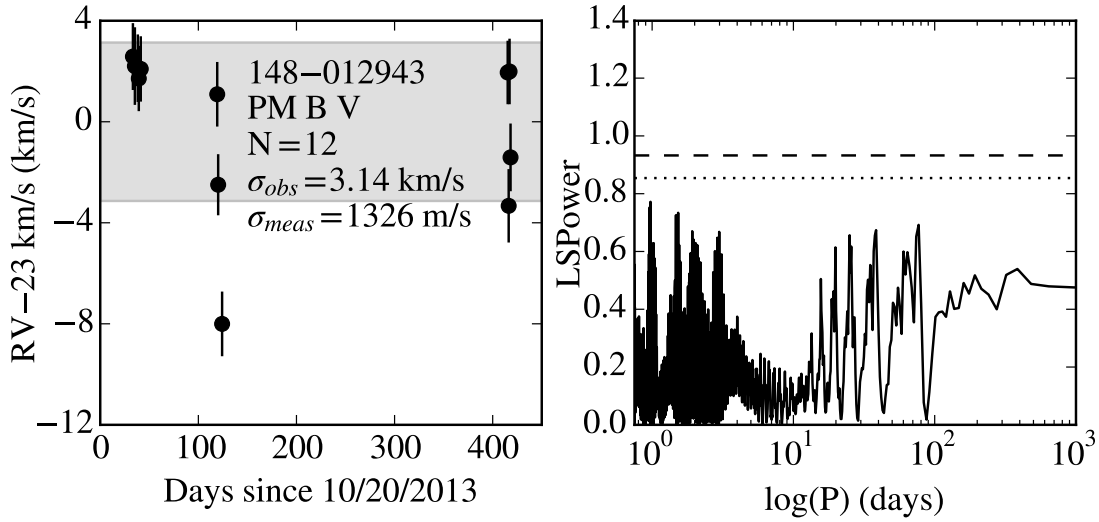

Figure B.22: 148-012943 is a binary possible member in NGC 2516 with a T_{eff} of 6669 ± 48 K and a $v_r \sin(i)$ of 95.1 ± 1.1 km/s. It has σ_{obs} = 3135 m/s and σ_{meas} = 1326 m/s. D03 reports $\log(L_x) \leq 29.95$ erg/s. Errors shown include the mean σ_{jitter}.

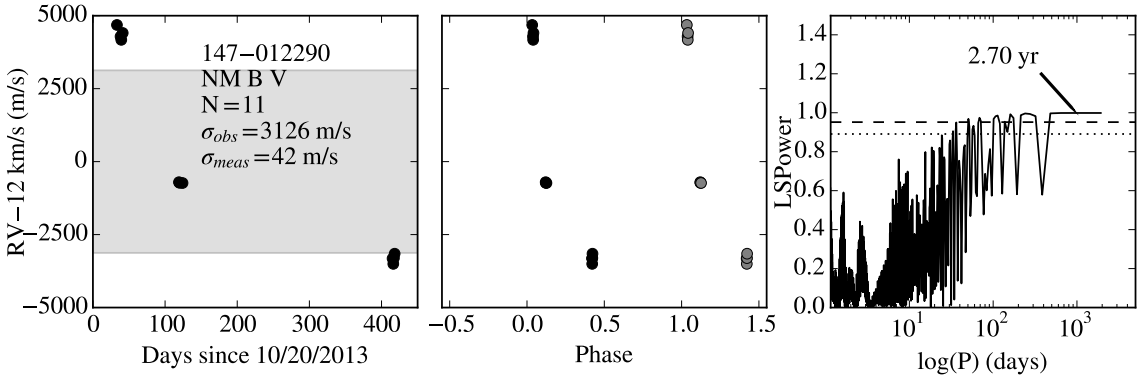

Figure B.23: 147-012290 is a binary non-member in NGC 2516 with a T_{eff} of 5160^{+18}_{-13} K and a $v_r \sin(i)$ of 3.4±0.2 km/s. It has σ_{obs} = 3126 m/s and σ_{meas} = 42 m/s. D03 reports $\log(L_x) \leq 29.19$ erg/s. The most significant periodogram peak is at 2.70 years. Grey points are duplicated data to guide the eye. Errors shown include the mean σ_{jitter}.

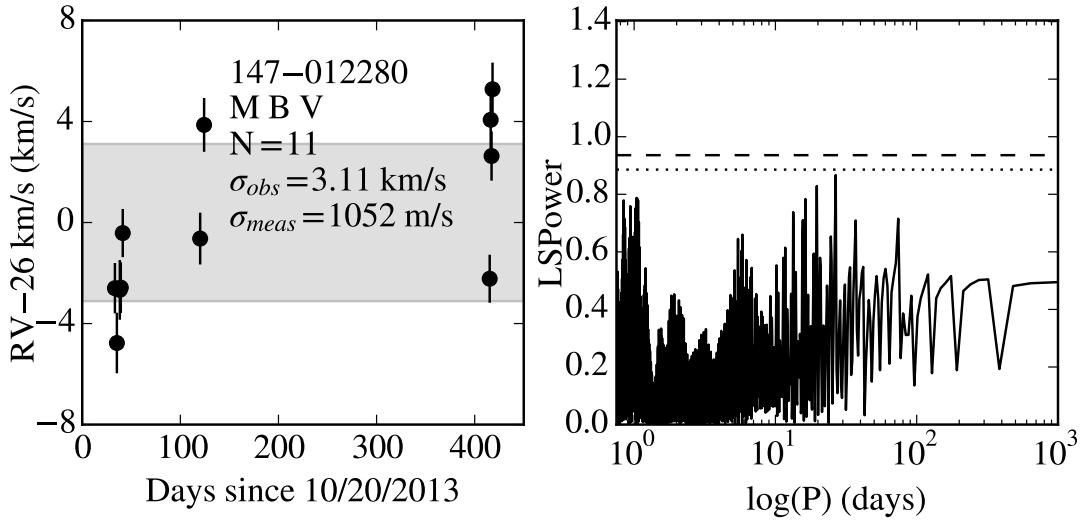

Figure B.24: 147-012280 is a binary member in NGC 2516 with a T_{eff} of 6828 ± 79 K and a $v_r \sin(i)$ of 69.9 ± 0.9 km/s. It has $\sigma_{obs} = 3111$ m/s and $\sigma_{meas} = 1052$ m/s. D03 reports a flux of 11.20 ± 1.16 10^{-6}cts^{-1}cm^{-2}. W04 target 92 is 0.26 arcseconds away and is not reported as binary. They report it is moderate in ACIS exposures with no variability. In HRC exposures it is moderate with no variability. Errors shown include the mean σ_{jitter}.

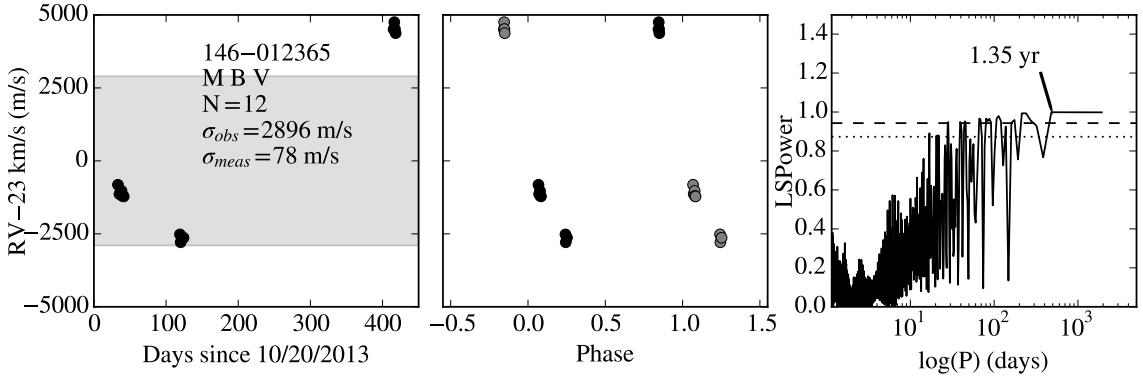

Figure B.25: 146-012365 is a binary member in NGC 2516 with a T_{eff} of 5774^{+21}_{-18} K and a $v_r \sin(i)$ of 6.3 ± 0.1 km/s. It has $\sigma_{obs} = 2896$ m/s and $\sigma_{meas} = 78$ m/s. D03 reports a flux of 3.29 ± 0.94 10^{-6}cts^{-1}cm^{-2}. The most significant periodogram peak is at 1.35 years. Grey points are duplicated data to guide the eye. Errors shown include the mean σ_{jitter}.

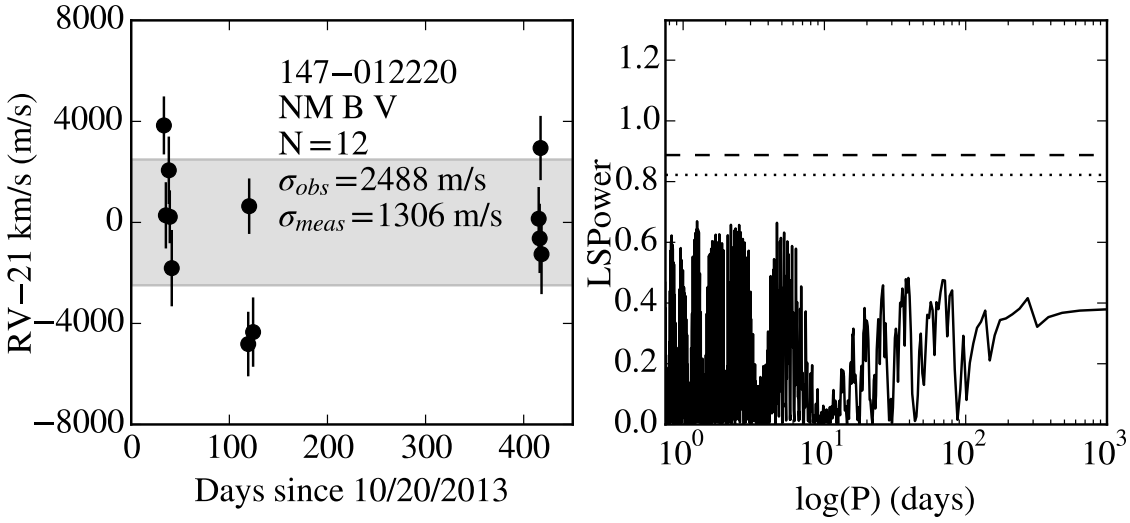

Figure B.26: 147-012220 is a binary non-member in NGC 2516 with a T_{eff} of 6887 ± 80 K and a $v_r \sin(i)$ of 76.5 ± 1.1 km/s. It has $\sigma_{obs} = 2488$ m/s and $\sigma_{meas} = 1306$ m/s. D03 reports $\log(L_x) \leq 28.77$ erg/s. Errors shown include the mean σ_{jitter}.

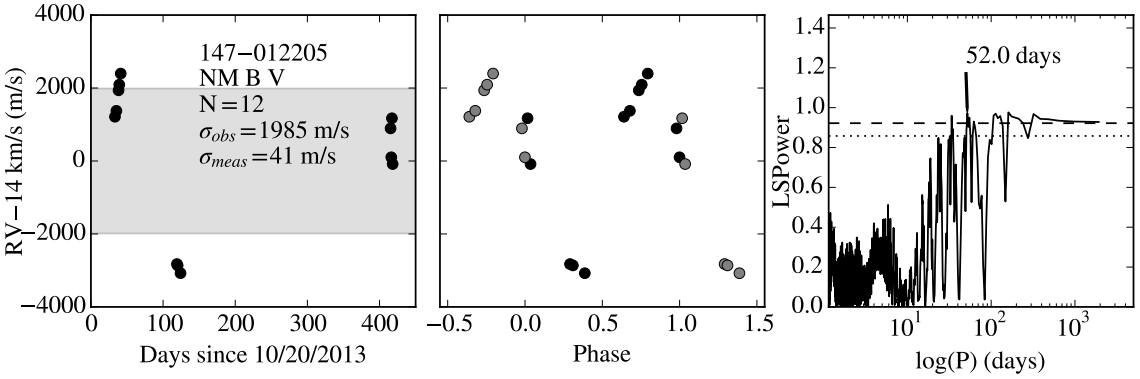

Figure B.27: 147-012205 is a binary non-member in NGC 2516 with a T_{eff} of 5631^{+21}_{-18} K and a $v_r \sin(i)$ of 4.0 ± 0.1 km/s. It has $\sigma_{obs} = 1985$ m/s and $\sigma_{meas} = 41$ m/s. D03 reports $\log(L_x) \leq 28.98$ erg/s. The most significant periodogram peak is at 52.0 days. Grey points are duplicated data to guide the eye. Errors shown include the mean σ_{jitter}.

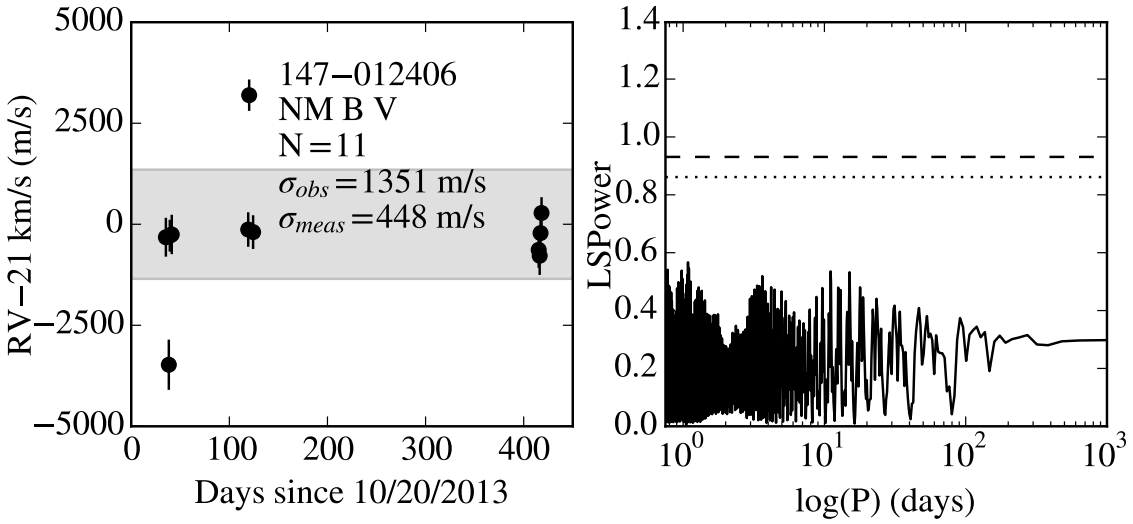

Figure B.28: 147-012406 is a binary non-member in NGC 2516 with a T_{eff} of 6645 ± 67 K and a $v_r \sin(i)$ of 36.2 ± 0.7 km/s. It has σ_{obs} = 1351 m/s and σ_{meas} = 448 m/s. D03 reports a flux of 4.77 ± 0.86 10^{-6}cts^{-1}cm^{-2}. W04 target 182 is 0.28 arcseconds away and is not reported as binary. They report it is bright in ACIS exposures with no variability. In HRC exposures it is moderate with no variability. Errors shown include the mean σ_{jitter}.

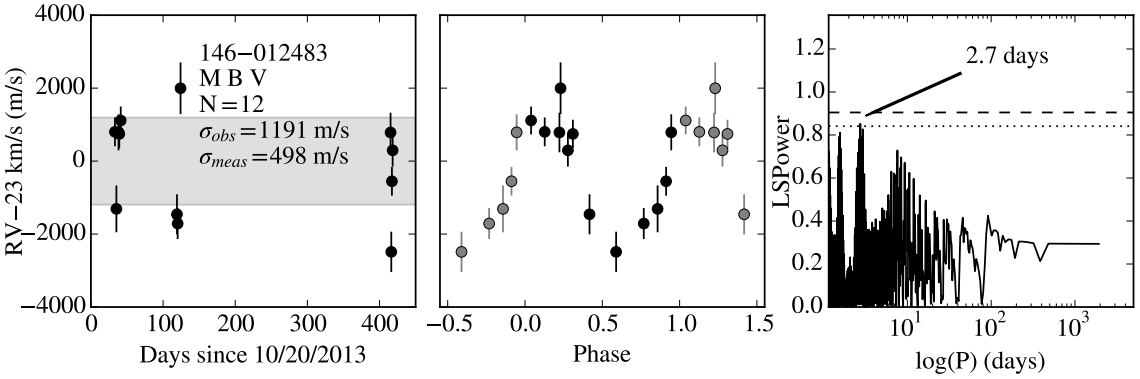

Figure B.29: 146-012483 is a binary member in NGC 2516 with a T_{eff} of 4774 ± 48 K and a $v_r \sin(i)$ of 44.7 ± 0.5 km/s. It has σ_{obs} = 1191 m/s and σ_{meas} = 498 m/s. D03 reports a flux of 23.89 ± 1.86 10^{-6}cts^{-1}cm^{-2}. W04 target 116 is 0.56 arcseconds away and is reported as binary. They report it is bright in ACIS exposures with no variability. In HRC exposures it is bright with no variability. The most significant periodogram peak is at 2.7 days. Grey points are duplicated data to guide the eye. Errors shown include the mean σ_{jitter}.

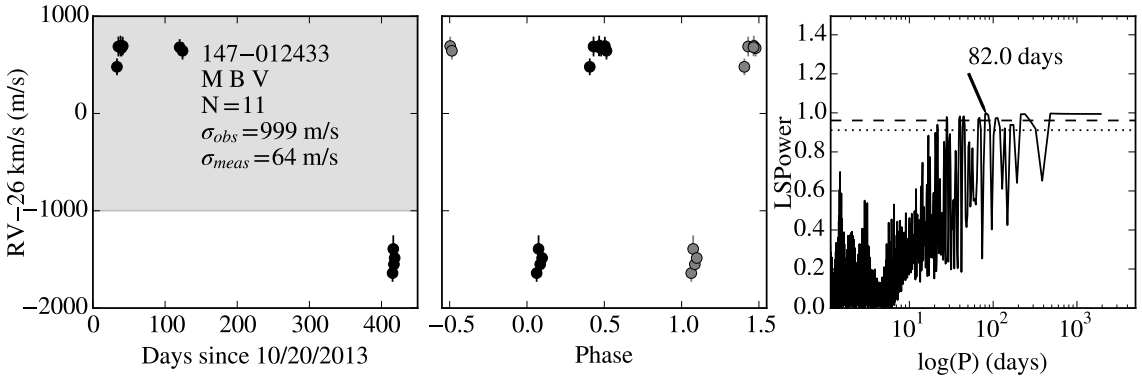

Figure B.30: 147-012433 is a binary member in NGC 2516 with a T_{eff} of 5002 ± 23 K and a $v_r \sin(i)$ of 4.1 ± 0.3 km/s. It has $\sigma_{obs} = 999$ m/s and $\sigma_{meas} = 64$ m/s. D03 reports $\log(L_x) \leq 29.44$ erg/s. The most significant periodogram peak is at 82.0 days. Grey points are duplicated data to guide the eye. Errors shown include the mean σ_{jitter}.

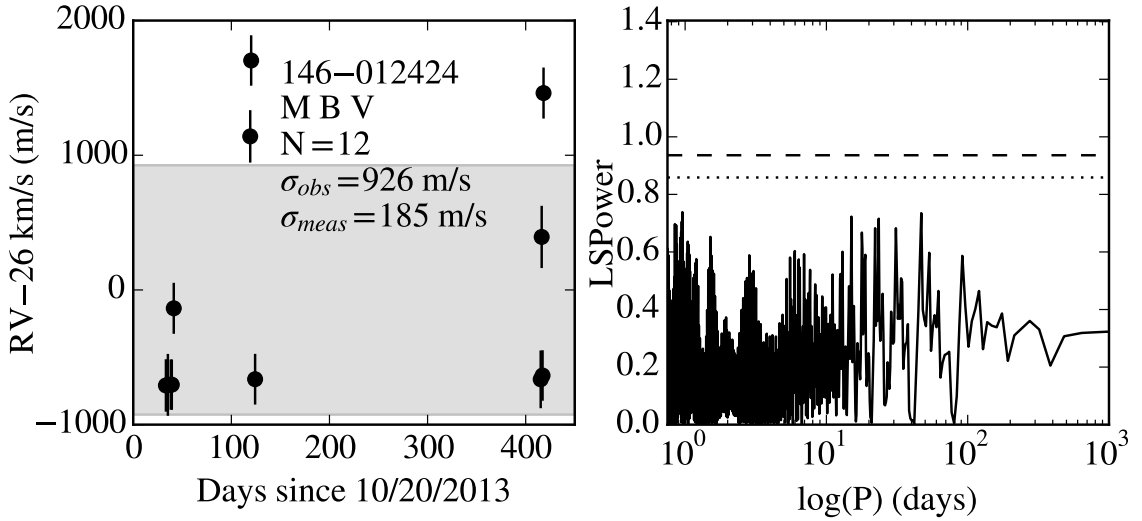

Figure B.31: 146-012424 is a binary member in NGC 2516 with a T_{eff} of 5863 ± 50 K and a $v_r \sin(i)$ of 20.6 ± 0.1 km/s. It has $\sigma_{obs} = 926$ m/s and $\sigma_{meas} = 185$ m/s. D03 reports a flux of 14.51 ± 2.19 10^{-6}cts^{-1}cm^{-2}. W04 target 71 is 0.67 arcseconds away and is reported as binary. They report it is faint in ACIS exposures. In HRC exposures it is bright with stochastic variability. Errors shown include the mean σ_{jitter}.

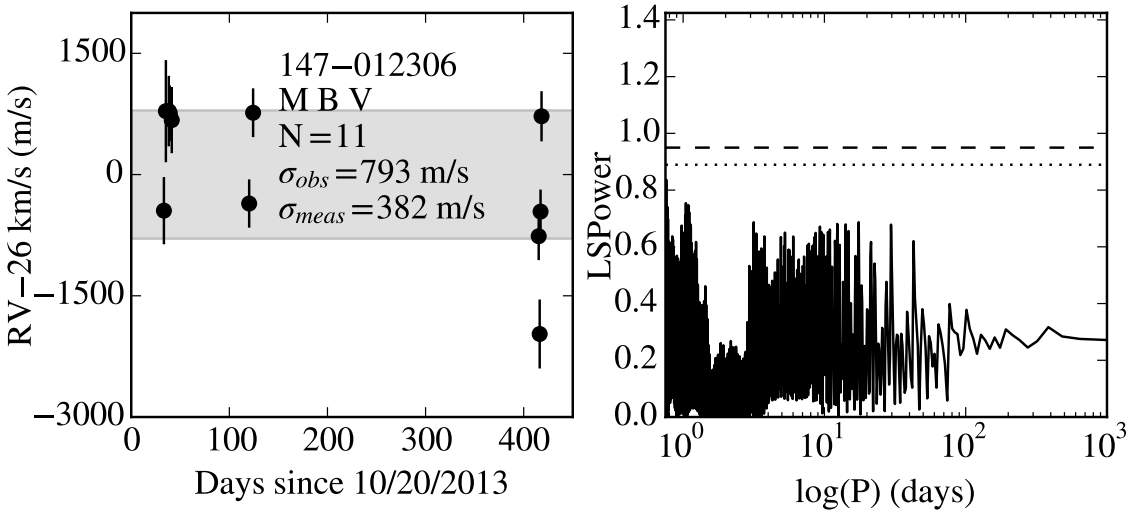

Figure B.32: 147-012306 is a binary member in NGC 2516 with a T_{eff} of 4911 ± 23 K and a $v_r \sin(i)$ of 38.2 ± 0.3 km/s. It has $\sigma_{obs} = 793$ m/s and $\sigma_{meas} = 382$ m/s. D03 reports a flux of 23.88 ± 1.40 10^{-6}cts^{-1}cm^{-2}. W04 target 115 is 0.34 arcseconds away and is not reported as binary. They report it is bright in ACIS exposures with no variability. In HRC exposures it is bright with only quiescent level variability. Errors shown include the mean σ_{jitter}.

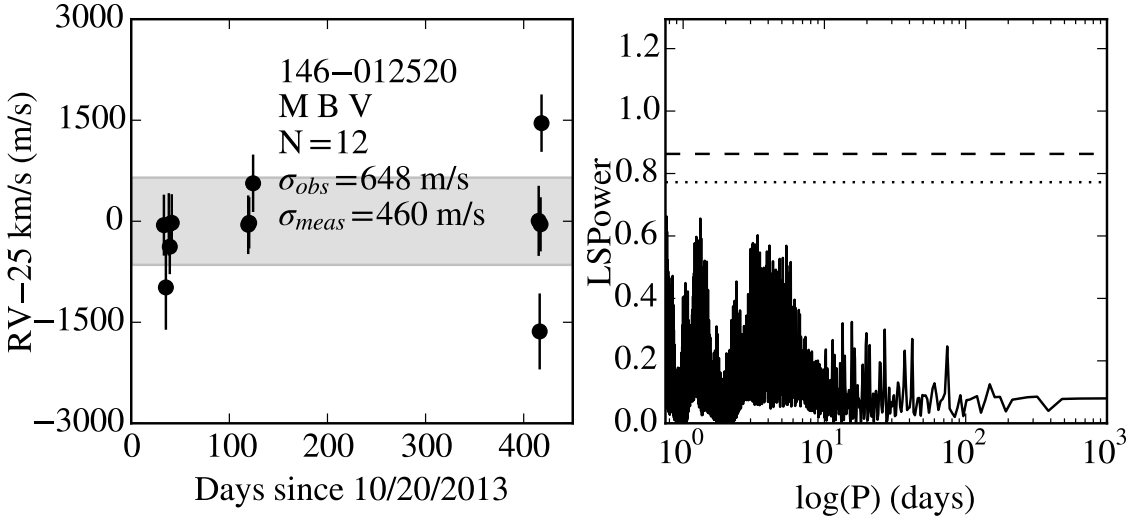

Figure B.33: 146-012520 is a binary member in NGC 2516 with a T_{eff} of 5279 ± 50 K and a $v_r \sin(i)$ of 47.7 ± 0.3 km/s. It has $\sigma_{obs} = 648$ m/s and $\sigma_{meas} = 460$ m/s. D03 reports a flux of 23.81 ± 2.19 10^{-6}cts^{-1}cm^{-2}. W04 target 152 is 0.75 arcseconds away and is not reported as binary. They report it is bright in ACIS exposures with no variability. In HRC exposures it is bright with stochastic variability. Errors shown include the mean σ_{jitter}.

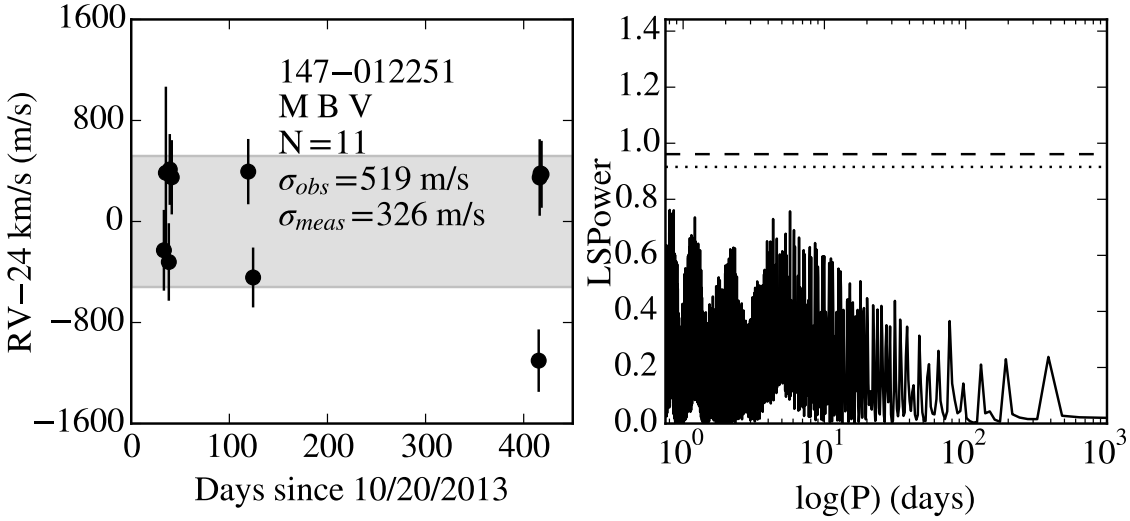

Figure B.34: 147-012251 is a binary member in NGC 2516 with a T_{eff} of 6319^{+36}_{-29} K and a $v_r \sin(i)$ of 24.5 ± 0.2 km/s. It has $\sigma_{obs} = 519$ m/s and $\sigma_{meas} = 326$ m/s. D03 reports a flux of 5.39 ± 1.06 10^{-6}cts^{-1}cm^{-2}. W04 target 61 is 0.73 arcseconds away and is not reported as binary. They report it is faint in ACIS exposures. In HRC exposures it is moderate with no variability. Errors shown include the mean σ_{jitter}.

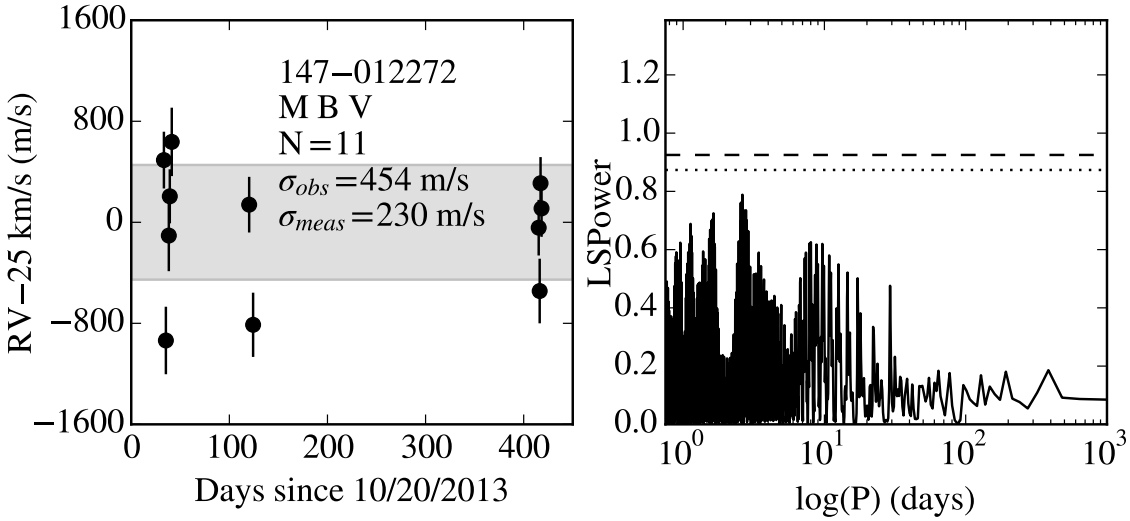

Figure B.35: 147-012272 is a binary member in NGC 2516 with a T_{eff} of 6444 ± 47 K and a $v_r \sin(i)$ of 22.1 ± 0.2 km/s. It has $\sigma_{obs} = 454$ m/s and $\sigma_{meas} = 230$ m/s. D03 reports a flux of 3.60 ± 0.65 10^{-6}cts^{-1}cm^{-2}. Errors shown include the mean σ_{jitter}.

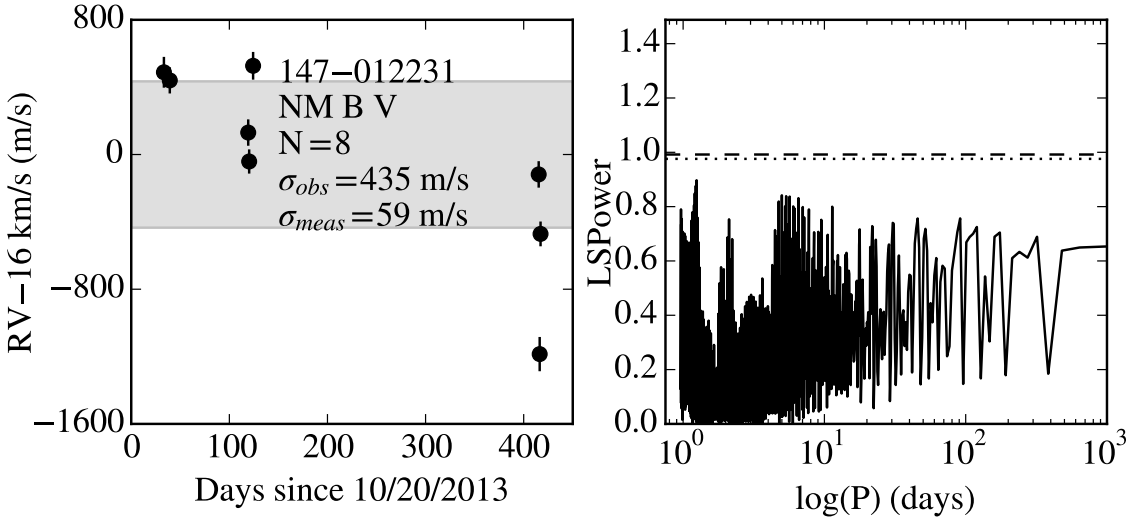

Figure B.36: 147-012231 is a binary non-member in NGC 2516 with a T_{eff} of 5250^{+26}_{-22} K and a $v_r \sin(i)$ of 4.5 ± 0.4 km/s. It has $\sigma_{obs} = 435$ m/s and $\sigma_{meas} = 59$ m/s. D03 reports $\log(L_x) \leq 28.99$ erg/s. Errors shown include the mean σ_{jitter}.

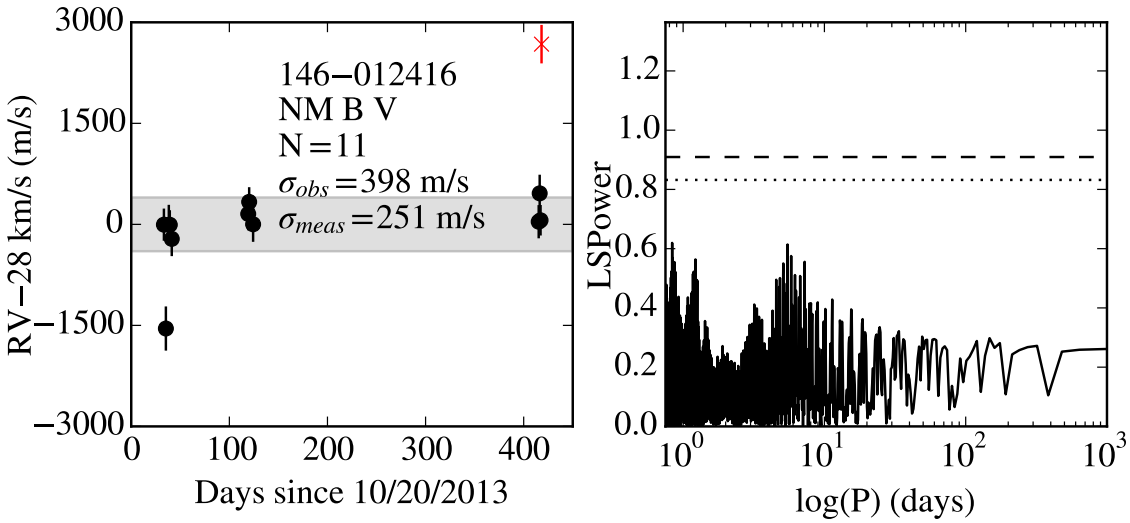

Figure B.37: 146-012416 is a binary non-member in NGC 2516 with a T_{eff} of 6118 ± 44 K and a $v_r \sin(i)$ of 25.0 ± 0.2 km/s. It has $\sigma_{obs} = 398$ m/s and $\sigma_{meas} = 251$ m/s. D03 reports a flux of 25.29 ± 1.88 10^{-6}cts^{-1}cm^{-2}. W04 target 60 is 0.42 arcseconds away and is reported as binary. They report it is bright in ACIS exposures with quiescent level variability. In HRC exposures it is bright with no variability. Red Xs are epochs excluded as $>3\sigma_{obs}$ outliers. Errors shown include the mean σ_{jitter}.

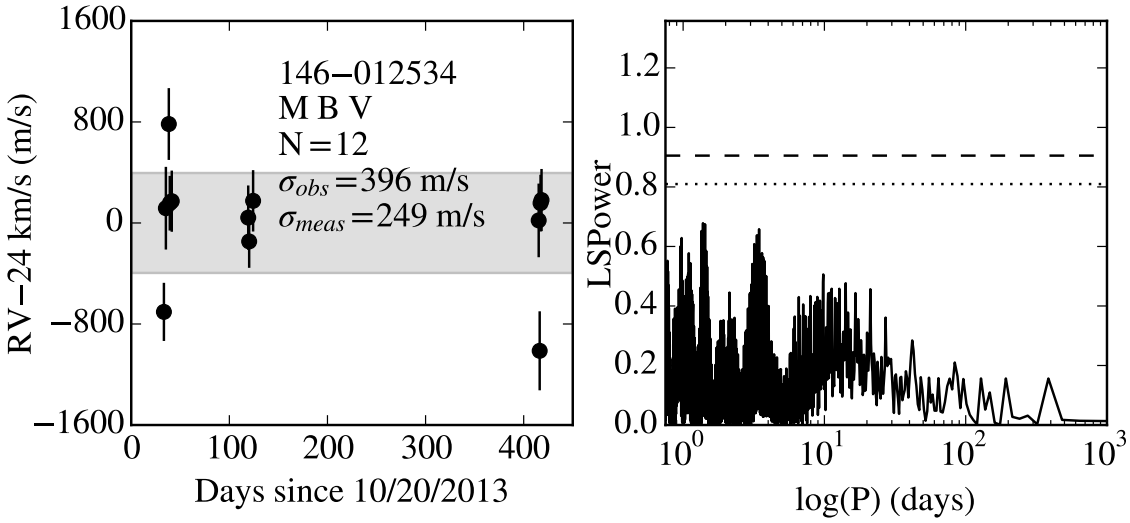

Figure B.38: 146-012534 is a binary member in NGC 2516 with a T_{eff} of 5141 ± 19 K and a $v_r \sin(i)$ of 29.8 ± 0.2 km/s. It has $\sigma_{obs} = 396$ m/s and $\sigma_{meas} = 249$ m/s. D03 reports a flux of 22.74 ± 2.05 10^{-6}cts^{-1}cm^{-2}. W04 target 156 is 0.45 arcseconds away and is not reported as binary. They report it is bright in ACIS exposures with stochastic variability. In HRC exposures it is bright with stochastic variability. Errors shown include the mean σ_{jitter}.

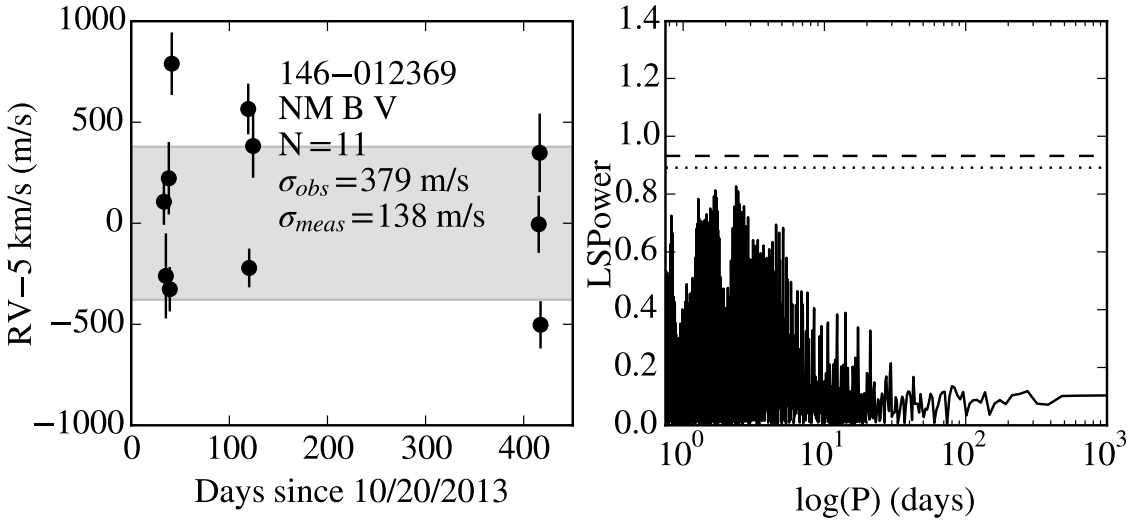

Figure B.39: 146-012369 is a binary non-member in NGC 2516 with a T_{eff} of 5791 ± 64 K and a $v_r \sin(i)$ of 7.2 ± 0.8 km/s. It has $\sigma_{obs} = 379$ m/s and $\sigma_{meas} = 138$ m/s. D03 reports a flux of 19.40 ± 1.23 10^{-6}cts^{-1}cm^{-2}. W04 target 27 is 0.61 arcseconds away and is not reported as binary. They report it is bright in ACIS exposures with flaring variability. In HRC exposures it is moderate with no variability. Errors shown include the mean σ_{jitter}.

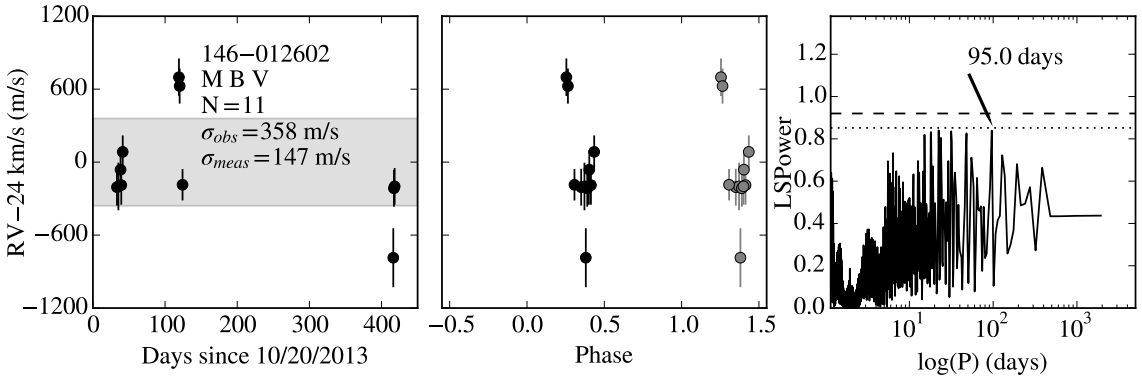

Figure B.40: 146-012602 is a binary member in NGC 2516 with a T_{eff} of 4775^{+18}_{-15} K and a $v_r \sin(i)$ of 14.8 ± 0.2 km/s. It has $\sigma_{obs} = 358$ m/s and $\sigma_{meas} = 147$ m/s. The most significant periodogram peak is at 95.0 days. Grey points are duplicated data to guide the eye. Errors shown include the mean σ_{jitter}.

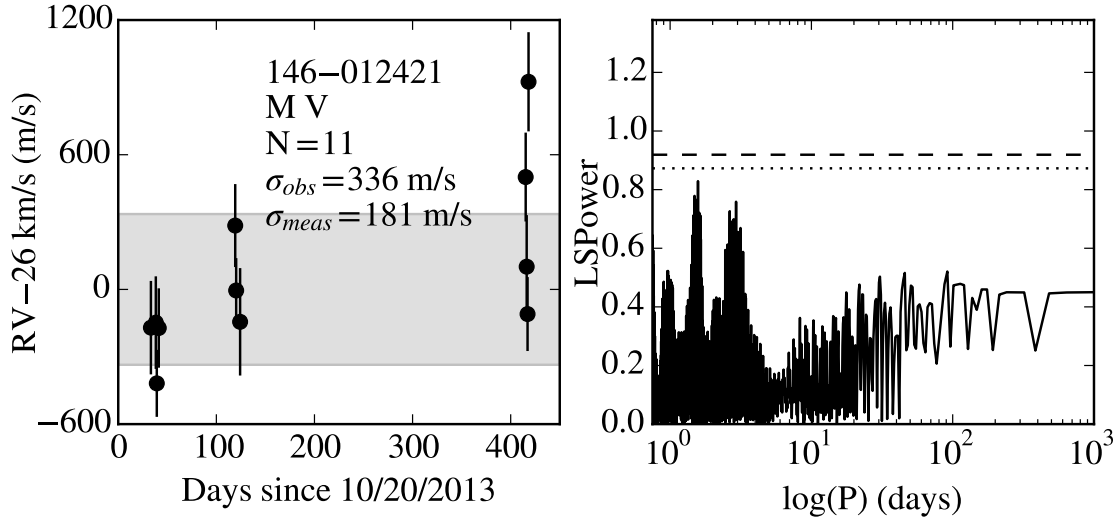

Figure B.41: 146-012421 is a member in NGC 2516 with a T_{eff} of 5009 ± 25 K and a $v_r \sin(i)$ of 18.0 ± 0.2 km/s. It has $\sigma_{obs} = 336$ m/s and $\sigma_{meas} = 181$ m/s. D03 reports a flux of 11.17 ± 1.31 10^{-6}cts^{-1}cm^{-2}. W04 target 67 is 0.71 arcseconds away and is not reported as binary. They report it is bright in ACIS exposures with no variability. In HRC exposures it is moderate with stochastic variability. Errors shown include the mean σ_{jitter}.

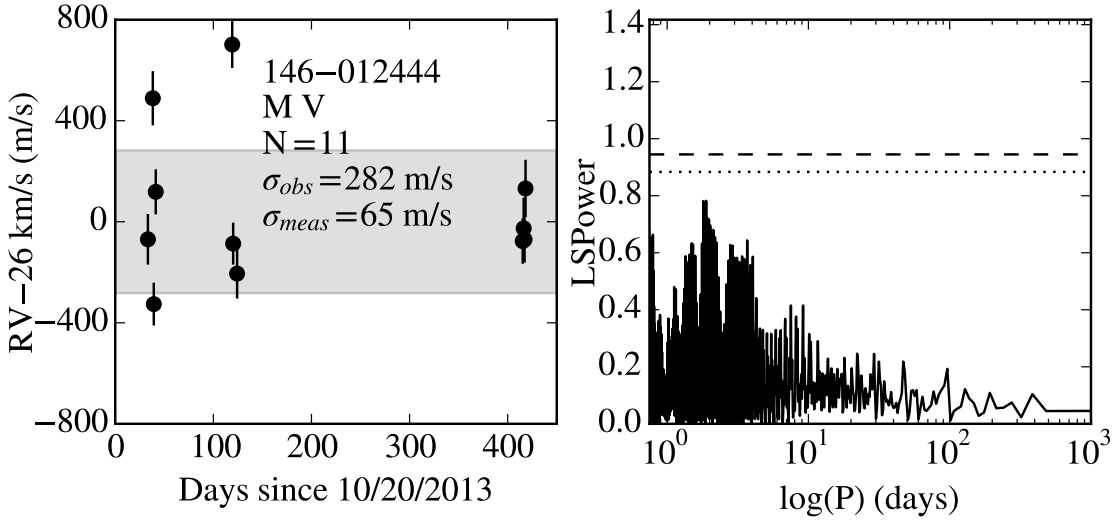

Figure B.42: 146-012444 is a member in NGC 2516 with a T_{eff} of 4850^{+18}_{-13} K and a $v_r \sin(i)$ of 5.0 ± 0.2 km/s. It has $\sigma_{obs} = 282$ m/s and $\sigma_{meas} = 65$ m/s. D03 reports $\log(L_x) \leq 28.84$ erg/s. Errors shown include the mean σ_{jitter}.

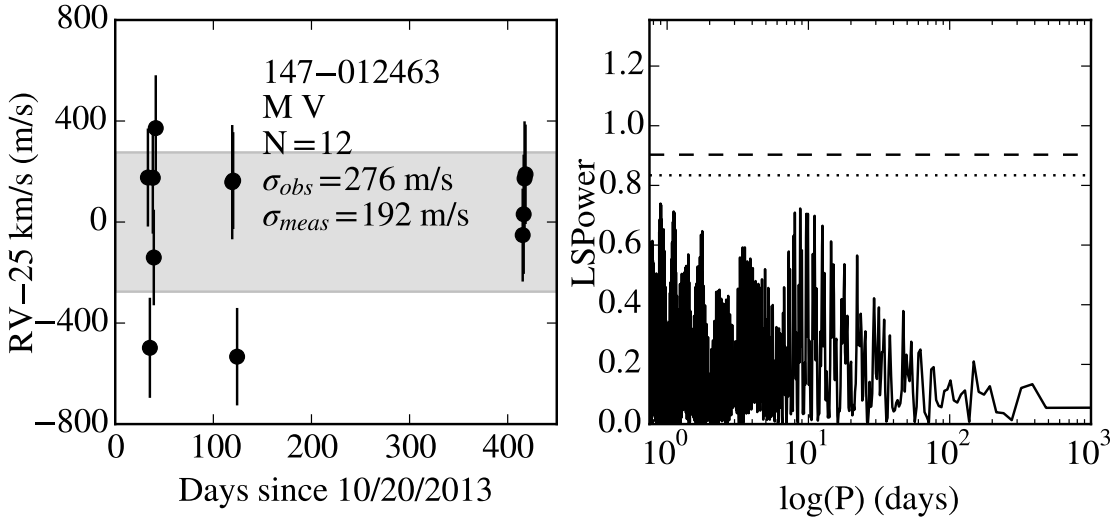

Figure B.43: 147-012463 is a member in NGC 2516 with a T_{eff} of 6199^{+35}_{-30} K and a $v_r \sin(i)$ of $20.9^{+0.2}_{-0.1}$ km/s. It has $\sigma_{obs} = 276$ m/s and $\sigma_{meas} = 192$ m/s. D03 reports $\log(L_x) \leq 30.29$ erg/s. Errors shown include the mean σ_{jitter}.

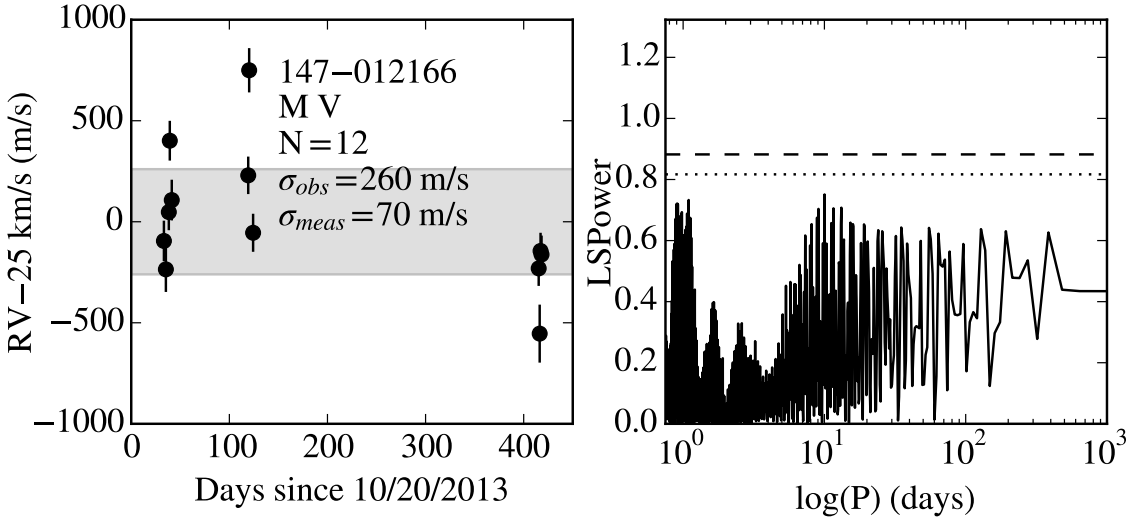

Figure B.44: 147-012166 is a member in NGC 2516 with a T_{eff} of 4693 ± 18 K and a $v_r \sin(i)$ of 5.4 ± 0.2 km/s. It has $\sigma_{obs} = 260$ m/s and $\sigma_{meas} = 70$ m/s. D03 reports a flux of 5.40 ± 2.01 10^{-6}cts^{-1}cm^{-2}. Errors shown include the mean σ_{jitter}.

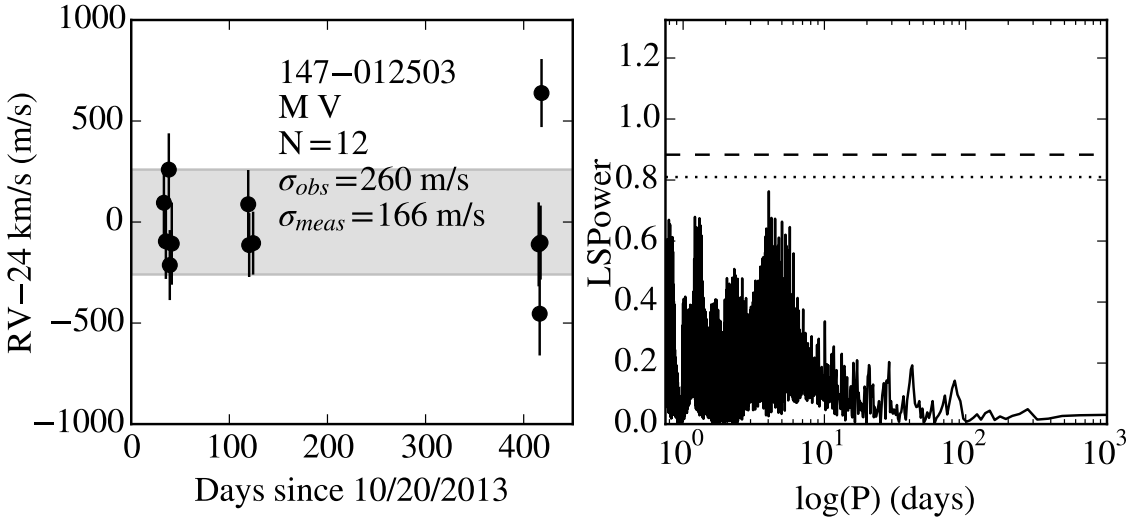

Figure B.45: 147-012503 is a member in NGC 2516 with a T_{eff} of 6133^{+35}_{-27} K and a $v_r \sin(i)$ of 18.1 ± 0.2 km/s. It has $\sigma_{obs} = 260$ m/s and $\sigma_{meas} = 166$ m/s. Errors shown include the mean σ_{jitter}.

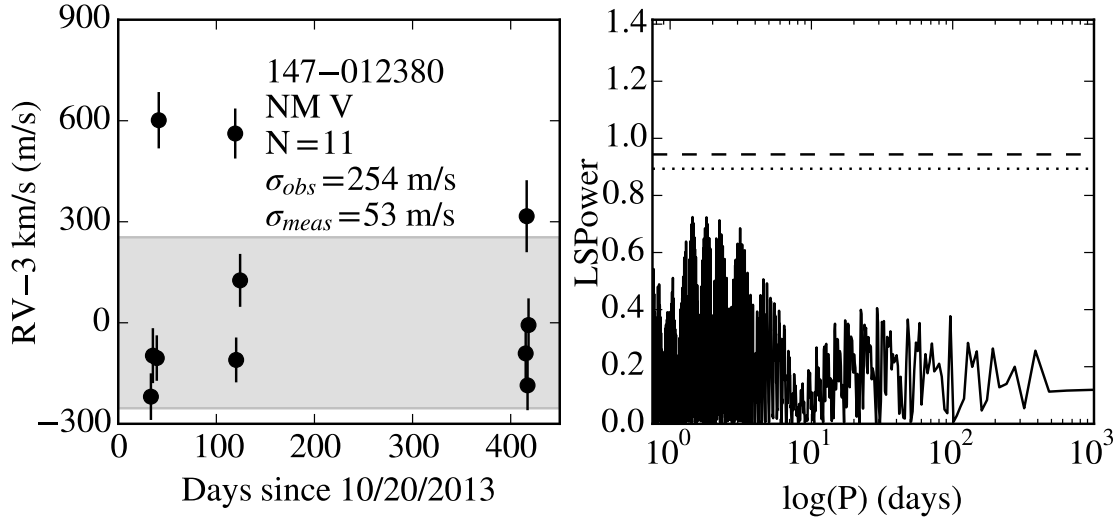

Figure B.46: 147-012380 is a non-member in NGC 2516 with a T_{eff} of 5030^{+18}_{-14} K and a $v_r \sin(i)$ of 3.2 ± 0.2 km/s. It has $\sigma_{obs} = 254$ m/s and $\sigma_{meas} = 53$ m/s. D03 reports $\log(L_x) \leq 29.07$ erg/s. Errors shown include the mean σ_{jitter}.

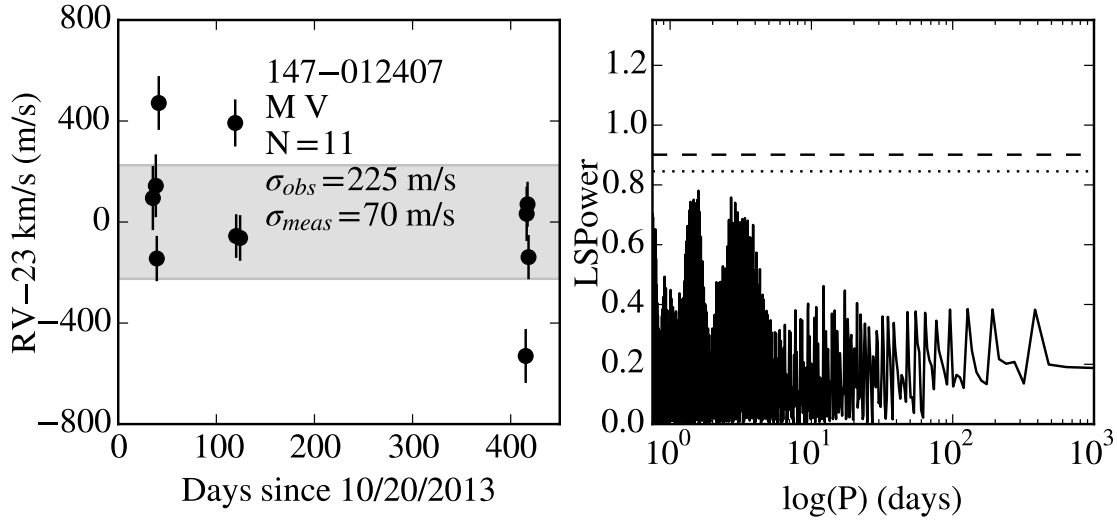

Figure B.47: 147-012407 is a member in NGC 2516 with a T_{eff} of 5057^{+18}_{-13} K and a $v_r \sin(i)$ of 7.3 ± 0.2 km/s. It has $\sigma_{obs} = 225$ m/s and $\sigma_{meas} = 70$ m/s. D03 reports a flux of 4.10 ± 1.75 10^{-6}cts^{-1}cm^{-2}. Errors shown include the mean σ_{jitter}.

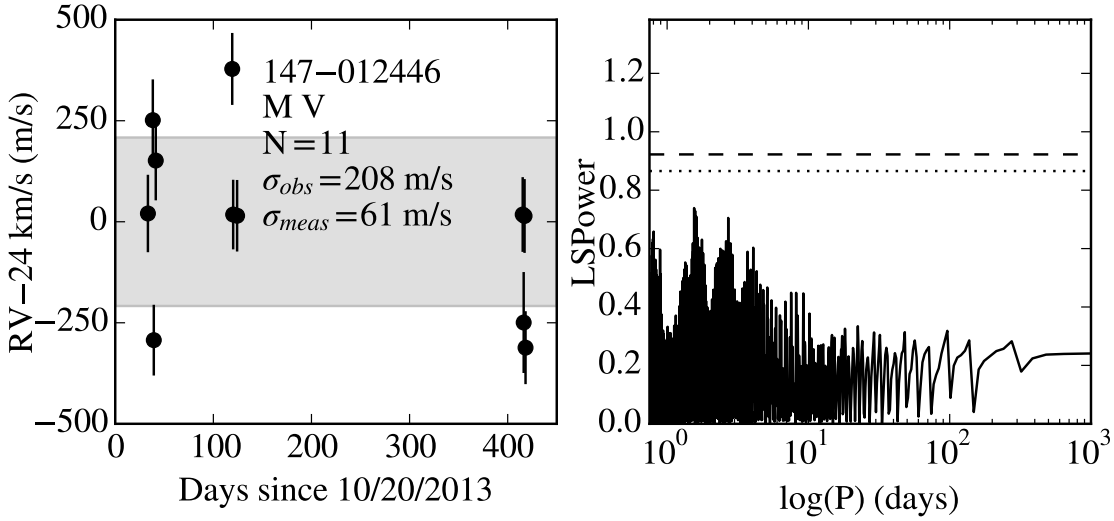

Figure B.48: 147-012446 is a member in NGC 2516 with a T_{eff} of 5030^{+18}_{-16} K and a $v_r \sin(i)$ of 6.3 ± 0.2 km/s. It has $\sigma_{obs} = 208$ m/s and $\sigma_{meas} = 61$ m/s. D03 reports $\log(L_x) \leq 30.09$ erg/s. Errors shown include the mean σ_{jitter}.

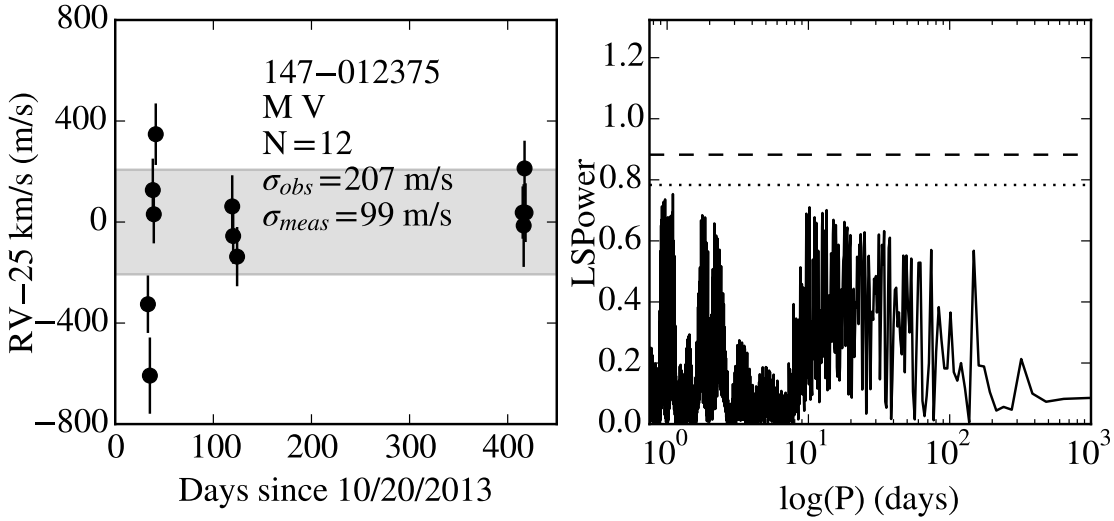

Figure B.49: 147-012375 is a member in NGC 2516 with a T_{eff} of 4759 ± 25 K and a $v_r \sin(i)$ of 10.7 ± 0.2 km/s. It has $\sigma_{obs} = 207$ m/s and $\sigma_{meas} = 99$ m/s. Errors shown include the mean σ_{jitter}.

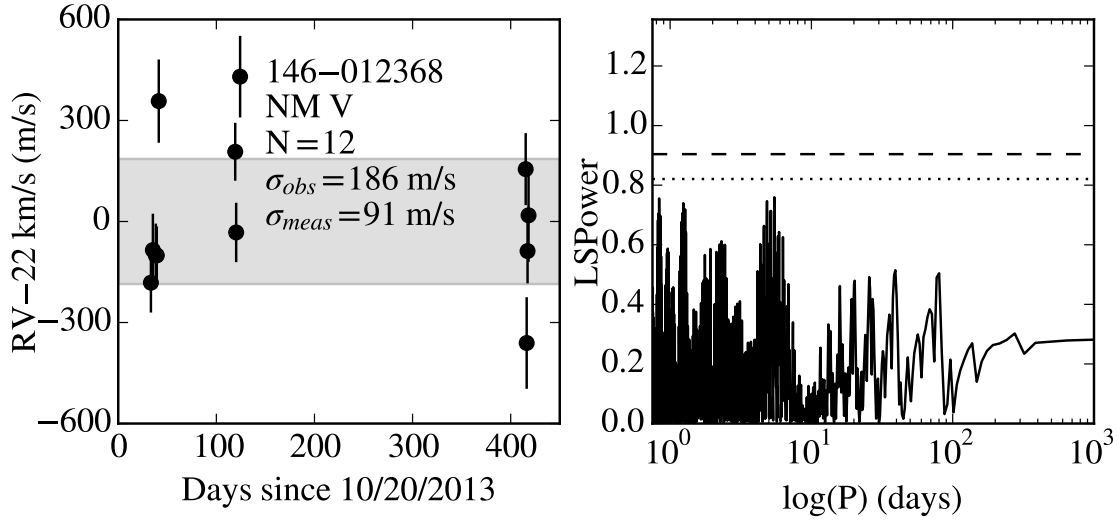

Figure B.50: 146-012368 is a non-member in NGC 2516 with a T_{eff} of 5609 ± 25 K and a $v_r \sin(i)$ of 6.5 ± 0.2 km/s. It has $\sigma_{obs} = 186$ m/s and $\sigma_{meas} = 91$ m/s. D03 reports a flux of $3.19 \pm 0.93\ 10^{-6}$cts^{-1}cm^{-2}. W04 target 24 is 1.95 arcseconds away and is reported as binary. They report it is faint in ACIS exposures. In HRC exposures it is moderate with no variability. Errors shown include the mean σ_{jitter}.

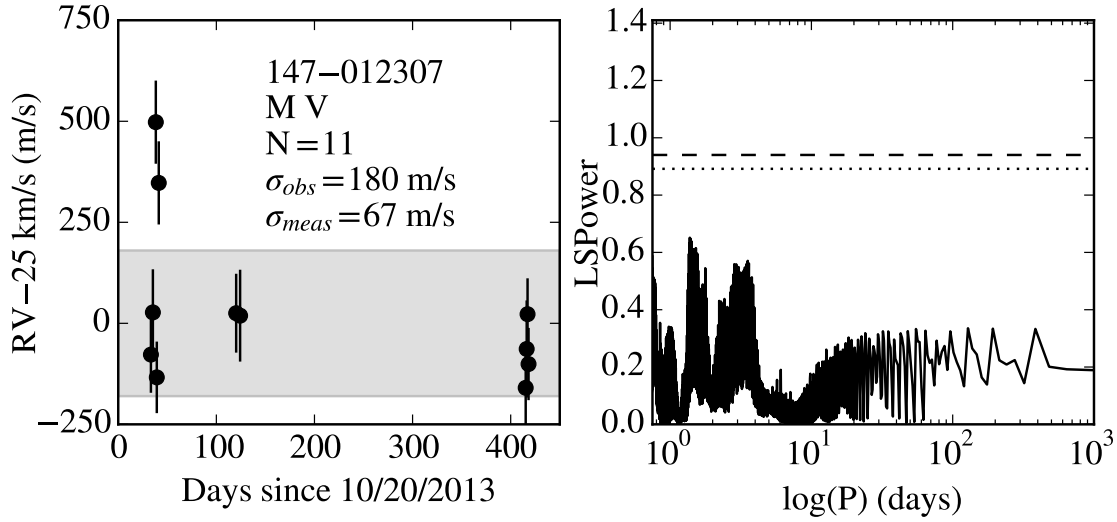

Figure B.51: 147-012307 is a member in NGC 2516 with a T_{eff} of 4940^{+18}_{-14} K and a $v_r \sin(i)$ of 6.0 ± 0.2 km/s. It has $\sigma_{obs} = 180$ m/s and $\sigma_{meas} = 67$ m/s. D03 reports a flux of $2.43 \pm 0.52\ 10^{-6}$cts^{-1}cm^{-2}. Errors shown include the mean σ_{jitter}.

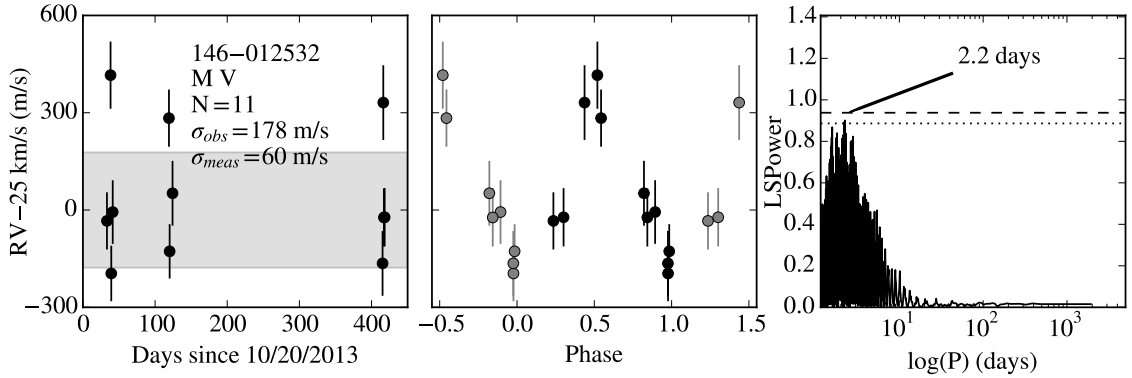

Figure B.52: 146-012532 is a member in NGC 2516 with a T_{eff} of 4854^{+18}_{-14} K and a $v_r \sin(i)$ of 4.7 ± 0.2 km/s. It has $\sigma_{obs} = 178$ m/s and $\sigma_{meas} = 60$ m/s. D03 reports a flux of 1.90 ± 0.86 10^{-6}cts^{-1}cm^{-2}. The most significant periodogram peak is at 2.2 days. Grey points are duplicated data to guide the eye. Errors shown include the mean σ_{jitter}.

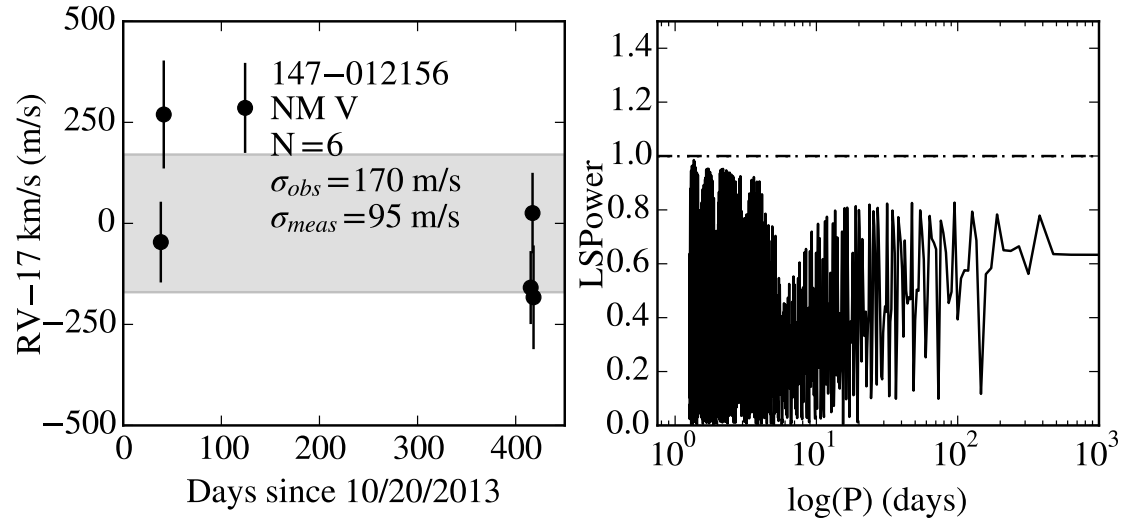

Figure B.53: 147-012156 is a non-member in NGC 2516 with a T_{eff} of 5125^{+24}_{-19} K and a $v_r \sin(i)$ of 4.9 ± 0.5 km/s. It has $\sigma_{obs} = 170$ m/s and $\sigma_{meas} = 95$ m/s. D03 reports $\log(L_x) \leq 29.37$ erg/s. Errors shown include the mean σ_{jitter}.

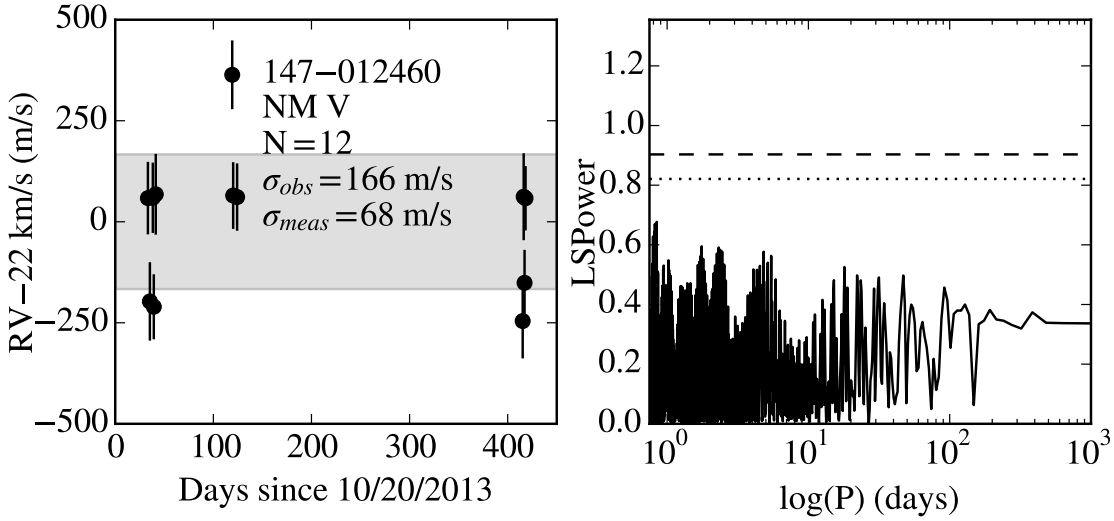

Figure B.54: 147-012460 is a non-member in NGC 2516 with a T_{eff} of 5163^{+17}_{-15} K and a $v_r \sin(i)$ of 7.3 ± 0.1 km/s. It has $\sigma_{obs} = 166$ m/s and $\sigma_{meas} = 68$ m/s. D03 reports $\log(L_x) \leq 29.99$ erg/s. Errors shown include the mean σ_{jitter}.

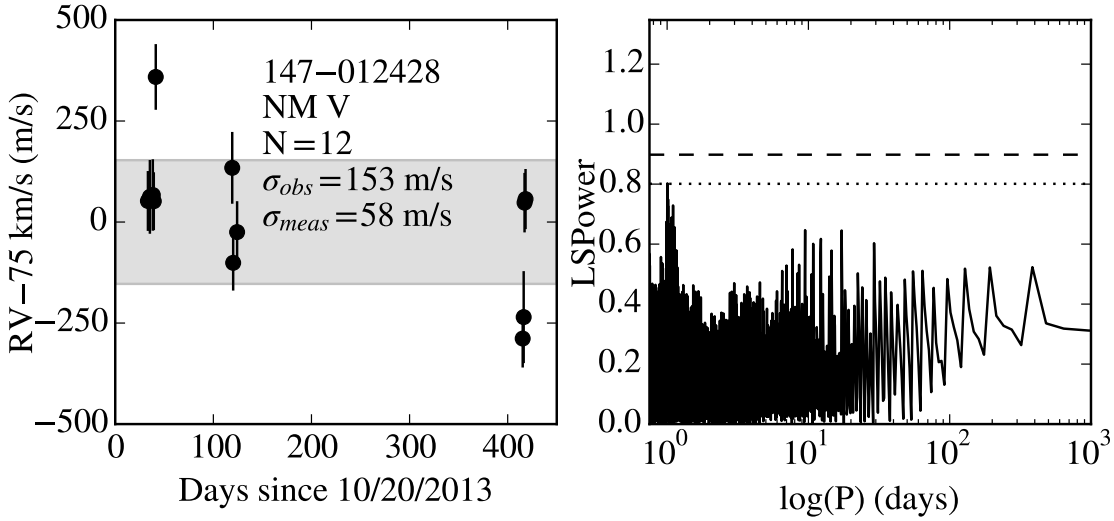

Figure B.55: 147-012428 is a non-member in NGC 2516 with a T_{eff} of 5240 ± 18 K and a $v_r \sin(i)$ of 2.9 ± 0.2 km/s. It has $\sigma_{obs} = 153$ m/s and $\sigma_{meas} = 58$ m/s. D03 reports $\log(L_x) \leq 29.89$ erg/s. Errors shown include the mean σ_{jitter}.

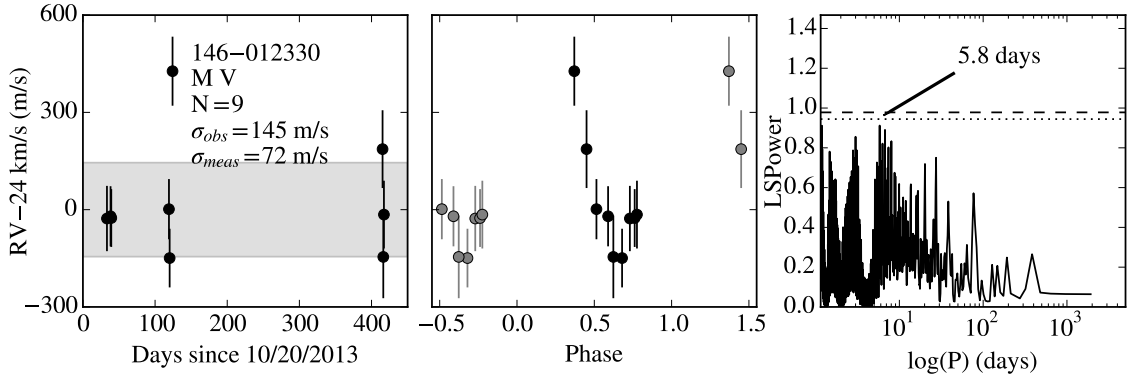

Figure B.56: 146-012330 is a member in NGC 2516 with a T_{eff} of 5058^{+20}_{-15} K and a $v_r \sin(i)$ of 6.4 ± 0.2 km/s. It has $\sigma_{obs} = 145$ m/s and $\sigma_{meas} = 72$ m/s. D03 reports $\log(L_x) \leq 29.24$ erg/s. The most significant periodogram peak is at 5.8 days. Grey points are duplicated data to guide the eye. Errors shown include the mean σ_{jitter}.

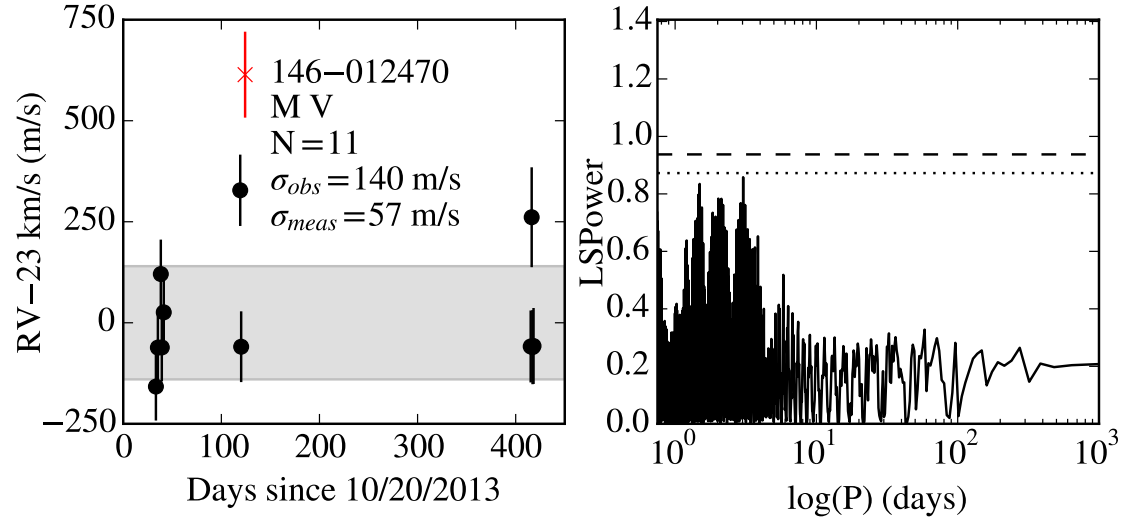

Figure B.57: 146-012470 is a member in NGC 2516 with a T_{eff} of 5307^{+22}_{-19} K and a $v_r \sin(i)$ of 3.9 ± 0.1 km/s. It has $\sigma_{obs} = 140$ m/s and $\sigma_{meas} = 57$ m/s. Red Xs are epochs excluded as $>3\sigma_{obs}$ outliers. Errors shown include the mean σ_{jitter}.

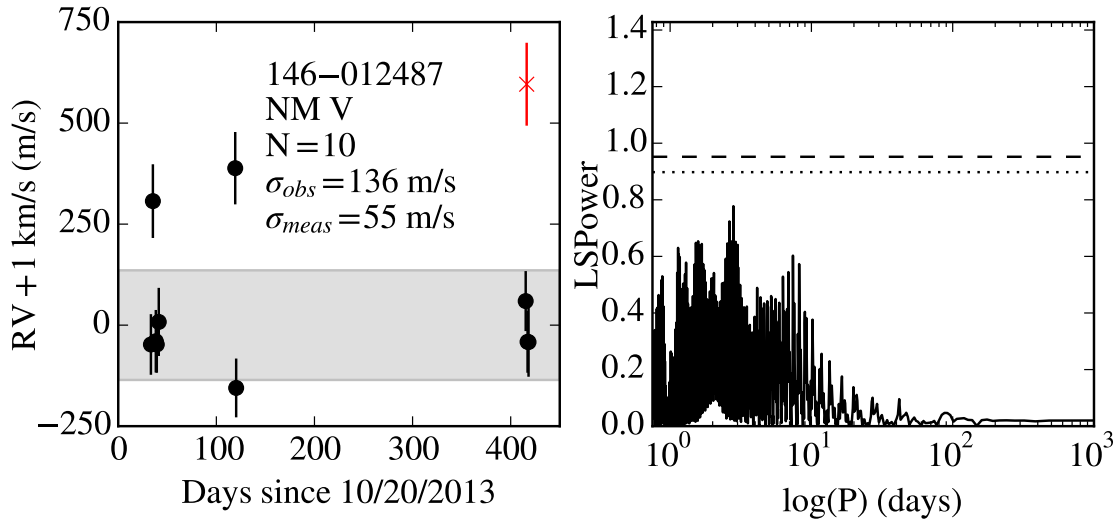

Figure B.58: 146-012487 is a non-member in NGC 2516 with a T_{eff} of 5058^{+19}_{-14} K and a $v_r \sin(i)$ of 3.7 ± 0.3 km/s. It has $\sigma_{obs} = 136$ m/s and $\sigma_{meas} = 55$ m/s. D03 reports a flux of 1.83 ± 0.83 10^{-6}cts^{-1}cm^{-2}. Red Xs are epochs excluded as $>3\sigma_{obs}$ outliers. Errors shown include the mean σ_{jitter}.

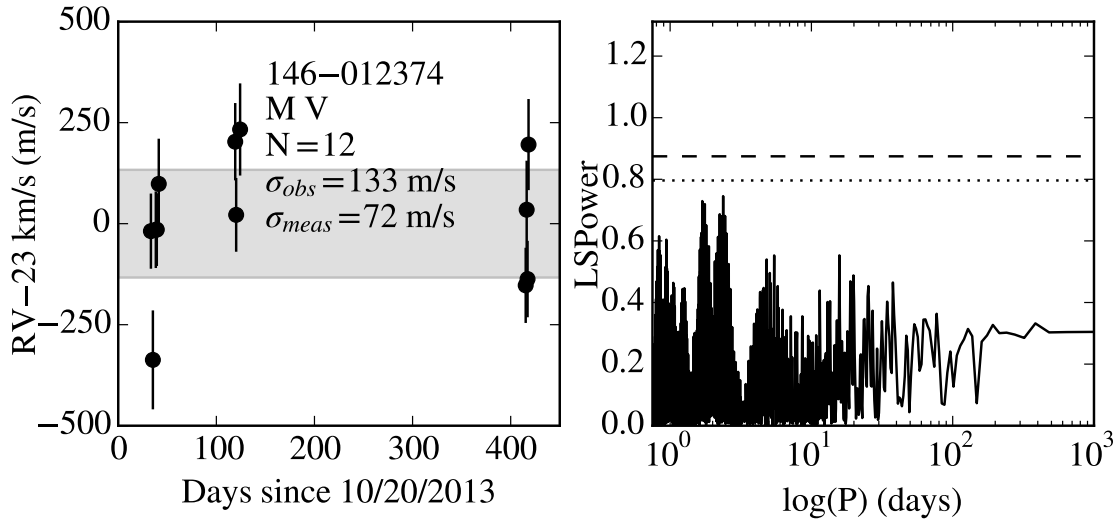

Figure B.59: 146-012374 is a member in NGC 2516 with a T_{eff} of 5516 ± 25 K and a $v_r \sin(i)$ of 6.0 ± 0.1 km/s. It has $\sigma_{obs} = 133$ m/s and $\sigma_{meas} = 72$ m/s. D03 reports a flux of 2.93 ± 0.53 10^{-6}cts^{-1}cm^{-2}. Errors shown include the mean σ_{jitter}.

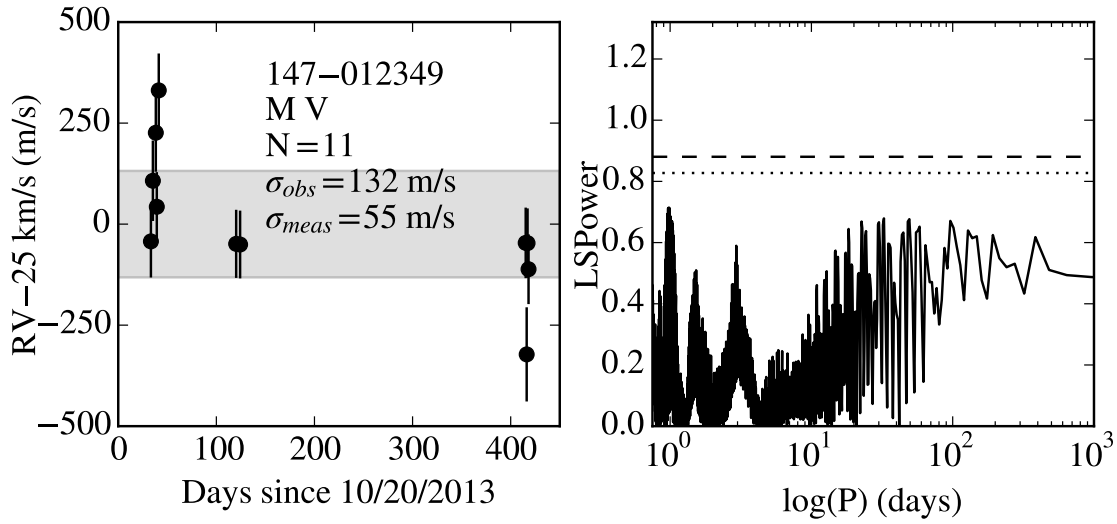

Figure B.60: 147-012349 is a member in NGC 2516 with a T_{eff} of 5162^{+18}_{-13} K and a $v_r \sin(i)$ of 4.6 ± 0.2 km/s. It has $\sigma_{obs} = 132$ m/s and $\sigma_{meas} = 55$ m/s. D03 reports a flux of 1.80 ± 0.53 10^{-6}cts^{-1}cm^{-2}. Errors shown include the mean σ_{jitter}.

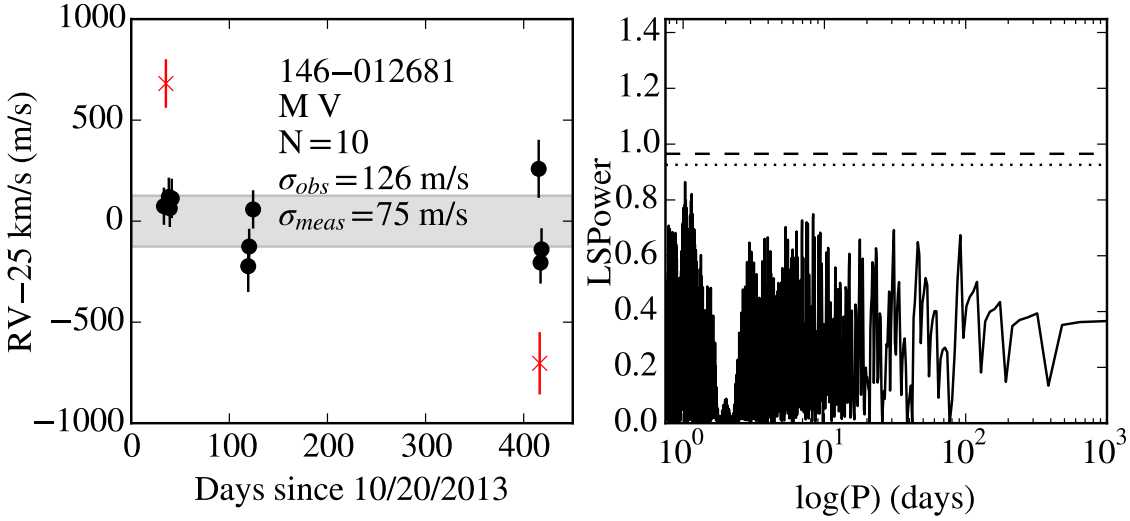

Figure B.61: 146-012681 is a member in NGC 2516 with a T_{eff} of 4881 ± 20 K and a $v_r \sin(i)$ of 5.9 ± 0.2 km/s. It has $\sigma_{obs} = 126$ m/s and $\sigma_{meas} = 75$ m/s. D03 reports $\log(L_x) \leq 30.39$ erg/s. Red Xs are epochs excluded as $>3\sigma_{obs}$ outliers. Errors shown include the mean σ_{jitter}.

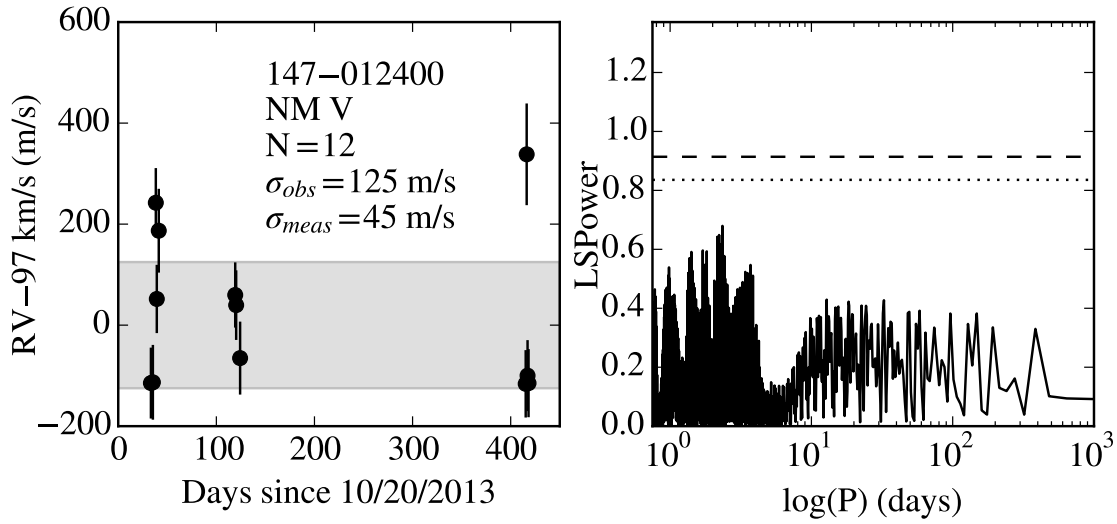

Figure B.62: 147-012400 is a non-member in NGC 2516 with a T_{eff} of 5040^{+17}_{-13} K and a $v_r \sin(i)$ of 2.7 ± 0.1 km/s. It has $\sigma_{obs} = 125$ m/s and $\sigma_{meas} = 45$ m/s. D03 reports $\log(L_x) \leq 29.60$ erg/s. Errors shown include the mean σ_{jitter}.

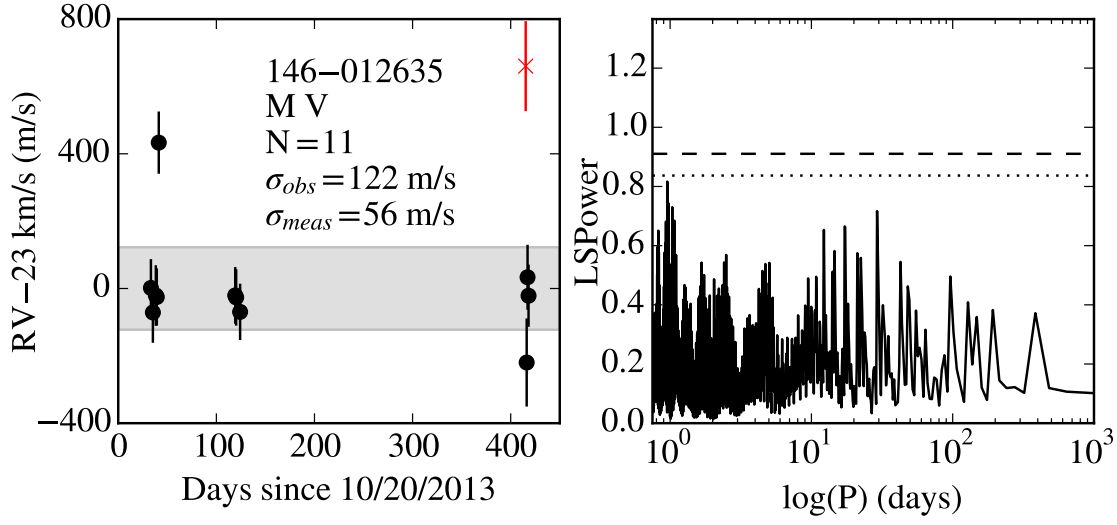

Figure B.63: 146-012635 is a member in NGC 2516 with a T_{eff} of 4738^{+18}_{-13} K and a $v_r \sin(i)$ of 5.6 ± 0.2 km/s. It has $\sigma_{obs} = 122$ m/s and $\sigma_{meas} = 56$ m/s. D03 reports $\log(L_x) \leq 29.56$ erg/s. Red Xs are epochs excluded as $>3\sigma_{obs}$ outliers. Errors shown include the mean σ_{jitter}.

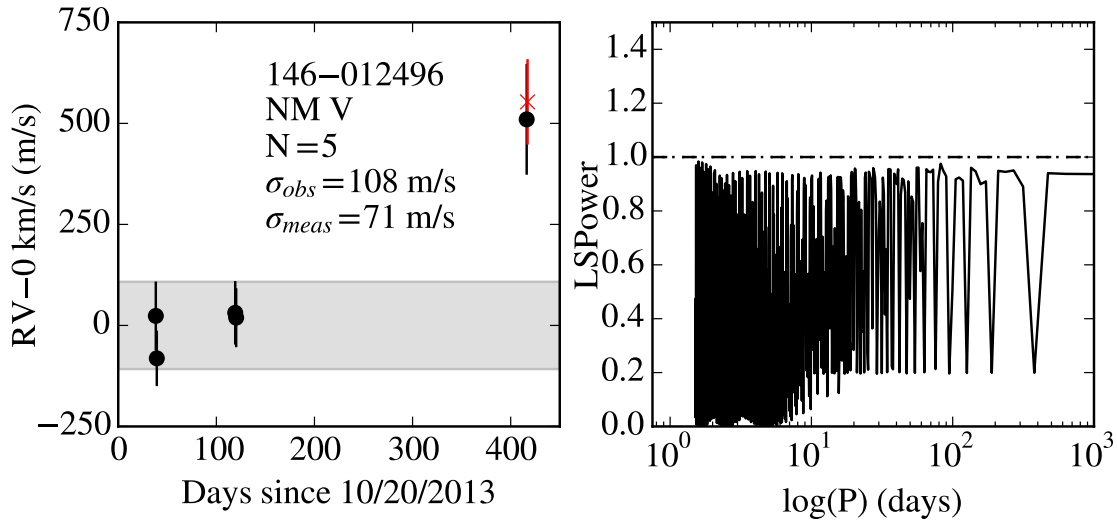

Figure B.64: 146-012496 is a non-member in NGC 2516 with a T_{eff} of 5111 ± 33 K and a $v_r \sin(i)$ of 2.9 ± 0.6 km/s. It has $\sigma_{obs} = 108$ m/s and $\sigma_{meas} = 71$ m/s. D03 reports $\log(L_x) \leq 28.74$ erg/s. Red Xs are epochs excluded as $>3\sigma_{obs}$ outliers. Errors shown include the mean σ_{jitter}.

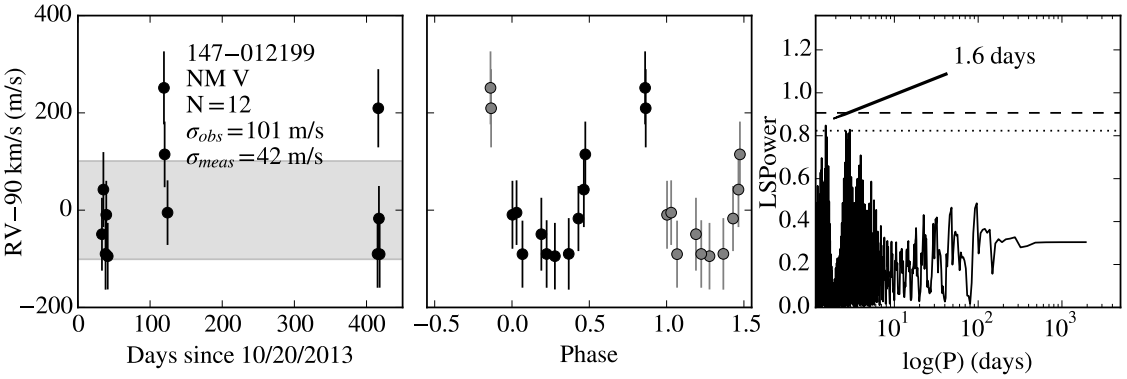

Figure B.65: 147-012199 is a non-member in NGC 2516 with a T_{eff} of 5067^{+17}_{-13} K and a $v_r \sin(i)$ of 2.7 ± 0.1 km/s. It has $\sigma_{obs} = 101$ m/s and $\sigma_{meas} = 42$ m/s. D03 reports $\log(L_x) \leq 28.91$ erg/s. The most significant periodogram peak is at 1.6 days. Grey points are duplicated data to guide the eye. Errors shown include the mean σ_{jitter}.

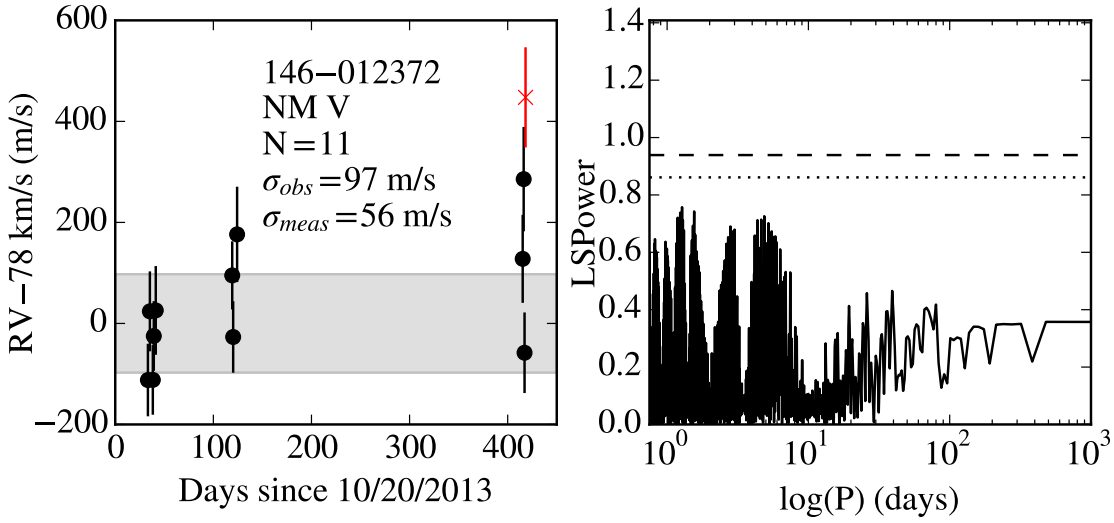

Figure B.66: 146-012372 is a non-member in NGC 2516 with a T_{eff} of 5194^{+18}_{-16} K and a $v_r \sin(i)$ of 3.3 ± 0.2 km/s. It has $\sigma_{obs} = 97$ m/s and $\sigma_{meas} = 56$ m/s. D03 reports $\log(L_x) \leq 29.51$ erg/s. Red Xs are epochs excluded as $>3\sigma_{obs}$ outliers. Errors shown include the mean σ_{jitter}.

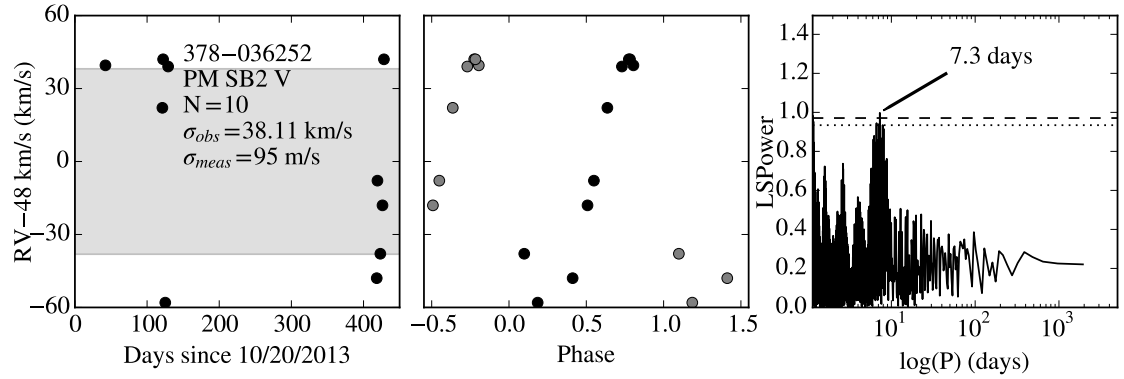

Figure B.67: 378-036252 is a double-lined binary possible member in NGC 2422 with a T_{eff} of 6557 ± 73 K and a $v_r \sin(i)$ of 9.8 ± 0.3 km/s. It has $\sigma_{obs} = 38107$ m/s and $\sigma_{meas} = 95$ m/s. The most significant periodogram peak is at 7.3 days. Grey points are duplicated data to guide the eye. Errors shown include the mean σ_{jitter}.

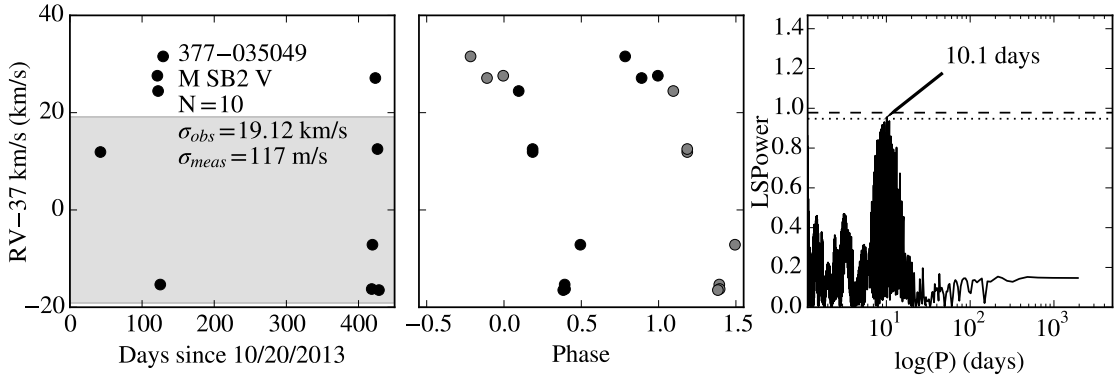

Figure B.68: 377-035049 is a double-lined binary member in NGC 2422 with a T_{eff} of 4988 ± 47 K and a $v_r \sin(i)$ of 6.8 ± 1.7 km/s. It has $\sigma_{obs} = 19124$ m/s and $\sigma_{meas} = 117$ m/s. The most significant periodogram peak is at 10.1 days. Grey points are duplicated data to guide the eye. Errors shown include the mean σ_{jitter}.

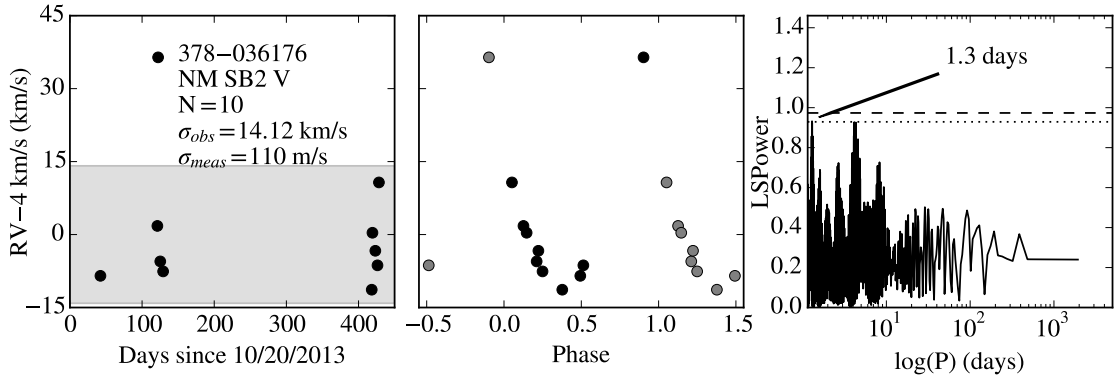

Figure B.69: 378-036176 is a double-lined binary non-member in NGC 2422 with a T_{eff} of 6102 ± 148 K and a $v_r \sin(i)$ of 9.1 ± 1.2 km/s. It has $\sigma_{obs} = 14124$ m/s and $\sigma_{meas} = 110$ m/s. The most significant periodogram peak is at 1.3 days. Grey points are duplicated data to guide the eye. Errors shown include the mean σ_{jitter}.

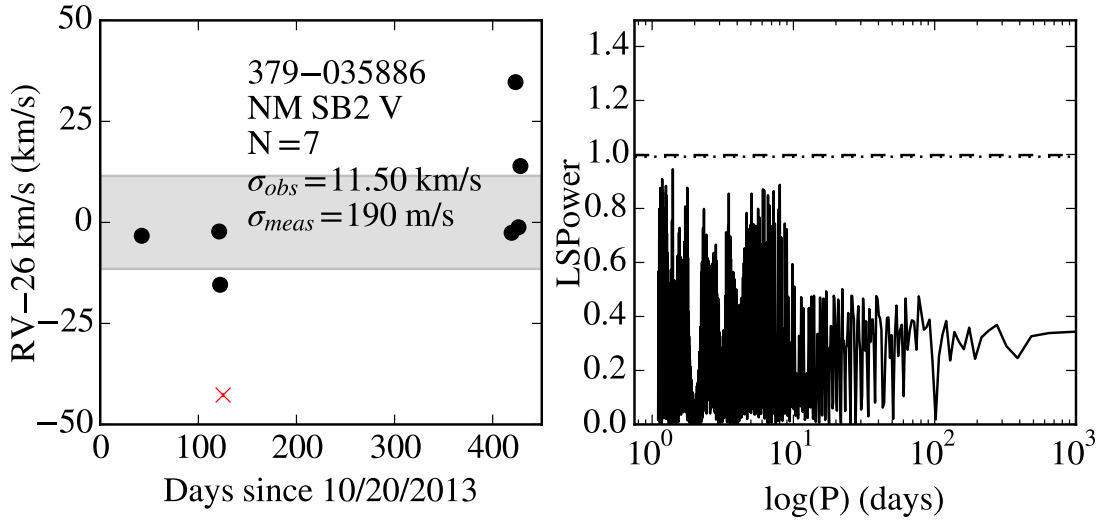

Figure B.70: 379-035886 is a double-lined binary non-member in NGC 2422 with a T_{eff} of 4999 ± 44 K and a $v_r \sin(i)$ of 9.2 ± 4.4 km/s. It has σ_{obs} = 11504 m/s and σ_{meas} = 190 m/s. Red Xs are epochs excluded as $>3\sigma_{obs}$ outliers. Errors shown include the mean σ_{jitter}.

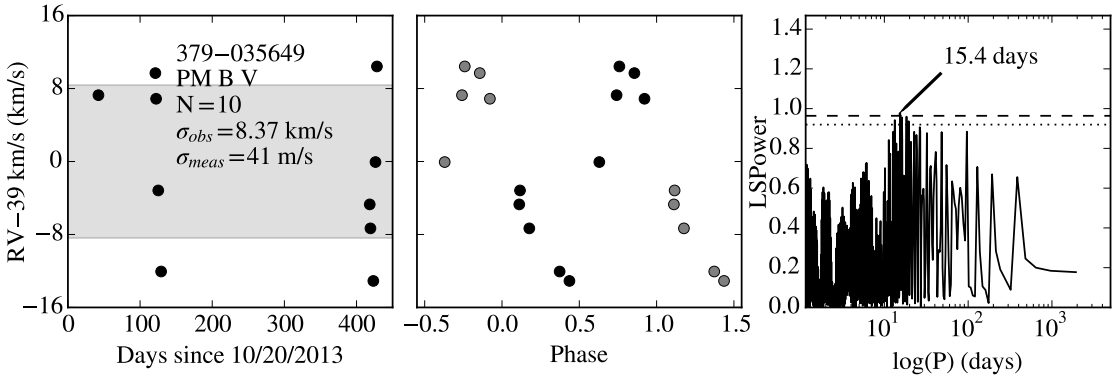

Figure B.71: 379-035649 is a binary possible member in NGC 2422 with a T_{eff} of 5533^{+23}_{-21} K and a $v_r \sin(i)$ of 4.4±0.1 km/s. It has σ_{obs} = 8366 m/s and σ_{meas} = 41 m/s. The most significant periodogram peak is at 15.4 days. Grey points are duplicated data to guide the eye. Errors shown include the mean σ_{jitter}.

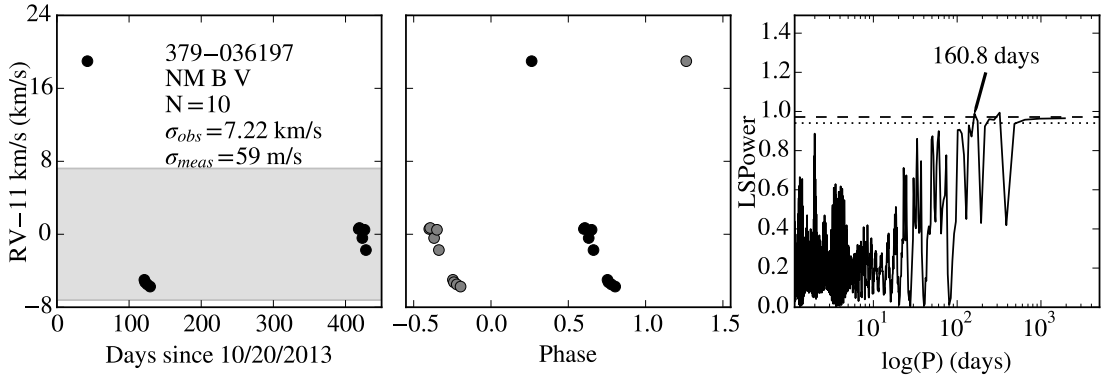

Figure B.72: 379-036197 is a binary non-member in NGC 2422 with a T_{eff} of 6299^{+38}_{-30} K and a $v_r \sin(i)$ of 6.6±0.2 km/s. It has $\sigma_{obs} = 7216$ m/s and $\sigma_{meas} = 59$ m/s. The most significant periodogram peak is at 160.8 days. Grey points are duplicated data to guide the eye. Errors shown include the mean σ_{jitter}.

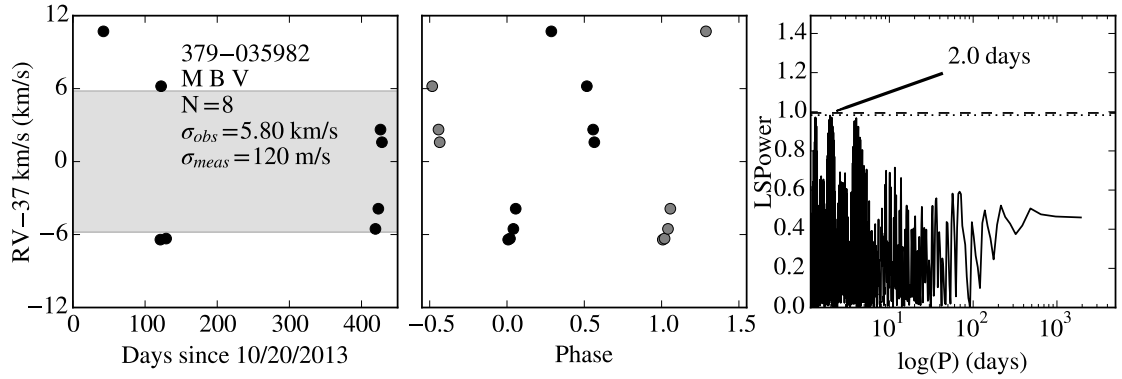

Figure B.73: 379-035982 is a binary member in NGC 2422 with a T_{eff} of 4765^{+21}_{-16} K and a $v_r \sin(i)$ of 14.1 ± 3.5 km/s. It has $\sigma_{obs} = 5799$ m/s and $\sigma_{meas} = 120$ m/s. The most significant periodogram peak is at 2.0 days. Grey points are duplicated data to guide the eye. Errors shown include the mean σ_{jitter}.

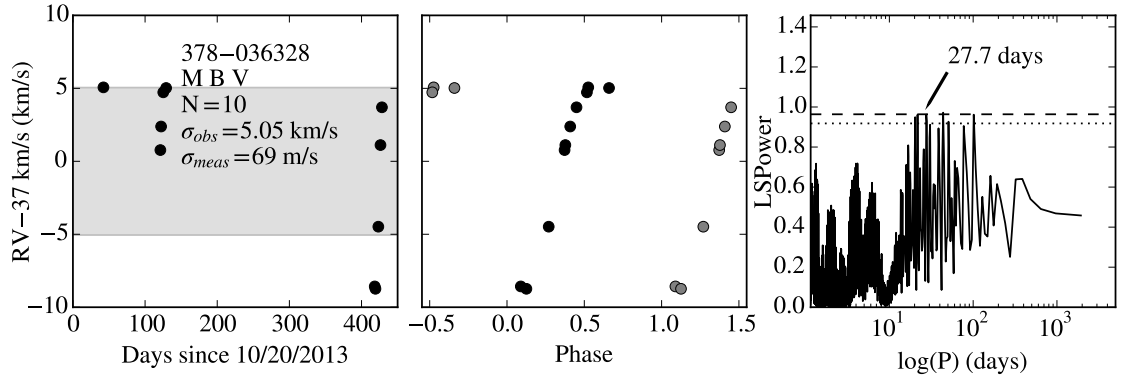

Figure B.74: 378-036328 is a binary member in NGC 2422 with a T_{eff} of 6222^{+38}_{-30} K and a $v_r \sin(i)$ of 7.9 ± 0.2 km/s. It has $\sigma_{obs} = 5051$ m/s and $\sigma_{meas} = 69$ m/s. The most significant periodogram peak is at 27.7 days. Grey points are duplicated data to guide the eye. Errors shown include the mean σ_{jitter}.

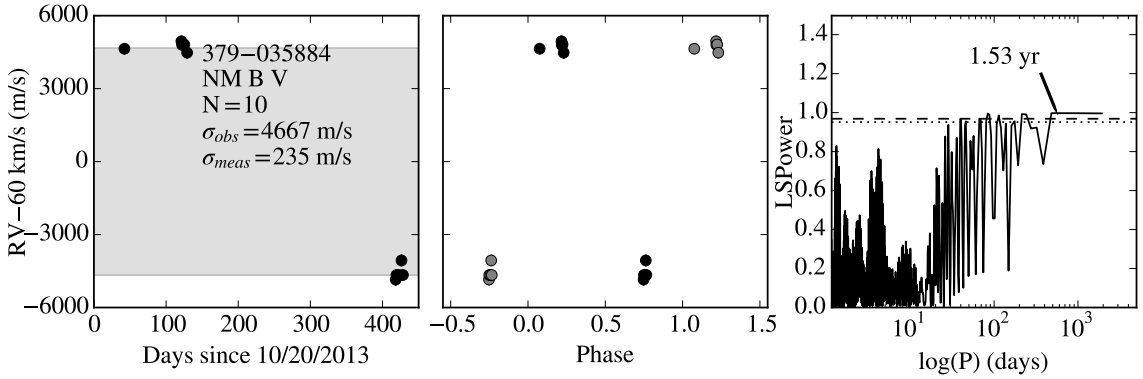

Figure B.75: 379-035884 is a binary non-member in NGC 2422 with a T_{eff} of 6846^{+52}_{-40} K and a $v_r \sin(i)$ of 19.0 ± 0.3 km/s. It has $\sigma_{obs} = 4667$ m/s and $\sigma_{meas} = 235$ m/s. The most significant periodogram peak is at 1.53 years. Grey points are duplicated data to guide the eye. Errors shown include the mean σ_{jitter}.

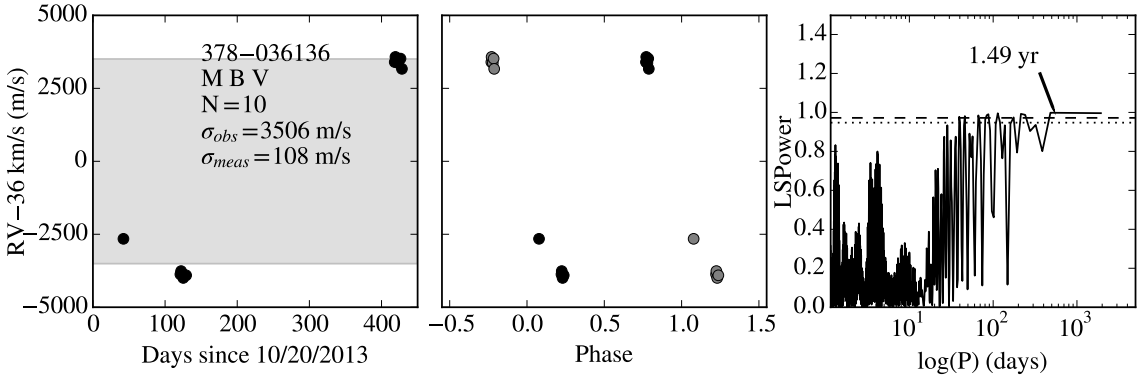

Figure B.76: 378-036136 is a binary member in NGC 2422 with a T_{eff} of 5469 ± 41 K and a $v_r \sin(i)$ of 9.0 ± 0.2 km/s. It has $\sigma_{obs} = 3506$ m/s and $\sigma_{meas} = 108$ m/s. The most significant periodogram peak is at 1.49 years. Grey points are duplicated data to guide the eye. Errors shown include the mean σ_{jitter}.

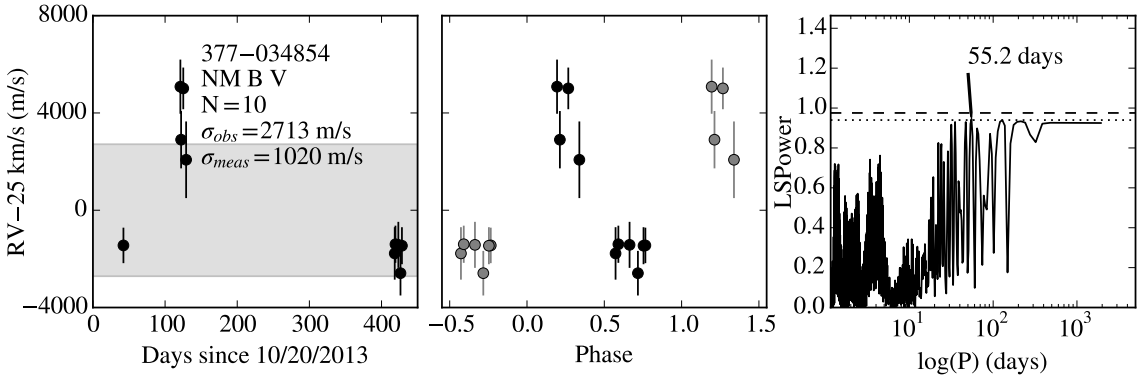

Figure B.77: 377-034854 is a binary non-member in NGC 2422 with a T_{eff} of 6543 ± 105 K and a $v_r \sin(i)$ of 38.3 ± 1.0 km/s. It has $\sigma_{obs} = 2713$ m/s and $\sigma_{meas} = 1020$ m/s. The most significant periodogram peak is at 55.2 days. Grey points are duplicated data to guide the eye. Errors shown include the mean σ_{jitter}.

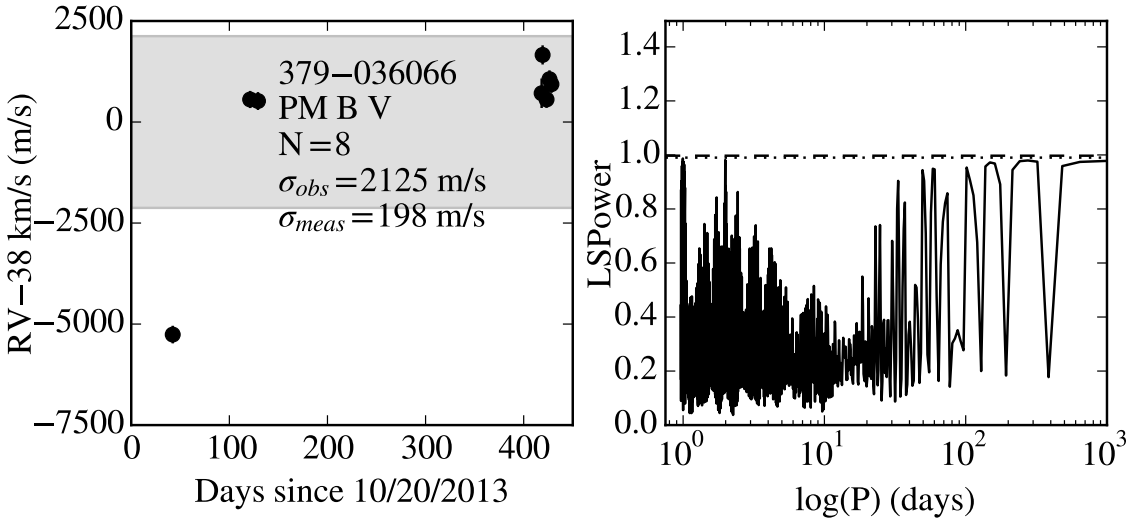

Figure B.78: 379-036066 is a binary possible member in NGC 2422 with a T_{eff} of 5894 ± 28 K and a $v_r \sin(i)$ of 21.6 ± 0.2 km/s. It has σ_{obs} = 2125 m/s and σ_{meas} = 198 m/s. Errors shown include the mean σ_{jitter}.

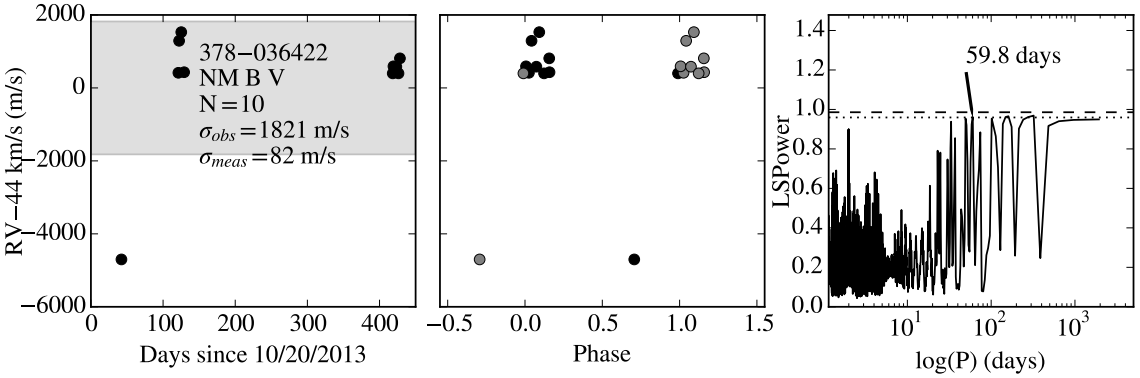

Figure B.79: 378-036422 is a binary non-member in NGC 2422 with a T_{eff} of 5310 ± 23 K and a $v_r \sin(i)$ of 10.9 ± 0.2 km/s. It has σ_{obs} = 1821 m/s and σ_{meas} = 82 m/s. The most significant periodogram peak is at 59.8 days. Grey points are duplicated data to guide the eye. Errors shown include the mean σ_{jitter}.

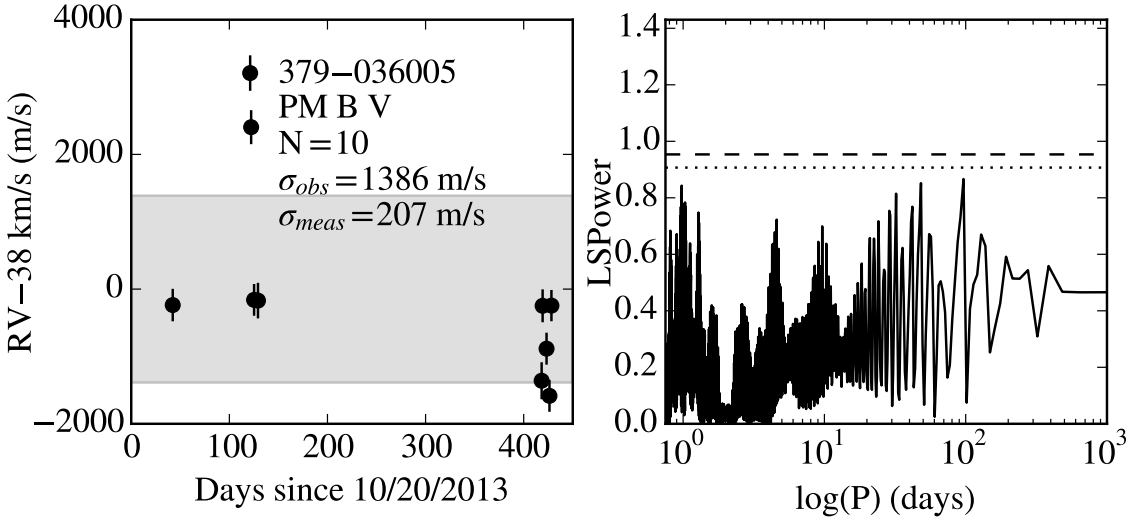

Figure B.80: 379-036005 is a binary possible member in NGC 2422 with a T_{eff} of 6261^{+38}_{-30} K and a $v_r \sin(i)$ of 19.1 ± 0.8 km/s. It has σ_{obs} = 1386 m/s and σ_{meas} = 207 m/s. Errors shown include the mean σ_{jitter}.

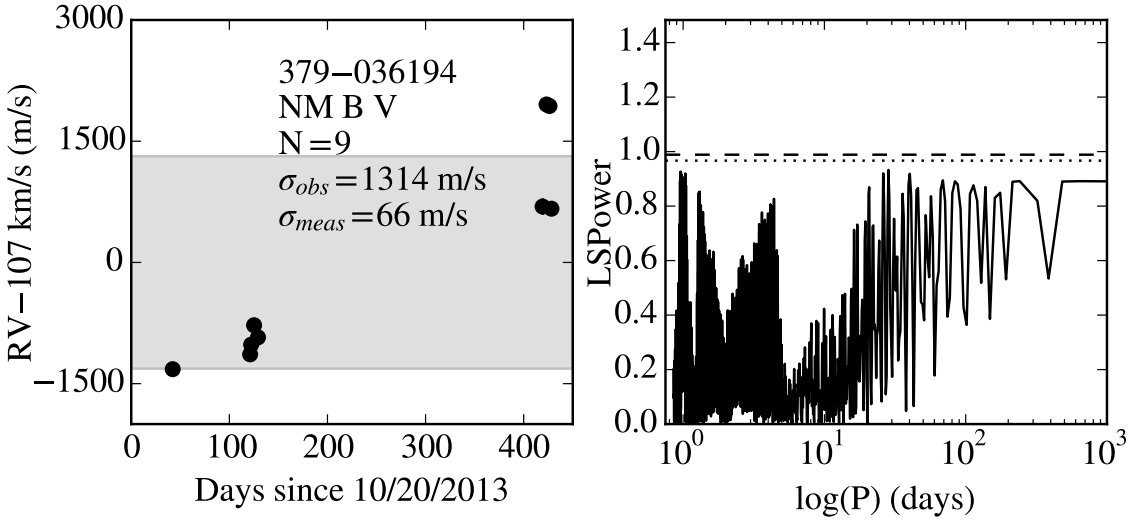

Figure B.81: 379-036194 is a binary non-member in NGC 2422 with a T_{eff} of 5425 ± 29 K and a $v_r \sin(i)$ of 4.1 ± 0.2 km/s. It has σ_{obs} = 1314 m/s and σ_{meas} = 66 m/s. Errors shown include the mean σ_{jitter}.

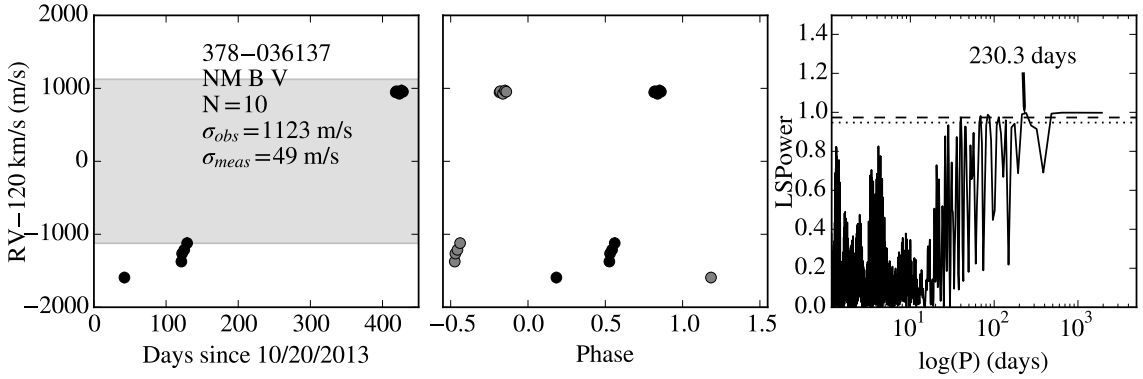

Figure B.82: 378-036137 is a binary non-member in NGC 2422 with a T_{eff} of 5503 ± 24 K and a $v_r \sin(i)$ of 3.0 ± 0.2 km/s. It has $\sigma_{obs} = 1123$ m/s and $\sigma_{meas} = 49$ m/s. The most significant periodogram peak is at 230.3 days. Grey points are duplicated data to guide the eye. Errors shown include the mean σ_{jitter}.

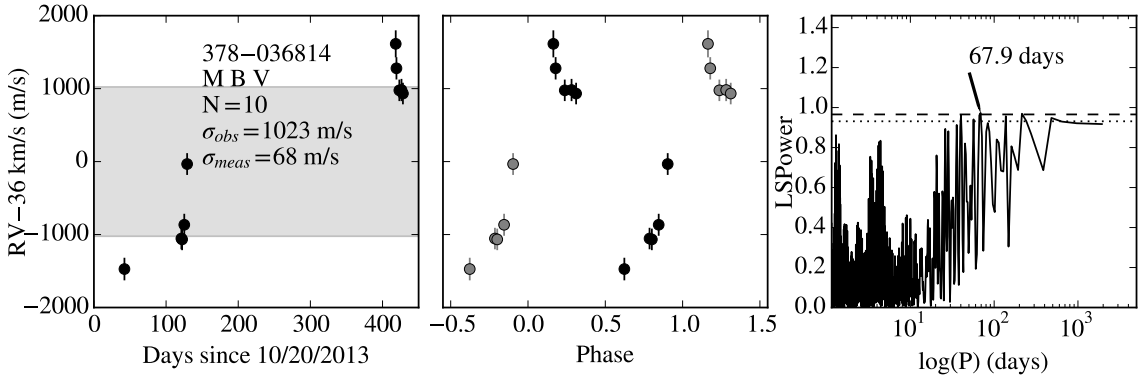

Figure B.83: 378-036814 is a binary member in NGC 2422 with a T_{eff} of 5098^{+19}_{-15} K and a $v_r \sin(i)$ of 6.9 ± 0.2 km/s. It has $\sigma_{obs} = 1023$ m/s and $\sigma_{meas} = 68$ m/s. The most significant periodogram peak is at 67.9 days. Grey points are duplicated data to guide the eye. Errors shown include the mean σ_{jitter}.

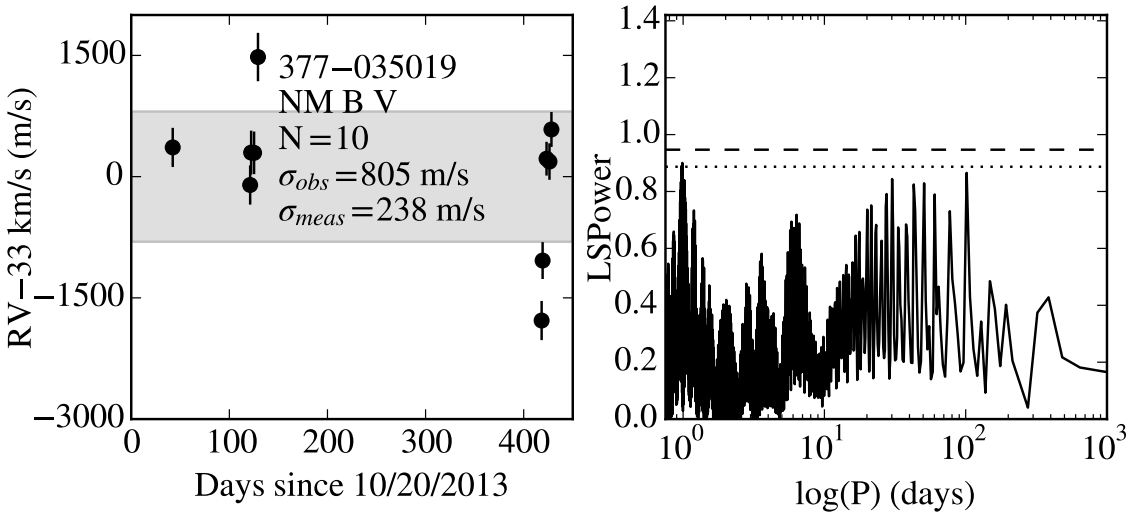

Figure B.84: 377-035019 is a binary non-member in NGC 2422 with a T_{eff} of 4555^{+19}_{-14} K and a $v_r \sin(i)$ of 35.2 ± 0.6 km/s. It has σ_{obs} = 805 m/s and σ_{meas} = 238 m/s. Errors shown include the mean σ_{jitter}.

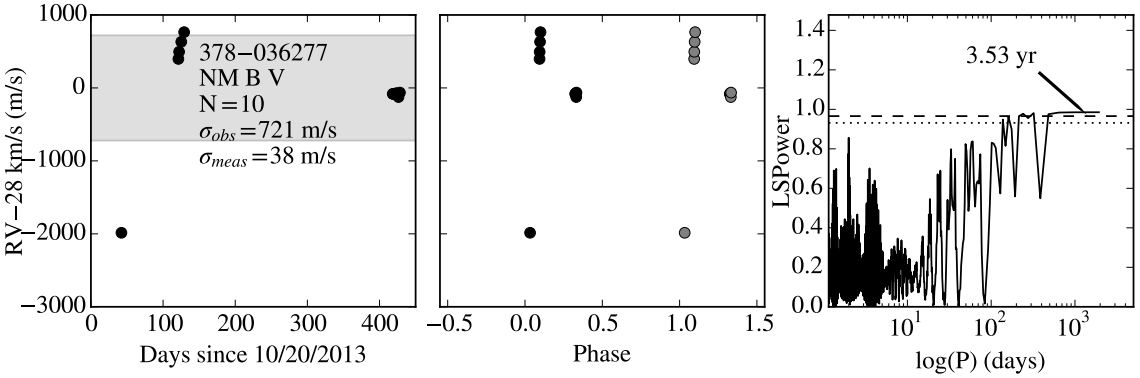

Figure B.85: 378-036277 is a binary non-member in NGC 2422 with a T_{eff} of 5382^{+23}_{-20} K and a $v_r \sin(i)$ of 3.4±0.1 km/s. It has σ_{obs} = 721 m/s and σ_{meas} = 38 m/s. The most significant periodogram peak is at 3.53 years. Grey points are duplicated data to guide the eye. Errors shown include the mean σ_{jitter}.

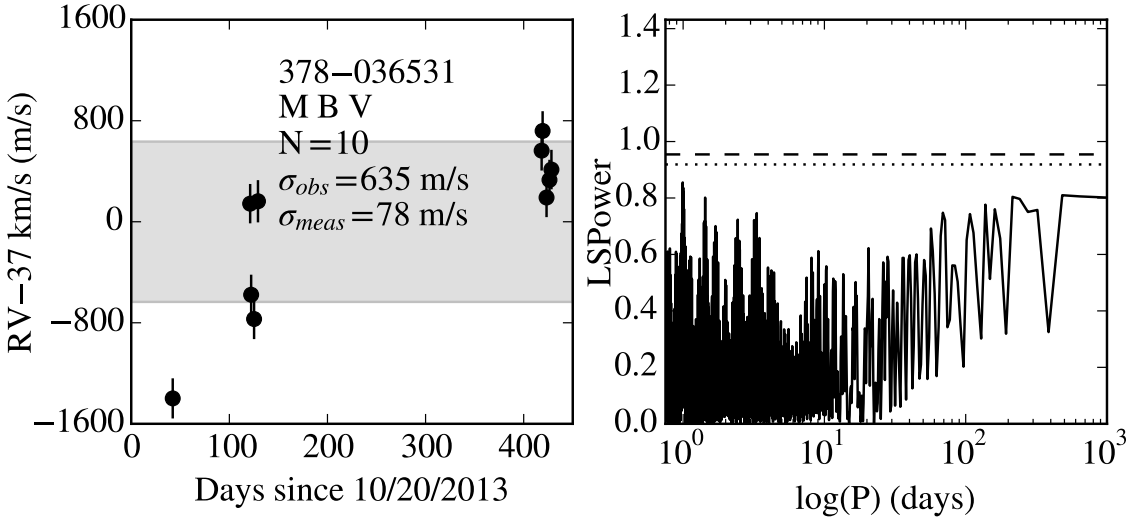

Figure B.86: 378-036531 is a binary member in NGC 2422 with a T_{eff} of 5559^{+23}_{-20} K and a $v_r \sin(i)$ of 10.2 ± 0.1 km/s. It has $\sigma_{obs} = 635$ m/s and $\sigma_{meas} = 78$ m/s. Errors shown include the mean σ_{jitter}.

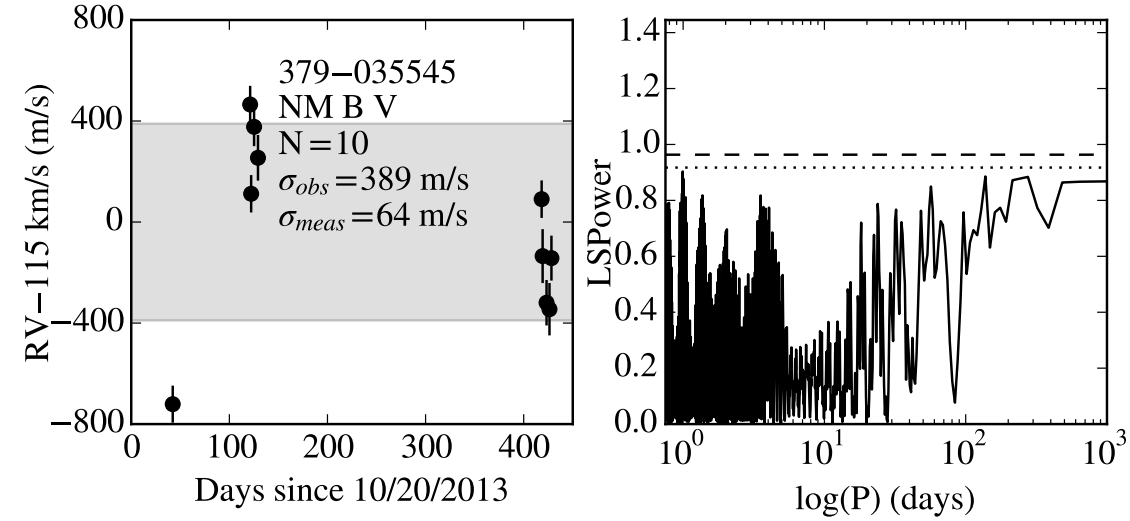

Figure B.87: 379-035545 is a binary non-member in NGC 2422 with a T_{eff} of 4980^{+19}_{-14} K and a $v_r \sin(i)$ of 4.3 ± 0.2 km/s. It has $\sigma_{obs} = 389$ m/s and $\sigma_{meas} = 64$ m/s. Errors shown include the mean σ_{jitter}.

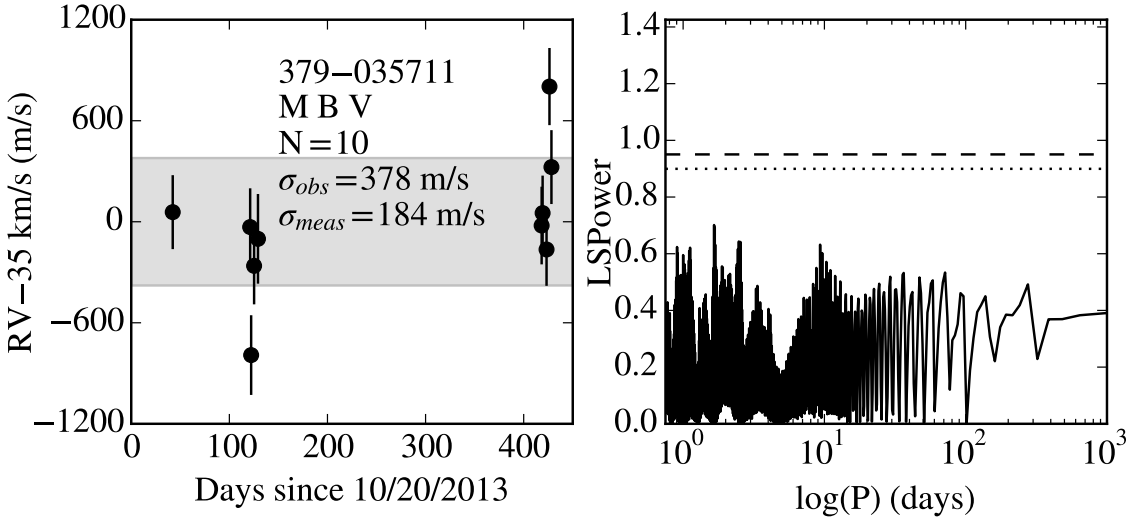

Figure B.88: 379-035711 is a binary member in NGC 2422 with a T_{eff} of 4531^{+19}_{-14} K and a $v_r \sin(i)$ of 27.5 ± 0.3 km/s. It has $\sigma_{obs} = 378$ m/s and $\sigma_{meas} = 184$ m/s. Errors shown include the mean σ_{jitter}.

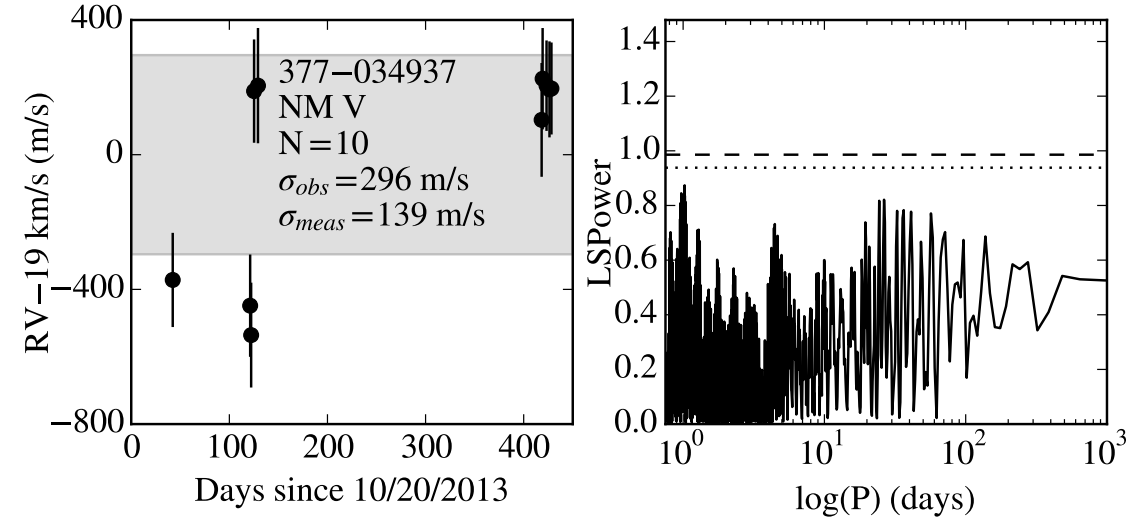

Figure B.89: 377-034937 is a non-member in NGC 2422 with a T_{eff} of 6563^{+38}_{-30} K and a $v_r \sin(i)$ of 17.0 ± 0.2 km/s. It has $\sigma_{obs} = 296$ m/s and $\sigma_{meas} = 139$ m/s. Errors shown include the mean σ_{jitter}.

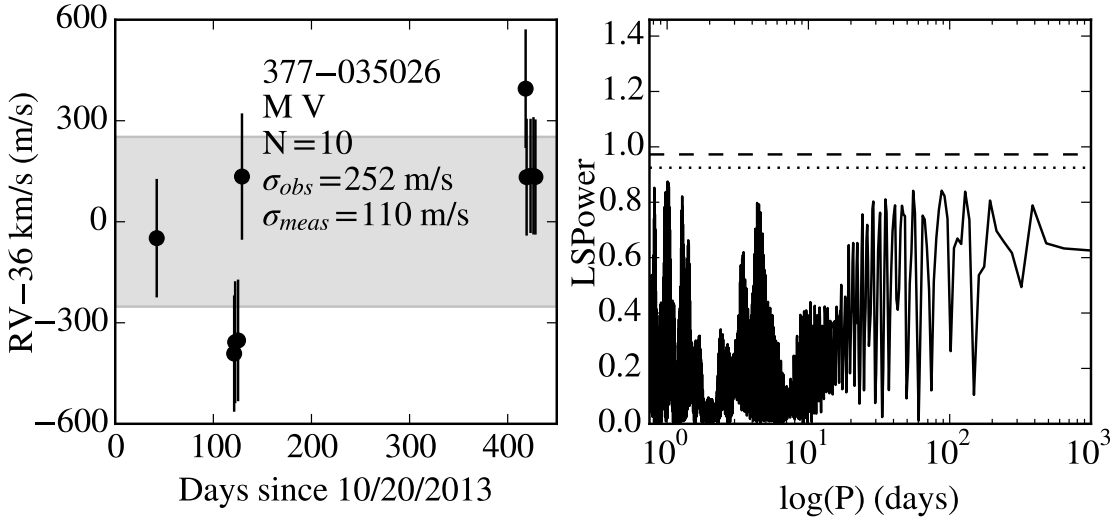

Figure B.90: 377-035026 is a member in NGC 2422 with a T_{eff} of 6082^{+23}_{-20} K and a $v_r \sin(i)$ of 14.5 ± 0.1 km/s. It has $\sigma_{obs} = 252$ m/s and $\sigma_{meas} = 110$ m/s. Errors shown include the mean σ_{jitter}.

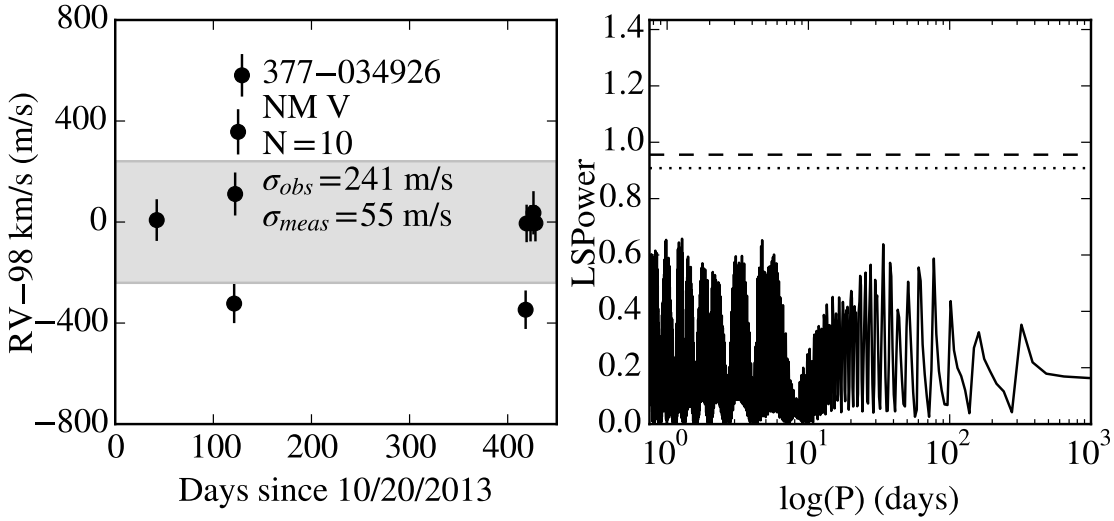

Figure B.91: 377-034926 is a non-member in NGC 2422 with a T_{eff} of 5214 ± 24 K and a $v_r \sin(i)$ of 4.1 ± 0.2 km/s. It has $\sigma_{obs} = 241$ m/s and $\sigma_{meas} = 55$ m/s. Errors shown include the mean σ_{jitter}.

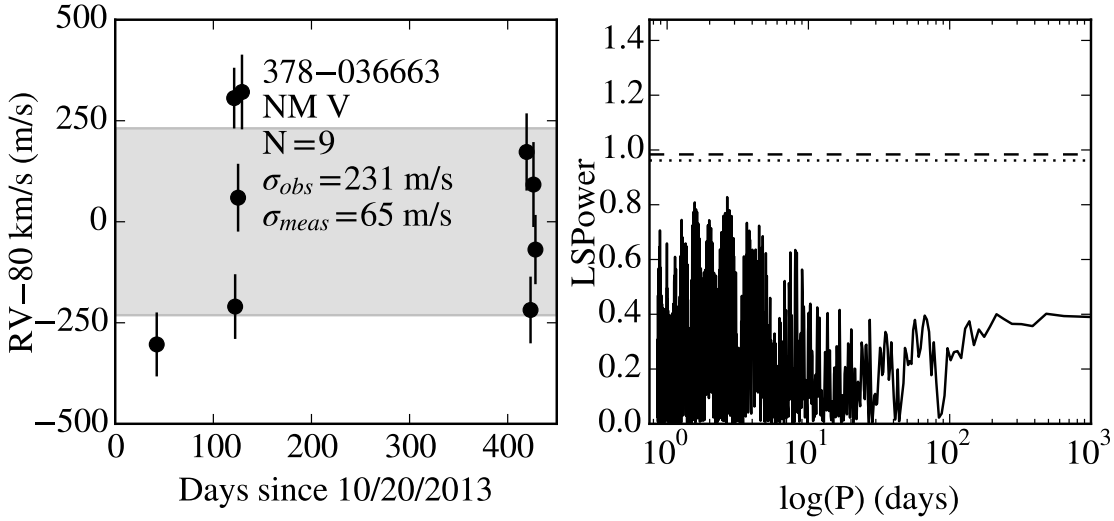

Figure B.92: 378-036663 is a non-member in NGC 2422 with a T_{eff} of 5397 ± 27 K and a $v_r \sin(i)$ of 3.9 ± 0.3 km/s. It has $\sigma_{obs} = 231$ m/s and $\sigma_{meas} = 65$ m/s. Errors shown include the mean σ_{jitter}.

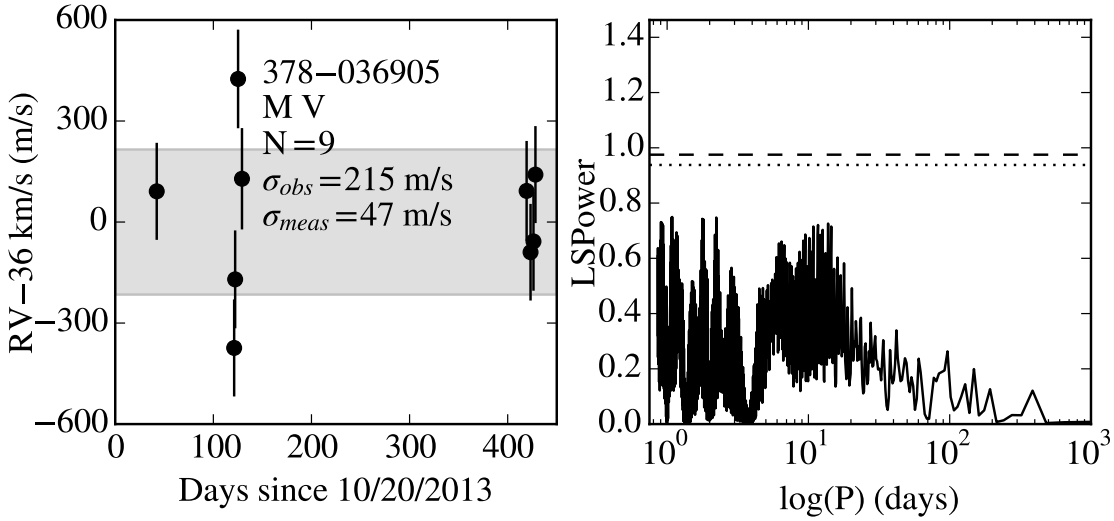

Figure B.93: 378-036905 is a member in NGC 2422 with a T_{eff} of 4636^{+20}_{-15} K and a $v_r \sin(i)$ of 3.6 ± 0.3 km/s. It has $\sigma_{obs} = 215$ m/s and $\sigma_{meas} = 47$ m/s. Errors shown include the mean σ_{jitter}.

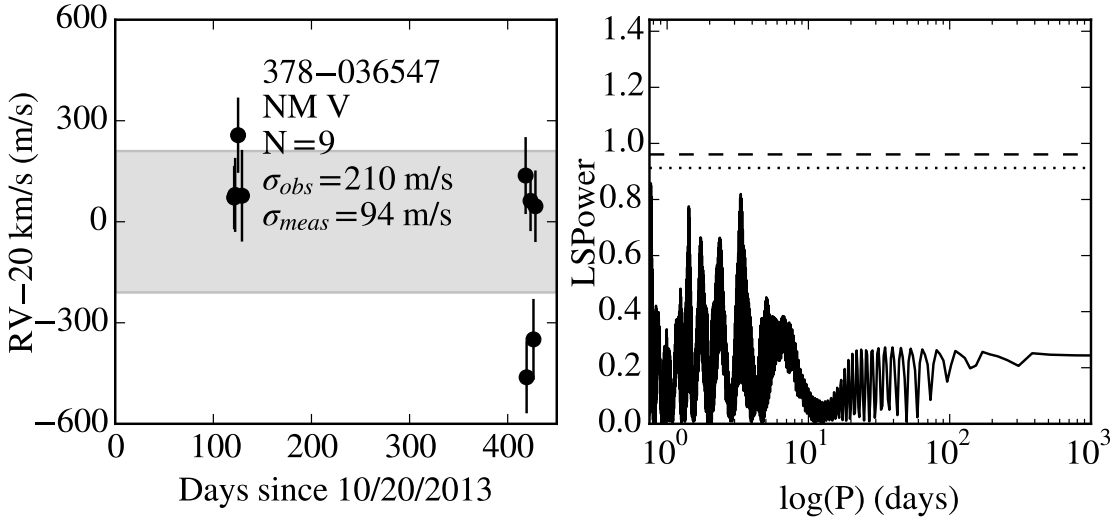

Figure B.94: 378-036547 is a non-member in NGC 2422 with a T_{eff} of 4800 ± 21 K and a $v_r \sin(i)$ of 5.1 ± 0.6 km/s. It has $\sigma_{obs} = 210$ m/s and $\sigma_{meas} = 94$ m/s. Errors shown include the mean σ_{jitter}.

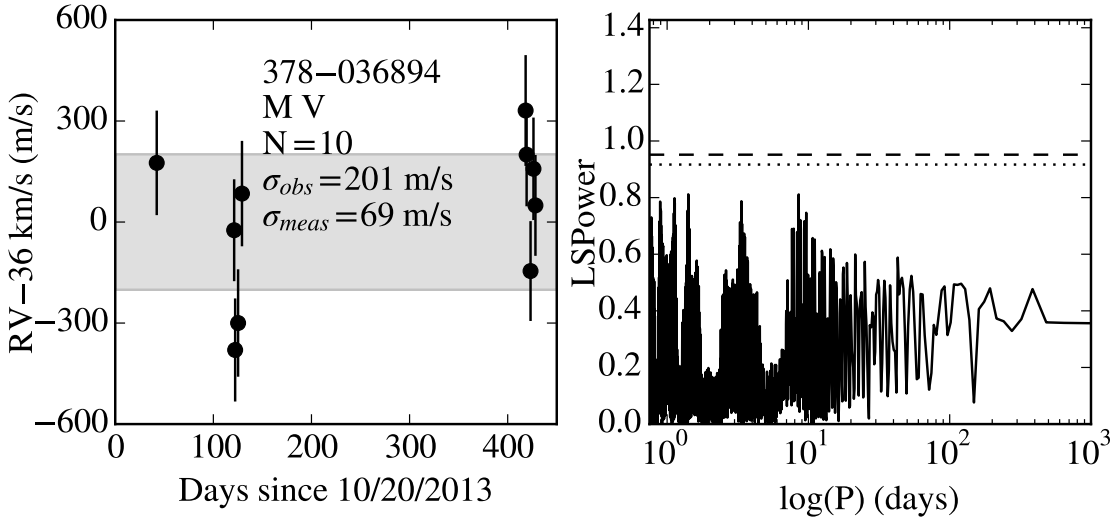

Figure B.95: 378-036894 is a member in NGC 2422 with a T_{eff} of 4902^{+19}_{-17} K and a $v_r \sin(i)$ of 8.1 ± 0.2 km/s. It has $\sigma_{obs} = 201$ m/s and $\sigma_{meas} = 69$ m/s. Errors shown include the mean σ_{jitter}.

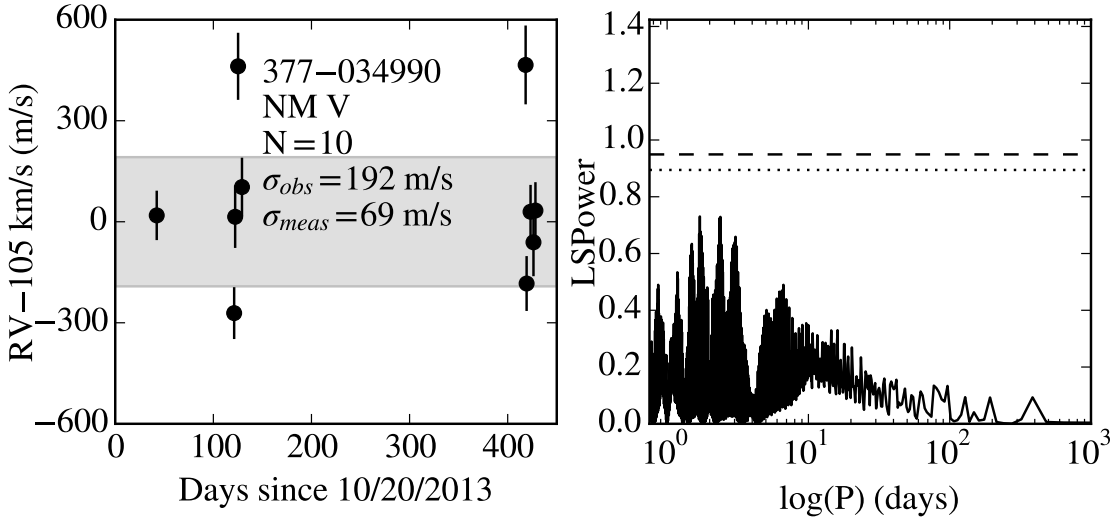

Figure B.96: 377-034990 is a non-member in NGC 2422 with a T_{eff} of 5230 ± 40 K and a $v_r \sin(i)$ of 4.2 ± 0.2 km/s. It has $\sigma_{obs} = 192$ m/s and $\sigma_{meas} = 69$ m/s. Errors shown include the mean σ_{jitter}.

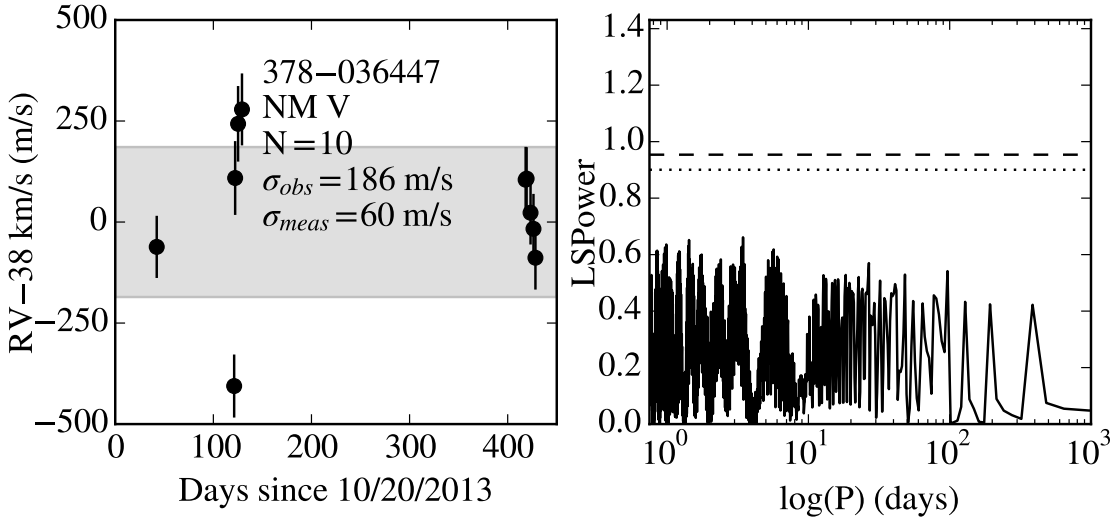

Figure B.97: 378-036447 is a non-member in NGC 2422 with a T_{eff} of 4864^{+19}_{-14} K and a $v_r \sin(i)$ of 6.4 ± 0.2 km/s. It has $\sigma_{obs} = 186$ m/s and $\sigma_{meas} = 60$ m/s. Errors shown include the mean σ_{jitter}.

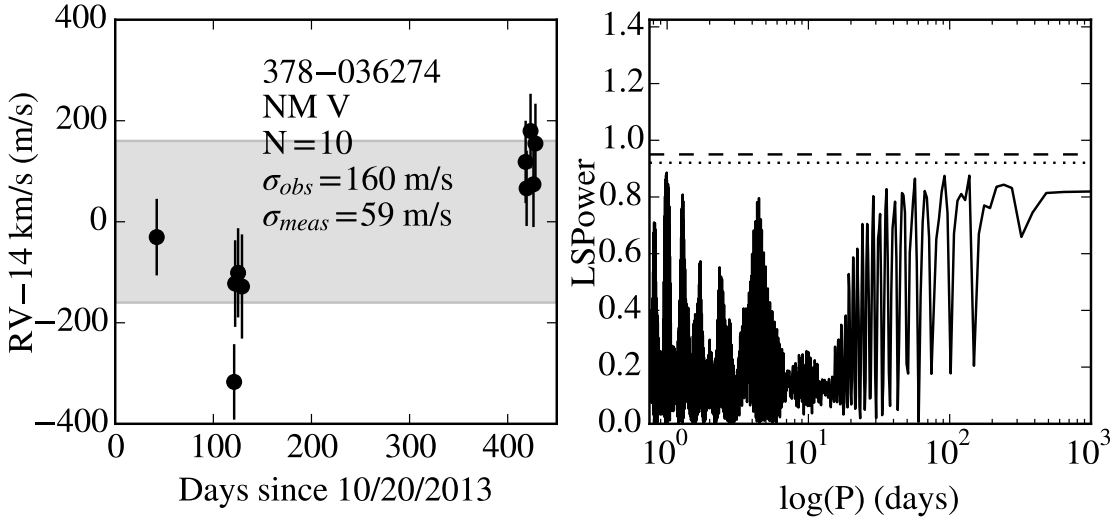

Figure B.98: 378-036274 is a non-member in NGC 2422 with a T_{eff} of 4852^{+19}_{-17} K and a $v_r \sin(i)$ of 3.5 ± 0.3 km/s. It has $\sigma_{obs} = 160$ m/s and $\sigma_{meas} = 59$ m/s. Errors shown include the mean σ_{jitter}.

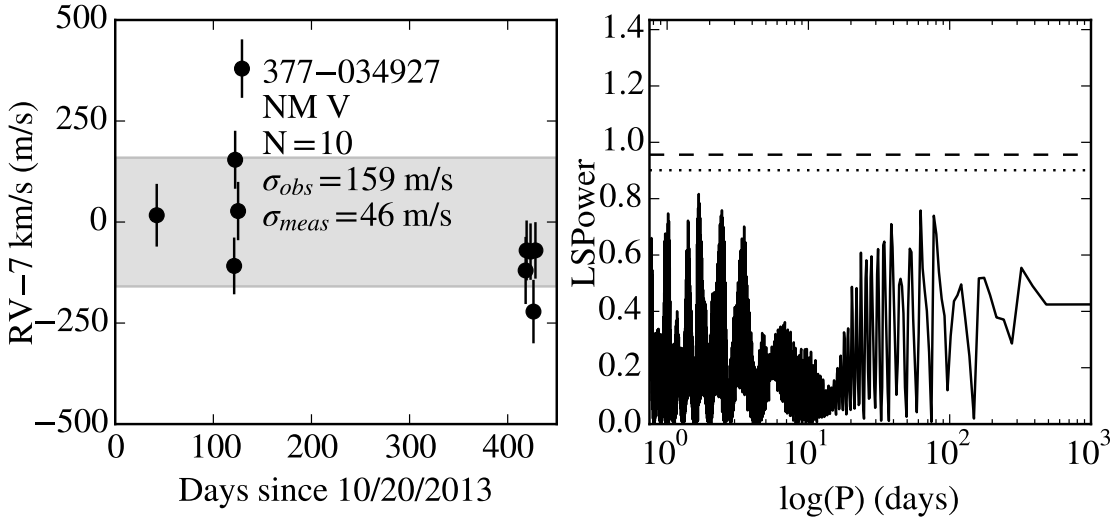

Figure B.99: 377-034927 is a non-member in NGC 2422 with a T_{eff} of 4773^{+19}_{-14} K and a $v_r \sin(i)$ of 3.3 ± 0.2 km/s. It has $\sigma_{obs} = 159$ m/s and $\sigma_{meas} = 46$ m/s. Errors shown include the mean σ_{jitter}.

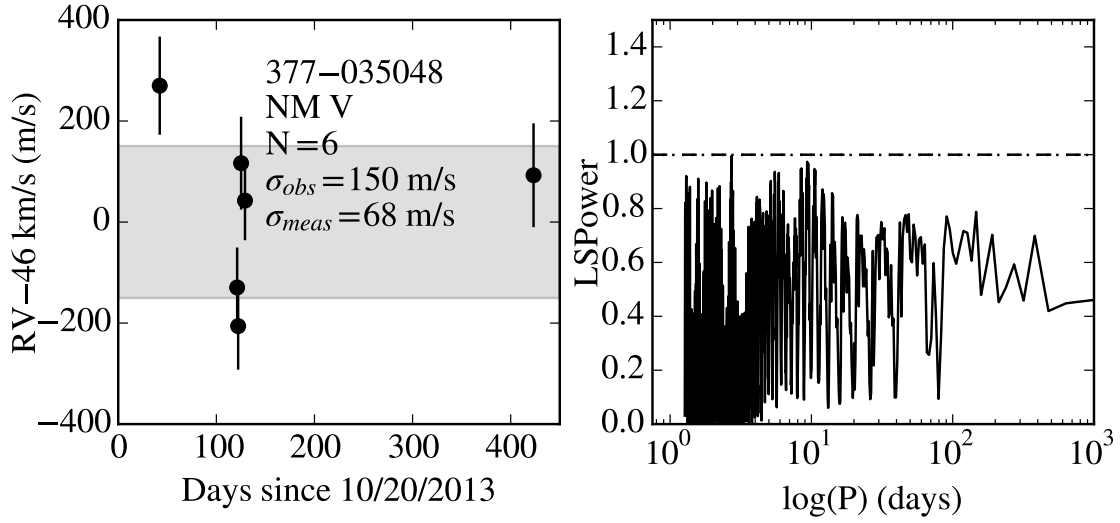

Figure B.100: 377-035048 is a non-member in NGC 2422 with a T_{eff} of 5125^{+24}_{-21} K and a $v_r \sin(i)$ of 3.2 ± 0.4 km/s. It has $\sigma_{obs} = 150$ m/s and $\sigma_{meas} = 68$ m/s. Errors shown include the mean σ_{jitter}.

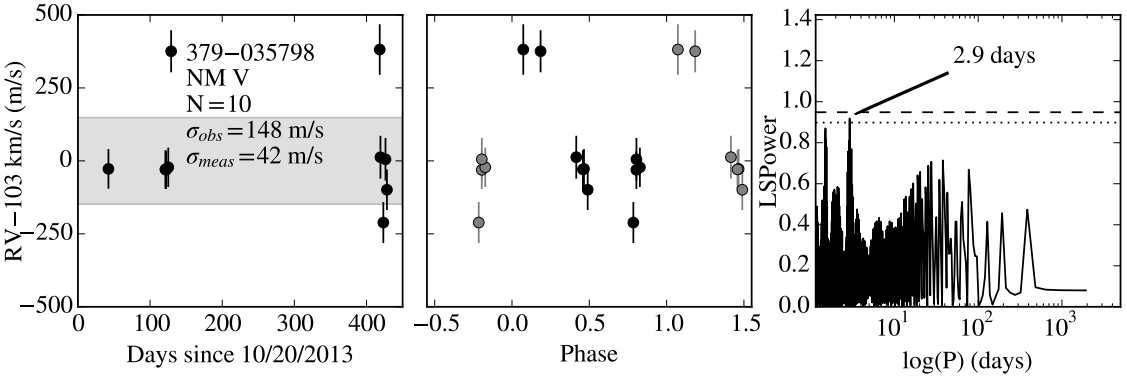

Figure B.101: 379-035798 is a non-member in NGC 2422 with a T_{eff} of 4839^{+19}_{-14} K and a $v_r \sin(i)$ of 3.9 ± 0.2 km/s. It has $\sigma_{obs} = 148$ m/s and $\sigma_{meas} = 42$ m/s. The most significant periodogram peak is at 2.9 days. Grey points are duplicated data to guide the eye. Errors shown include the mean σ_{jitter}.

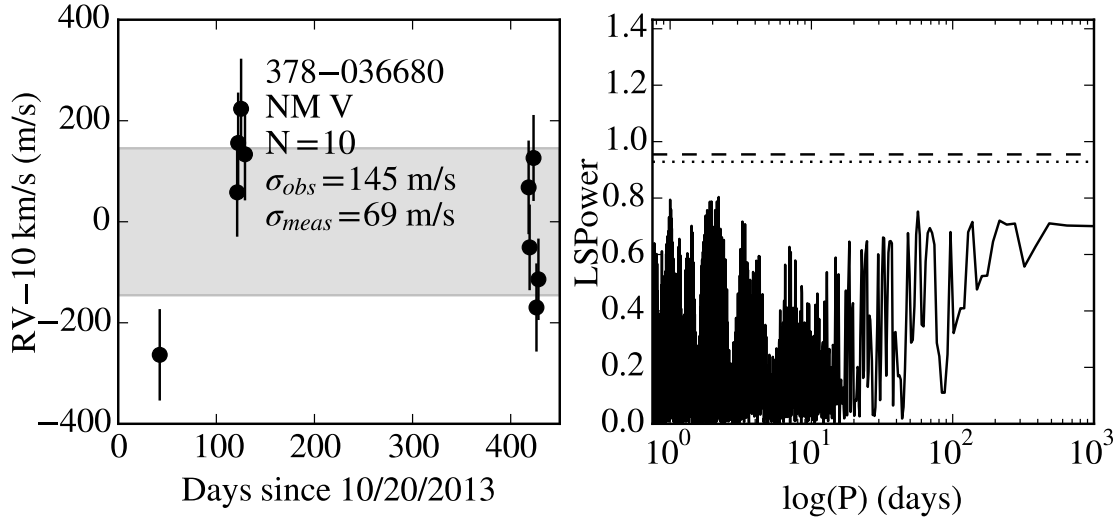

Figure B.102: 378-036680 is a non-member in NGC 2422 with a T_{eff} of 5472^{+23}_{-20} K and a $v_r \sin(i)$ of 7.1 ± 0.1 km/s. It has $\sigma_{obs} = 145$ m/s and $\sigma_{meas} = 69$ m/s. Errors shown include the mean σ_{jitter}.

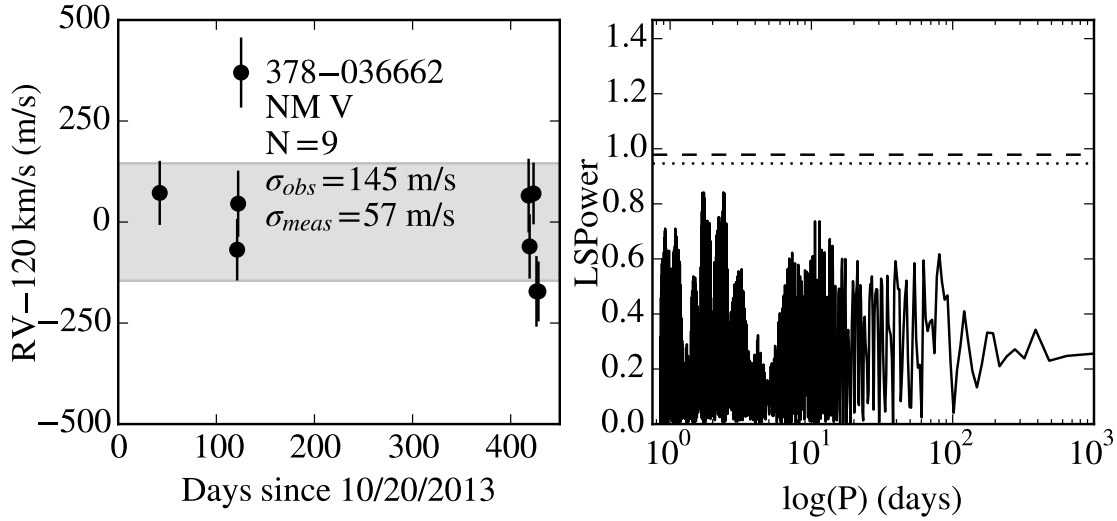

Figure B.103: 378-036662 is a non-member in NGC 2422 with a T_{eff} of 4857^{+20}_{-15} K and a $v_r \sin(i)$ of 3.4 ± 0.2 km/s. It has $\sigma_{obs} = 145$ m/s and $\sigma_{meas} = 57$ m/s. Errors shown include the mean σ_{jitter}.

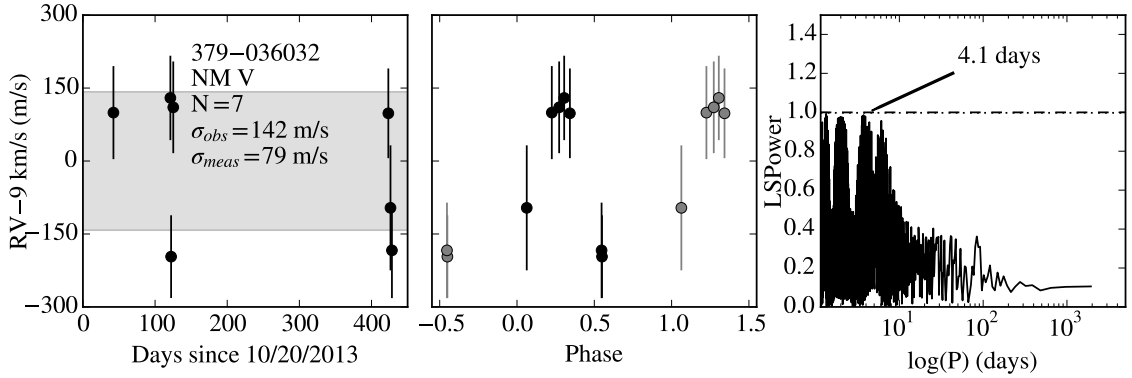

Figure B.104: 379-036032 is a non-member in NGC 2422 with a T_{eff} of 5776 ± 54 K and a $v_r \sin(i)$ of 3.1 ± 0.5 km/s. It has $\sigma_{obs} = 142$ m/s and $\sigma_{meas} = 79$ m/s. The most significant periodogram peak is at 4.1 days. Grey points are duplicated data to guide the eye. Errors shown include the mean σ_{jitter}.

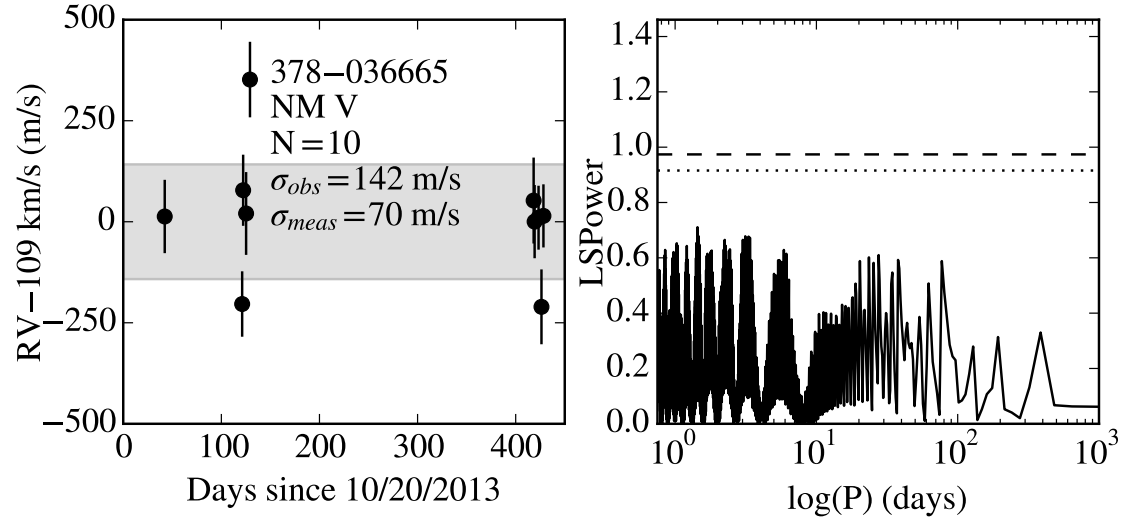

Figure B.105: 378-036665 is a non-member in NGC 2422 with a T_{eff} of 5303 ± 29 K and a $v_r \sin(i)$ of 4.8 ± 0.2 km/s. It has $\sigma_{obs} = 142$ m/s and $\sigma_{meas} = 70$ m/s. Errors shown include the mean σ_{jitter}.

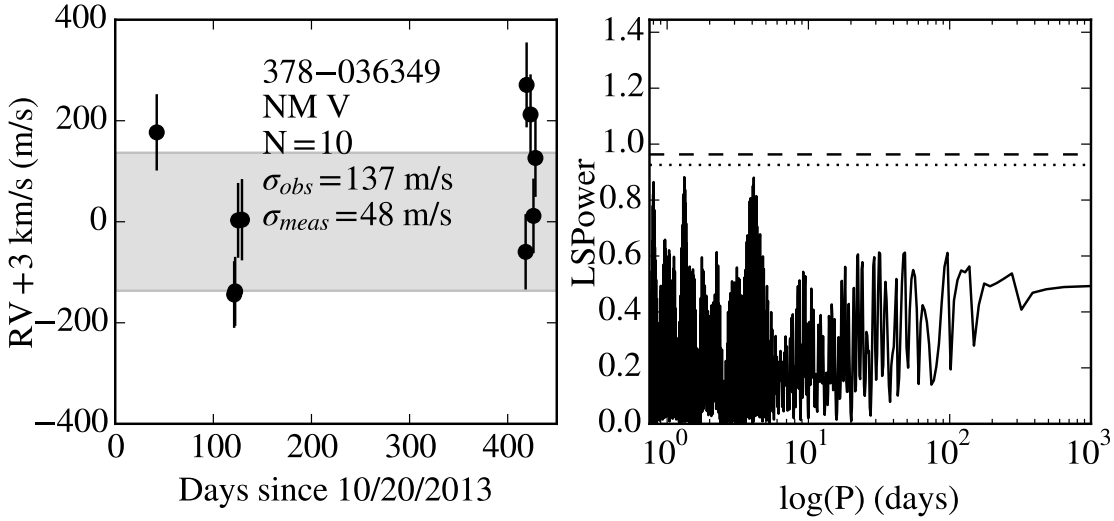

Figure B.106: 378-036349 is a non-member in NGC 2422 with a T_{eff} of 4806^{+19}_{-14} K and a $v_r \sin(i)$ of 3.9 ± 0.2 km/s. It has $\sigma_{obs} = 137$ m/s and $\sigma_{meas} = 48$ m/s. Errors shown include the mean σ_{jitter}.

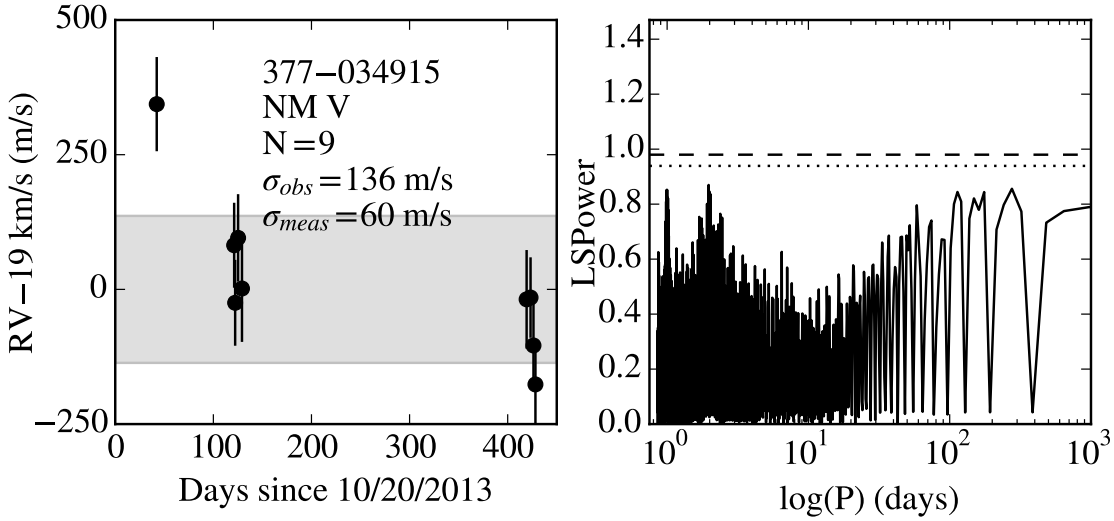

Figure B.107: 377-034915 is a non-member in NGC 2422 with a T_{eff} of 4880^{+20}_{-17} K and a $v_r \sin(i)$ of 2.7 ± 0.3 km/s. It has $\sigma_{obs} = 136$ m/s and $\sigma_{meas} = 60$ m/s. Errors shown include the mean σ_{jitter}.

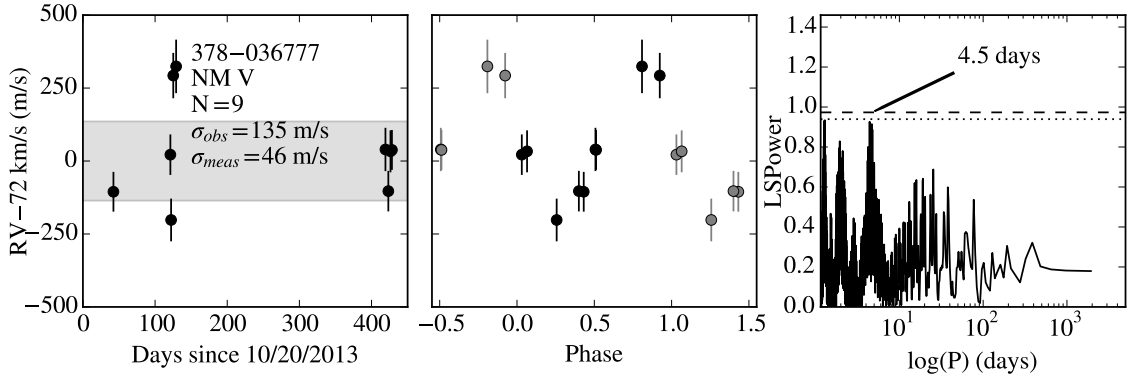

Figure B.108: 378-036777 is a non-member in NGC 2422 with a T_{eff} of 5143^{+20}_{-15} K and a $v_r \sin(i)$ of 3.4 ± 0.2 km/s. It has $\sigma_{obs} = 135$ m/s and $\sigma_{meas} = 46$ m/s. The most significant periodogram peak is at 4.5 days. Grey points are duplicated data to guide the eye. Errors shown include the mean σ_{jitter}.

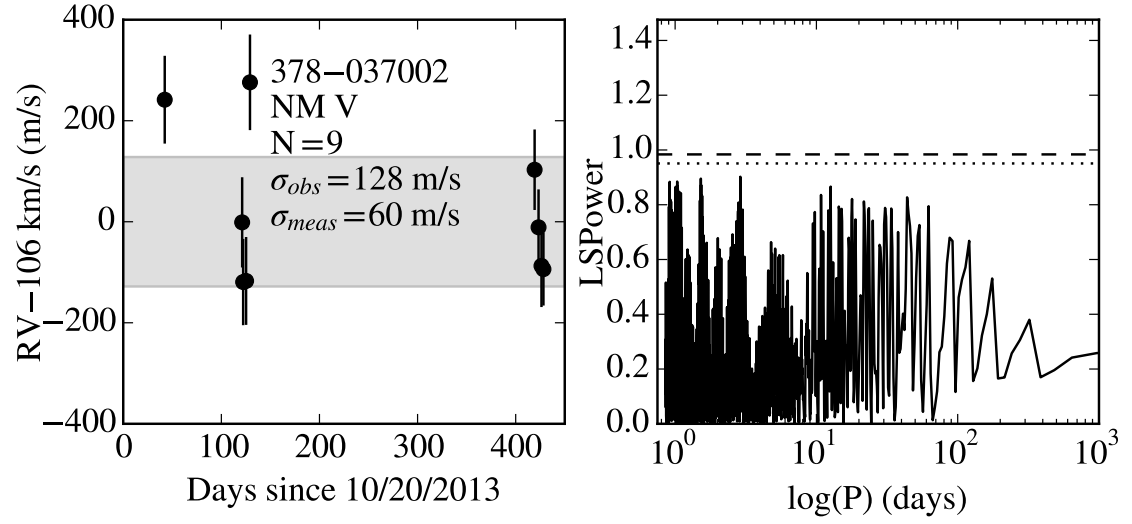

Figure B.109: 378-037002 is a non-member in NGC 2422 with a T_{eff} of 5288^{+25}_{-22} K and a $v_r \sin(i)$ of 3.7 ± 0.3 km/s. It has $\sigma_{obs} = 128$ m/s and $\sigma_{meas} = 60$ m/s. Errors shown include the mean σ_{jitter}.

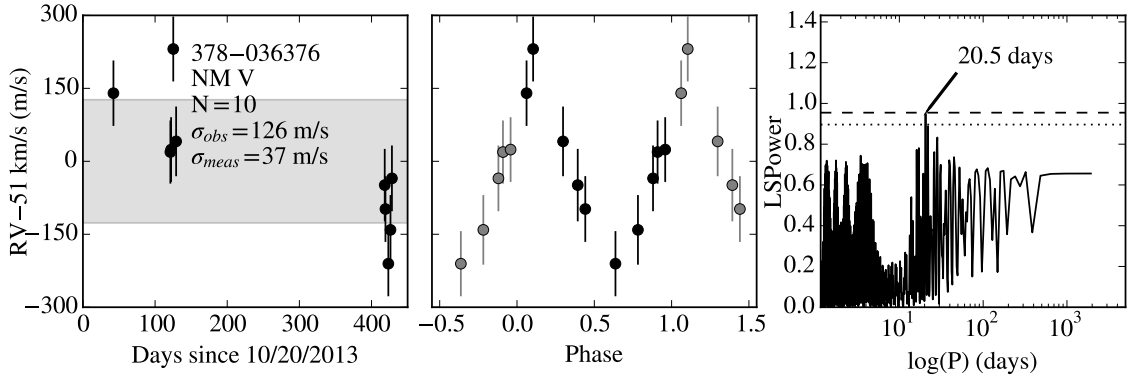

Figure B.110: 378-036376 is a non-member in NGC 2422 with a T_{eff} of 5468^{+23}_{-20} K and a $v_r \sin(i)$ of 3.7 ± 0.2 km/s. It has $\sigma_{obs} = 126$ m/s and $\sigma_{meas} = 37$ m/s. The most significant periodogram peak is at 20.5 days. Grey points are duplicated data to guide the eye. Errors shown include the mean σ_{jitter}.

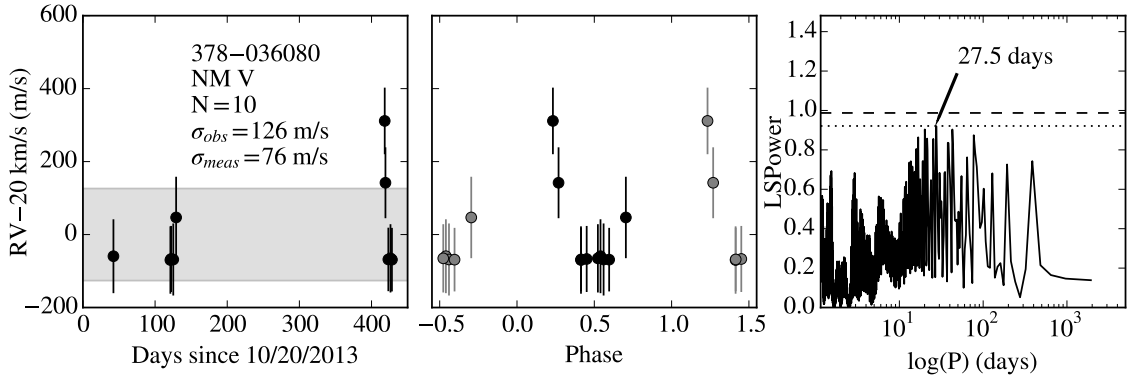

Figure B.111: 378-036080 is a non-member in NGC 2422 with a T_{eff} of 5784 ± 28 K and a $v_r \sin(i)$ of 3.3 ± 0.2 km/s. It has $\sigma_{obs} = 126$ m/s and $\sigma_{meas} = 76$ m/s. The most significant periodogram peak is at 27.5 days. Grey points are duplicated data to guide the eye. Errors shown include the mean σ_{jitter}.

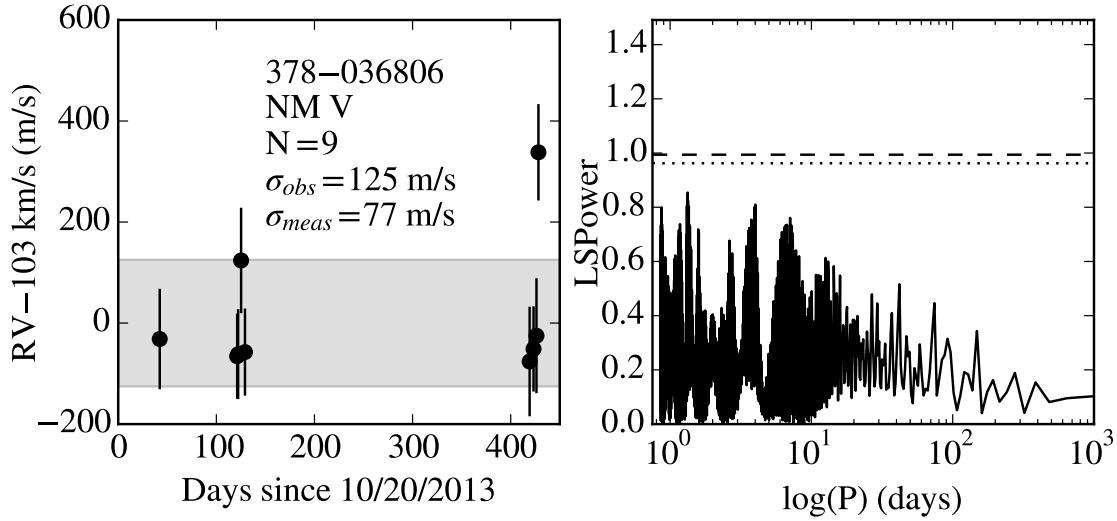

Figure B.112: 378-036806 is a non-member in NGC 2422 with a T_{eff} of 5420 ± 27 K and a $v_r \sin(i)$ of 4.2 ± 0.4 km/s. It has $\sigma_{obs} = 125$ m/s and $\sigma_{meas} = 77$ m/s. Errors shown include the mean σ_{jitter}.

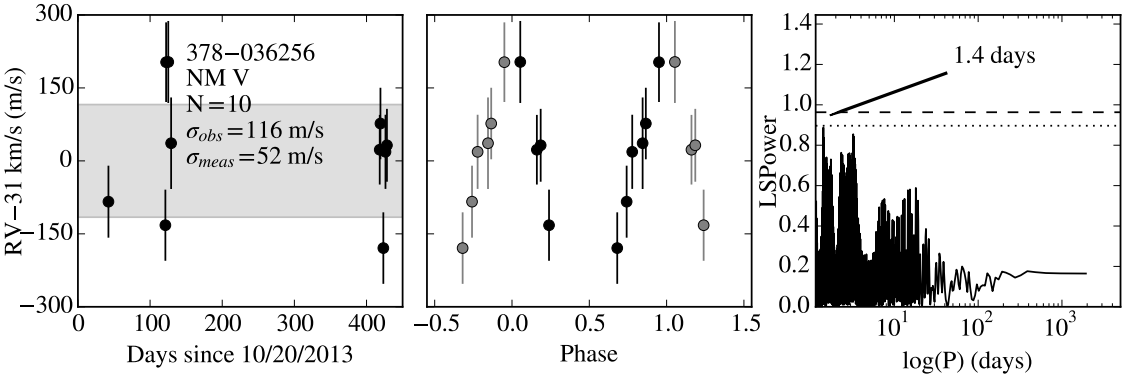

Figure B.113: 378-036256 is a non-member in NGC 2422 with a T_{eff} of 5002^{+19}_{-17} K and a $v_r \sin(i)$ of 3.4 ± 0.3 km/s. It has $\sigma_{obs} = 116$ m/s and $\sigma_{meas} = 52$ m/s. The most significant periodogram peak is at 1.4 days. Grey points are duplicated data to guide the eye. Errors shown include the mean σ_{jitter}.

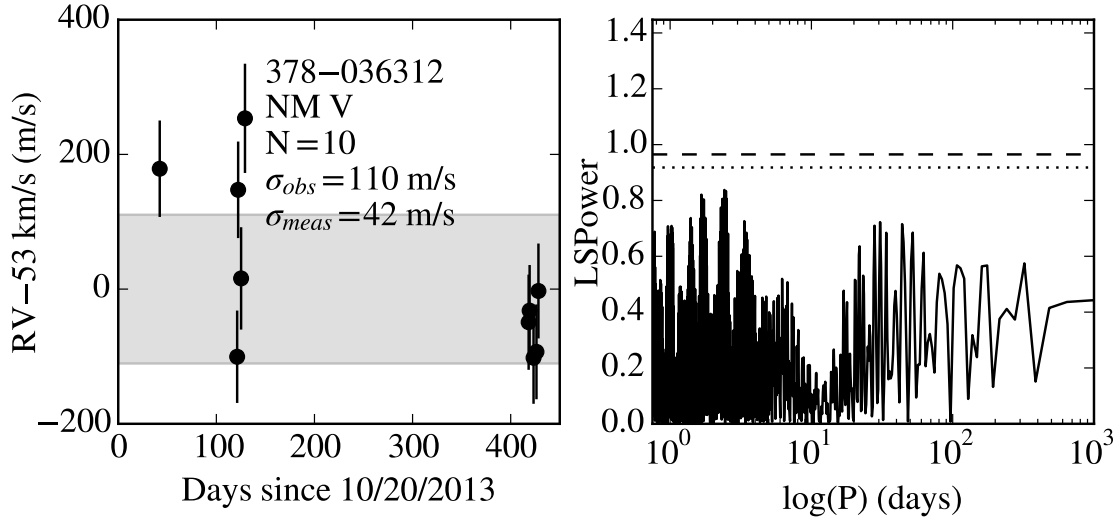

Figure B.114: 378-036312 is a non-member in NGC 2422 with a T_{eff} of 5289^{+23}_{-20} K and a $v_r \sin(i)$ of 3.5 ± 0.2 km/s. It has $\sigma_{obs} = 110$ m/s and $\sigma_{meas} = 42$ m/s. Errors shown include the mean σ_{jitter}.

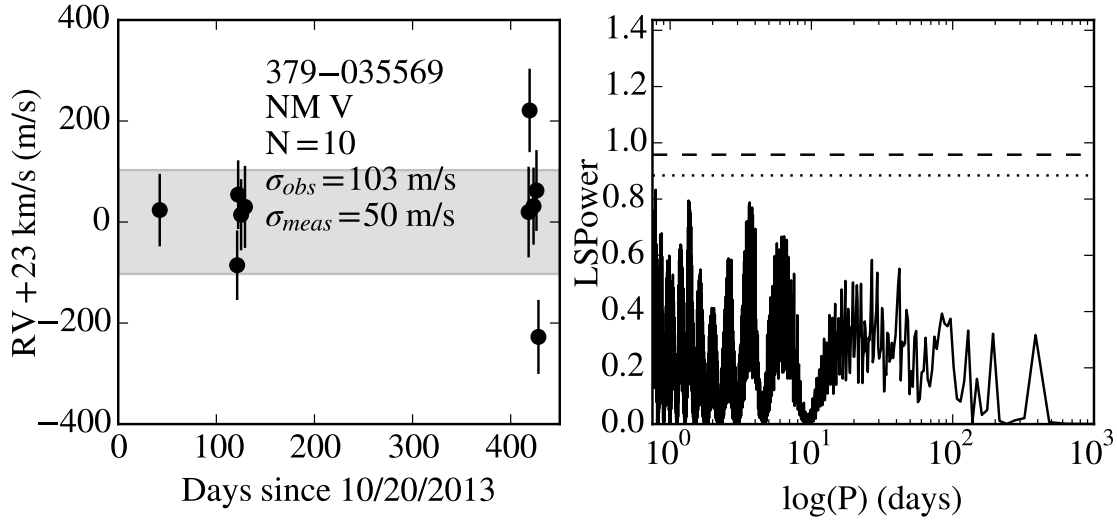

Figure B.115: 379-035569 is a non-member in NGC 2422 with a T_{eff} of 5064^{+19}_{-14} K and a $v_r \sin(i)$ of 3.0 ± 0.4 km/s. It has $\sigma_{obs} = 103$ m/s and $\sigma_{meas} = 50$ m/s. Errors shown include the mean σ_{jitter}.

BIBLIOGRAPHY

BIBLIOGRAPHY

Aaronson, M. 1983, ApJ, 266, L11

Adams, F. C., & Laughlin, G. 2006, *ApJ*, 649, 1004

Adibekyan, V. Z., Sousa, S. G., Santos, N. C., et al. 2012, *A&A*, 545, A32

Bailey, J. I. I., White, R. J., Blake, C. H., et al. 2012, ApJ, 749, 16

Bailey, J. I., Mateo, M. L., Bagish, A. P., Crane, J. D. & Slater, C. T. in (McLean, I. S., Ramsay, S. K. & Takami, H.) SPIE, 2012, SPIE Astronomical Telescopes + Instrumentation, 8446, 84465G

Bailey, J. I., Mateo, M., White, R. J., et al. 2016, AJ, submitted

Baruteau, C., Crida, A., Paardekooper, S.-J., et al. 2014, Protostars and Planets VI, 667

Bean, J. L., Seifahrt, A., Hartman, H., et al. 2010, *ApJ*, 713, 410

Bechtol, K., Drlica-Wagner, A., Balbinot, E., et al. 2015, *ApJ*, 807, 50

Belokurov, V., Zucker, D. B., Evans, N. W., et al. 2007, *ApJ*, 654, 897

Bertaux, J. L., Lallement, R., Ferron, S., Boonne, C. & Bodichon, R. 2014, A&A, 564, 46

Blake, C. H., Charbonneau, D., White, R. J., Marley, M. S., & Saumon, D. 2007, *ApJ*, 666, 1198

Blake, C. H., Charbonneau, D., & White, R. J. 2010, *ApJ*, 723, 684

Blanc, G., et al. 2016, in preparation

Bonnivard, V., Combet, C., Maurin, D., et al. 2015, *ApJ*, 808, L36

Boss, A. P. 1997, Science, 276, 1836

Bragaglia, A., & Tosi, M. 2006, *AJ*, 131, 1544

Briceño, C., in preparation

Brucalassi, A., Pasquini, L., Saglia, R., et al. 2014, *A&A*, 561, L9

Butler, R. P., Marcy, G. W., Williams, E., et al. 1996, PASP, 108, 500

Casagrande, L., Ramrez, I., Melndez, J., Bessell, M. & Asplund, M. 2010, A&A, 512, 54

Casagrande, L., Schoenrich, R., Asplund, M., et al. 2011, *A&A*, 530, A138

Chabrier, G., Johansen, A., Janson, M., & Rafikov, R. 2014, Protostars and Planets VI, 619

Charbonneau, D., Brown, T. M., Burrows, A., & Laughlin, G. 2007, Protostars and Planets V, 701

Ciardi, D. R., van Eyken, J. C., Barnes, J. W., et al. 2015, *ApJ*, 809, 42

Ciddor, P. E. 1996, Applied Optics LP, 35, 1566

Cochran, W. D. 1988, ApJ, 334, 349

Coelho, P. R. T. 2014, *MNRAS*, 440, 1027

Crockett, C. J., Mahmud, N. I., Prato, L., et al. 2011, *ApJ*, 735, 78

Crockett, C. J., Mahmud, N. I., Prato, L., et al. 2012, *ApJ*, 761, 164

Damiani, F., Flaccomio, E., Micela, G., et al. 2003, *ApJ*, 588, 1009

Duchêne, G., Delgado-Donate, E., Haisch, K. E., Jr., Loinard, L., & Rodríguez, L. F. 2007, Protostars and Planets V, 379

Duchêne, G., & Kraus, A. 2013, *ARA&A*, 51, 269

Eastman, J., Gaudi, B. S., & Agol, E. 2013, *PASP*, 125, 83

Edlén, B. 1966, Metrologia, 2, 71

Fabricant, D., Fata, R., Roll, J., et al. 2005, *PASP*, 117, 1411

Fabrycky, D., & Tremaine, S. 2007, *ApJ*, 669, 1298

Figueira, P., Pepe, F., Lovis, C., & Mayor, M. 2010, *A&A*, 515, A106

Fortney, J. J., & Nettelmann, N. 2010, *Space Sci. Rev.*, 152, 423

Fortney, J. J., Marley, M. S., Saumon, D., & Lodders, K. 2008, *ApJ*, 683, 1104

Galvagni, M., Hayfield, T., Boley, A., et al. 2012, *MNRAS*, 427, 1725

Ge, J., Thomas, N. B., Li, R., et al. 2015, American Astronomical Society Meeting Abstracts, 225, #409.03

Geller, A. M., Mathieu, R. D., Braden, E. K., et al. 2010, *AJ*, 139, 1383

Głębocki, R., & Gnaciński, P. 2005, 13th Cambridge Workshop on Cool Stars, Stellar Systems and the Sun, 560, 571

Goldreich, P. & Tremaine, S. 1980, *ApJ*, 241, 425

Gray, D. F. 1992, Camb. Astrophys. Ser., Vol. 20

Griffin, R., & Griffin, R. 1973, *MNRAS*, 162, 255

Han, E., Wang, S. X., Wright, J. T., et al. 2014, *PASP*, 126, 827

Helled, R., Bodenheimer, P., Podolak, M., et al. 2014, Protostars and Planets VI, 643

Herbig, G. H., & Soderblom, D. R. 1982, *ApJ*, 252, 610

Hill, J. M., Angel, J. R. P., Scott, J. S., Lindley, D., & Hintzen, P. 1980, *ApJ*, 242, L69

Hillenbrand, L., Isaacson, H., Marcy, G., et al. 2015, 18th Cambridge Workshop on Cool Stars, Stellar Systems, and the Sun, 18, 759

Howell, S. B., Sobeck, C., Haas, M., et al. 2014, *PASP*, 126, 398

Hubeny, I. & Lanz, T. 2011, ascl soft, 09022

Huerta, M., Johns-Krull, C. M., Prato, L., Hartigan, P., & Jaffe, D. T. 2008, *ApJ*, 678, 472

Husser, T. O., Wende-von Berg, S., Dreizler, S., et al. 2013, A&A, 553, A6

Huélamo, N., Figueira, P., Bonfils, X., et al. 2008, *A&A*, 489, L9

Isani, S. 2001, CFHT Director/Agent Model Rev. 3, http://software.cfht.hawaii.edu/director/

Jeffries, R. D., Thurston, M. R. & Hambly, N. C. 2001, A&A, 375, 863

Johnson, J. A., Howard, A. W., Bowler, B. P., et al. 2010, *PASP*, 122, 701

Johnson, C. I., McDonald, I., Pilachowski, C. A., et al. 2015, *AJ*, 149, 71

Johnson, C. I., Rich, R. M., Pilachowski, C. A., et al. 2015, *AJ*, 150, 63

Jones, A., Noll, S., Kausch, W., Szyszka, C., & Kimeswenger, S. 2013, *A&A*, 560, A91

Jurić, M., & Tremaine, S. 2008, *ApJ*, 686, 603

Kharchenko, N. V., Piskunov, A. E., Rser, S., Schilbach, E. & Scholz, R. D. 2005, A&A, 438, 1163

Kley, W., & Nelson, R. P. 2012, *ARA&A*, 50, 211

Koposov, S. E., Belokurov, V., Torrealba, G., & Evans, N. W. 2015, *ApJ*, 805, 130

Kordopatis, G., Gilmore, G., Steinmetz, M., et al. 2013, *AJ*, 146, 134

Kounkel, M., Hartmann, L. W., Tobin, J. J., et al. 2016, *ApJ*, submitted

Kroupa, P., & Petr-Gotzens, M. G. 2011, *A&A*, 529, A92

Kurucz, R. L. 2005, Memorie della Societa Astronomica Italiana Supplementi, 8, 189

Lagrange, A.-M., Meunier, N., Chauvin, G., et al. 2013, *A&A*, 559, A83

Lagrange, A.-M., Meunier, N., Chauvin, G., et al. 2013, *A&A*, 559, A83

Lang, D., Hogg, D. W., Mierle, K., Blanton, M., & Roweis, S. 2010, *AJ*, 139, 1782

Lin, D. N. C., Bodenheimer, P., & Richardson, D. C. 1996, *Nature*, 380, 606

Lindegren, L., Lammers, U., Hobbs, D., O'Mullane, W., Bastian, U., Hernandez, J. 2012, A&A, 538, 78

Lindegren, L. 2010, IAUS, 261, 296

Loktin, A. V., Gerasimenko, T. P., & Malysheva, L. K. 2001, Astronomical and Astrophysical Transactions, 20, 607

Mahmud, N. I., Crockett, C. J., Johns-Krull, C. M., et al. 2011, *ApJ*, 736, 123

Mann, A. W., Gaidos, E., Mace, G. N., et al. 2015, arXiv:1512.00483

Markwardt, C. B. 2009, Astronomical Data Analysis Software and Systems XVIII, 411, 251

Marley, M. S., Fortney, J., Seager, S., & Barman, T. 2007, Protostars and Planets V, 733

Mateo, M., Olszewski, E. W., & Walker, M. G. 2008, ApJ, 675, 201

Mateo, M., Bailey, J. I., Crane, J., et al. in (McLean, I. S., Ramsay, S. K. & Takami, H.)
SPIE, 2012, SPIE Astronomical Telescopes + Instrumentation, 8446, 84464Y84464Y19

McConnachie, A. W. 2012, *AJ*, 144, 4

Meibom, S., Torres, G., Fressin, F., et al. 2013, *Nature*, 499, 55

Meynet, G., Mermilliod, J.-C., & Maeder, A. 1993, *A&AS*, 98, 477

Mizuno, H. 1980, PThPh, 64, 544

Mordasini, C., Alibert, Y., Klahr, H., & Henning, T. 2012, *A&A*, 547, A111

Environmental Modeling Center, 2003: The GFS Atmospheric Model. NCEP Office Note 442, Global Climate and Weather Modeling Branch, EMC, Camp Springs, Maryland.

Nelder, J. A. & Mead, R. 1965, Computer Journal, 7, 308

Neves, V., Santos, N. C., Sousa, S. G., Correia, A. C. M., & Israelian, G. 2009, *A&A*, 497, 563

Nissen, P. E. 1988, *A&A*, 199, 146

Noll, S., Kausch, W., Barden, M., et al. 2012, *A&A*, 543, A92

Paegert, M., Stassun, K. G., De Lee, N., et al. 2015, *AJ*, 149, 186

Parker, R. J., Goodwin, S. P., Kroupa, P., & Kouwenhoven, M. B. N. 2009, *MNRAS*, 397, 1577

Pasquini, L., Avila, G., Blecha, A., et al. 2002, The Messenger, 110, 1

Paulson, D. B. & Yelda, S. 2006, *PASP*, 118, 706

Paulson, D. B., Cochran, W. D., & Hatzes, A. P. 2004, *AJ*, 127, 3579

Paunzen, E., Heiter, U., Netopil, M., & Soubiran, C. 2010, *A&A*, 517, A32

Pepe, F., Lovis, C., Sgransan, D., et al. 2011, A&A, 534, A58

Pickering, E. C., 1890, Annals of Harvard College Observatory, 27, 1

Pillitteri, I., Micela, G., Damiani, F., & Sciortino, S. 2006, *A&A*, 450, 993

Prato, L., Huerta, M., Johns-Krull, C. M., et al. 2008, *ApJ*, 687, L103

Prisinzano, L., Micela, G., Sciortino, S. & Favata, F. 2003, A&A, 404, 927

Queloz, D., Allain, S., Mermilliod, J.-C., Bouvier, J., & Mayor, M. 1998, *A&A*, 335, 183

Quinn, S. N., White, R. J., Latham, D. W., et al. 2012, *ApJ*, 756, L33

Quinn, S. N., White, R. J., Latham, D. W., et al. 2014, *ApJ*, 787, 27

Rasio, F. A., & Ford, E. B. 1996, Science, 274, 954

Ribas, I. 2010, Proc. IAU, 5, 3

Robin, A. C., Reylé, C., Derrière, S., & Picaud, S. 2003, *A&A*, 409, 523

Roederer, I. U., Mateo, M., Bailey, J. I., III, et al. 2015, arXiv:1510.06414

Roederer, I. U., Mateo, M., Bailey, J. I., III, et al. 2015, arXiv:1510.06414

Rothman, Gordon, Barbe, et al. 2009, *J. Quant. Spec. Radiat. Transf.*, 110, 533

Santos N. C., Israelian G., Mayor M., et al. 2005, A&A, 437, 1127

Schlafly, E. F., & Finkbeiner, D. P. 2011, *ApJ*, 737, 103

Seifahrt, A., Käufl, H. U., Zängl, G., et al. 2010, The Messenger, 142, 21

Soubiran, C., Jasniewicz, G., Chemin, L., et al. 2013, A&A, 552, 64

Sousa, S. G., Santos, N. C., Mayor, M., et al. 2008, *A&A*, 487, 373

Sung, H., Bessell, M. S., Lee, B.-W. & Lee, S.-G. 2002, AJ, 123, 290

Terndrup, D. M., Pinsonneault, M., Jeffries, R. D., et al. 2002, ApJ, 576, 950

Tsantaki, M., Sousa, S. G., Adibekyan, V. Z., et al. 2013, *A&A*, 555, A150

Udry, S., & Santos, N. C. 2007, *ARA&A*, 45, 397

Valenti, J. A., & Fischer, D. A. 2005, *ApJS*, 159, 141

Walker, M. G., Mateo, M., Olszewski, E. W., et al. 2007, *ApJS*, 171, 389

Walker, M. G., Mateo, M., Olszewski, E. W., Gnedin, O. Y., Wang, X., Sen, B., & Woodroofe, M. 2007, ApJ, 667, L53

Walker, M. G., Mateo, M., & Olszewski, E. W. 2009, AJ, 137, 3100

Walker, M. G., Mateo, M., Olszewski, E. W., et al. 2015, *ApJ*, 808, 108

Walker, M. G., Olszewski, E. W., & Mateo, M. 2015, *MNRAS*, 448, 2717

Walker, M. G., Mateo, M., Olszewski, E. W., et al. *ApJ*, submitted

Wallace, L., Hinkle, K. H., Livingston, W. C. & Davis, S. P. 2011, ApJS, 195, 6

Wang, J., & Fischer, D. A. 2015, *AJ*, 149, 14

Willman, B., Blanton, M. R., West, A. A., et al. 2005, *AJ*, 129, 2692

Wolk, S. J., Harnden, F. R., Jr., Murray, S. S., et al. 2004, *ApJ*, 606, 466

Wright, J. T., Marcy, G. W., Howard, A. W., et al. 2012, *ApJ*, 753, 160

Wright, J. T., Roy, A., Mahadevan, S., et al. 2013, *ApJ*, 770, 119

Zacharias, N., Finch, C. T., Girard, T. M., et al. 2013, AJ, 145, 44

Zucker, D. B., Belokurov, V., Evans, N. W., et al. 2006, *ApJ*, 643, L103

de Laverny, P., Recio-Blanco, A., Worley, C. C., & Plez, B. 2012, *A&A*, 544, A126

van Dokkum, P. G. 2001, *PASP*, 113, 1420